NASA CR- 132345

BOEING

(NASA-CR-132345) ANALYSIS AND TESTING OF AEROELASTIC MODEL STABILITY AUGMENTATION SYSTEMS Final Report (Boeing Co., Wichita, Kans.) ~~167~~ 178 p HC $10.50 CSCL 01A G3/01

N74-11807

Unclas 22456

NASA CR- 132345

THE BOEING COMPANY
WICHITA DIVISION

CODE IDENT. NO. 81205

NUMBER D3-9245 REV LTR

INITIAL RELEASE DATE OCT 15 1973

TITLE Analysis and Testing of Aeroelastic Model Stability Augmentation Systems - Final Report

MODEL CONTRACT NAS1-11833

ISSUE NO. ISSUED TO

PREPARED BY Francis D. Sevart Suresh M. Patel
F. Sevart S. Patel

SUPERVISED BY G.E. Hodges
G. E. Hodges

APPROVED BY G.O. Thompson
G. O. Thompson

APPROVED BY

Unclassified

SECURITY CLASSIFICATION OF THIS PAGE (When Data Entered)

REPORT DOCUMENTATION PAGE		READ INSTRUCTIONS BEFORE COMPLETING FORM
1. REPORT NUMBER D3-9245	2. GOVT ACCESSION NO.	3. RECIPIENT'S CATALOG NUMBER
4. TITLE (and Subtitle) ANALYSIS AND TESTING OF AEROELASTIC MODEL STABILITY AUGMENTATION SYSTEMS - FINAL REPORT		5. TYPE OF REPORT & PERIOD COVERED Final Report 6-28-72 thru 9-28-73 6. PERFORMING ORG. REPORT NUMBER D3-9245
7. AUTHOR(s) Francis D. Sevart Suresh M. Patel		8. CONTRACT OR GRANT NUMBER(s) NAS1-11833
9. PERFORMING ORGANIZATION NAME AND ADDRESS The Boeing Company 3801 S. Oliver Wichita, Kansas 67210		10. PROGRAM ELEMENT, PROJECT, TASK AREA & WORK UNIT NUMBERS
11. CONTROLLING OFFICE NAME AND ADDRESS NASA-Langley Research Center Hampton, Virginia 23665		12. REPORT DATE 8 October 1973 13. NUMBER OF PAGES 166
14. MONITORING AGENCY NAME & ADDRESS(if different from Controlling Office)		15. SECURITY CLASS. (of this report) Unclassified 15a. DECLASSIFICATION/DOWNGRADING SCHEDULE

16. DISTRIBUTION STATEMENT (of this Report)

Distribution Unlimited

17. DISTRIBUTION STATEMENT (of the abstract entered in Block 20, if different from Report)

18. SUPPLEMENTARY NOTES

19. KEY WORDS (Continue on reverse side if necessary and identify by block number)

Aeroelastic Models
Flutter Suppression Systems
Ride Control Systems
Maneuver Load Control Systems

20. ABSTRACT (Continue on reverse side if necessary and identify by block number)

This document is the final report of analyses and testing of stability augmentation systems accomplished under NASA-Langley Contract NAS1-11833 and is intended to be used as a working reference in future program activities. The document describes testing of Dr. Nissim's flutter suppression concept accomplished on the NASA 1/17 scale supersonic transport wing model. Analytical results show a 9.0 percent increase in model flutter true airspeed at Mach - 0.9. An initial evaluation of a conventional flutter suppression system shows that the flutter mode damping ratio can be increased to $\zeta = 0.2$ using leading

20. (Cont.)

and trailing edge control surfaces at a speed 9.8 percent above the flutter speed. Further analysis of the conventional system is required to determine the actual flutter speed improvement and to define a configuration for testing on the wing model.

A ride control system using horizontal canards was analyzed for the 1.30 scale B-52E aeroelastic model and the full scale CCV airplane. The ride control system reduces pilot station RMS vertical acceleration due to random gusts more than 30 percent. Analysis of the full scale airplane maneuver load control system shows a reduction of 10 percent in the wing root design moment.

LIMITATIONS

Distribution unlimited.

THIS DOCUMENT IS CONTROLLED BY 75620 - Flight Controls Development
ORGANIZATION

ALL REVISIONS TO THIS DOCUMENT SHALL BE APPROVED BY THE ABOVE NOTED ORGANIZATION PRIOR TO RELEASE.

ABSTRACT

This document is the final report of analyses and testing of stability augmentation systems accomplished under NASA-Langley Research Center Contract NAS1-11833 and is intended to be used as a working reference in future program activities. The document describes testing of Dr. Nissim's flutter suppression concept accomplished on the NASA 1/17 scale supersonic transport wing model. Analytical results show a 9.0 percent increase in model flutter true airspeed at Mach = 0.9. An initial evaluation of a conventional flutter suppression system shows that the flutter mode damping ratio can be increased to $\zeta = 0.2$ using leading and trailing edge control surfaces at a speed 9.8 percent above the flutter speed. Further analysis of the conventional system is required to determine the actual flutter speed improvement and to define a configuration for testing on the wing model.

A ride control system using horizontal canards was analyzed for the 1/30 scale B-52E aeroelastic model and the full scale CCV airplane. The ride control system reduces pilot station RMS vertical acceleration due to random gusts more than 30 percent. Analysis of the full scale airplane maneuver load control system shows a reduction of 10 percent in the wing root design moment.

RETRIEVAL REFERENCE WORDS:
Aeroelastic Models
Flutter Suppression Systems
Ride Control Systems
Maneuver Load Control Systems

REV LTR:

TABLE OF CONTENTS

TABLE OF CONTENTS

FIGURES

FIGURES (Cont.)

FIGURES (Cont.)

FIGURES (Cont.)

TABLES

1.0 INTRODUCTION

This document is the final report of stability augmentation system analyses and testing accomplished from 28 June 1972 to 28 Sept.1973 under NASA Langley Research Center Contract NAS1-11833. This study is a continuation of work accomplished under NASA Contract NAS1-10885 from 25 May 1971 to 24 May 1972 (reference 1) and is intended to be used as a working reference in future program activities.

Section 2.0 describes flutter suppression system analysis and synthesis conducted on the NASA one-seventeenth scale supersonic transport wing model. Mechanization and testing of the leading and trailing edge surface actuation systems are also discussed in this section.

Section 3.0 discusses the ride control system analyses for a 375,000 pound gross weight B-52E airplane and the NASA one-thirtieth scale B-52E aeroelastic model. Mechanization and testing of the model horizontal canards are also described in Section 3.0.

Analyses of the B-52E airplane maneuver load control system are contained in Section 4.0.

2.0 SST WING MODEL FLUTTER SUPPRESSION SYSTEM

This section describes an evaluation study of the flutter suppression system (FSS) concept developed by Dr. Eliahu Nissim on the NASA one-seventeenth scale supersonic transport (SST) wing model. The study demonstrated feasibility of testing the active flutter mode control system on the SST wing model in the Langley transonic dynamic wind tunnel. The system was mechanized on the model using Boeing-developed electrohydraulic actuation systems for the model control surfaces. Wind tunnel testing was conducted with Boeing support in January and May, 1973.

2.1 Background and Introduction

An analytical study was conducted under Contract NAS1-10885 in 1971 and 1972 to determine performance of Dr. Nissim's flutter suppression system on a five degree-of-freedom SST wing math model. The system required complex feedback gains and ideal actuation systems. Results of this study are contained in Section 2.0 of Boeing Document D3-8884 (Reference 1). Based on these results, midspan control surfaces and feedback accelerometers located along the inboard edge of the surfaces at 30 percent and 70 percent of the wing chord were selected for wind tunnel demonstration.

Analyses presented in this report were conducted for a nine-degree-of-freedom math model with the flutter suppression system approximated for practical mechanization and the ideal system as specified by Dr. Nissim. Primary objectives of the current analyses were to determine open and closed loop flutter dynamic pressures at Mach 0.9 and 0.6 using the non-ideal system. The results, presented in Section 2.3, show that flutter dynamic pressure increases of 18.4 percent at Mach 0.9 and 15.1 percent at Mach 0.6 can be attained with the flutter suppression system.

An analog simulation study was conducted to evaluate performance of the non-ideal flutter suppression system on the model in the presence of wind tunnel turbulence. Test condition of Mach 0.9 and 136 psf dynamic pressure was selected for the study. Section 2.4 describes the simulated equations, approximated flutter suppression system and results of the study.

A study was initiated to synthesize an independent flutter suppression system with real gains and linear filters using the surfaces and sensors used in the NASA system. Results of this study are discussed in Section 2.5.

Section 2.6 discusses development of electrohydraulic actuation systems for the model leading and trailing edge control surfaces, and installation of the systems in the model.

2.2 Math Model

Ground vibration tests (GVT) of the wing model with the control surface actuation systems installed were conducted at NASA to measure plate type mode shapes of the first ten vibration modes. Generalized mass and stiffness estimated from the GVT data were used to generate equations of motion for the wing model for Mach 0.9

and 0.6. The equations were written with wind tunnel velocity and fluid mass density as explicit functions to permit variations in dynamic pressure by varying either the velocity or the mass density, or both. A 95 percent Freon and 5 percent air environment was assumed for the wind tunnel.

In the equations, structural damping was assumed to be zero. Doublet-lattice unsteady lifting surface theory was used to obtain aerodynamic loading. The resulting complex matrices of unsteady aerodynamic coefficients were transformed through a curve fitting procedure to rational functions of the Laplace transform operator, S, with fourth order denominators. The equations were then rearranged to the form

$$\left(s^2[M+\rho C_1] + s[D+\rho V C_2] + [K+\rho V^2 C_3] + \rho V^2 \sum_{K=1}^{4} [D_K]\left[\frac{s}{s+Vd_{Kj}}\right]\right)\{q_j(s)\}$$

$$+ \rho V\left([R_0] + \sum_{i=1}^{4} [R_i]\left[\frac{s}{s+Vb_i}\right]\right)\{W_g\} = \{0\}$$

where:

$\{q_j(s)\}$ = Elastic and control surface displacement degrees-of-freedom

s = Laplace transform operator

ρ = Fluid mass density (95% Freon, 5% air)

V = Velocity of fluid relative to the wind

W_g = Vertical gust

$[M], [K], [D]$ = Structural mass, stiffness, and damping

$[C_1], [C_2], [C_3]$ = Aerodynamic parameters

$[b_i], [d_{Kj}]$ = Lift growth parameters

$[R_0]$ = Vertical gust coefficients

$[R_i], [D_K]$ = Parameters associated with unsteady aerodynamics.

Numerical values of the matrix elements for the two test conditions are presented in Section 2.7. Locations of the control surfaces and doublet-lattice panels are shown in Figure 2.1. The sign convention used in the equations is:

X - Positive aft

Y - Positive outboard

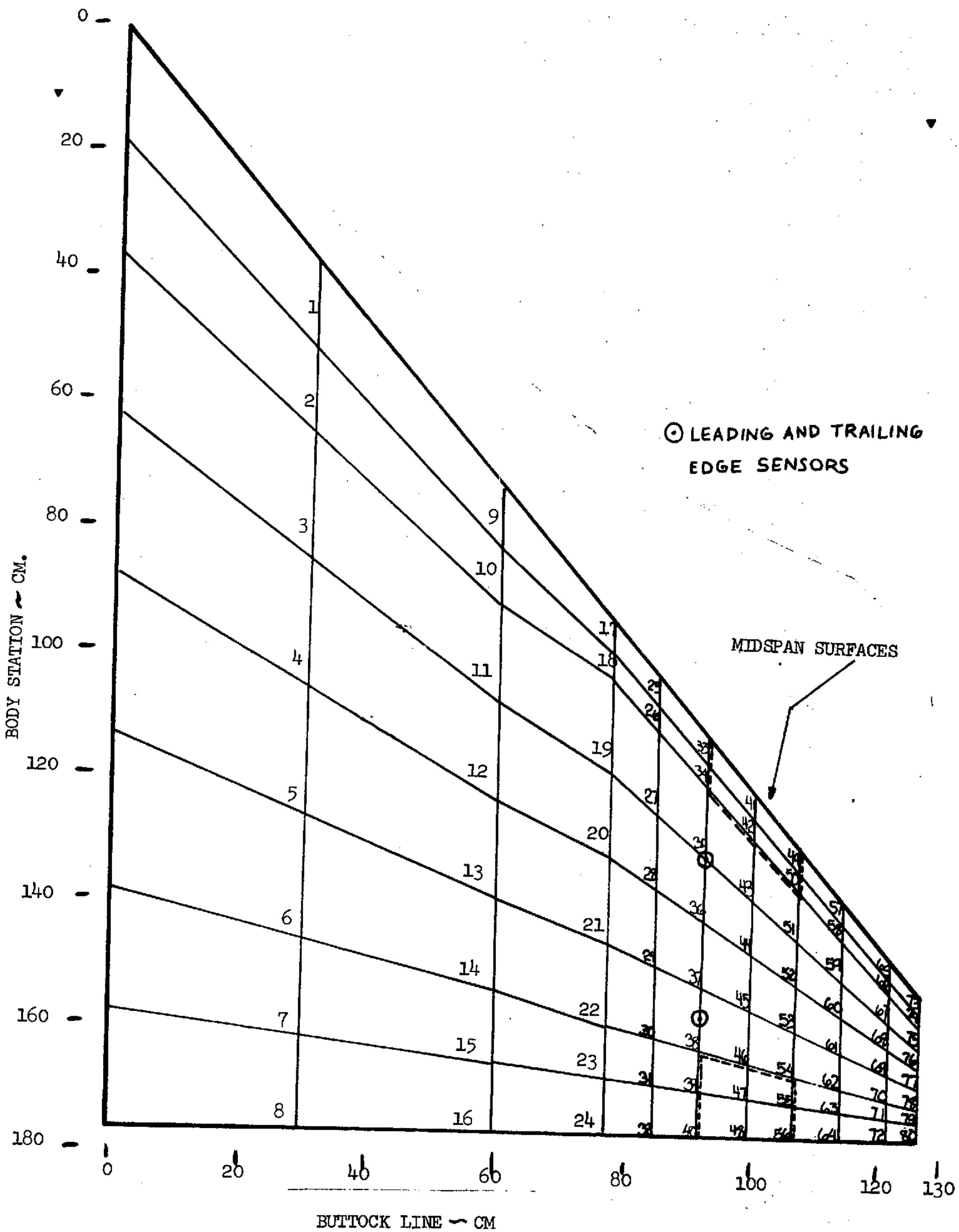

FIGURE 2.1: DOUBLET-LATTICE PANELS

Z - Positive up

Trailing edge surface displacement - Positive trailing edge down

Leading edge surface displacement - Positive leading edge up

The spanwise lengths of the two control surfaces included in the equations of motion were 5.88 inches or 11.76 percent of the wing semispan. The trailing edge surface width was 20 percent of wing chord. However, a constant width of 3.65 inches was used for the leading edge surface so that the surface could be installed in the model without cutting the aluminum alloy plate that formed the model elastic structure.

2.3 Flutter Suppression System Evaluation

All model analyses were conducted with the tenth elastic mode excluded from the equations of motion because the generalized mass of this mode could not be accurately estimated from the GVT data.

The ideal flutter suppression system (Reference 1) required feedback variables proportional to displacements, but in phase with rates. Since mechanization of a constant phase lead with constant gains at all frequencies was not practical, a method was developed which closely approximated the ideal system in the flutter frequency range. The approximation was based on the assumption that as the flutter condition was approached, the sensor outputs would be primarily sinusoidal signals at the flutter mode frequency. For a sine wave, the 90 degree phase lead can be obtained by dividing the signal derivative by its frequency in radians per second. Therefore, the imaginary gains of the control law were approximated by S/ω, where 'S' is the Laplace operator and 'ω' is the flutter mode frequency in radians per second.

A constant frequency of 75 radians per second was assumed for analyses at both conditions. The following transfer function represented the leading and trailing edge actuation system:

$$\frac{\delta_{Surface}}{\delta_{Command}} = \frac{.8\ (S + 10)(408)^2}{(S + 8)(S^2 + (.7)(408)\ S + 408^2)} \quad \frac{\text{deg}}{\text{deg}}$$

Accelerometers were used for feedback sensors and the sensor outputs were integrated to obtain rates and displacements. Integration was mechanized using, $S/(S^2 + 2S + 1)$, to reduce low frequency drift in the closed loop system. Figure 2.2 is a block diagram of the mechanized flutter suppression system.

2.3.1 Mach 0.9 FSS Analysis

Analyses were conducted at Mach 0.9 using the approximated FSS described in Section 2.3. The fluid velocity was assumed constant at 457 fps and the dynamic pressure was varied by changing the wind tunnel fluid density.

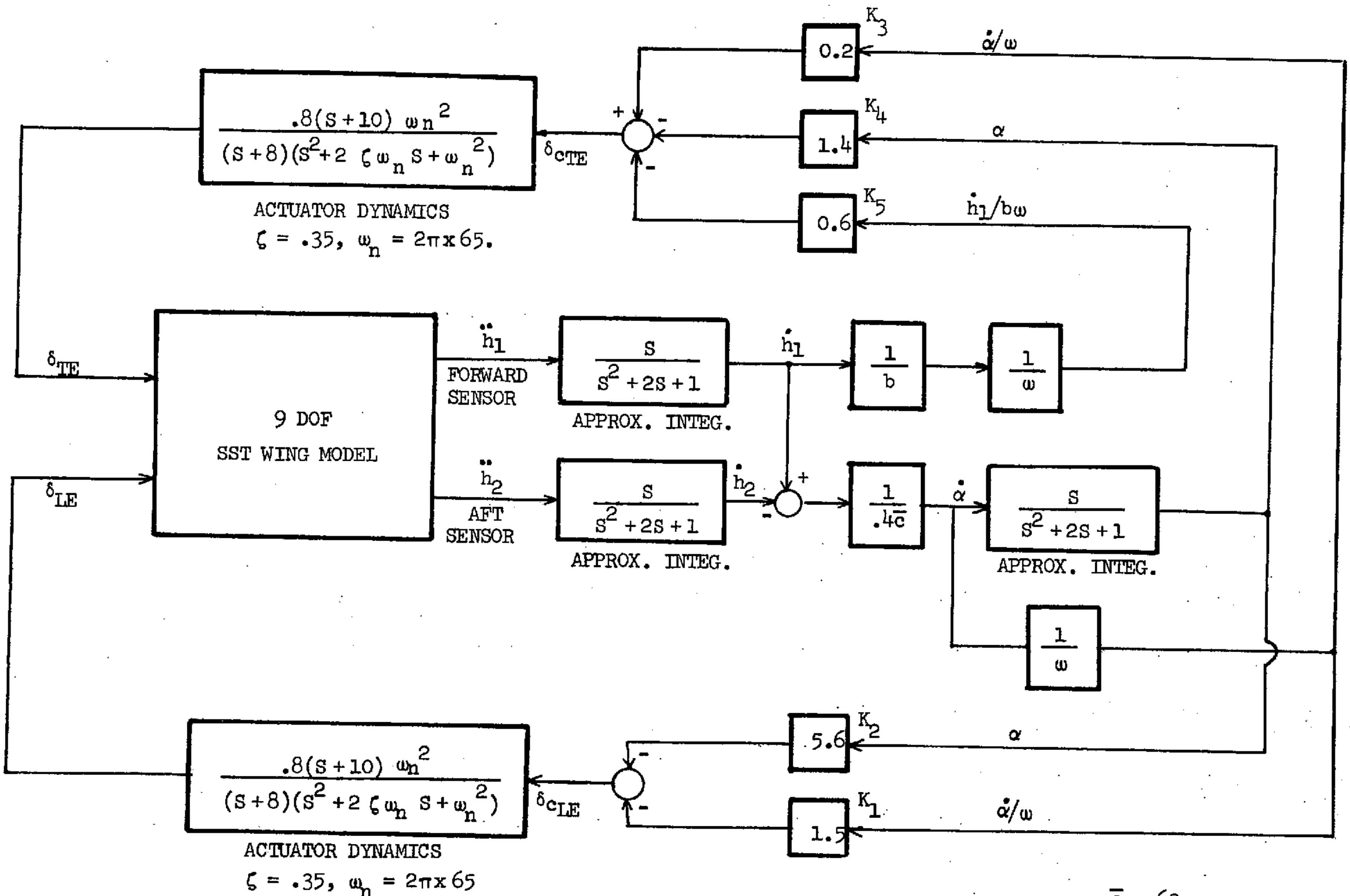

$\bar{c}$ = 63 cm

b = $\frac{1}{2}\bar{c}$

ω = 75 Rad/Sec

FIGURE 2.2 : MECHANIZED FLUTTER SUPPRESSION SYSTEM BLOCK DIAGRAM

Figure 2.3 illustrates the stability behavior of the open and closed loop model characteristic roots with increase in dynamic pressure. The open and closed loop dynamic pressure root locus of the flutter mode is expanded in Figure 2.4. The open loop first elastic mode crosses the imaginary axis at 141.5 psf dynamic pressure and the closed loop flutter dynamic pressure is 167.5 psf. This represents an increase of 18.4 percent in dynamic pressure and nine percent in wind tunnel flutter speed. The closed loop characteristic roots were also obtained with the following FSS variations:

a. Ideal FSS at 135 and 155 psf dynamic pressures.

b. Twice nominal feedback gains at 125, 145, 155 and 170 psf dynamic pressures.

c. Washouts with time constants of 1, 2 and 5 Hz included in both FSS channels.

The effects of gains and washout time constant variations and a comparison of ideal and approximated FSS are shown in Table 2-I. Figure 2.5 shows plots of open and closed loop flutter mode damping ratio versus dynamic pressure.

2.3.2 Mach 0.6 FSS Analysis

The FSS shown in Figure 2.2 was also used for Mach 0.6 analysis. Wind tunnel fluid velocity was constant at 307.6 fps and dynamic pressure was varied by changing wind tunnel fluid mass density.

The open and closed loop dynamic pressure root loci, Figures 2.6 and 2.7, show similar root locus for the flutter mode. The second vibration mode becomes unstable at 185.5 psf with the FSS off, but the flutter dynamic pressure increases to 213.5 psf with the FSS on. Therefore, 15.1 percent increase in flutter dynamic pressure and 7.3 percent increase in flutter speed are attained with the FSS. Figure 2.8 shows open and closed loop flutter mode damping ratios as a function of wind tunnel dynamic pressure.

2.4 Analog Simulation Study

An analog simulation study was conducted to evaluate the flutter suppression system as it would be mechanized for the wind tunnel testing. The five degree-of-freedom math model developed under Contract NAS1-10885 (see Reference 1) was used with the unsteady aerodynamics omitted. These equations were used because the simulation study was conducted before the new equations were generated. The feedback control law was approximated by a period measuring system to estimate the instantaneous frequency of the feedback signal. Actuator and preamplifier dynamics and approximate integrators were included in the simulation. Wind tunnel turbulence was simulated by low frequency (0.1 to 32 Hz) white noise. Figure 2.9 shows a block diagram of the closed loop system. The actuator dynamics shown in the block diagram were based on preliminary estimates of the actuation system capability.

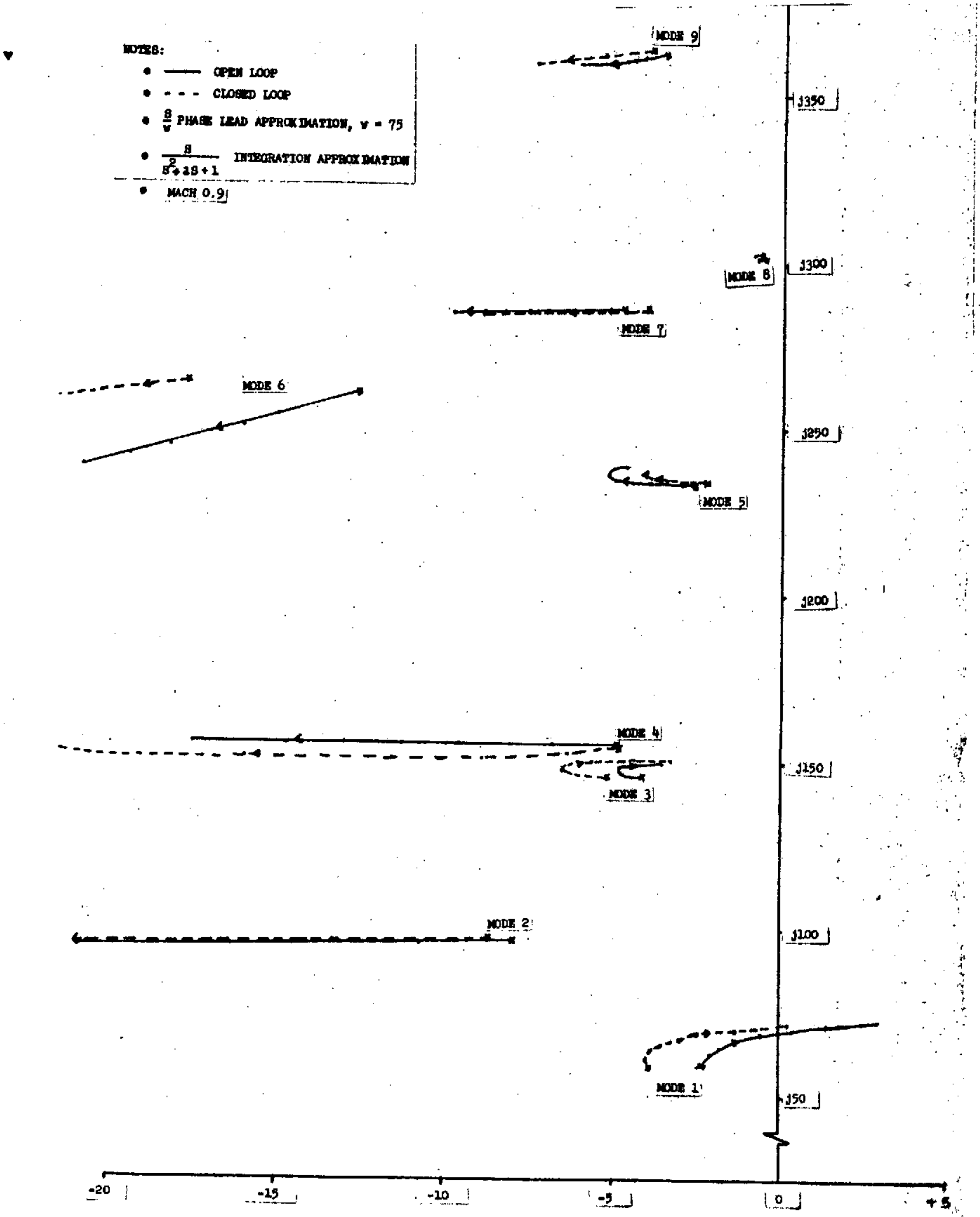

FIGURE 2.3: MACH 0.9 DYNAMIC PRESSURE ROOT LOCUS

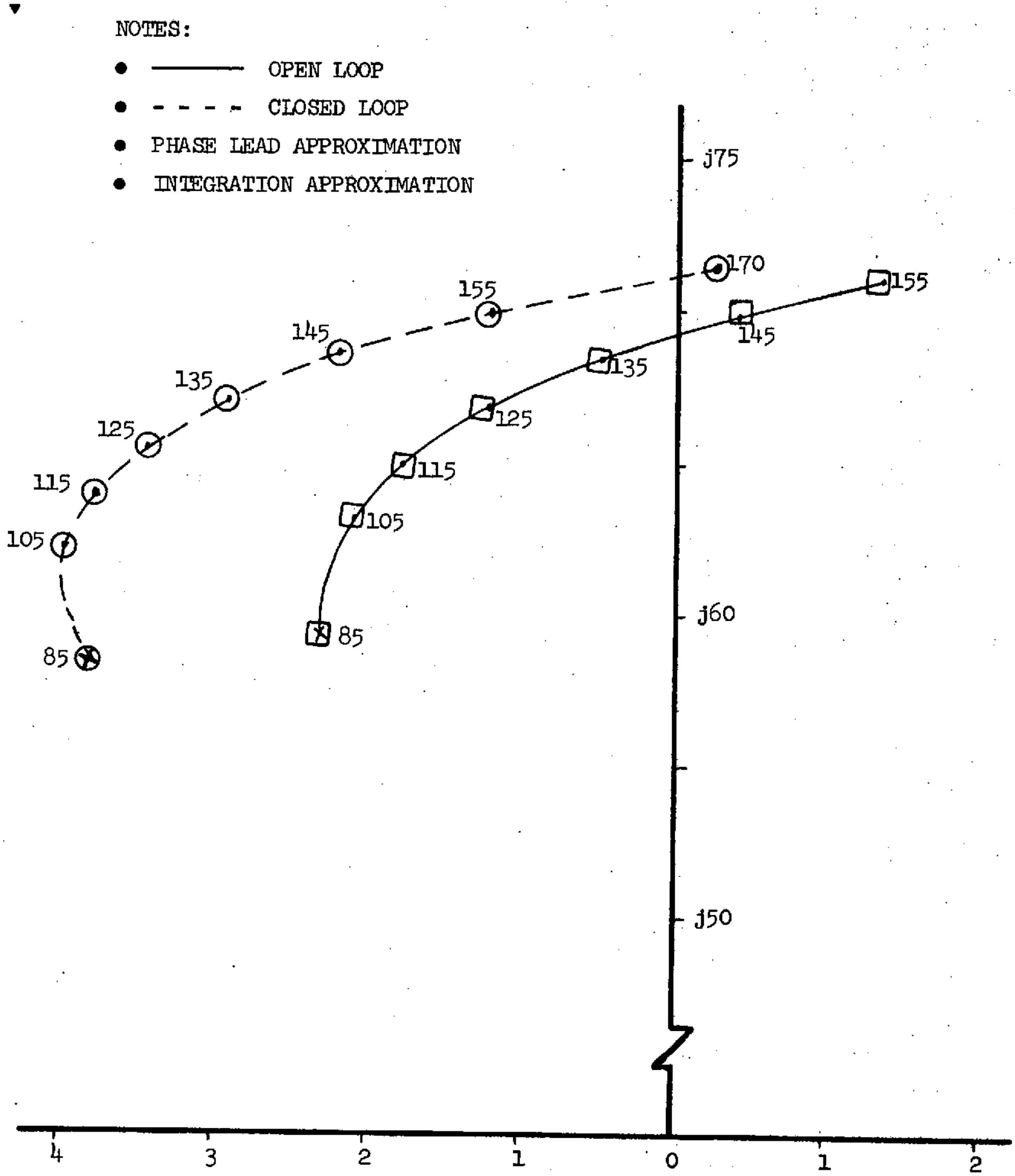

FIGURE 2.4 MACH 0.9 FLUTTER MODE DYNAMIC PRESSURE ROOT LOCUS

TABLE 2-I : FLUTTER MODE DAMPING RATIO

MACH 0.9

DYNAMIC PRESSURE psf	OPEN LOOP	CLOSED LOOP					
		IDEAL FSS	APPROXIMATED FSS				
			NOMINAL GAIN	NOMINAL GAIN X 2	1 HZ WASHOUT	2 HZ WASHOUT	5 HZ WASHOUT
85	0.039		0.066		0.064		0.053
105	0.034		0.065		0.063		0.050
115	0.028		0.061		0.059		0.046
125	0.019		0.054	0.099	0.052		0.039
135	0.008	0.053	0.045		0.043		0.029
145	-0.0048		0.0327	0.082	0.0309	0.0282	0.0177
155	-0.019	0.0301	0.019	0.069	0.0170	0.0145	0.0043
170	-0.0404		-0.003	0.048	-0.003	-0.007	

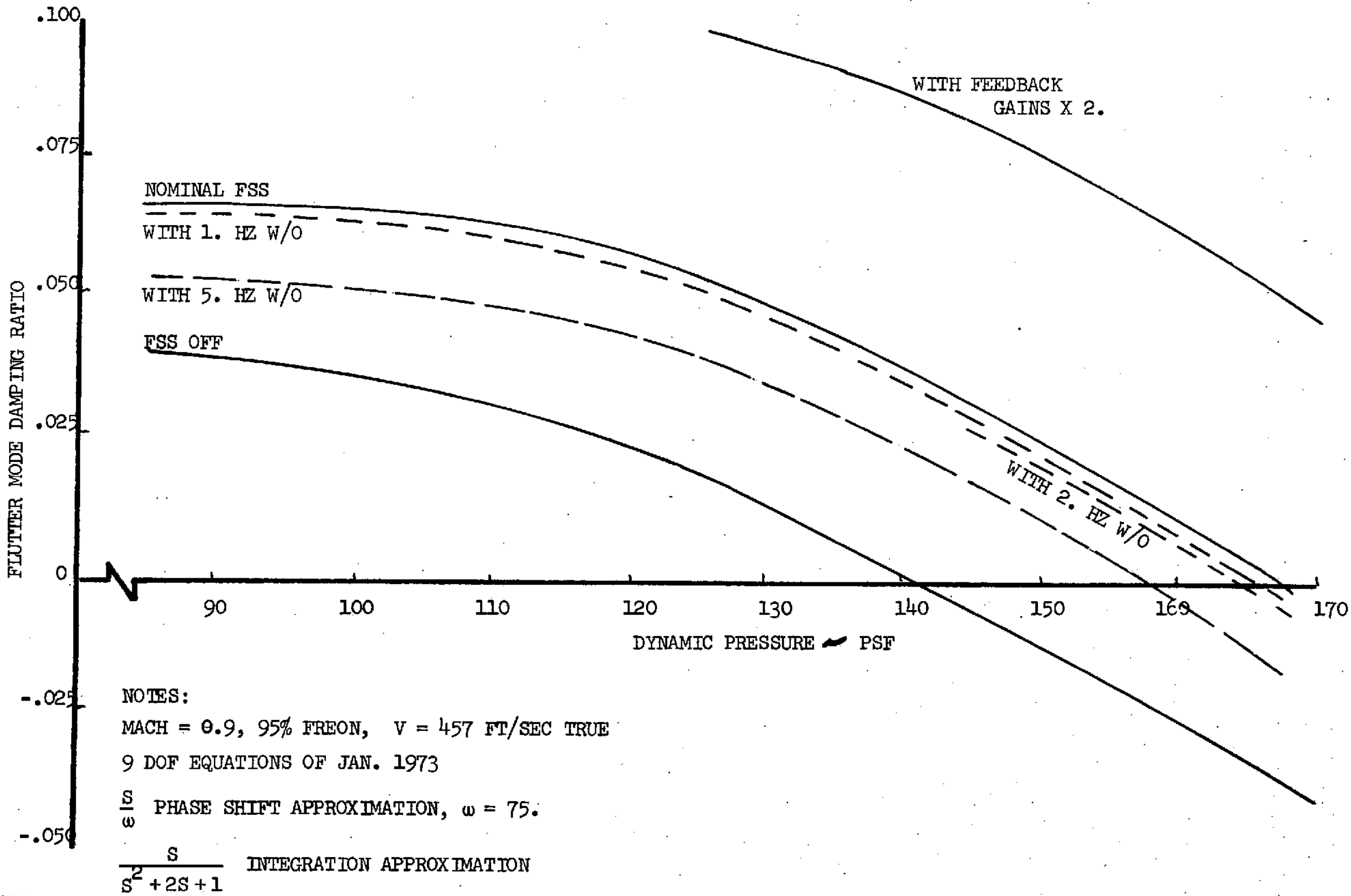

FIGURE 2.5: FLUTTER SUPPRESSION SYSTEM EVALUATION

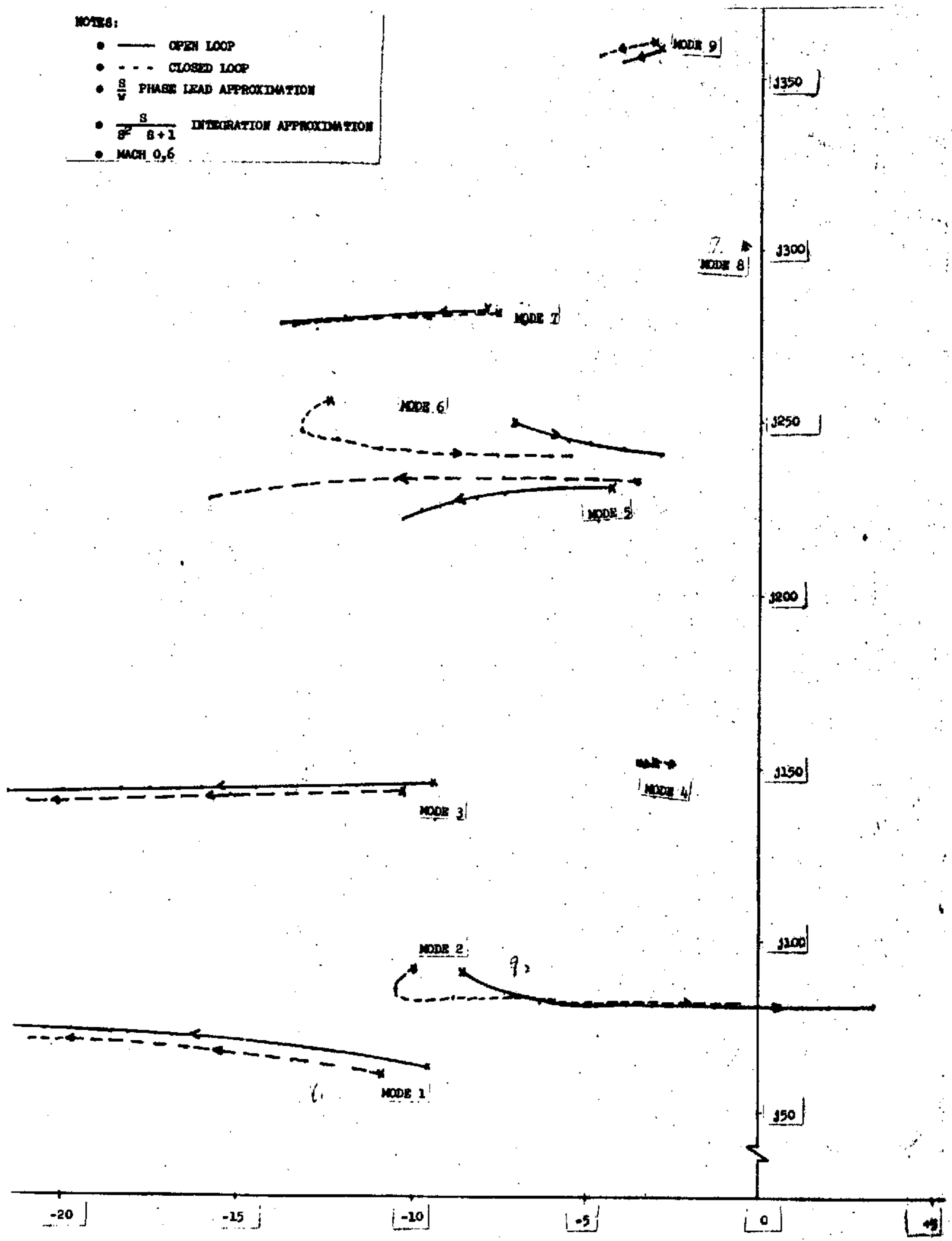

FIGURE 2.6: MACH 0.9 DYNAMIC PRESSURE ROOT LOCUS

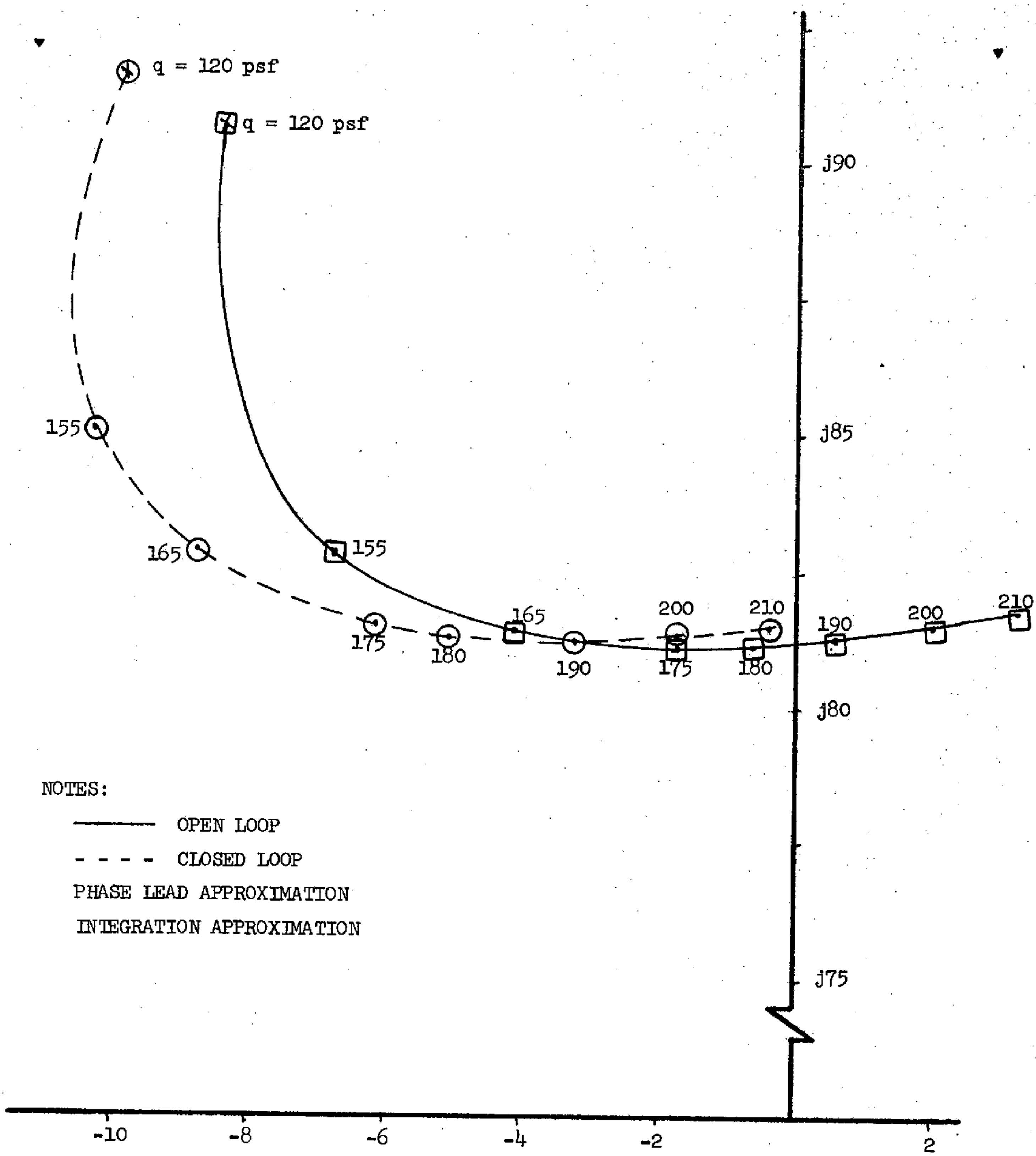

FIGURE 2.7 MACH 0.6 FLUTTER MODE DYNAMIC PRESSURE ROOT LOCUS

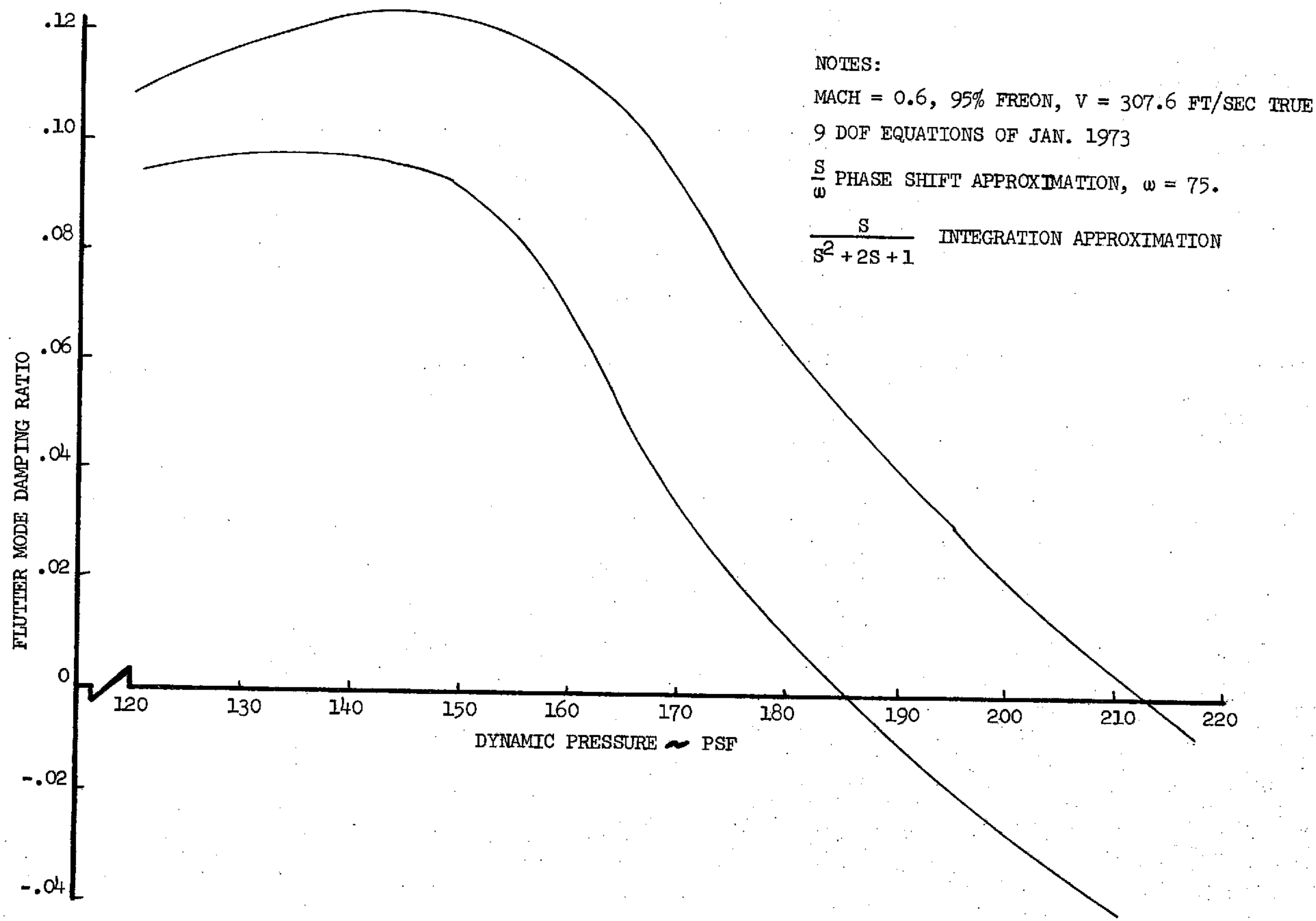

FIGURE 2.8: FLUTTER SUPPRESSION SYSTEM EVALUATION

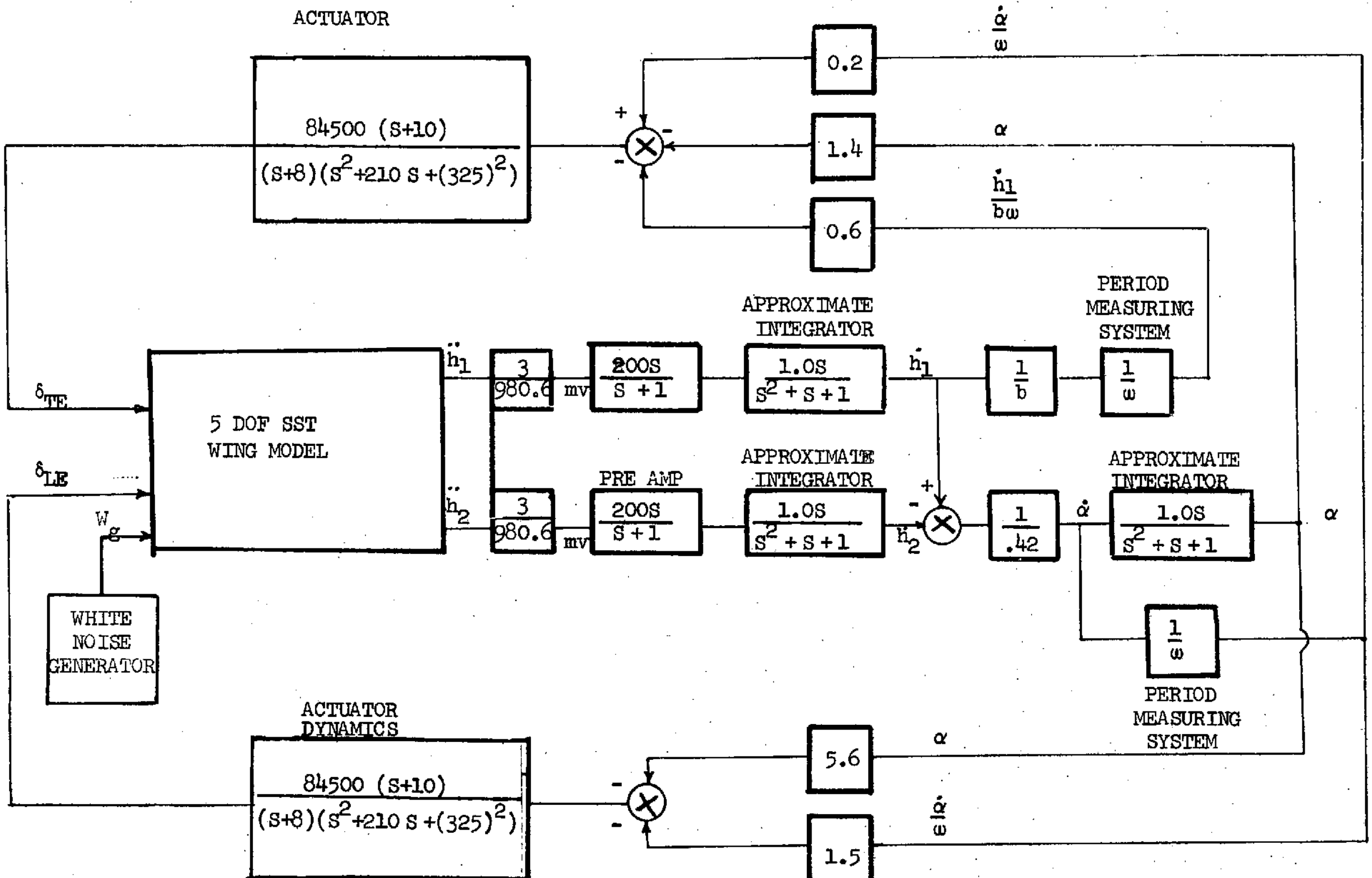

FIGURE 2.9: CLOSED LOOP SYSTEM BLOCK DIAGRAM

2.4.1 Mathematical Model

The math model was simplified to permit simulation of the full five degrees-of-freedom on one EAI 231R console. Effects of unsteady aerodynamics were omitted from the equations by replacing $s/(s+vd_{Kj})$ and $s/(s+vb_i)$ by s/vd_{Kj} and s/vb_i

For further simplification, these equations were written in the form shown below:

$$\{[I]s^2+[N_2]^{-1}[N_1]s+[N_2]^{-1}[N_0]\}\,q_j+\{[N_2]^{-1}[Y_1]+[N_2]^{-1}[Y_2]s\}\,W_g=\{0\}$$

where $[I]$ = Identity matrix

$$[N_2]^{-1}=[M+\rho C_1]^{-1}$$

$$[N_1]=[D+\rho v C_2+\rho v\sum_{K=1}^{4}\frac{D_K}{d_{Kj}}]$$

$$[N_0]=[K+\rho v^2 C_3]$$

$$[Y_1]=[\rho v R_0]$$

$$[Y_2]=[\rho\sum_{i=1}^{4}\frac{R_i}{b_i}]$$

The simulation study was conducted at Mach 0.9 and 136 psf dynamic pressure. The flutter mode was unstable at this condition as shown by the listing of open loop roots in Table 2-II.

TABLE 2-II

OPEN LOOP ROOTS AT MACH 0.9 AND 136 PSF DYNAMIC PRESSURE

Mode	Root
1	+ 1.76 ± j 72.51
2	-23.51 ± j 85.7
3	-30.54 ± j 131.8
4	-12.13 ± j 229.1
5	-34.54 ± j 287.9

2.4.2 Control Law Approximation

The ideal control law of the flutter suppression system was:

$$\begin{Bmatrix} \delta_{LE} \\ \delta_{TE} \end{Bmatrix} = \begin{bmatrix} 0 & -5.6 \\ 0 & -1.4 \end{bmatrix} \begin{Bmatrix} h_1/b \\ \alpha \end{Bmatrix} + e^{j90^\circ} \begin{bmatrix} 0 & -1.5 \\ -.6 & .2 \end{bmatrix} \begin{Bmatrix} h_1/b \\ \alpha \end{Bmatrix}$$

where

$\alpha = \frac{1}{.4\bar{c}}\left(h_1 - h_2\right)$ - Approximate wing angle of attack - Radians, positive leading edge up

δ_{LE} = Leading edge control surface deflection - Radians, positive leading edge up

δ_{TE} = Trailing edge control surface deflection - Radians, positive trailing edge down

h_1 = Vertical displacement at 30 percent chord - positive up

h_2 = Vertical displacement at 70 percent chord - positive up

$\bar{c}$ = Wing chord length at sensor locations

$b = \bar{c}/2$

The surfaces on the mid-span strip and the sensors located along the inboard edge of the strip were utilized for the system.

The 90 degree phase lead of the control law was approximated by $\frac{S}{\omega}$ for physical realization and, therefore, the control law was revised to:

$$\begin{Bmatrix} \delta_{LE} \\ \delta_{TE} \end{Bmatrix} = \begin{bmatrix} 0 & -5.6 \\ 0 & -1.4 \end{bmatrix} \begin{Bmatrix} h_1/b \\ \alpha \end{Bmatrix} + \frac{S}{\omega} \begin{bmatrix} 0 & -1.5 \\ -.6 & .2 \end{bmatrix} \begin{Bmatrix} h_1/b \\ \alpha \end{Bmatrix}$$

The period measuring system shown in Figure 2.10 generated a voltage proportional to the period of the input signal. Figure 2.11 compares calculated and measured voltage at the output of period measuring system for different frequencies of the input signal.

The flutter suppression system was further approximated with $S/(S^2 + S + 1)$ approximate integration and assumed preamplifier dynamics of $S/(S+1)$ and electro-hydraulic actuator dynamics of

$$\frac{\delta_{Surface}}{\delta_{Command}} = \frac{84500(S+10)}{(S+8)(S^2+210\,S+325^2)} \quad \frac{\text{deg}}{\text{deg}}$$

were used in the feedback.

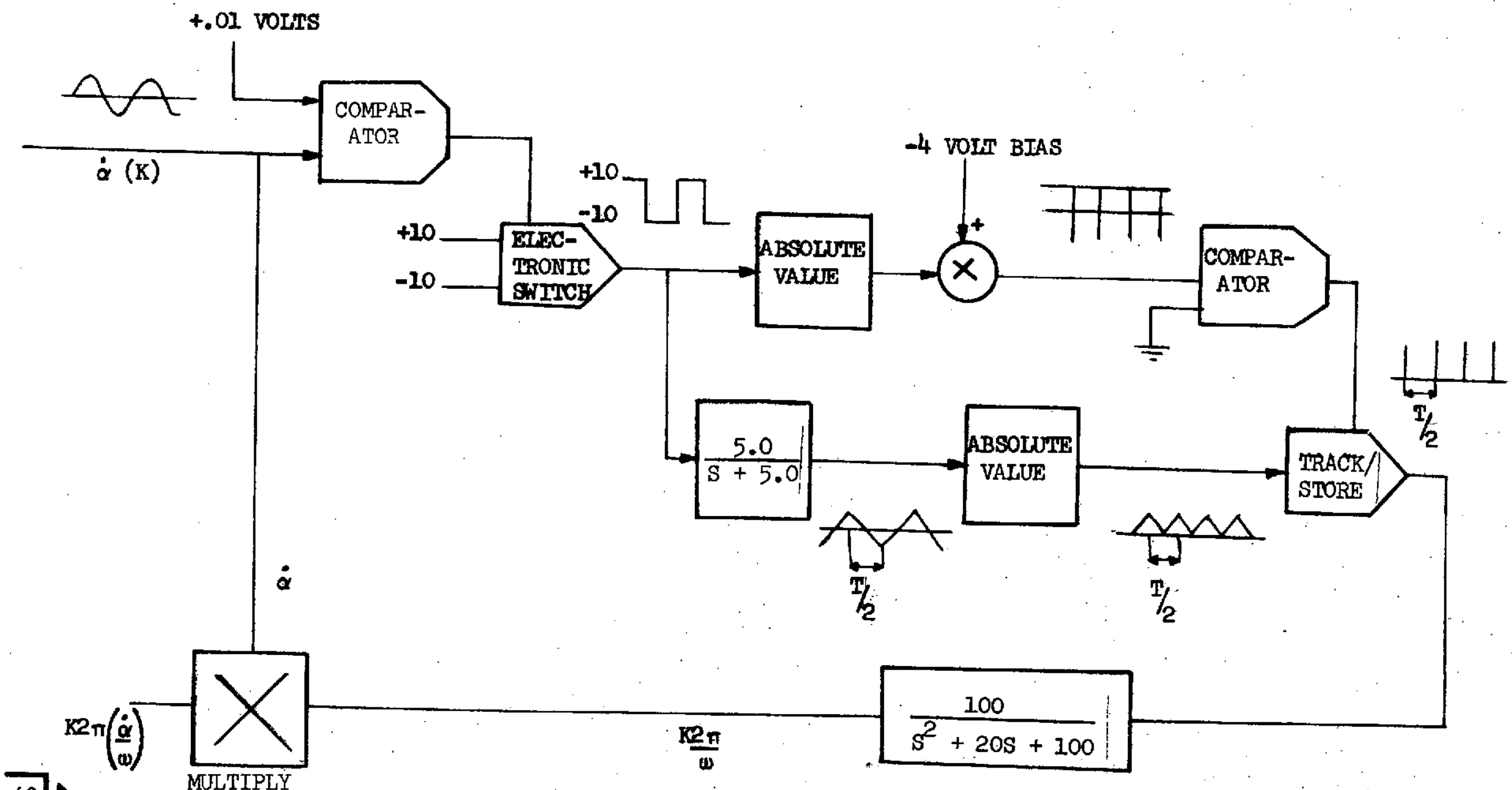

FIGURE 2.10: **PERIOD MEASURING SYSTEM**

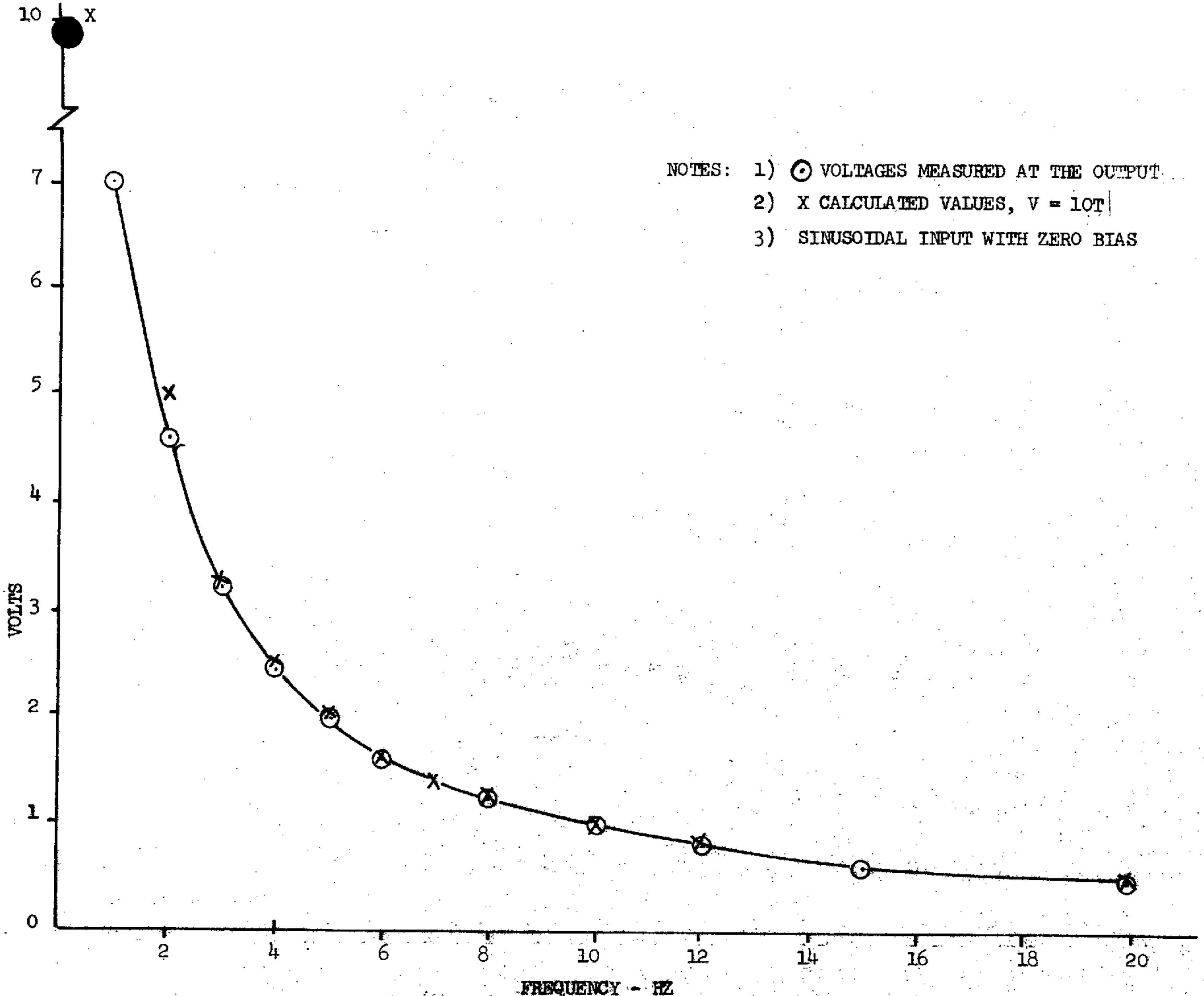

FIGURE 2.11: COMPARISON OF CALCULATED AND MEASURED VOLTAGES AT THE OUTPUT OF PERIOD MEASURING SYSTEM

2.4.3 Results of the Simulation Study

Effects of the period measuring system, feedback gain variations, wind tunnel turbulence and actuator dynamics variations are discussed in the following paragraphs.

Open and closed loop modal responses to a .573 degree step input to the trailing edge surface are shown in Figure 2.12. Nominal gains with a constant frequency of 75 rad/sec in the 'S/ω' channel were used for the control law.

Figure 2.13 shows closed loop responses with a constant 75 rad/sec frequency and with the period measuring system in the out-of-phase channel of the control law. A comparison of the responses in Figure 2.13 indicates that identical system performance is obtained with either the constant frequency of 75 rad/sec or the period measuring system in the feedback.

The control law gain variation study was conducted with constant 75 rad/sec frequency in the S/ω channel. Responses to 0.573 degree step trailing edge surface commands are shown in Figure 2.14 with:

a. Only the out-of-phase gains

b. Only the real gains.

Closed loop responses in Figure 2.14 show that the nominal out-of-phase gains have negligible influence on the FSS performance. However, when the out-of-phase gains were increased by factors of four or more with nominal real gains, a high frequency mode (probably the fifth elastic and actuator coupled mode) became unstable. A typical high frequency instability due to increased $\delta_{TE}/\dot{h}_1$ gain is shown in Figure 2.15.

The effects of the real gains, δ_{LE}/α and δ_{TE}/α, on closed loop flutter mode damping ratio are shown in Figures 2.16 and 2.17, from which it appears that δ_{TE}/α is the most effective gain of the control law. Gain variations in Figures 2.16 and 2.17 were made with the remaining out-of-phase and real gains at nominal values. When δ_{TE}/α gain is zero, the closed loop flutter mode becomes neutrally stable, but a substantial increase in damping is attained when this gain is doubled.

Wind tunnel turbulence was simulated by low frequency Gaussian white noise filtered through a first order lag. The turbulence excited the inherent instability of the open loop model, but as shown in Figure 2.18, the closed loop turbulence responses were stable. The period measuring system was used to realize the out-of-phase gain of the control law.

A deviation from the ideal FSS is caused by extra gain and phase introduced into the feedback by the actuator dynamics. The nominal actuator dynamics presented in Section 2.4.2 introduced an attenuation of 0.835 and a phase lage of 10 degrees at the flutter mode frequency of 11.5 Hz. Figure 2.19(a) shows the closed loop responses with actuator dynamics of:

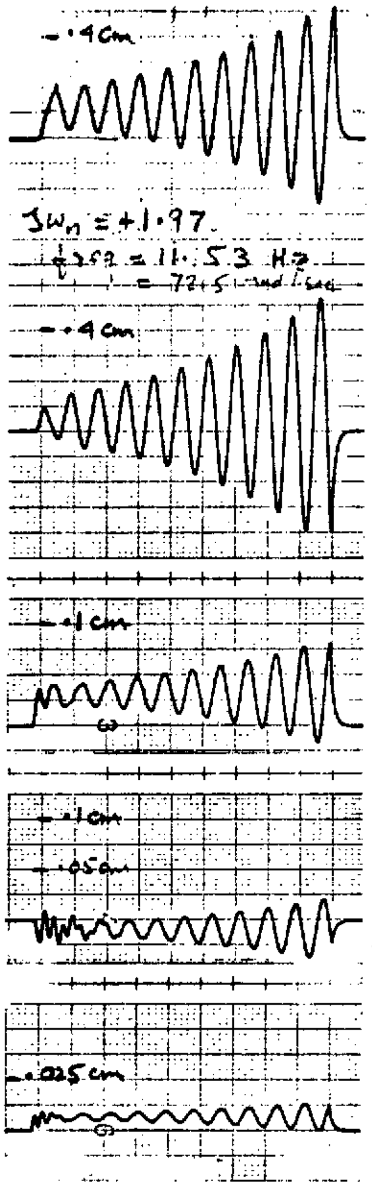

(a) OPEN LOOP

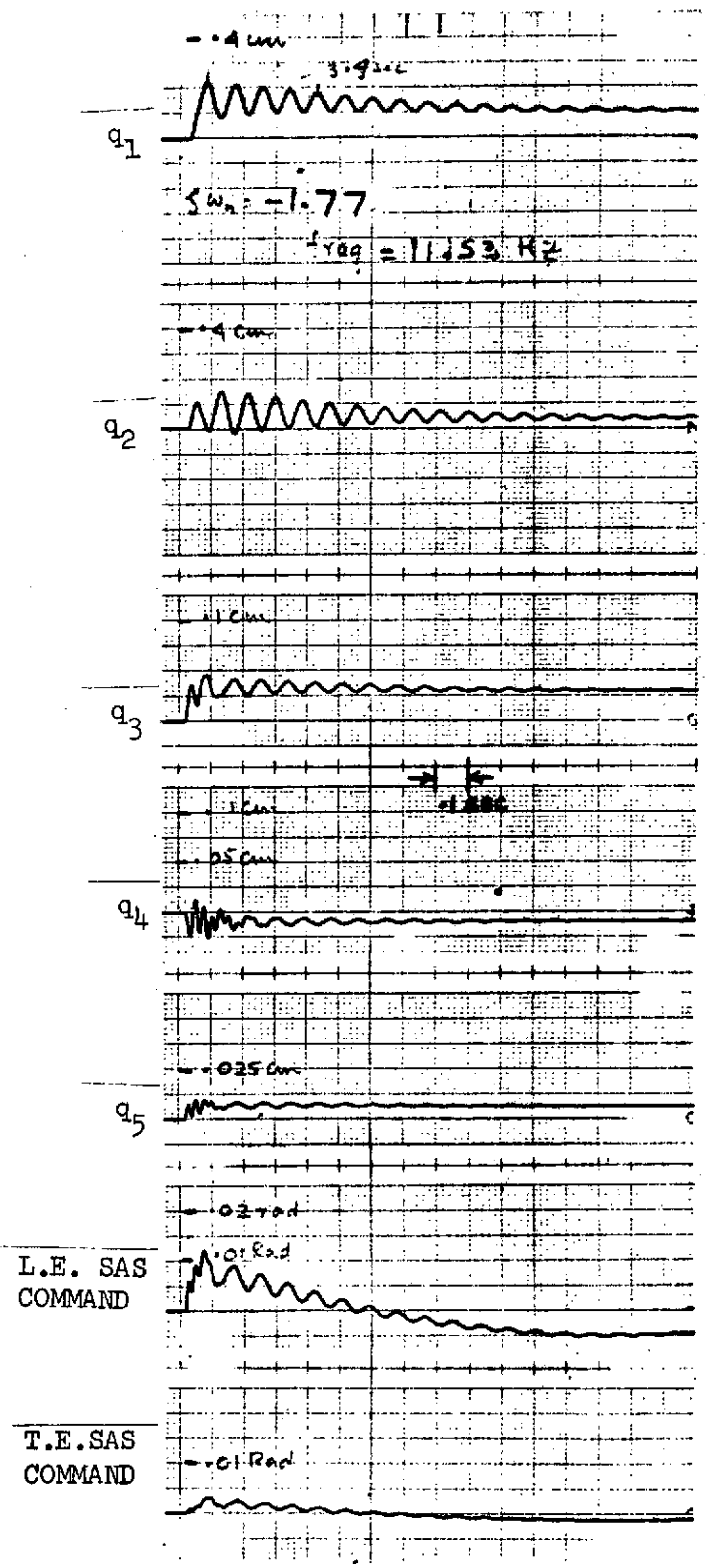

(b) CLOSED LOOP

FIGURE 2.12: OPEN AND CLOSED LOOP MODEL RESPONSES

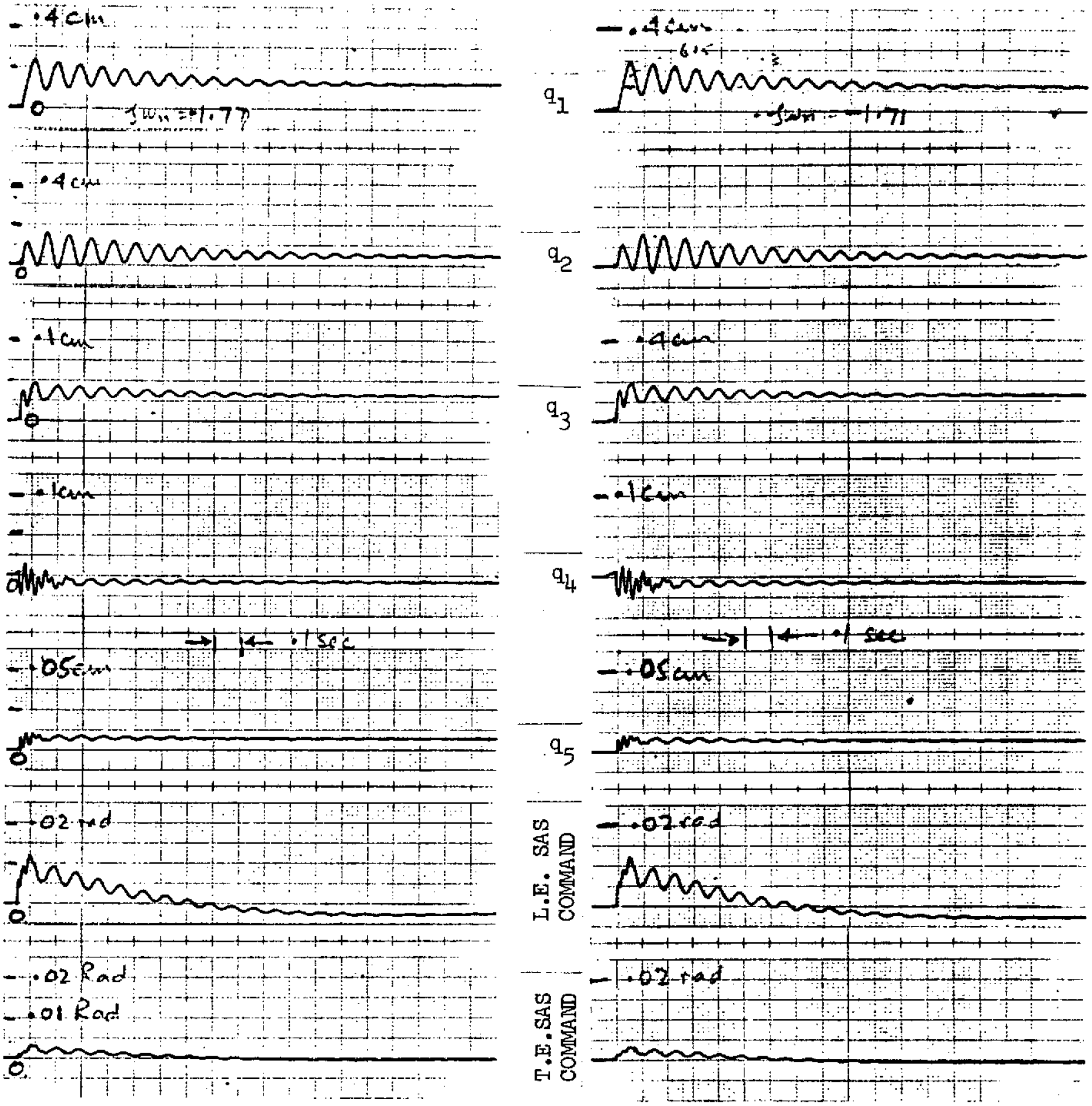

(a) WITH CONSTANT FREQUENCY OF 75 RAD/SEC

(b) WITH PERIOD MEASURING SYSTEM

FIGURE 2.13: COMPARISON OF CLOSED LOOP RESPONSES

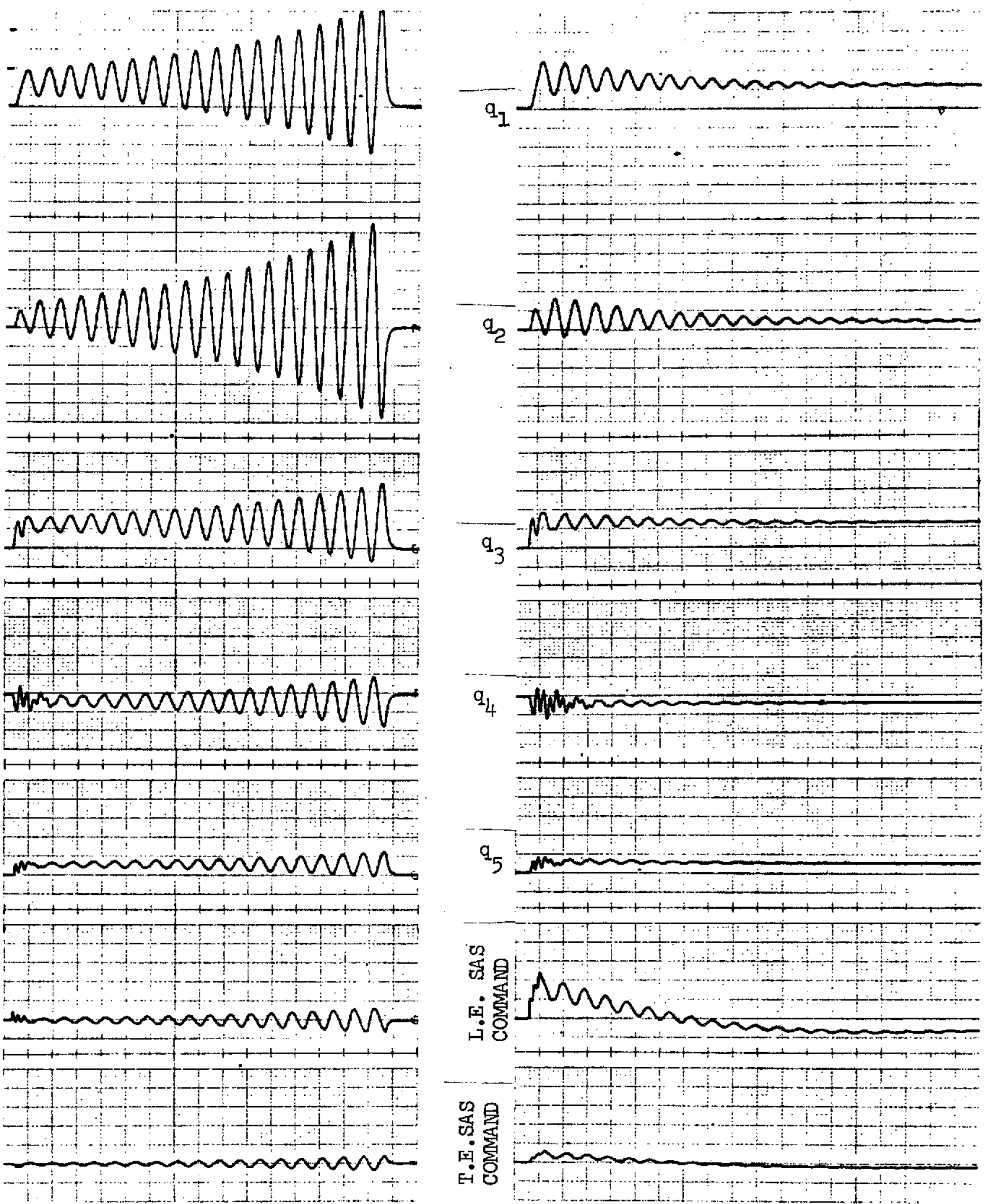

(a) OUT-OF-PHASE GAINS ONLY

(b) REAL GAINS ONLY

FIGURE 2.14: EFFECTS OF REAL AND OUT OF PHASE GAINS

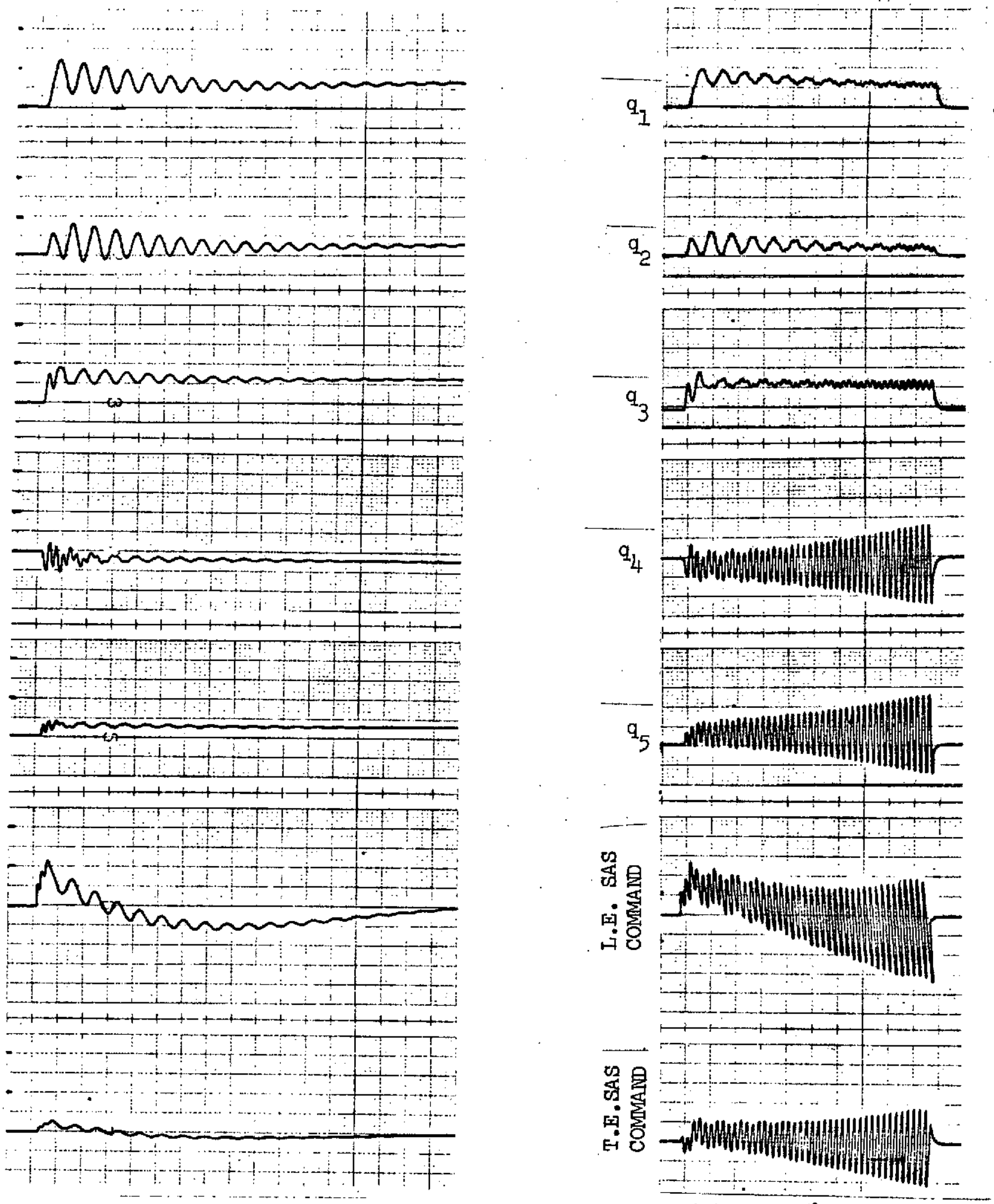

(a) $K_{\delta_{TE}/\dot{h}_1} = 0$

(b) $K_{\delta_{TE}/\dot{h}_1}$ = NOM x 4.5 = 2.7

FIGURE 2.15: $\delta_{TE}/\dot{h}_1$ LOOP GAIN VARIATION

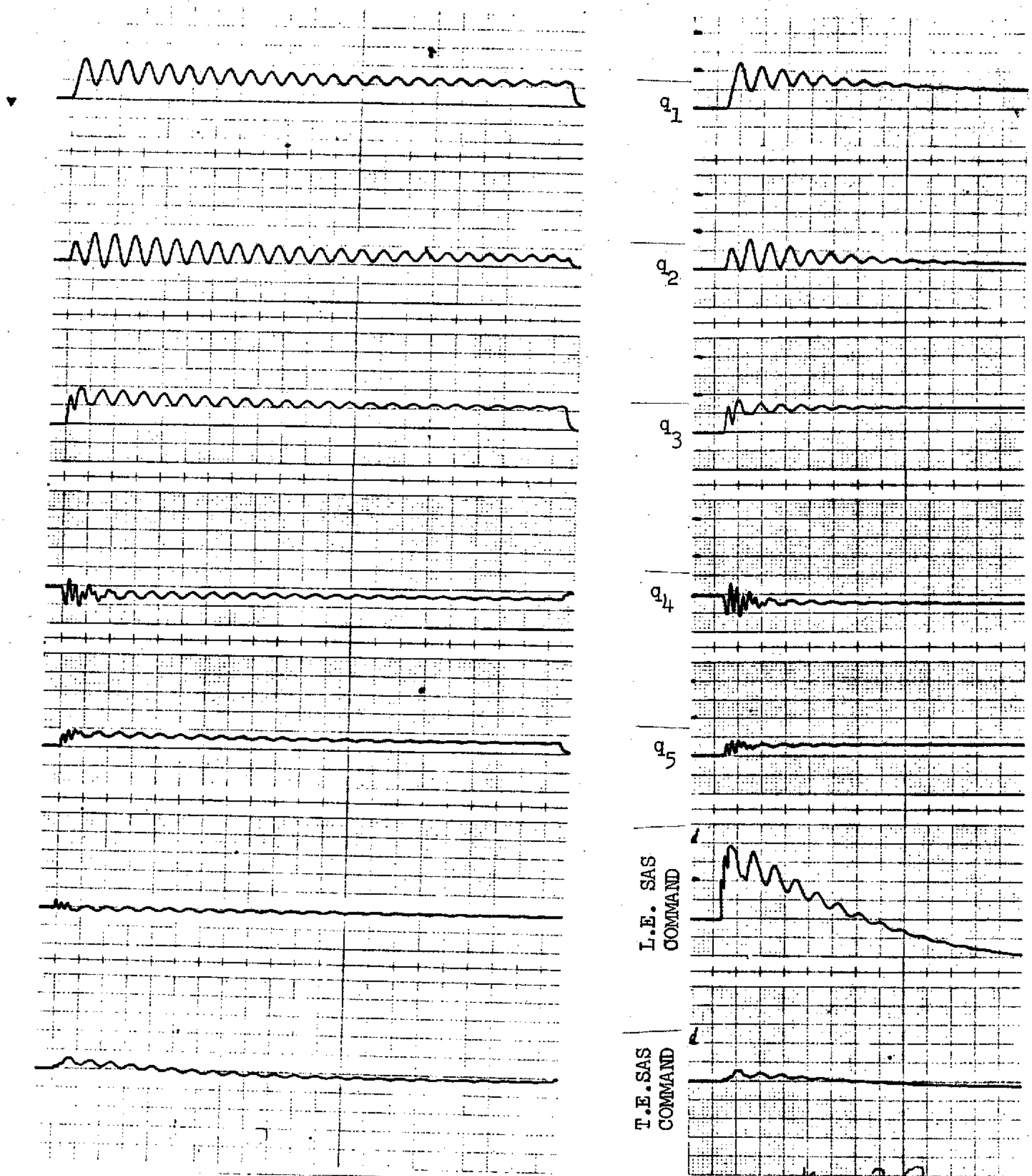

(a) $K_{\delta_{LE}/\alpha} = 0$

(b) $K_{\delta_{LE}/\alpha}$ = NOM x 2 = 11.2

FIGURE 2.16: δ_{LE}/α LOOP GAIN VARIATION

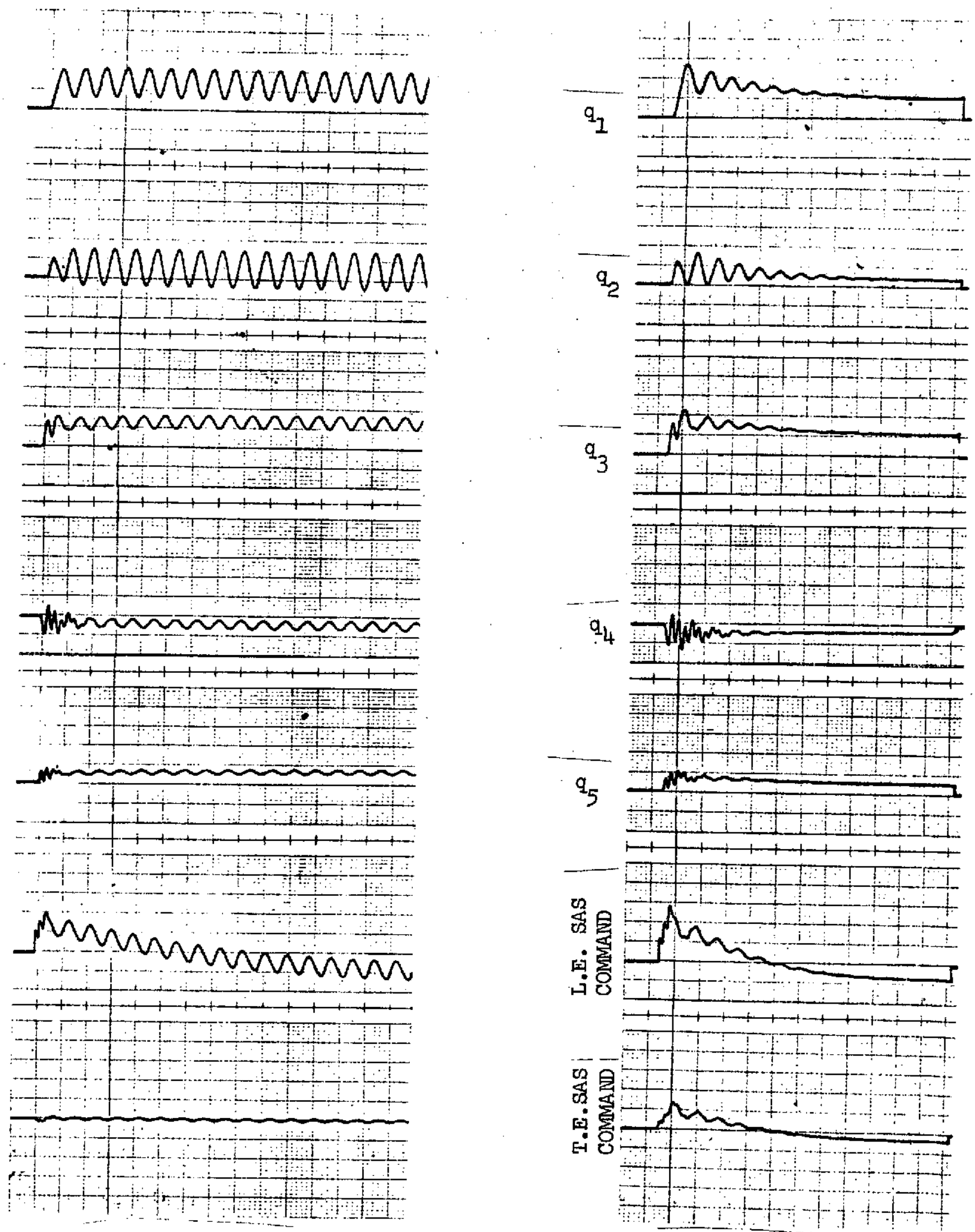

(a) $K_{\delta_{TE}}/\alpha = 0$

(b) $K_{\delta_{TE}}/\dot{\alpha}$ = NOM x 2 = 2.8

FIGURE 2.17: δ_{TE}/α LOOP GAIN VARIATION

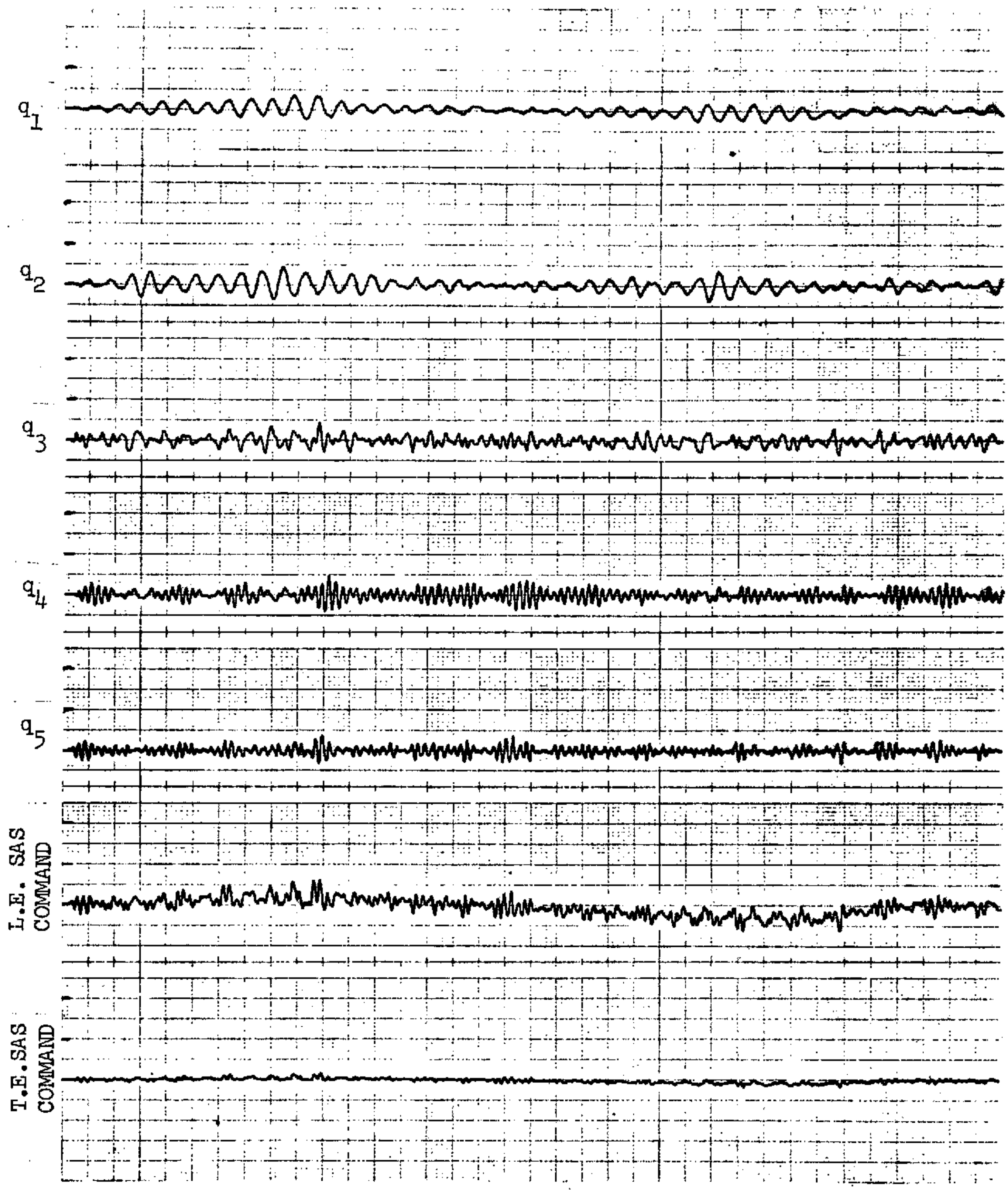

FIGURE 2.18: CLOSED LOOP MODEL RESPONSE TO TURBULENCE

$$\frac{\delta_{Surface}}{\delta_{Command}} = \frac{(490)^2}{s^2 + (0.428)(490)\, s + (490)^2} \quad \frac{deg}{deg}$$

which has a gain of 1.012 and phase lag of 3.7 degrees at 11.5 Hz. Effects of larger phase lag on FSS performance is shown by closed loop responses in Figure 2.19(b) with actuator gain of 1.005 and phase lag of 48 degrees at the flutter mode frequency. Responses in Figure 2.19 were obtained with nominal system gains and constant frequency of 75 rad/sec in the out-of-phase channel. A comparison of the responses in Figure 2.19 indicates that larger phase lag in the control law decreases the FSS performance.

Approximate integrators were used to derive rate and displacements from the accelerometer outputs because perfect integrators would introduce large low frequency (less than 1.0 rad/sec) gains. Effects of perfect integrators in the system are shown in Figure 2.20 which exhibit a steady drift caused by perfect integration of the low frequency components of the white noise. The same responses with the approximate integrators are shown in Figure 2.18. The responses shown in Figures 2.12 through 2.19 were also obtained with the approximate integrators.

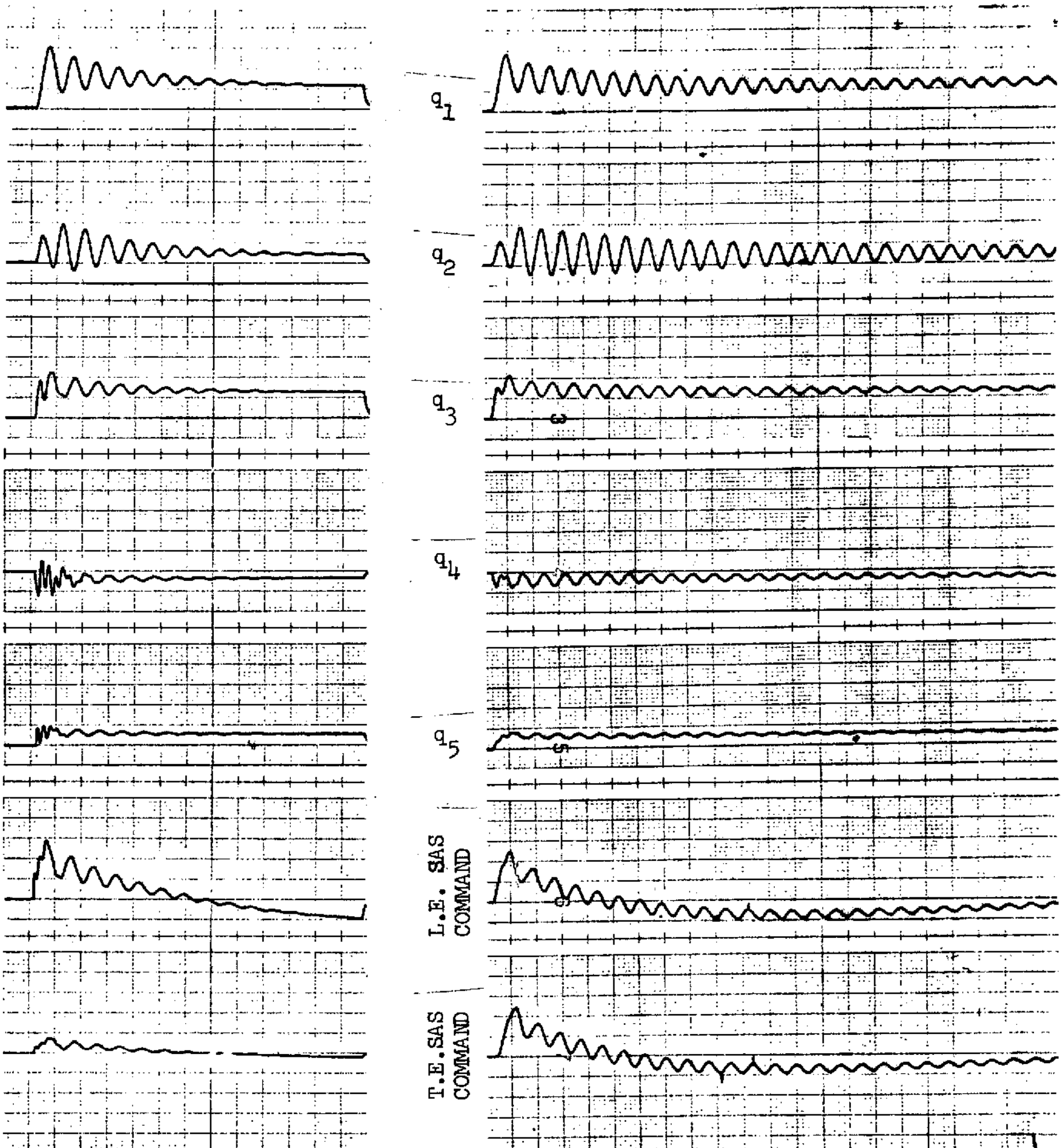

(a) $\dfrac{\delta_S}{\delta_C} = \dfrac{490^2}{S^2 + 210S + 490^2}$

(b) $\dfrac{\delta_S}{\delta_C} = \dfrac{125^2}{S^2 + 160S + 125^2}$

FIGURE 2.19: EFFECTS OF ACTUATOR DYNAMICS

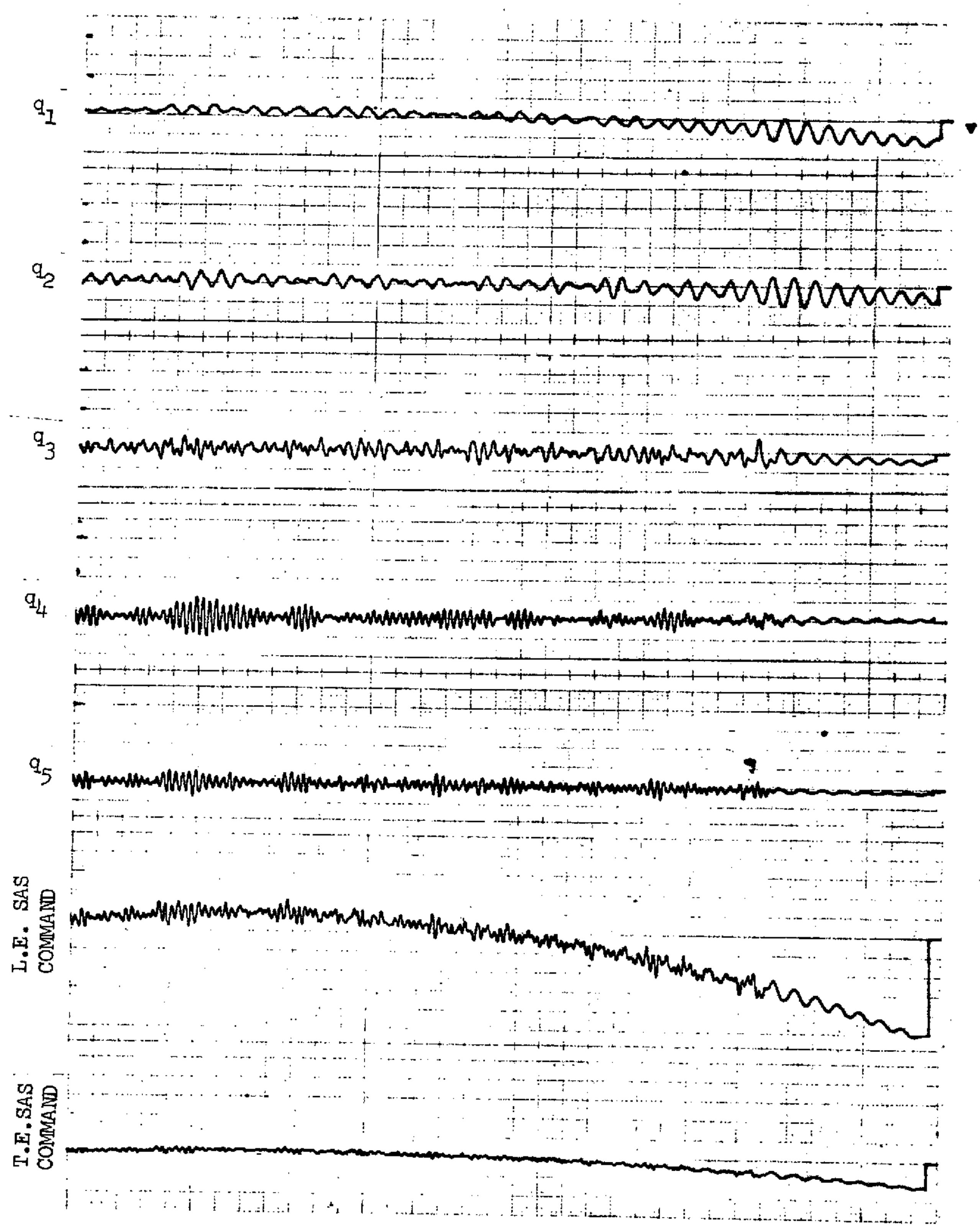

FIGURE 2.20: LOW FREQUENCY DRIFT DUE TO PERFECT INTEGRATOR.

2.5 Synthesis of New Flutter Suppression System

An analysis was started to synthesize a flutter suppression system for the wing model using a conventional root locus analysis. The desired system would be independent of the system developed by Dr. Nissim, but it would utilize the same accelerometer locations and control surfaces. The analysis is not complete, but a system has been developed that provides better than 0.2 damping on the flutter mode at Mach 0.9 and 170 lb/ft^2 dynamic pressure.

2.5.1 Performance Objective

The performance objective for the new flutter suppression system is to provide at least 30 percent increase in flutter velocity for the wing model at Mach 0.6, 0.7, 0.8 and 0.9, without significantly destabilizing any other structural vibration mode. The system gains need not be the same for each Mach number, but it is desired that any feedback filtering required be invariant through the Mach number range.

The performance objective translates into a 69 percent increase in dynamic pressure at flutter over the unaugmented model. The predicted increase in dynamic pressure for the NASA system was only 18 percent at Mach 0.9 and 15.1 percent at Mach 0.6 (see Section 2.3).

The new system will require no modification to the model for the wind tunnel tests. It is desired that the system can be mechanized on an analog computer so that a change from the NASA system can be accomplished by at most a change in patch boards and resetting potentiometer coefficients on the computer. This will facilitate testing of both systems during one wind tunnel entry.

2.5.2 Synthesis Study

Analyses have been completed at only one condition, Mach 0.9 and 170 lb/ft^2 dynamic pressure. The nine degree-of-freedom equations of motion discussed in Section 2.2 were used. The leading and trailing edge control surface electrohydraulic actuation systems were represented by the transfer function used in the evaluation of the NASA system discussed in Section 2.3.

The synthesis study began with a brief evaluation of feedback formed by several combinations of the two accelerometer signals. The combinations were evaluated using one surface at a time. The best leading edge surface system evaluated to date uses differential acceleration ($\ddot{h}_1 - \ddot{h}_2$) to work the wing torsion mode, as shown in the leading edge surface loop of the block diagram shown in Figure 2.21. The root locus of this system, Figures 2.22 a, b and c, shows that the flutter mode is stabilized and that none of the higher frequency modes are destabilized at the nominal gain. The open and closed loop damping ratios for all nine modes are tabulated in Table 2-III.

The trailing edge surface system uses the aft accelerometer output as shown in the block diagram in Figure 2.21. This system also stabilizes the flutter

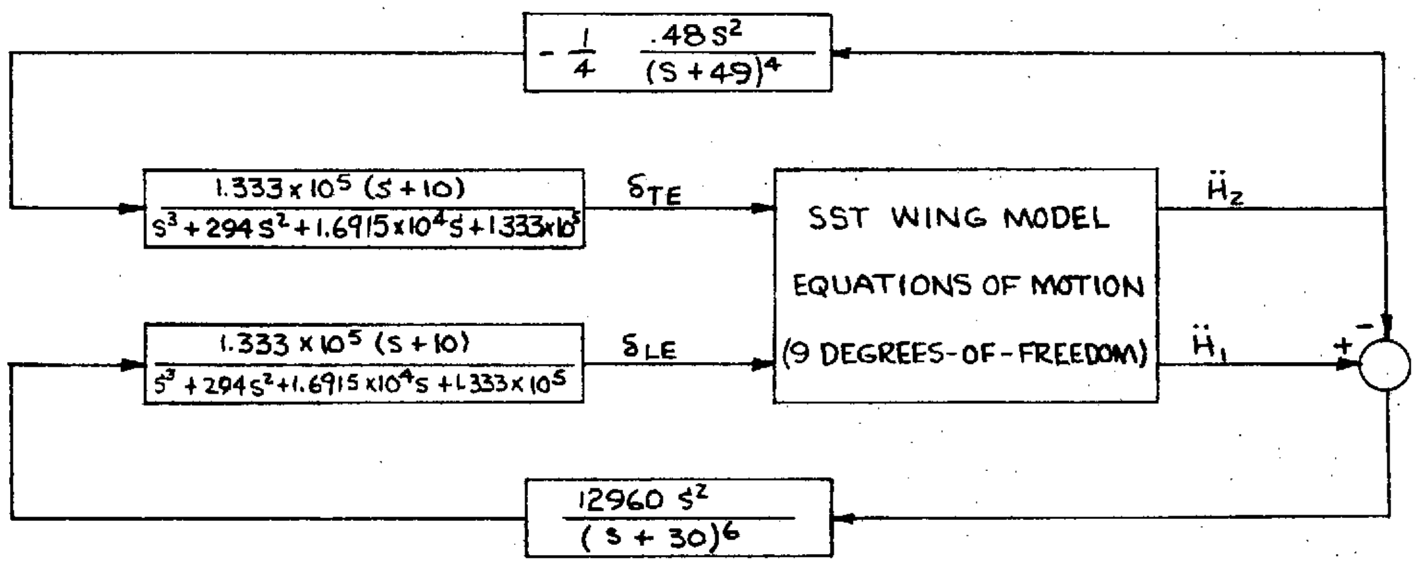

FIGURE 2.21

PRELIMINARY FLUTTER MODE CONTROL SYSTEM BLOCK DIAGRAM

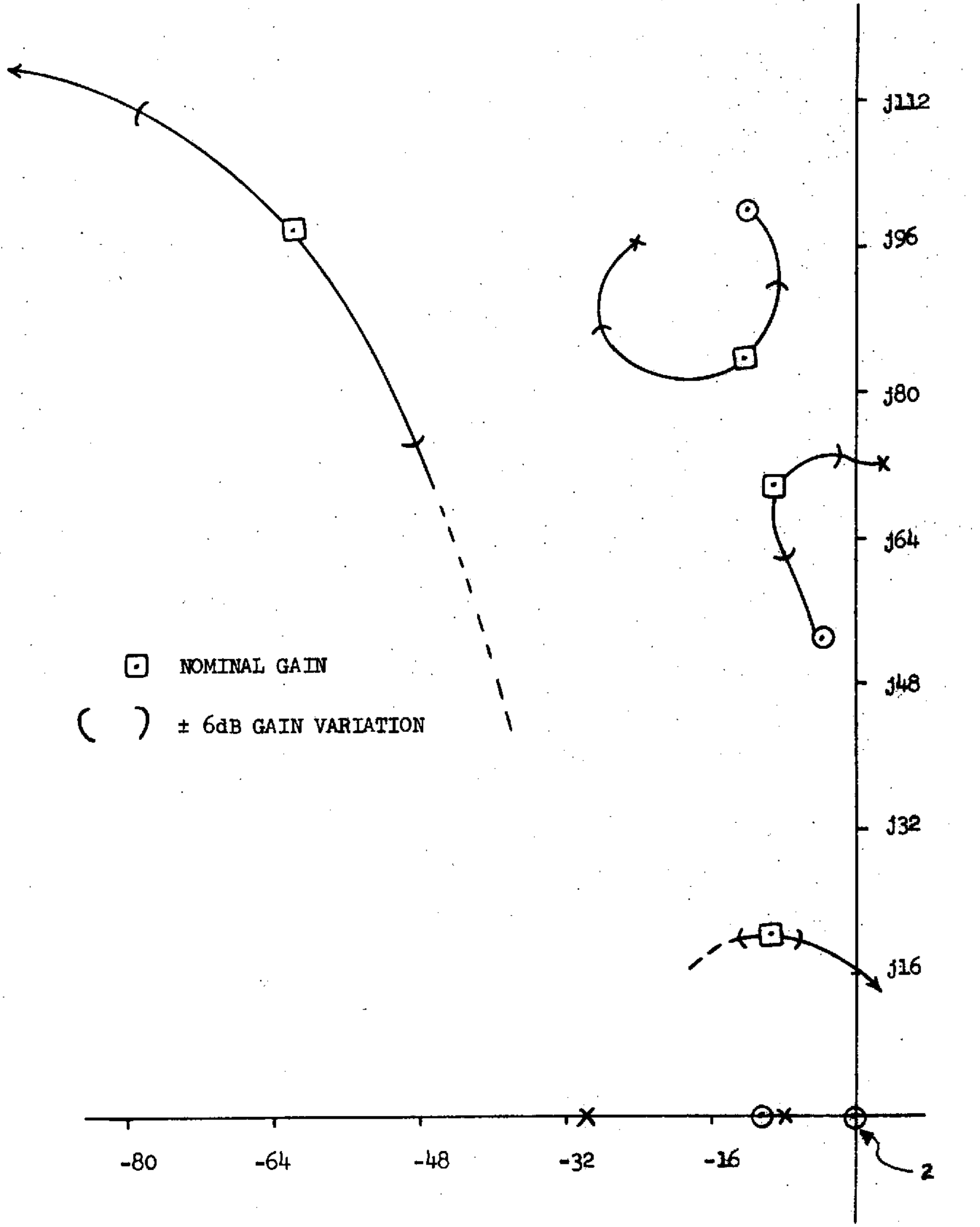

FIGURE 2.22a

LEADING EDGE SURFACE SYSTEM GAIN ROOT LOCUS

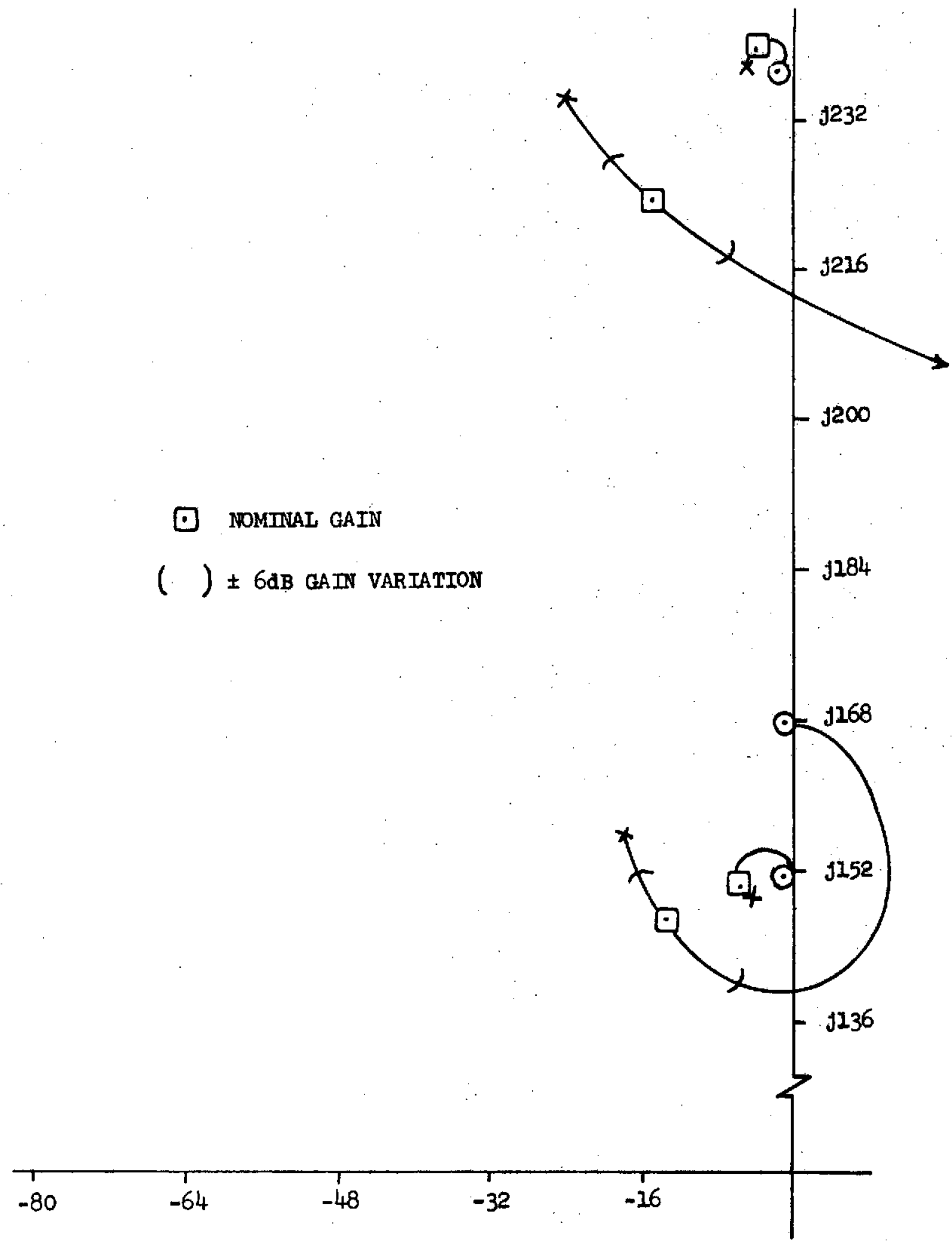

FIGURE 2.22b

LEADING EDGE SURFACE SYSTEM GAIN ROOT LOCUS

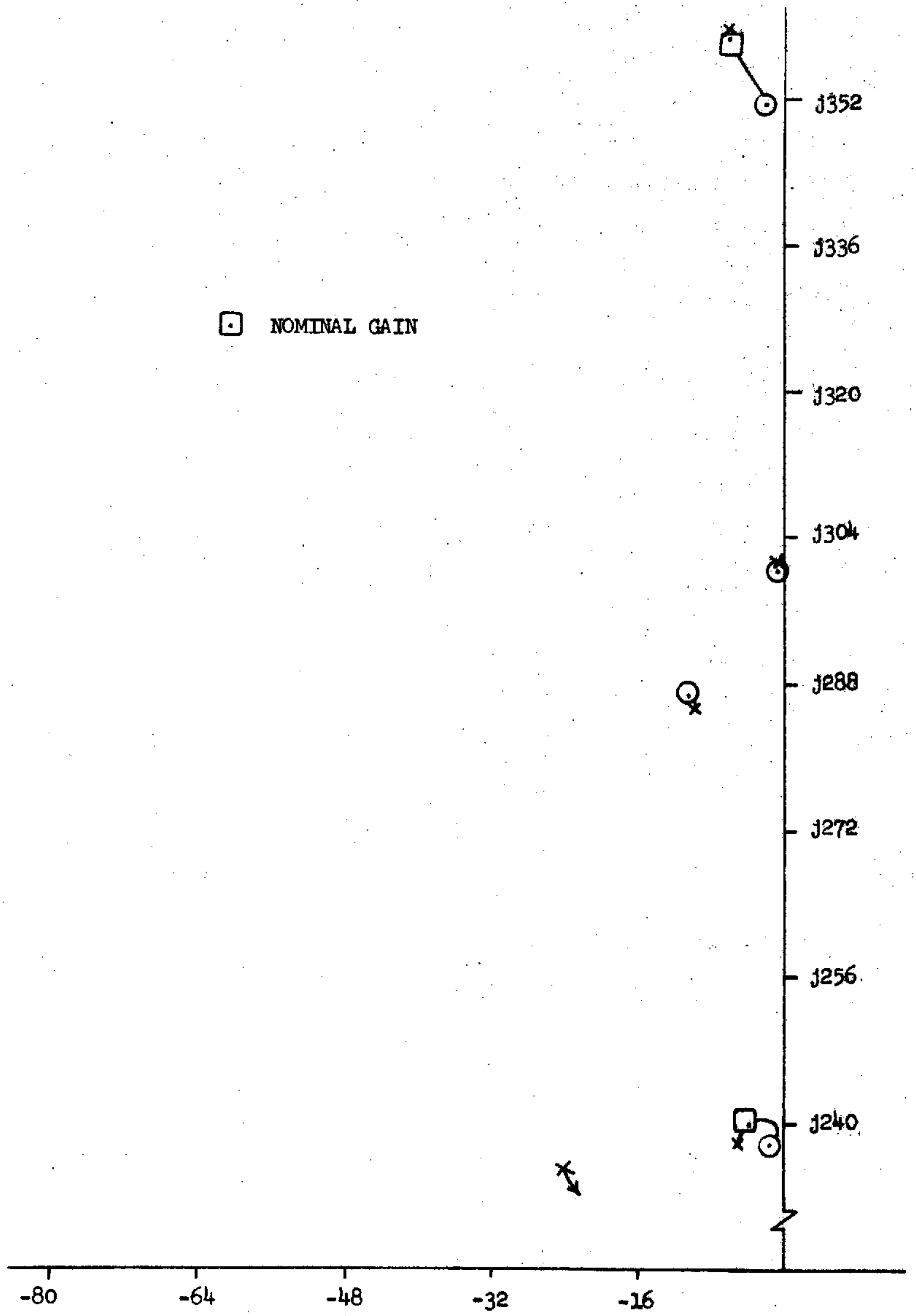

FIGURE 2.22c

LEADING EDGE SURFACE SYSTEM GAIN ROOT LOCUS

TABLE 2-III

WING MODEL FLUTTER SUPPRESSION SYSTEM STABILITY

Mode	Free Wing Pole Location		Damping Ratios			
	σ	ω	Free Wing	Leading Edge Surface System Only	Preliminary Combined System	Trailing Edge Surface System Only
9	- 6.09	360.0	0.0169	0.0166	-	0.0191
8	- 0.740	301.0	0.00245	0.00243	-	0.00445
7	- 9.81	285.0	0.0343	0.0350	-	0.0238
6	- 4.64	238.0	0.0195	0.0154	0.0158	0.0111
5	-23.2	235.0	0.0985	0.0656	0.1015	0.1566
4	-17.5	157.0	0.1108	0.0901	0.2512	0.0748
3	- 3.61	150.0	0.0241	0.0360	0.0278	0.00919
2	-24.5	96.9	0.2452	0.1451	0.0767	0.2170
1	2.94	72.6	-0.0404	0.1343	0.2022	0.0636

mode while slightly decreasing damping of some of the higher frequency modes (see Table 2-III). The root locus for this system is shown in Figures 2.23 a, b and c.

The block diagram shown in Figure 2.21 shows one combination of the two systems that offers definite potential. The leading edge surface system is used at nominal gain, and the trailing edge surface system gain at one-fourth the nominal gain. Damping of the first six modes with this system is also shown in Table 2-III.

Figure 2.24 shows the analytical q-ζ plot at Mach 0.9 for the basic wing and the approximate Nissim system. Damping of the flutter mode at the one condition analyzed is shown on this figure for the nominal leading and trailing edge surface systems and the combination of the two. This figure illustrates the potential increase in flutter dynamic pressure with this system.

2.5.3 Remaining Work

A flutter suppression system using the model leading and trailing edge control surfaces has been synthesized to provide better than 0.2 damping ratio at Mach 0.9 and 170 lb/ft^2 dynamic pressure. This system must be evaluated at other dynamic pressures at Mach 0.9 to establish a complete V-ζ trend. The system should also be evaluated at Mach 0.6 to determine any changes that are required.

The final system will be evaluated to determine the leading and trailing edge control surface activity required to give the predicted performance.

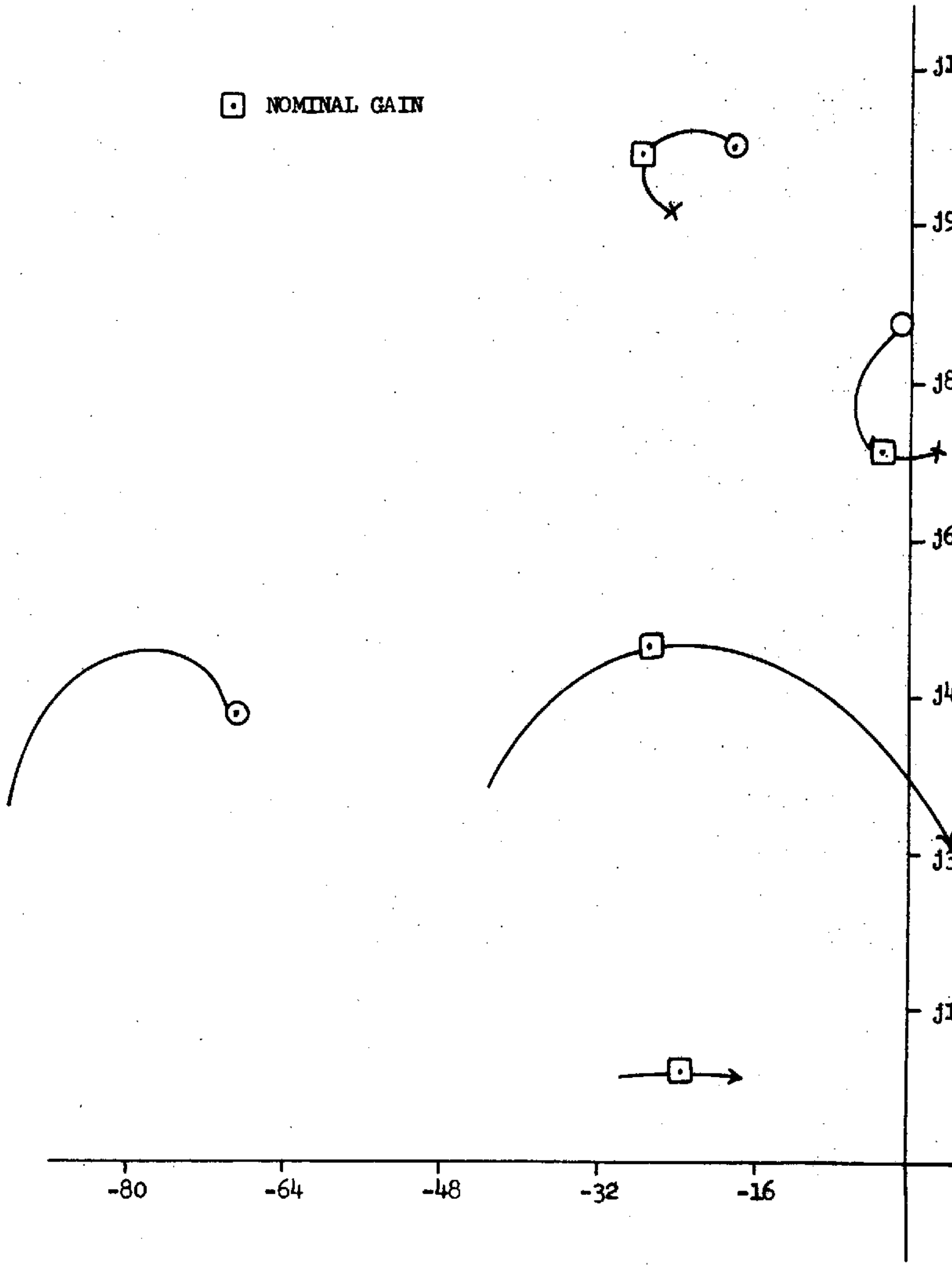

FIGURE 2.23a

TRAILING EDGE SURFACE SYSTEM GAIN ROOT LOCUS

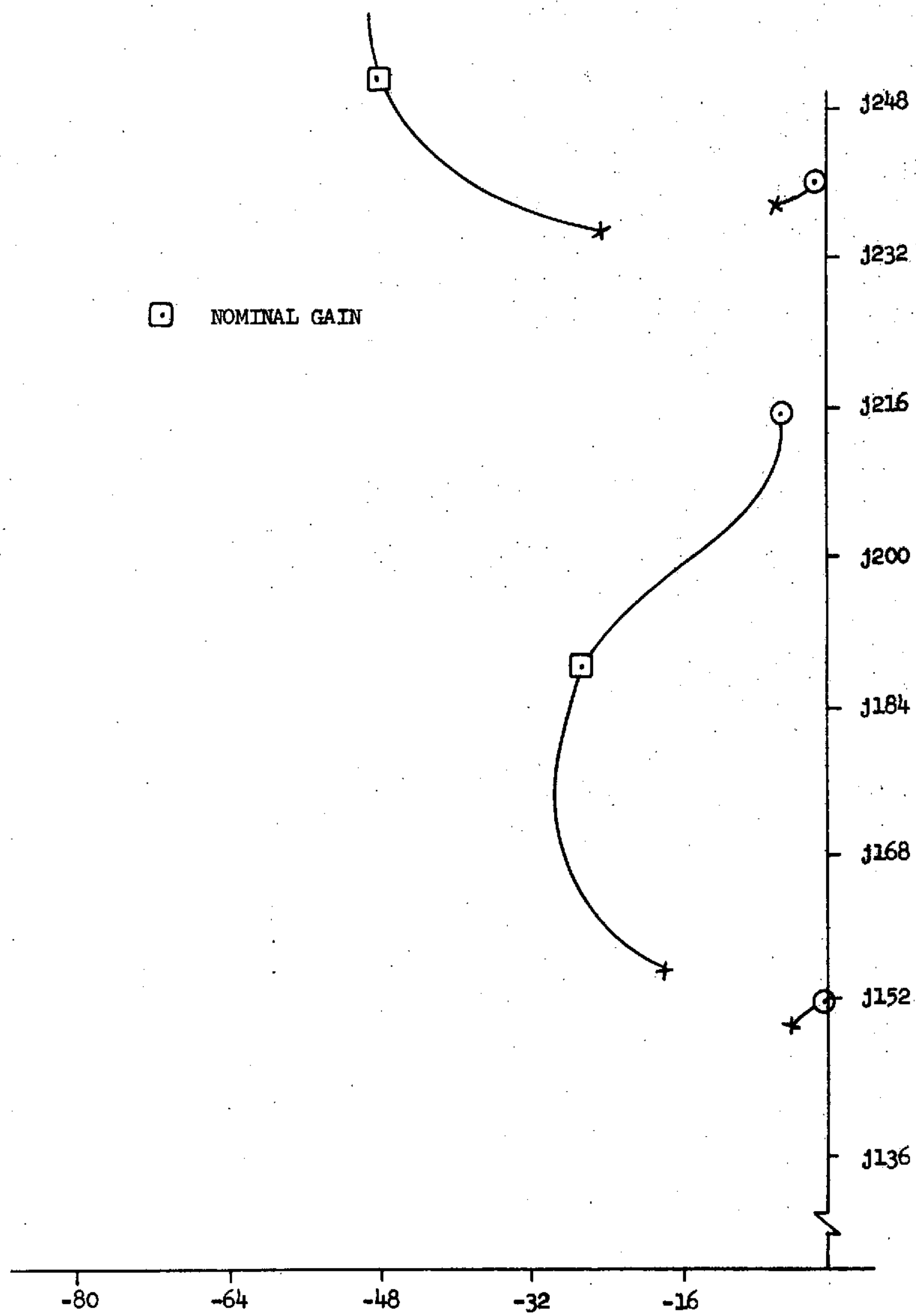

FIGURE 2.23b

TRAILING EDGE SURFACE SYSTEM GAIN ROOT LOCUS

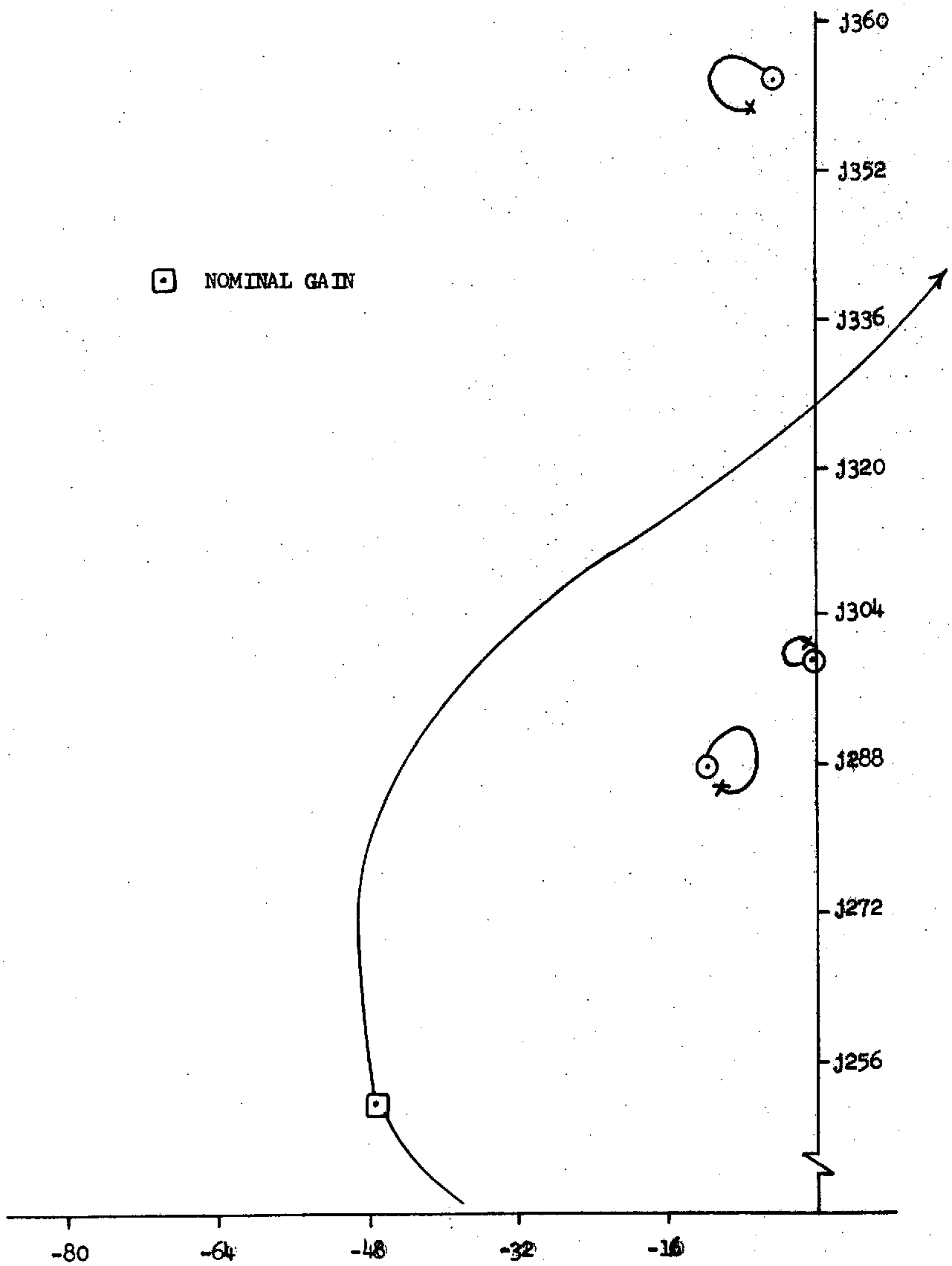

FIGURE 2.23c

TRAILING EDGE SURFACE SYSTEM GAIN ROOT LOCUS

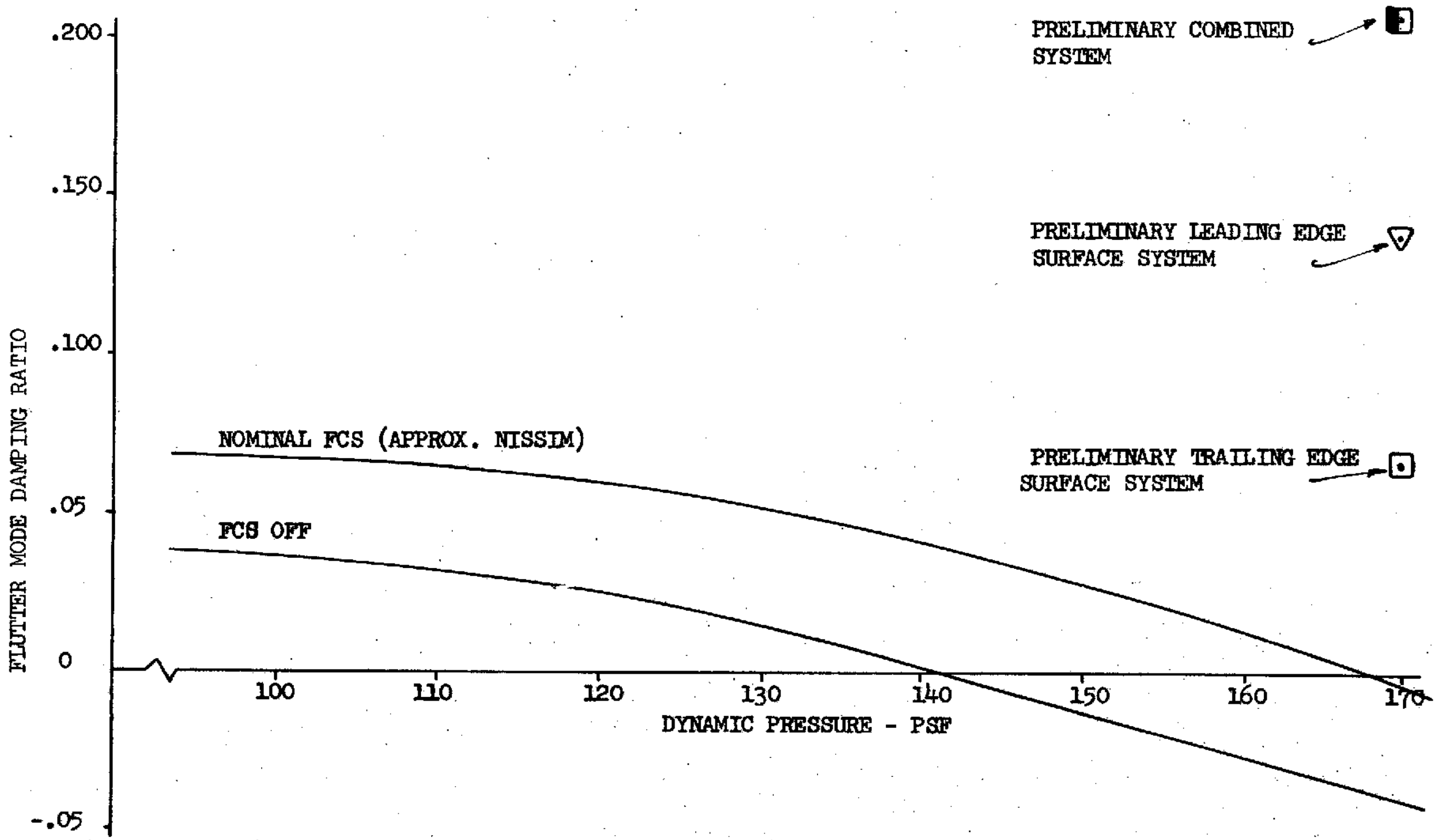

FIGURE 2.24

PRELIMINARY FLUTTER SUPPRESSION SYSTEM PERFORMANCE COMPARED TO THE PRESENT SYSTEM (MACH 0.9)

2.6 Control Surface Mechanization

Development of electrohydraulic actuation systems for the model leading and trailing edge control surfaces was initiated under Contract NAS1-10885 in 1971. Components for the systems were selected and assembled for breadboard testing. Results of breadboard testing this system indicated that the trailing edge surface actuation system would be unstable with position feedback only. An approximate, linearized mathematical model was developed to predict the additional feedback compensation required for stability. The work accomplished under this contract, including drawings for installation of the systems in the model, is documented in Section 3.0 of Reference 1.

This section describes the completion of analyses and installation and testing of the systems in the model. This work was accomplished at Boeing-Wichita under Contract NAS1-11833. The model was returned to NASA and used in testing the flutter suppression system developed by Dr. Nissim in January and May, 1973.

The following paragraphs are written to complement Section 3.0 of Reference 1. The same nomenclature will be used here.

2.6.1 Baseline System

Results of testing the baseline system were used in Reference 1 to develop an approximate, linear mathematical model. The equations derived accounted for the hydraulic fluid between the servovalve and actuator as an equivalent second order fluid-actuator mode. Servovalve dynamics and structural compliance of the actuator shaft were included. Testing of the baseline system with the model trailing edge control surface showed the system to be unstable at the desired position loop gain. Required additional feedback compensation was identified through a root locus analysis of these equations. The compensation was incorporated into the baseline system and predicted stability verified through dynamic testing.

2.6.1.1 Analysis

The block diagram of the baseline system with position feedback is shown in Figure 2.25 (see Figure 3.9 of Reference 1). The position loop gain root locus shown in Figure 2.26 predicts the system instability encountered during dynamic testing. As position feedback gain increases, the actuator pole at the origin and the lower frequency hydraulic fluid-actuator inertia pole come together and split off the real axis to form the dominant closed loop mode. This mode crosses the imaginary axis at about 4.0 volt/deg position gain. The coupled control surface mode becomes unstable at about 1.5 volt/deg. The servovalve mode becomes better damped as position loop gain is increased.

Correlation of the instability encountered in testing the baseline system with the analytical model is not clear from the root locus. The instability appeared as a sustained 55.9 Hz oscillation at about 550 psi supply pressure. This lower pressure would give different servovalve and actuator dynamic characteristics than were assumed in the mathematical model. It should be noted that the mathe-

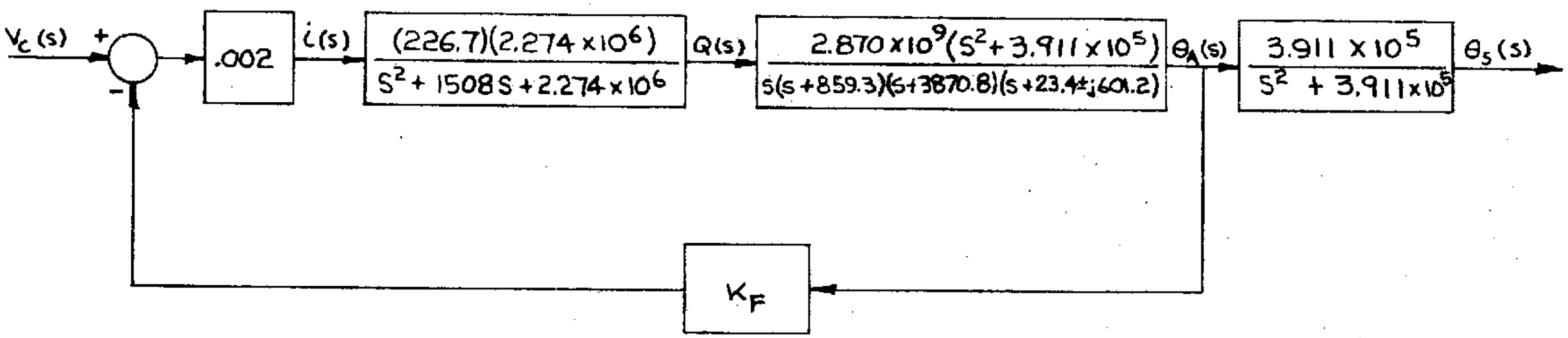

FIGURE 2.25

BLOCK DIAGRAM OF BASELINE SYSTEM WITH T.E. CONTROL SURFACE
POSITION FEEDBACK ONLY

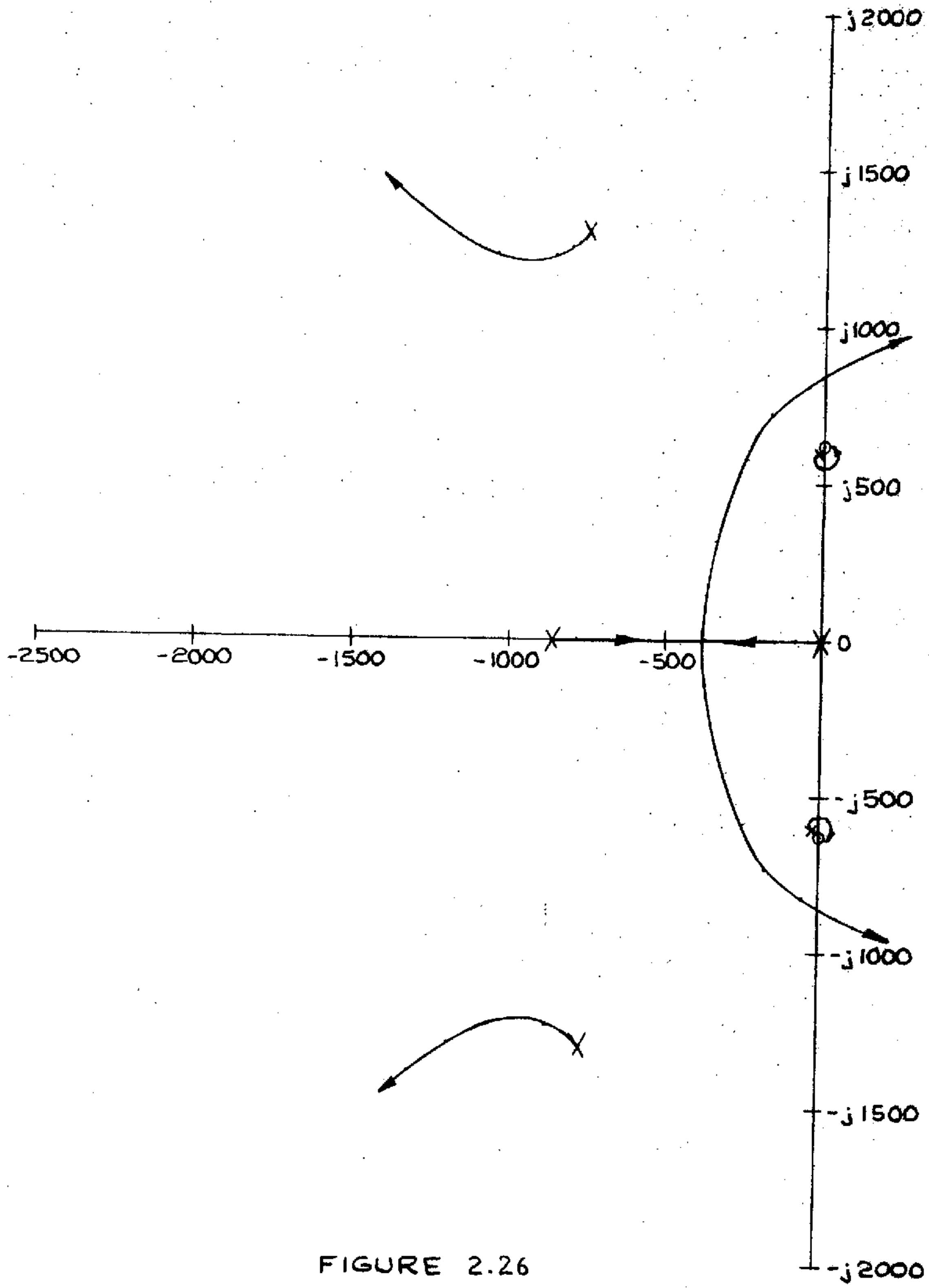

FIGURE 2.26

BASELINE ACTUATION SYSTEM ROOT LOCUS

POSITION FEEDBACK ONLY

matical model was developed to predict trends for determination of additional feedback compensation required to stabilize the system. A discussion of the limitations of the derived equations is presented on page 68 of Reference 1.

Actuator shaft angular rate feedback was investigated as potential feedback for the actuation system. The gain root locus of the rate feedback loop, Figure 2.27, with 1.01 volt/deg position gain (426.5/sec position loop gain) indicates rate feedback would increase the dominant mode damping. However, a potential instability of the coupled control surface mode was predicted. Physical size of d.c. tachometers would not permit installation at the actuator shaft. Thus approximate derivative of the shaft angular position was analyzed but the results were not acceptable.

The actuator and surface equations of motion were subsequently used to derive the transfer function relating differential pressure across the actuator vane (load pressure) to shaft angular position. This was done to permit evaluation of load pressure feedback for the system. The two equations of motion, derived in Reference 1, are

$$I_{EQ}\frac{d^2\theta_A}{dt^2} + D_{EQ}\frac{d\theta_A}{dt} + K_s\theta_A - K_s\theta_s = C_A(P_1 - P_2) \triangleq C_A P_L$$

$$-K_s\theta_A + I_s\frac{d^2\theta_s}{dt^2} + K_s\theta_s = 0$$

Assuming zero initial conditions, the Laplace transform of the equations is

$$(I_{EQ}s^2 + D_{EQ}s + K_s)\theta_A(s) - K_s\theta_s(s) = C_A P_L(s)$$

$$-K_s\theta_A(s) + (I_s s^2 + K_s)\theta_s(s) = 0$$

The surface angular deflection, θ_s, can be eliminated to produce

$$(I_{EQ}s^2 + D_{EQ}s + K_s)\theta_A(s) - \frac{K_s\omega_s^2}{s^2+\omega_s^2}\theta_A(s) = C_A P_L(s)$$

where $\omega_s^2 = K_s/I_s$. From this equation, the desired transfer function can be formed:

$$\frac{P_L}{\theta_A}(s) = \frac{(s^2+\omega_s^2)(I_{EQ}s^2 + D_{EQ}s + K_s) - K_s\omega_s^2}{C_A(s^2+\omega_s^2)} \ \text{PSI/RAD}$$

which can be reduced to the form

$$\frac{P_L}{\theta_A}(s) = \frac{I_{EQ}}{57.3\,C_A}\left[\frac{s\left\{s^3 + \frac{D_{EQ}}{I_{EQ}}s^2 + \left(\frac{K_s}{I_{EQ}} + \omega_s^2\right)s + \frac{D_{EQ}}{I_{EQ}}\omega_s^2\right\}}{s^2+\omega_s^2}\right] \text{PSI/DEG}$$

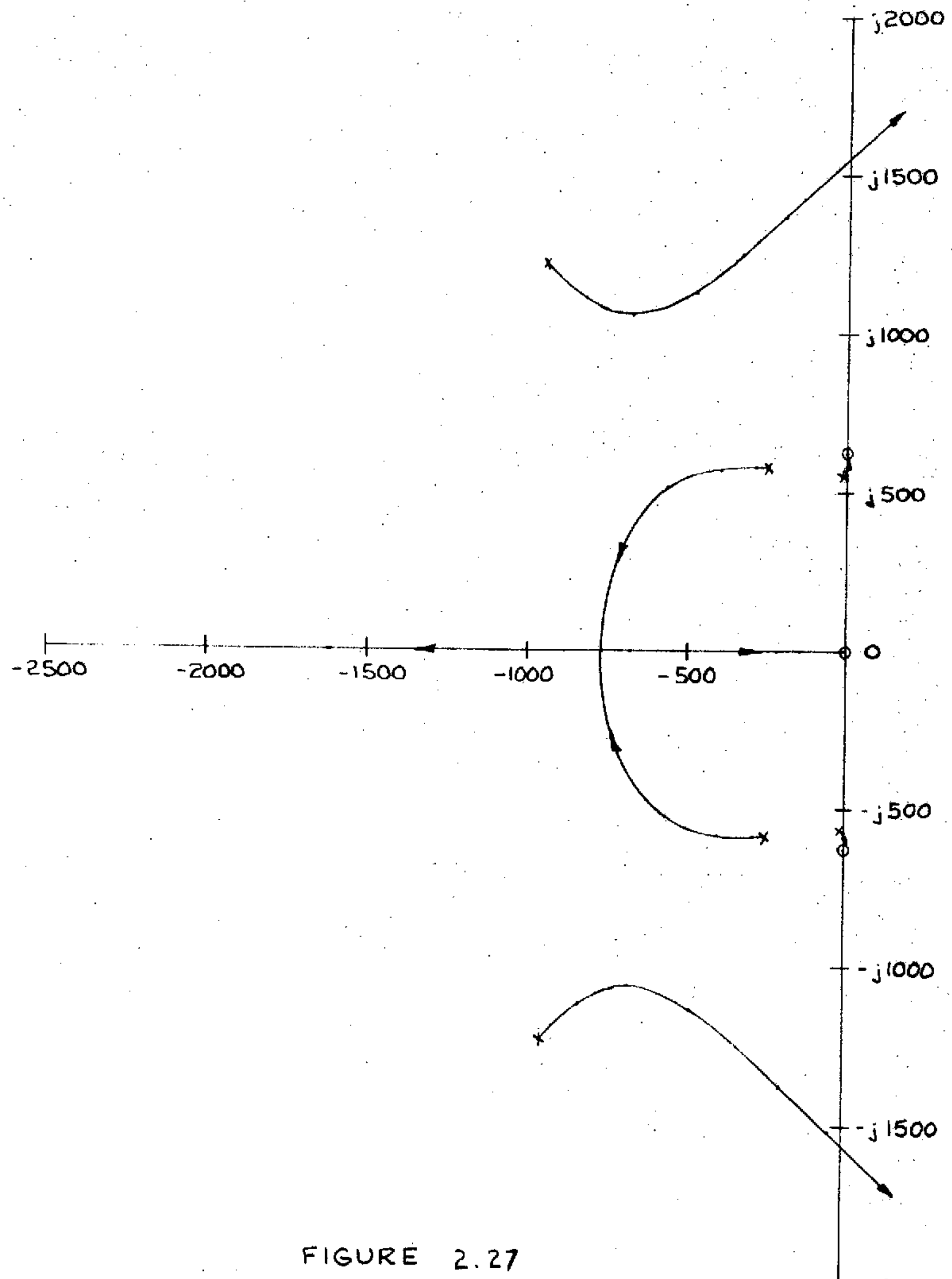

FIGURE 2.27

BASELINE ACTUATION SYSTEM ROOT LOCUS

ANGULAR RATE FEEDBACK WITH 426.5/SEC POSITION LOOP GAIN

Substituting values for I_{EQ}, D_{EQ}, C_A, K_s and ω_s^2 determined in Reference 1, the transfer function becomes

$$\frac{P_L}{\theta_A}(s) = \frac{.00084}{57.3(.0615)} \left[\frac{s\left\{ s^3 + 4.777\times10^3 s^2 + \left(\frac{368.9}{.00084} + 3.911\times10^5\right)s + 4.777\times10^3\left(3.911\times10^5\right)\right\}}{s^2 + 3.911\times10^5} \right]$$

$$= 2.383\times10^{-4} \frac{\left[s\left\{ s^3 + 4777 s^2 + 8.303\times10^5 s + 1.868\times10^9 \right\}\right]}{s^2 + 3.911\times10^5}$$

$$= 2.383\times10^{-4} \frac{\left[s\left(s + 46.06 \pm j629.768\right)\left(s + 4684.88\right)\right]}{s \pm j625.38} \quad \mathrm{PSI/DEG}$$

Figure 2.28 shows the actuation system block diagram with load pressure feedback for 1.01 volt/deg position feedback gain. The load pressure feedback signal is passed through a washout to eliminate steady state position errors due to a static load on the actuator.

The root locus for this case is shown in Figure 2.29. As the pressure feedback gain is increased, damping of the dominant second order increases, but the servovalve damping decreases, indicating that a relatively low gain must be used. Damping of the coupled control surface mode increases slightly, due primarily to the complex zeros being off the imaginary axis, rather than on the axis for the shaft rate feedback root locus.

2.6.1.2 Testing

Load pressure feedback was added to the baseline actuation system and subsequent testing showed that the system could be stabilized. CEC strain gage pressure transducers, part number 4-326-0008, were installed at the servovalve control ports and differential pressure formed on an EAI TR-48 analog computer. The washout for the load pressure feedback was also formed on the analog computer.

Figure 2.30 shows a frequency response of the baseline system with load pressure feedback. This response was obtained with only 0.75 volt/deg position feedback gain. The amplitude is flat within ±0.20 degrees up to 50 Hz, but the phase lag is greater than desired in the 5 to 25 Hz range. No attempt was made to improve the baseline system performance. The primary result of the baseline system testing is the fact that load pressure feedback with washout would give a stable system with the degree of damping on the dominant mode adjustable by adjusting the pressure feedback gain.

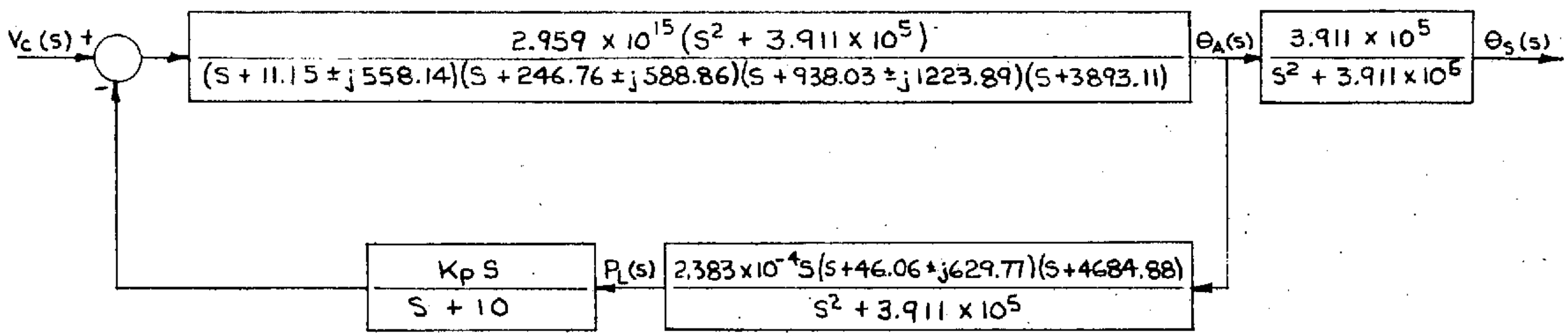

FIGURE 2.28

BLOCK DIAGRAM OF BASELINE SYSTEM WITH T.E. CONTROL SURFACE POSITION FEEDBACK GAIN 1.01 VOLT/DEG

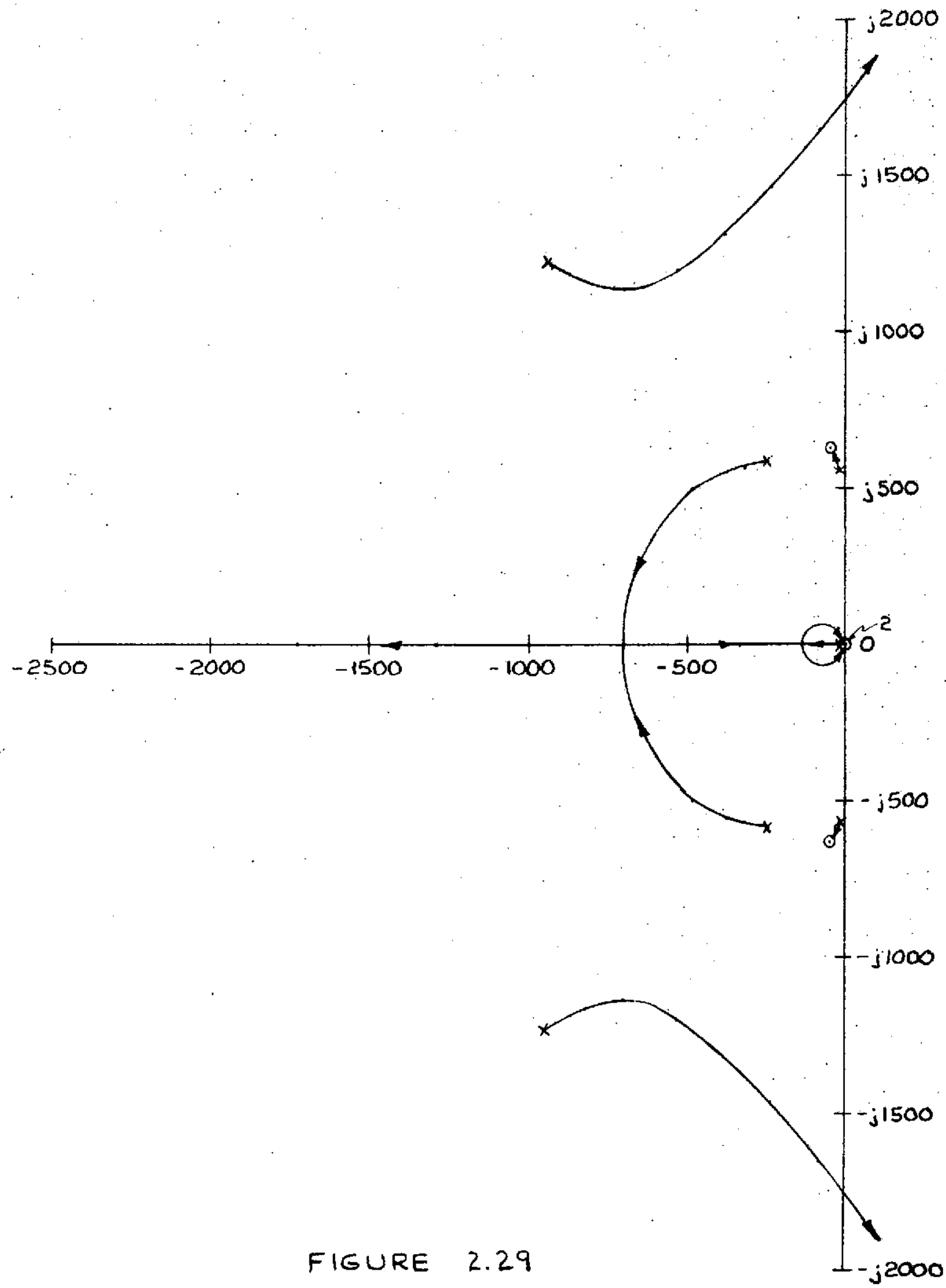

FIGURE 2.29

BASELINE ACTUATION SYSTEM ROOT LOCUS

PRESSURE FEEDBACK WITH 426.5/SEC POSITION LOOP GAIN

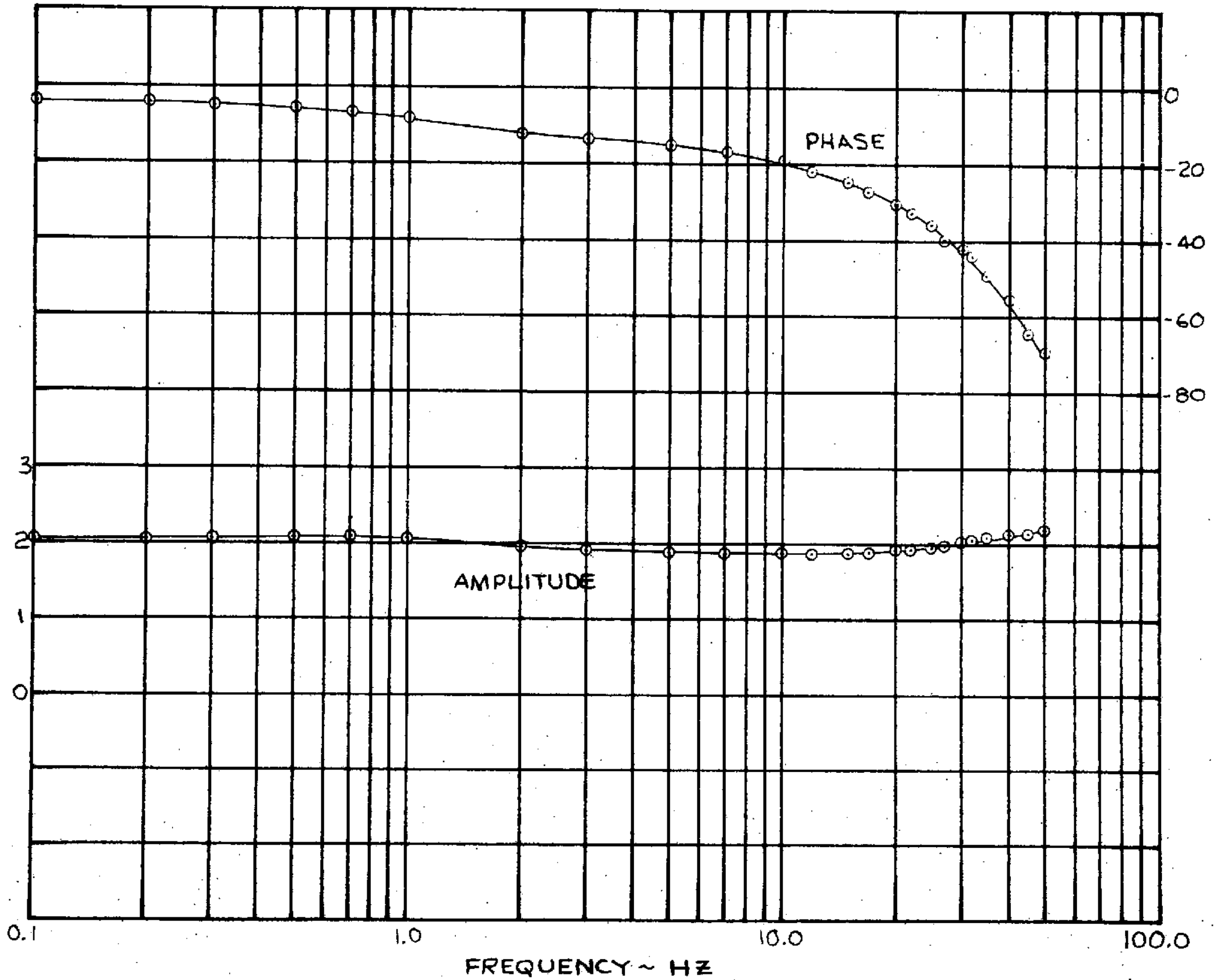

FIGURE 2.30
FREQUENCY RESPONSE OF BASELINE SYSTEM WITH T.E. CONTROL SURFACE

NOTE: POSITION GAIN .75 VOLT/DEG, LOAD PRESSURE GAIN $\approx$ .007 VOLT/PSI, 2.04 SIN $(2\pi f)t$ DEG COMMAND

2.6.2 Model Modification

The wing model was modified at Boeing-Wichita to incorporate electro-hydraulic actuation systems for the leading and trailing edge control surfaces. The model had been received from NASA with the surfaces already fabricated. Angular position transducers were developed, using silicon photocells, to mount at the actuator shafts without violating the wing surfaces.

After the systems were installed, they were tested to verify that satisfactory performance for the flutter suppression system testing could be attained. The model was then reshipped to NASA, where engineering support was provided in setting up the model and conducting wind tunnel tests.

2.6.2.1 Actuation System Installation

Figure 2.31 is a photograph of the model with the complete actuation systems installed. The servovalves were mounted on the aluminum plate at the wing inboard edge, which is under the fuselage fairing when the model is mounted in the wind tunnel test section. The hydraulic lines, and wiring for the position transducers, were laid in troughs cut into the balsa forming the airfoil shape. These troughs, and the area around the actuators, were covered prior to the wind tunnel tests.

The photograph in Figure 2.32 shows the details of the trailing edge surface actuator installation. The actuator is cantilevered aft from the model aluminum alloy structural plate so the actuator shaft lines up with the surface hinge line. The aluminum tubing the surface is mounted on was split so the actuator shaft could slip into the tubing inner diameter. A special clamp was fabricated to slip over the tubing to effect coupling of the actuator shaft and surface by tightening the screw in the clamp. Subsequent testing showed this method to be ineffective, so a tapered pin was installed through the tubing and actuator shaft. The leading edge surface actuator, shown in Figure 2.33, was installed in a similar manner, with the actuator cantilevered forward to align the actuator shaft with the surface hinge line.

Special elbow fittings were fabricated for both actuators to provide O-ring seal at the actuator ports. Clippard Instrument Laboratory, Inc., #10-32 to 1/8-inch tubing connectors (Part Number 11923) were modified to add O-ring seal where the tubing connects to the elbow fittings.

Both photographs show the angular position transducers installed on the actuators. The photocell assemblies consist of two Sensor Technology, Inc. ST-203 cells mounted on a common brass base with 0.010 inch gap between the cells. The assemblies are mounted on phenolic cylinders which in turn mount on the actuator shaft. General Electric #328 6-volt d.c. instrument lamps are used as the light source. The lamps mount in sockets supported by phenolic blocks that are cantilevered from the actuator bodies. A semicircular disk is installed in the phenolic to create a semicircular area of light encompassing half of both cells in the null position. As the cell assemblies rotate with the actuator shafts, the change in illumination area of the cells is proportional

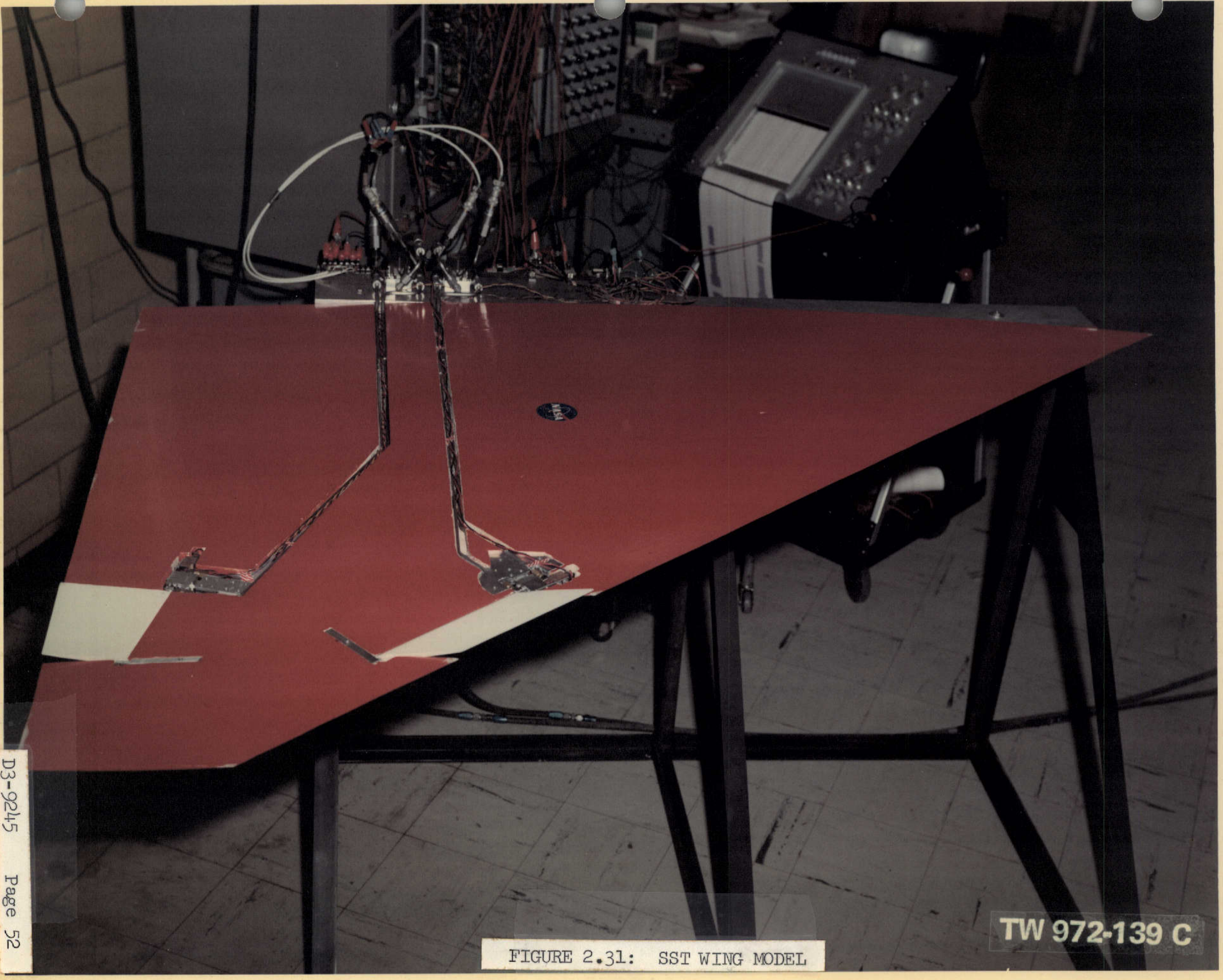

FIGURE 2.31: SST WING MODEL

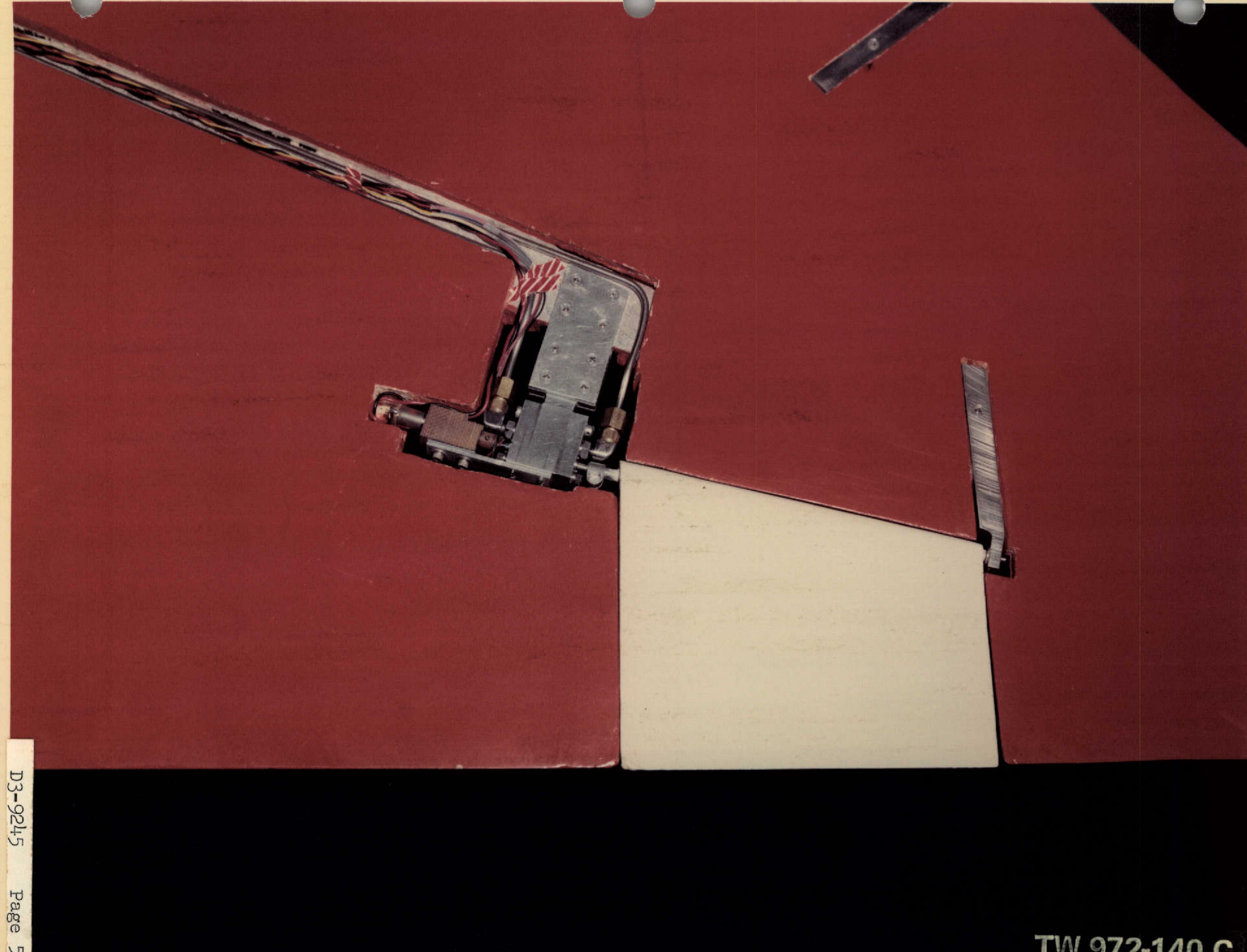

FIGURE 2.32: TRAILING EDGE SURFACE ACTUATOR INSTALLATION

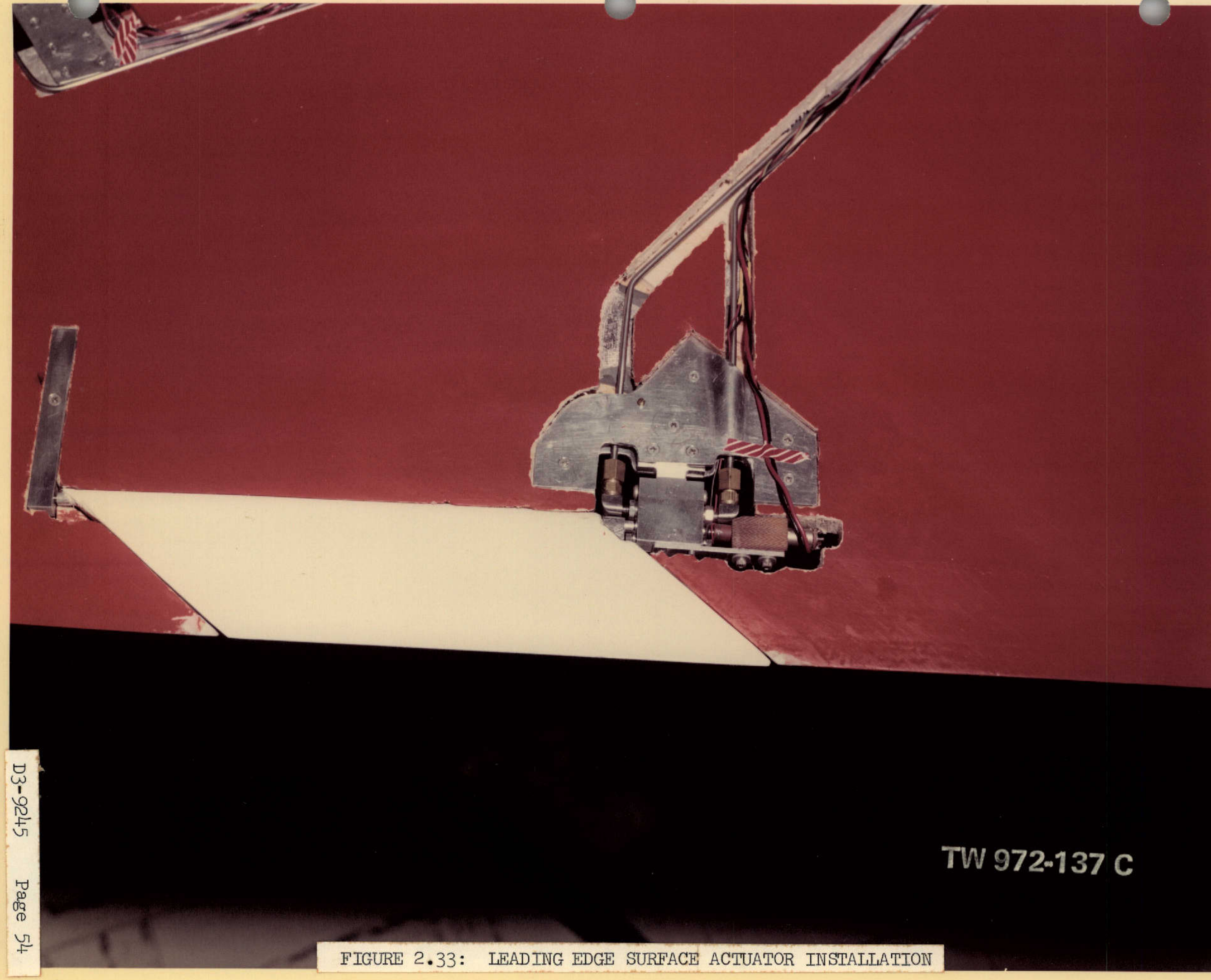

FIGURE 2.33: LEADING EDGE SURFACE ACTUATOR INSTALLATION

to the tangent of the angle of rotation. Twenty-turn, 500 ohm trim potentiometers are used to load the cells and provide balance for the cells' outputs with the wiper wired to the brass base.

Linearity was measured by mounting a transducer on a shaft with a New England Instrument 78ESB102 potentiometer mounted on the other end of the shaft and comparing output voltages for a given displacement. The transducer and potentiometer output voltages were scaled on the TR-48 analog computer. Plots of angular displacement indicated by the transducers versus displacements indicated by the potentiometer are shown in Figures 2.34 and 2.35. These plots show good linearity in the ±10 degree range of the actuators.

2.6.2.2 Test Results

Both actuation systems were tested after installation in the model to demonstrate that desired performance could be attained. Feedback loops for the systems were mechanized on a TR-48 analog computer which was also used for input/output functions. The general test set-up is shown in Figure 2.31.

Frequency responses for the two systems are shown in Figures 2.36 and 2.37. These responses, for two degree input amplitude, show actuator amplitude flat to within 0.24 degree in the 5 to 25 Hz range. Phase shift in this range is 26 degrees for the leading edge actuation system and 23 degrees for the trailing edge system. The leading edge surface actuator had more friction than the trailing edge surface actuator, as indicated in the hysteresis plots shown in Figures 2.38 and 2.39. Hysteresis of the leading edge system measured about ±0.08 degrees, with only ±0.04 degrees measured on the trailing edge system. The leading edge surface actuator was new and not completely broken in when this data was recorded.

The system step responses, Figures 2.40 and 2.41, indicate slightly less damping for down surface displacements (positive deflection) than for up displacements. The desired damping ratio on the dominant second order was 0.30. The trailing edge system peak overshoot indicates about 0.4 damping, and the leading edge about 0.3.

No attempt was made to improve the system performance because different pressure transducers were to be installed at NASA. The phase requirement for the flutter suppression system was later relaxed to 20 degrees or less at the 12 Hz flutter mode frequency, across the actuation systems. The goal of no more than 15 degrees phase lag at 25 Hz (as stated in Reference 1) was found through system evaluation analyses to be unnecessary.

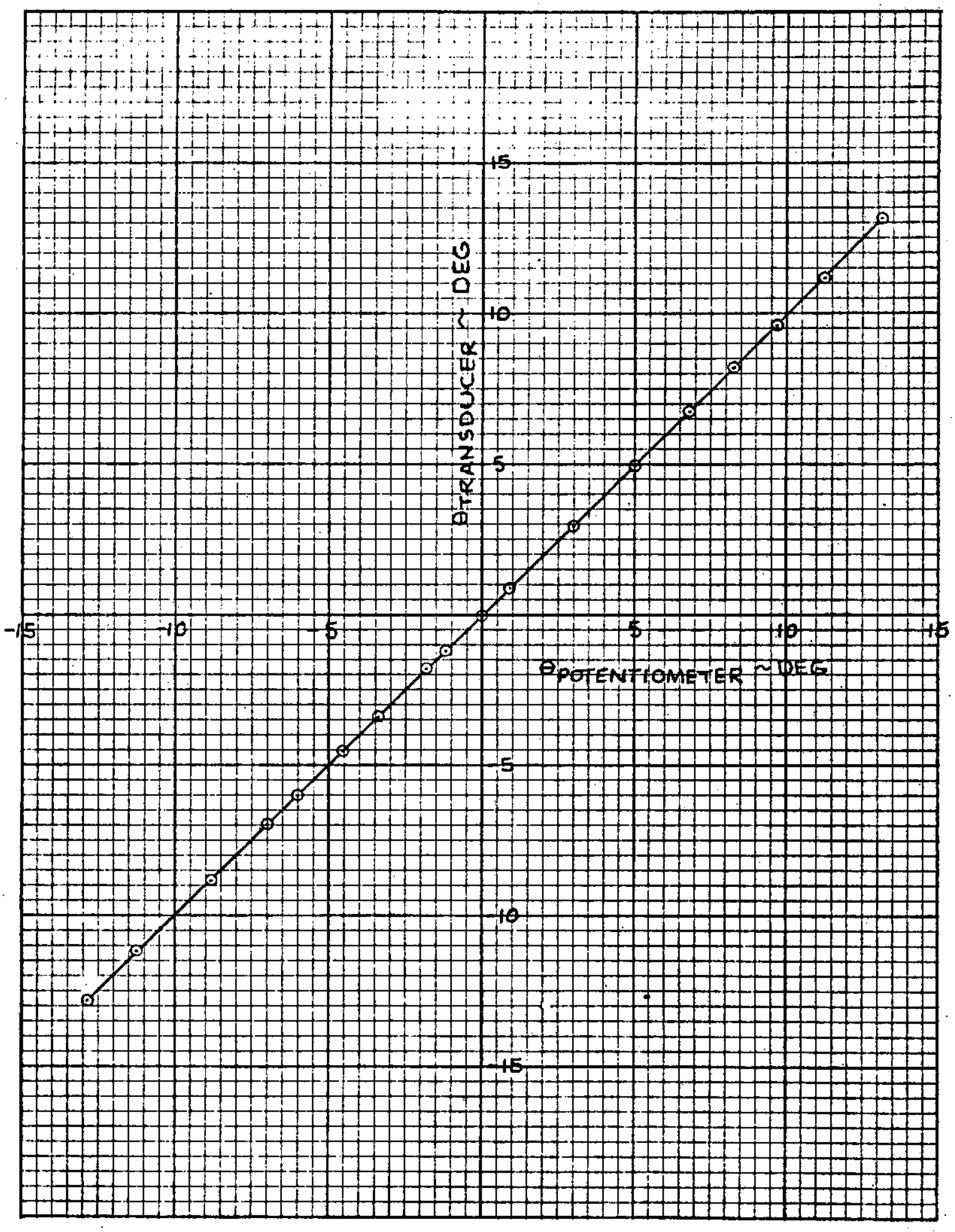

FIGURE 2.34

PHOTOCELL ANGULAR POSITION TRANSDUCER LINEARITY
(LEADING EDGE SURFACE)

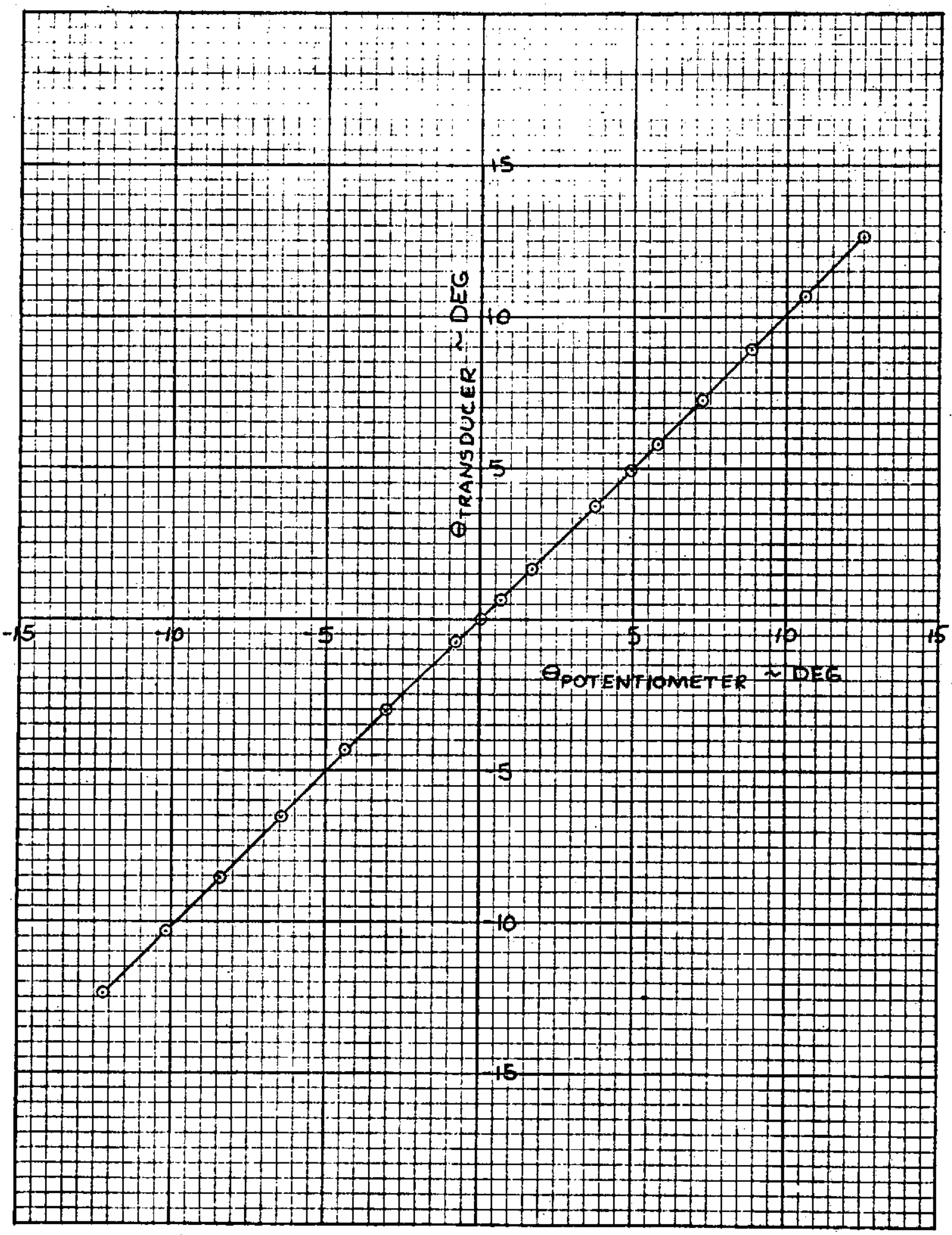

FIGURE 2.35

PHOTOCELL ANGULAR POSITION TRANSDUCER LINEARITY
(TRAILING EDGE SURFACE)

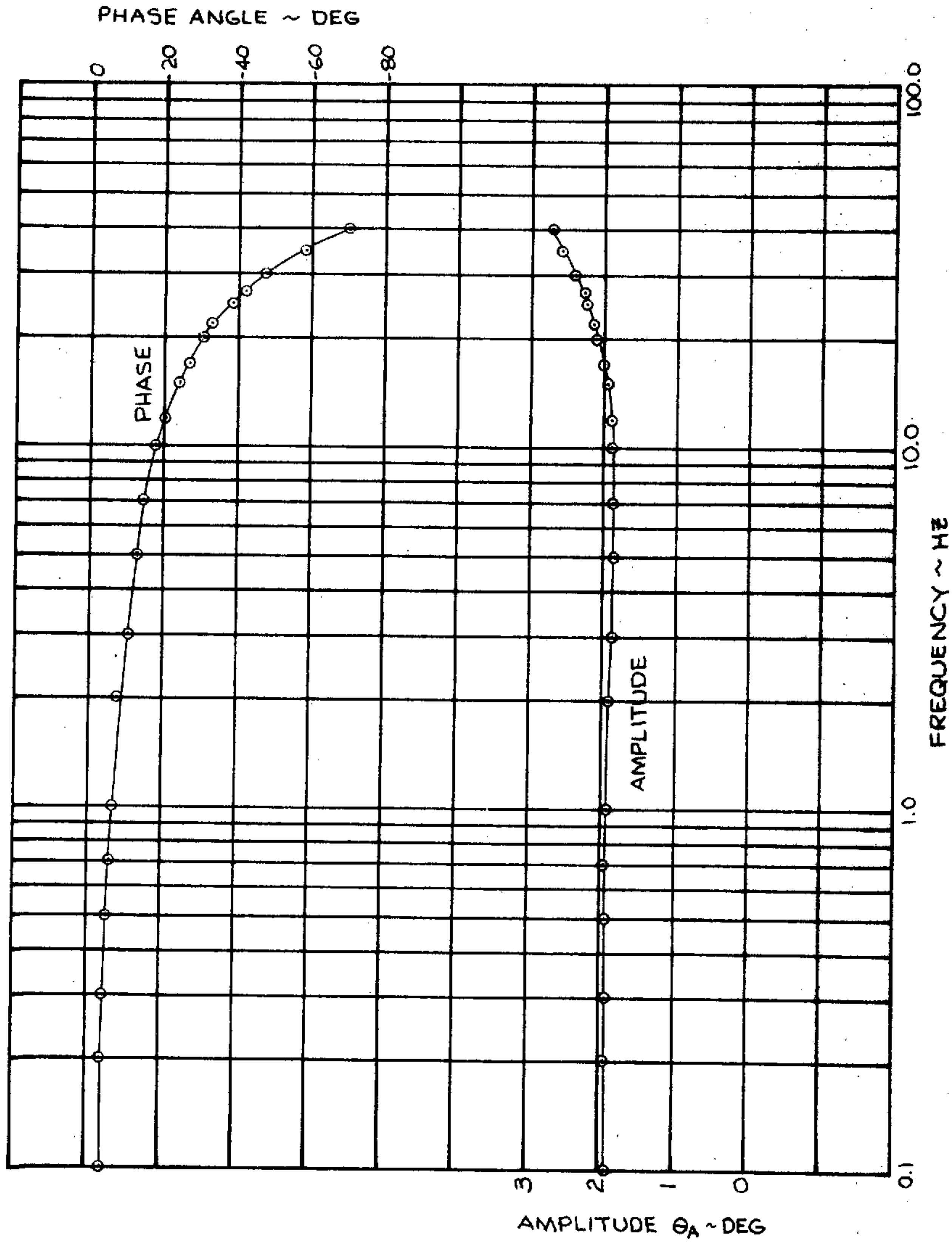

FIGURE 2.36
LEADING EDGE SURFACE ACTUATION SYSTEM FREQUENCY RESPONSE

NOTE: POSITION FEEDBACK .93 VOLT/DEG, LOAD PRESSURE FEEDBACK $\approx .006\, s/(s+10)$ VOLT/PSI, 2.00 SIN$(2\pi f)t$ DEG COMMAND

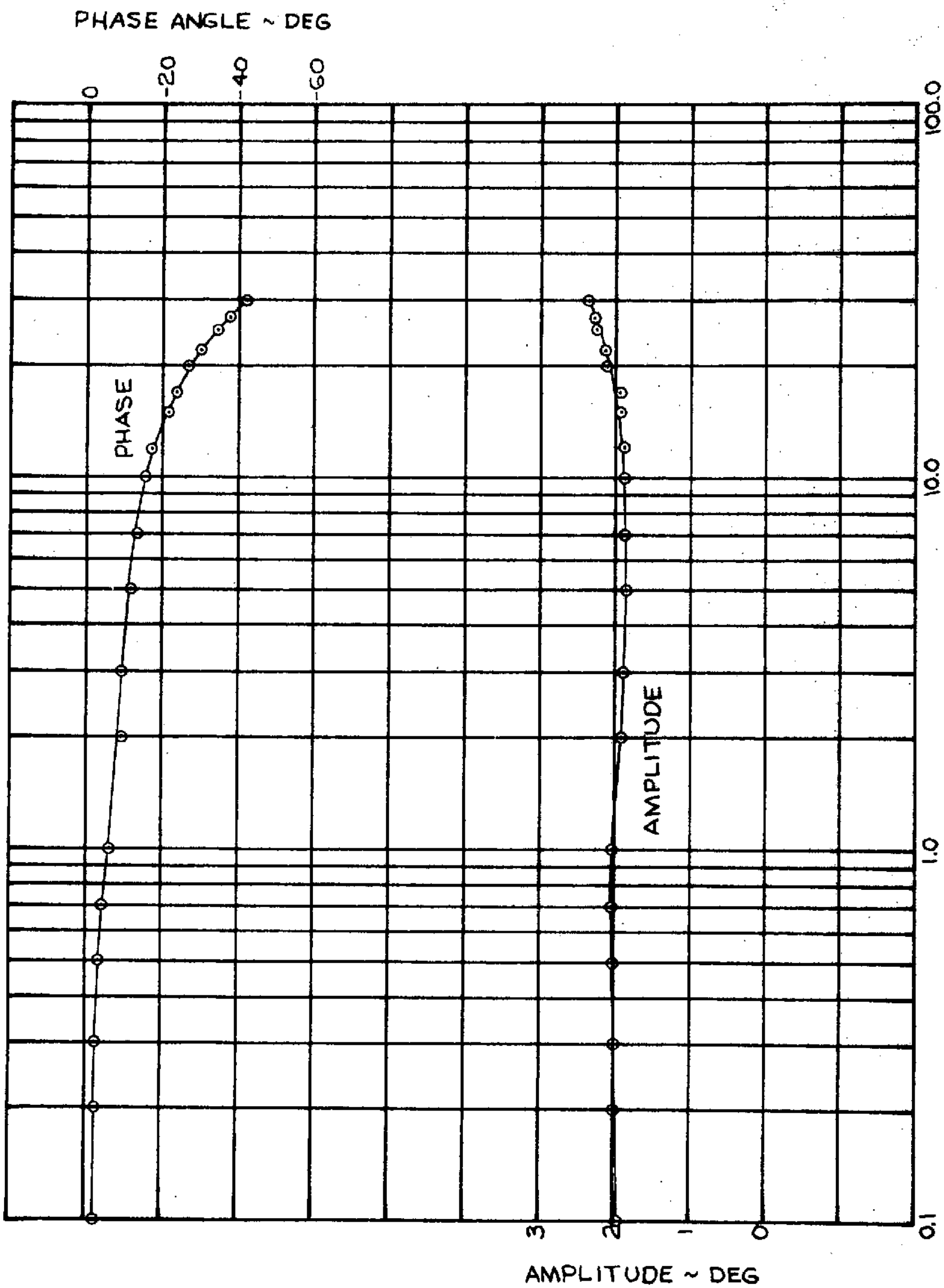

FIGURE 2.37
TRAILING EDGE SURFACE ACTUATION SYSTEM FREQUENCY RESPONSE

NOTE: POSITION FEEDBACK .93 VOLT/DEG, LOAD PRESSURE FEEDBACK $\approx .008\,S/(S+10)$ VOLT/PSI, 2.00 SIN $(2\pi f)t$ DEG COMMAND

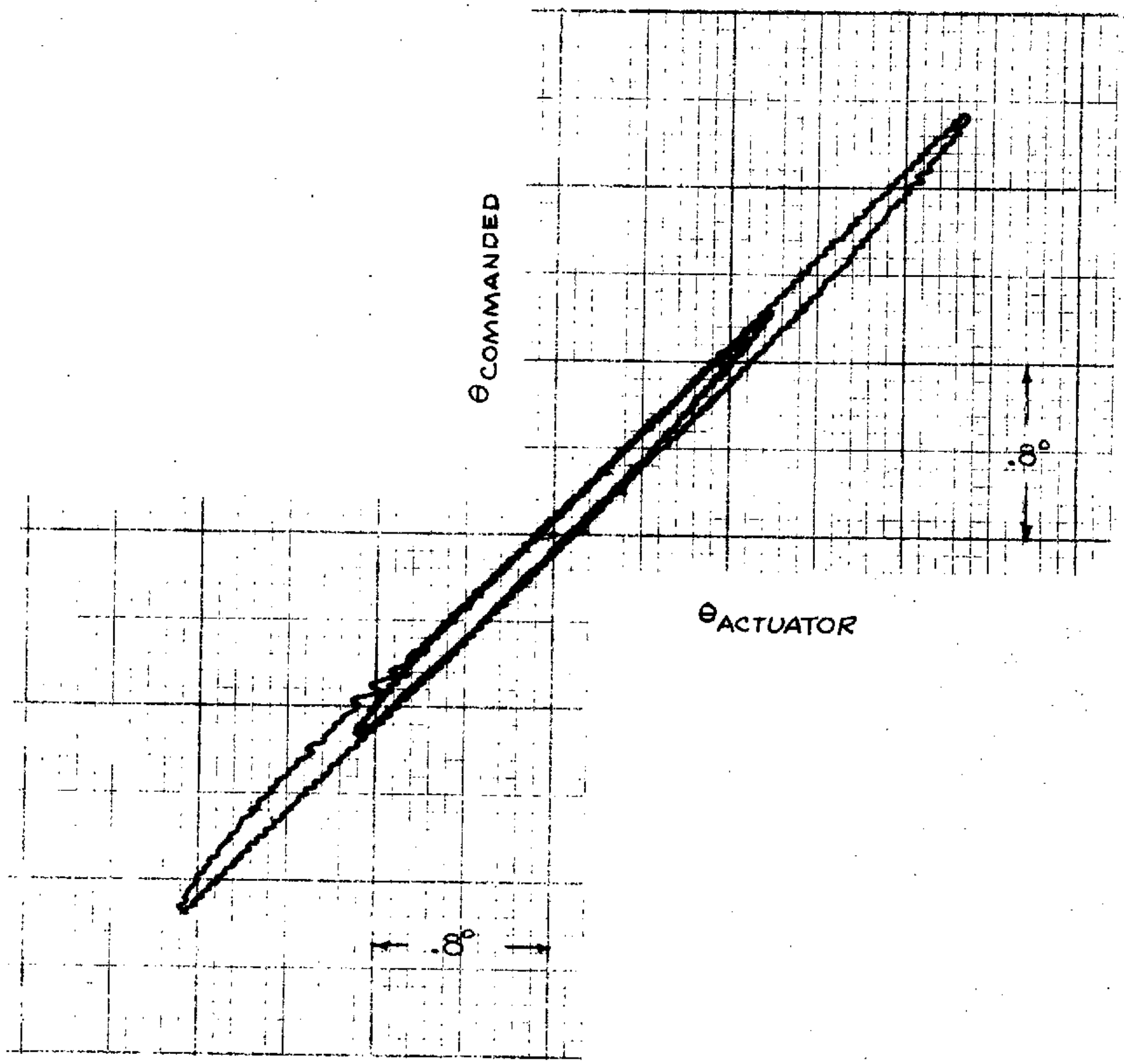

FIGURE 2.38

LEADING EDGE SURFACE ACTUATION SYSTEM

HYSTERESIS

NOTE: POSITION FEEDBACK .93 VOLT/DEG; LOAD PRESSURE FEEDBACK .006 S/(S+10) VOLT/PSI; PHOTOCELL ANGULAR POSITION TRANSDUCER; 0.1 HZ TRIANGULAR WAVE INPUT.

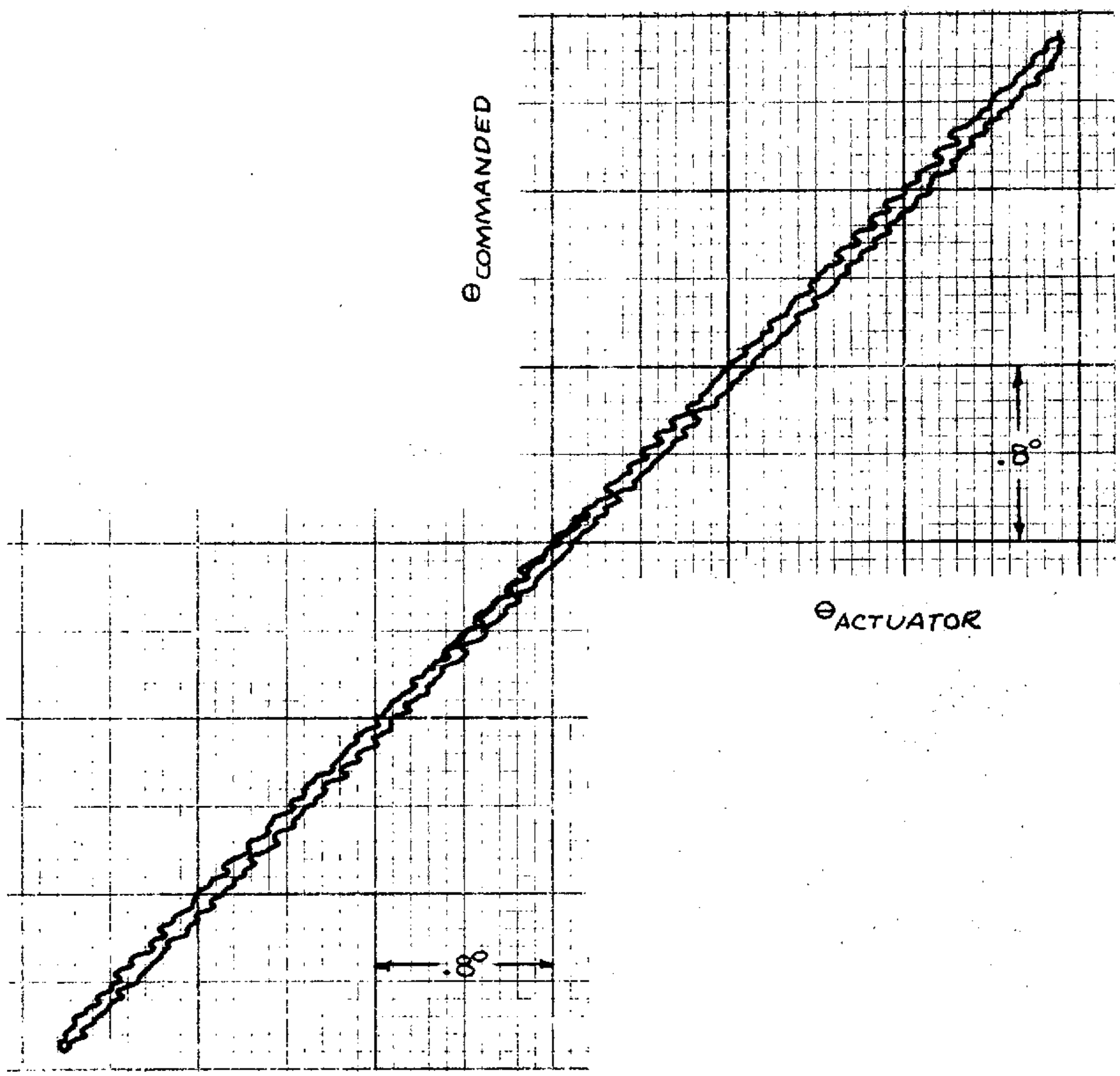

FIGURE 2.39

TRAILING EDGE SURFACE ACTUATION SYSTEM HYSTERESIS

NOTE: POSITION FEEDBACK .93 VOLT/DEG; LOAD PRESSURE FEEDBACK .008 S/(S+10) VOLT/PSI; PHOTOCELL ANGULAR POSITION TRANSDUCER; 0.1 HZ TRIANGULAR WAVE INPUT. NO ATTEMPT WAS MADE TO CENTER PLOT AT (0,0).

NOTE: POSITION FEEDBACK .93 VOLT/DEG; LOAD PRESSURE FEEDBACK .006 s/(s+10) VOLT/PSI; PHOTOCELL ANGULAR POSITION TRANSDUCER.

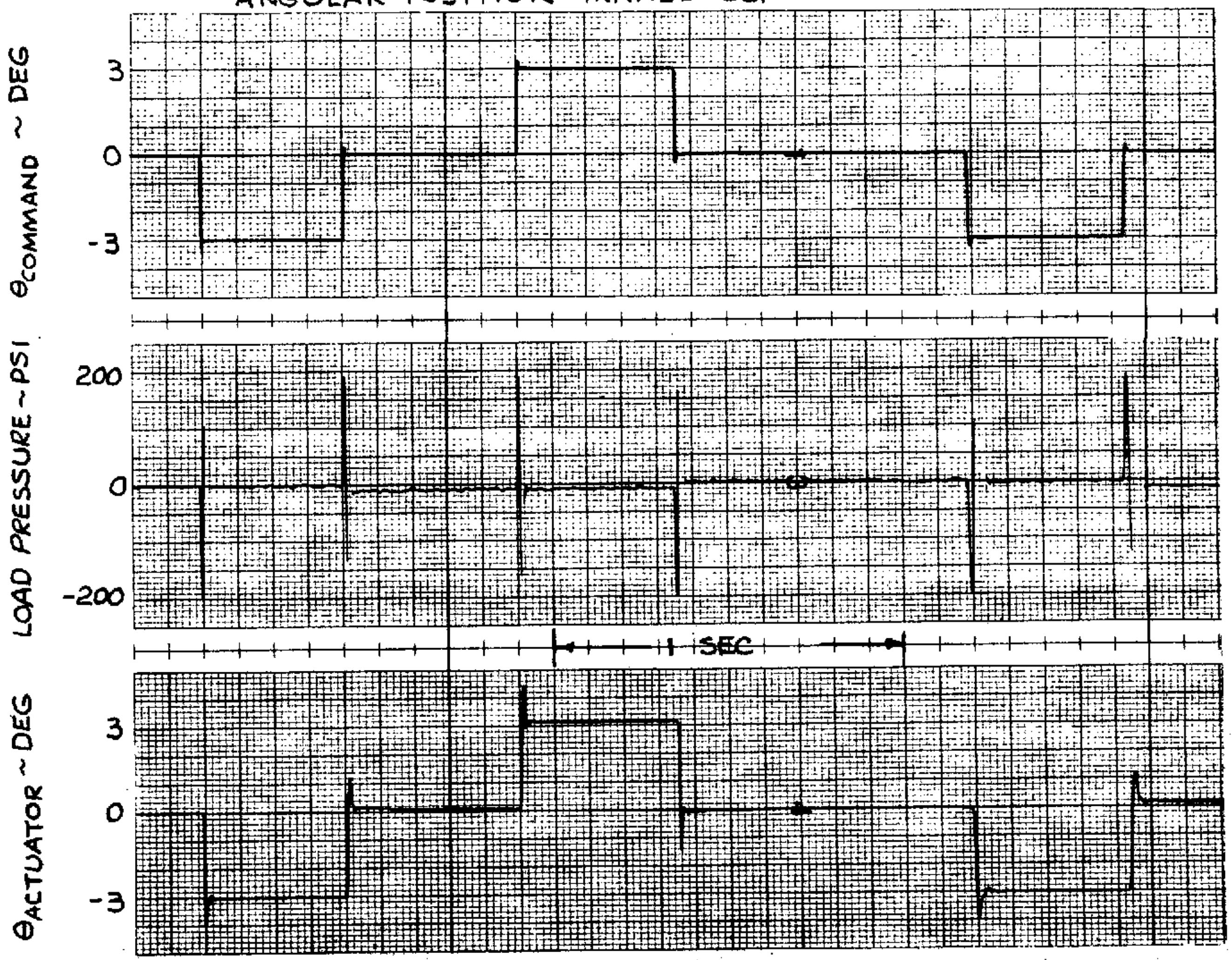

FIGURE 2.40 LEADING EDGE SURFACE ACTUATION SYSTEM TRANSIENT RESPONSES

NOTE: POSITION FEEDBACK .93 VOLT/DEG; LOAD PRESSURE FEEDBACK .008 S/(S+10) VOLT/PSI;
PHOTOCELL ANGULAR POSITION TRANSDUCER

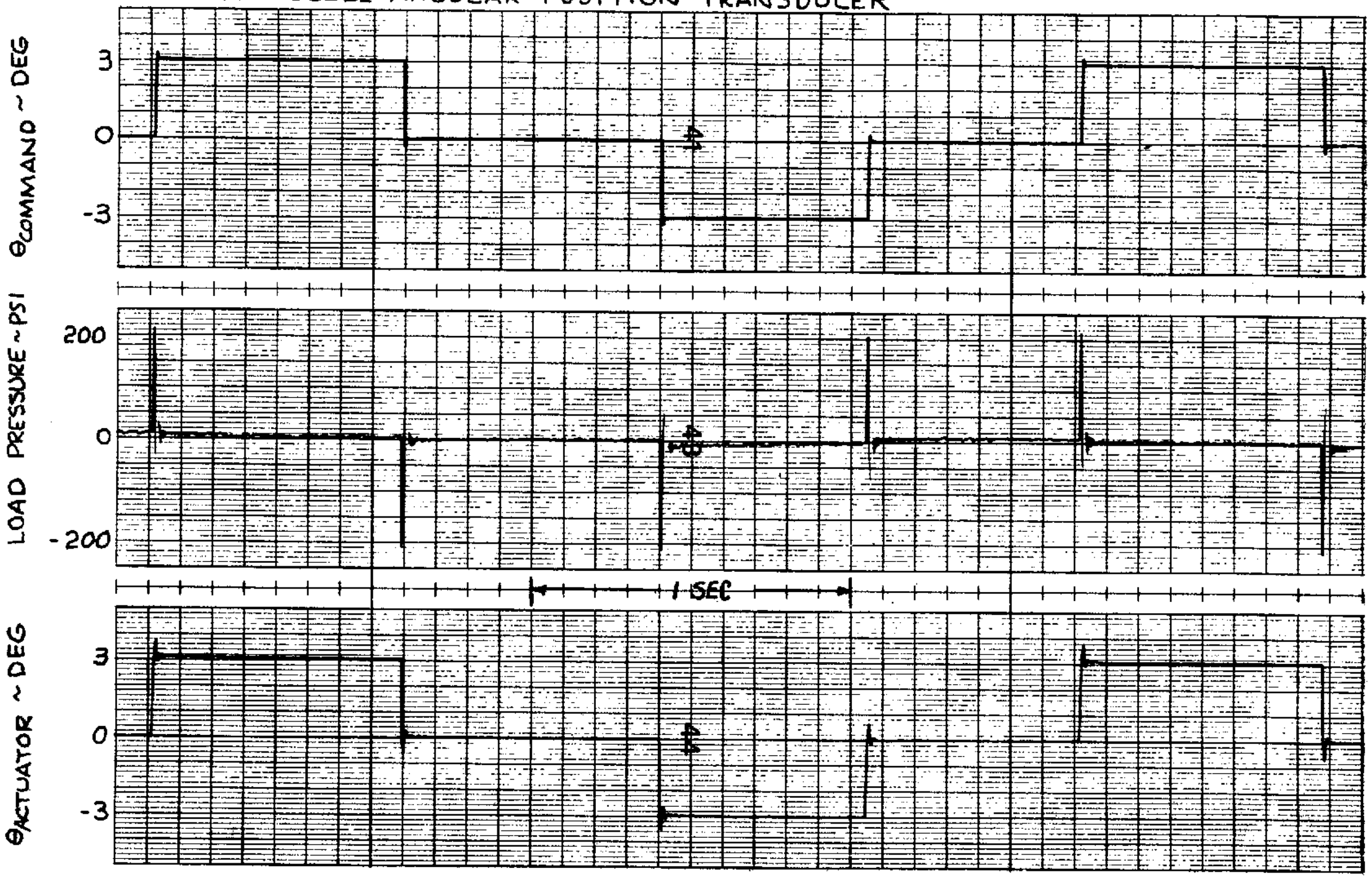

TRAILING EDGE SURFACE ACTUATION SYSTEM TRANSIENT RESPONSES

FIGURE 2.41

2.7 Supporting Data

This section contains a listing of numerical values of the equations of motion described in Section 2.2. Generalized mass and stiffness estimated from GVT data are the same for Mach 0.9 and Mach 0.6 test conditions. Structural damping was assumed to be zero. The first ten elements of the 12 x 1 $\{q_j\}$ vector represent ten elastic modes of vibration; the eleventh and twelfth elements are for the leading and trailing edge control surfaces. Model coefficients are given for accelerations on the midspan strip as shown below:

$$\left\{\ddot{h}_i(S)\right\} = S^2 \left[PHI1\right] \left\{q_j\right\}$$

where $\left\{\ddot{h}_i(S)\right\}$ are accelerations at locations shown in Table 2-IV

$\left\{q_j\right\}$ is the generalized degree-of-freedom vector

$\left[PHI1\right]$ is the modal matrix.

TABLE 2-IV

LOCATIONS OF ACCELERATION GIVEN BY MODAL MATRIX

Row	Spanwise Location			Chordwise Location	
1	Midspan	Surface;	Inboard Edge	30	Percent (from L.E.)
2	"	"	Inboard Edge	70	"
3	"	"	Centerline	30	"
4	"	"	Centerline	70	"
5	"	"	Outboard Edge	30	"
6	"	"	Outboard Edge	70	"

'M' 12 X 12

ROW 1					
3.0720E 03	1.1772E-04	1.0514E-04	7.8321E-05	5.8293E-05	1.8729E-04
-4.8280E-06	-7.3552E-05	7.0512E-05	-1.3614E-04	1.0535E 02	-4.3709E 02
ROW 2					
1.1789E-04	9.7750E 02	6.6996E-05	1.2696E-05	1.2040E-05	8.0824E-05
-3.3482E-06	-1.2971E-05	5.9068E-05	-1.6928E-04	7.9526E 01	-2.6679E 02
ROW 3					
7.5817E-05	4.0054E-05	2.3390E 03	2.8133E-05	3.1590E-06	5.6267E-05
-1.1206E-05	-7.9870E-06	3.8147E-06	-9.5606E-05	-4.3982E 01	-2.9337E 02
ROW 4					
7.9811E-05	1.5676E-05	1.6451E-05	1.4400E 03	6.5565E-06	5.3406E-05
-8.4639E-06	-9.4771E-06	7.6294E-06	-2.7895E-05	-1.5349E 01	-2.2260E 02
ROW 5					
3.3855E-05	1.9133E-05	7.5102E-06	7.6294E-06	3.9700E 03	-7.0572E-05
-1.7166E-05	-6.4373E-06	-1.0490E-05	-4.7684E-06	-1.0477E 02	-1.6427E 02
ROW 6					
1.3907E-04	6.5744E-05	3.8147E-05	1.7166E-05	-6.9619E-05	1.6400E 03
-1.2696E-05	-4.2915E-06	-1.1158E-04	-8.5831E-05	-2.2101E 02	-3.4512E 02
ROW 7					
-5.6215E-06	-2.7902E-06	-1.0133E-05	-6.4373E-06	-1.4186E-05	-1.0014E-05
7.0200E 02	7.5772E-06	-1.3998E-05	1.3113E-05	-1.5567E 01	1.2374E 02
ROW 8					
-7.7486E-05	-1.4794E-05	-8.3447E-06	-1.1086E-05	-2.4439E-06	-1.9073E-06
1.1414E-05	5.0400E 03	-4.7684E-07	8.4400E-05	3.2984E 01	2.2946E 02
ROW 9					
7.3135E-05	3.4213E-05	4.7684E-06	6.4373E-06	-5.7220E-06	-1.1063E-04
-1.1444E-05	-6.0797E-06	2.8900E 03	-2.8610E-06	-1.5010E 02	-1.3232E 02
ROW 10					
-1.3695E-04	-1.5473E-04	-1.2565E-04	-3.3326E-05	-2.8610E-06	-8.8692E-05
1.4186E-05	8.5175E-05	-3.8147E-06	2.0000E 03 *	6.9292E 01	4.3310E 02
ROW 11					
1.0535E 02	7.9526E 01	-4.3982E 01	-1.5349E 01	-1.0477E 02	-2.2101E 02
-1.5567E 01	3.2984E 01	-1.5010E 02	6.9292E 01	5.6409E 02	0.0
ROW 12					
-4.3709E 02	-2.6674E 02	-2.9337E 02	-2.2260E 02	-1.6427E 02	-3.4512E 02
1.2374E 02	2.2946E 02	-1.3232E 02	4.3310E 02	0.0	3.3831E 03

* MODE 10 MASS HAS NOT BEEN DETERMINED -- THIS IS A DUMMY VALUE

'D' 12 X 12

ROW 1

0.0	0.0	0.0	0.0	0.0	0.0
0.0	0.0	0.0	0.0	0.0	0.0

ROW 2

0.0	0.0	0.0	0.0	0.0	0.0
0.0	0.0	0.0	0.0	0.0	0.0

ROW 3

0.0	0.0	0.0	0.0	0.0	0.0
0.0	0.0	0.0	0.0	0.0	0.0

ROW 4

0.0	0.0	0.0	0.0	0.0	0.0
0.0	0.0	0.0	0.0	0.0	0.0

ROW 5

0.0	0.0	0.0	0.0	0.0	0.0
0.0	0.0	0.0	0.0	0.0	0.0

ROW 6

0.0	0.0	0.0	0.0	0.0	0.0
0.0	0.0	0.0	0.0	0.0	0.0

ROW 7

0.0	0.0	0.0	0.0	0.0	0.0
0.0	0.0	0.0	0.0	0.0	0.0

ROW 8

0.0	0.0	0.0	0.0	0.0	0.0
0.0	0.0	0.0	0.0	0.0	0.0

ROW 9

0.0	0.0	0.0	0.0	0.0	0.0
0.0	0.0	0.0	0.0	0.0	0.0

ROW 10

0.0	0.0	0.0	0.0	0.0	0.0
0.0	0.0	0.0	0.0	0.0	0.0

ROW 11

0.0	0.0	0.0	0.0	0.0	0.0
0.0	0.0	0.0	0.0	0.0	0.0

ROW 12

0.0	0.0	0.0	0.0	0.0	0.0
0.0	0.0	0.0	0.0	0.0	0.0

'K' 12 X 12

ROW						
ROW 1	6.7674E 06	0.0	0.0	0.0	0.0	0.0
	0.0	0.0	0.0	0.0	0.0	0.0
ROW 2	0.0	9.3792E 06	0.0	0.0	0.0	0.0
	0.0	0.0	0.0	0.0	0.0	0.0
ROW 3	0.0	0.0	4.8872E 07	0.0	0.0	0.0
	0.0	0.0	0.0	0.0	0.0	0.0
ROW 4	0.0	0.0	0.0	3.4431E 07	0.0	0.0
	0.0	0.0	0.0	0.0	0.0	0.0
ROW 5	0.0	0.0	0.0	0.0	2.1730E 08	0.0
	0.0	0.0	0.0	0.0	0.0	0.0
ROW 6	0.0	0.0	0.0	0.0	0.0	1.2139E 08
	0.0	0.0	0.0	0.0	0.0	0.0
ROW 7	0.0	0.0	0.0	0.0	0.0	0.0
	5.8286E 07	0.0	0.0	0.0	0.0	0.0
ROW 8	0.0	0.0	0.0	0.0	0.0	0.0
	0.0	4.6130E 08	0.0	0.0	0.0	0.0
ROW 9	0.0	0.0	0.0	0.0	0.0	0.0
	0.0	0.0	3.8473E 08	0.0	0.0	0.0
ROW 10	0.0	0.0	0.0	0.0	0.0	0.0
	0.0	0.0	0.0	3.3154E 08 *	0.0	0.0
ROW 11	0.0	0.0	0.0	0.0	0.0	0.0
	0.0	0.0	0.0	0.0	0.0	0.0
ROW 12	0.0	0.0	0.0	0.0	0.0	0.0
	0.0	0.0	0.0	0.0	0.0	0.0

* MODE 10 MASS HAS NOT BEEN DETERMINED -- THIS IS ω^2 x DUMMY-MASS

'C_1' 12 X 12 MACH 0.9

ROW 1
2.6467E 04 9.9644E 03 1.3435E 04 1.0677E 04 8.1419E 03 1.3821E 04
-1.3848E 03 -4.0106E 03 3.9076E 02 -2.5775E 03 2.4467E 03 -1.5074E 04

ROW 2
1.2228E 04 8.8070E 03 9.3125E 03 7.3292E 03 3.2459E 03 2.9954E 03
6.0269E 02 3.6104E 02 -1.2903E 03 2.1091E 03 2.6054E 03 -5.2026E 03

ROW 3
3.3107E 03 4.6284E 03 1.9543E 04 1.2159E 04 7.0661E 03 1.1065E 04
9.5093E 02 -1.3474E 03 3.6133E 03 1.0653E 03 -1.9027E 02 -9.6160E 03

ROW 4
-1.8075E 02 3.8531E 03 1.3127E 04 1.0095E 04 6.4792E 03 7.6750E 03
2.2445E 03 9.4208E 02 -7.7972E 02 3.4769E 03 4.5307E 02 -5.3676E 03

ROW 5
1.8052E 03 7.9127E 02 8.9838E 03 8.9736E 03 1.4628E 04 1.5807E 04
6.7479E 03 4.4561E 03 4.8626E 03 3.4428E 02 -2.0143E 03 -1.0409E 04

ROW 6
1.8913E 03 -8.8104E 02 2.0127E 04 1.3566E 04 1.8202E 04 2.7650E 04
5.2078E 03 1.1710E 02 1.1458E 04 -3.8186E 03 -5.2668E 03 -2.0492E 04

ROW 7
4.5189E 03 3.1636E 03 -2.9230E 03 1.3558E 03 6.1710E 03 2.3748E 03
9.4977E 03 1.0743E 04 2.7479E 03 6.5230E 03 -2.7270E 02 5.3716E 03

ROW 8
-6.3904E 03 3.9782E 03 -7.4609E 03 -1.2435E 03 3.6912E 03 -2.2254E 03
9.8670E 03 1.2257E 04 1.3906E 03 8.1378E 03 7.8693E 02 1.0189E 04

ROW 9
2.6034E 03 4.2806E 03 1.5479E 03 4.2895E 01 7.3699E 03 5.0798E 03
9.9091E 03 1.0999E 04 1.8483E 04 -2.3772E 03 -2.9590E 03 -1.6397E 03

ROW 10
1.2750E 03 1.6591E 03 2.1804E 03 3.5814E 03 8.5865E 02 3.2476E 03
2.6201E 03 2.3910E 03 -3.2514E 03 1.3306E 04 4.6537E 02 9.9479E 03

ROW 11
3.1179E 03 -4.5142E 02 -9.0975E 02 -7.7212E 01 1.1880E 01 3.3985E 02
-1.5120E 03 -1.7400E 03 -4.4489E 03 1.6140E 03 1.0968E 04 -4.0021E 02

ROW 12
-1.9835E 03 -2.6120E 03 -8.9216E 03 -5.5151E 03 2.4341E 03 -8.5271E 03
5.3084E 03 5.6953E 03 1.0904E 04 1.4416E 04 -6.2585E 02 6.5928E 04

'C_2'   12 X 12   MACH 0.9

ROW						
ROW 1	4.4740E 03	2.5110E 03	9.8090E 02	1.0967E 03	8.5447E 02	7.6876E 02
	5.9705E 02	5.2165E 02	1.5836E 03	-8.2641E 02	-5.9306E 02	-5.0901E 03
ROW 2	2.5163E 03	2.2208E 03	1.1877E 03	1.1995E 03	9.1100E 02	7.0756E 02
	8.4472E 02	7.9099E 02	1.5921E 03	-4.7200E 02	-9.4926E 02	-2.5257E 03
ROW 3	1.3904E 03	1.4276E 03	1.8018E 03	1.5254E 03	1.1344E 03	1.7115E 03
	4.0621E 02	3.3066E 01	1.1437E 03	-1.6023E 02	-1.7745E 02	-2.8808E 03
ROW 4	-1.3869E 03	1.3816E 03	1.5532E 03	1.4847E 03	1.1696E 03	1.4313E 03
	6.5636E 02	3.7401E 02	1.1673E 03	-1.0574E 02	-3.7136E 02	-1.9584E 03
ROW 5	8.3309E 02	6.4459E 02	8.7561E 02	1.0301E 03	1.4270E 03	1.8431E 03
	7.7138E 02	4.2696E 02	1.2335E 03	5.3245E 01	4.2476E 02	-1.2735E 03
ROW 6	9.3276E 02	2.5416E 02	1.1076E 03	1.1071E 03	1.6797E 03	3.1036E 03
	2.8898E 02	-3.9782E 02	1.2212E 03	9.0135E 01	1.4950E 03	-3.4395E 03
ROW 7	8.6047E 01	4.7623E 02	4.1216E 02	5.6835E 02	7.3410E 02	4.6305E 02
	1.0551E 03	1.0700E 03	1.2667E 03	2.7589E 02	9.4583E 01	1.9805E 03
ROW 8	-5.1920E 01	4.9811E 02	2.1298E 02	3.9160E 02	4.7562E 02	-1.5040E 02
	1.1546E 03	1.3288E 03	1.1805E 03	3.2760E 02	-1.6335E 02	3.1450E 03
ROW 9	4.0470E 02	3.8449E 02	3.3763E 02	3.2964E 02	1.0587E 03	1.7627E 03
	6.6239E 02	3.7314E 02	2.2426E 03	-4.4486E 02	7.2640E 02	-4.4370E 02
ROW 10	-5.2670E 02	-3.0266E 01	-2.5441E 02	2.0658E 02	-4.6411E 01	-3.4788E 02
	4.1571E 02	5.4670E 02	-2.1459E 02	1.1195E 03	3.1808E 02	5.2703E 03
ROW 11	5.2437E 02	5.3401E 02	-1.2386E 02	-3.5158E 01	-7.4291E 02	-1.5144E 03
	-7.7832E 01	2.5077E 02	-7.6703E 02	3.2809E 02	9.8826E 02	-1.5973E 02
ROW 12	-3.6572E 03	-2.4307E 03	-1.6146E 03	-1.5819E 03	-1.8113E 03	-3.3633E 03
	-1.3251E 02	6.2814E 02	-2.5493E 03	1.9991E 03	3.7269E 02	3.5435E 04

REV LTR:

E-3033 R1

'C_3' 12 X 12 MACH 0.9

ROW						
ROW 1	4.2084E 01	-1.1312E-01	1.0234E-02	7.8683E-01	9.1332E-01	1.7955E 02
	7.3411E 00	-3.6712E 01	1.5347E 02	-8.8734E 01	9.7514E 00	-1.1926E 03
ROW 2	2.4104E 01	-2.7796E-01	5.9243E-01	4.6520E 01	7.1108E-01	1.4314E 02
	2.0951E 00	-3.0841E 01	9.6191E 01	-4.4641E 01	-9.4333E 00	-6.8390E 02
ROW 3	-6.5663E 00	1.4796E 01	-1.5968E 01	-6.6136E 00	7.4069E 00	-2.3540E 01
	2.2395E 01	2.6160E 01	3.2509E 01	1.3139E 01	6.5945E 01	-4.9411E 02
ROW 4	2.1070E 00	8.8706E 00	1.2664E 00	7.3096E 00	1.8185E 01	2.7042E 01
	1.6508E 01	1.2356E 01	4.3177E 01	8.7735E-01	3.5510E 01	-4.2608E 02
ROW 5	-2.1037E 00	5.7262E-01	-1.8558E-01	-1.1346E 00	-1.5717E 01	-3.9495E 01
	1.6430E 01	2.6660E 01	6.3631E 00	2.1049E 01	6.2681E 01	-3.0430E 02
ROW 6	-2.1474E 01	6.1336E 00	-6.4746E 01	-3.4246E 01	-6.6460E 01	-1.5580E 02
	3.4033E 01	7.3131E 01	-2.7148E 01	5.1730E 01	1.4986E 02	-4.5895E 02
ROW 7	1.0138E-01	-2.7563E 00	1.1228E-01	1.3492E-01	1.9491E-01	4.6086E-01
	-6.0773E 00	-1.6142E 01	5.1143E 00	9.5926E 00	-2.6226E 01	8.3447E 01
ROW 8	1.7232E-01	-5.0916E 00	2.9714E-01	2.4933E-01	3.8845E-01	9.0337E-01
	-1.3808E 01	-3.4797E 01	1.6180E 01	-2.9741E 00	-6.3892E 01	1.9230E 02
ROW 9	-5.4705E 00	-3.2295E-01	-3.7130E 01	-2.0334E 01	-2.5359E 01	-4.6860E 01
	-6.1948E 00	7.5835E 00	-6.1991E 01	5.6847E 01	5.3721E 01	-1.7449E 02
ROW 10	5.6282E 00	-1.2919E 00	-2.2415E-01	1.4244E-01	2.4364E-01	5.1682E 01
	2.0934E 00	-9.0623E 00	4.0907E 01	-2.0750E 01	-6.5485E 01	4.4993E 02
ROW 11	2.2014E 01	-7.0895E 00	5.6326E-01	3.4240E-01	4.9875E-01	1.1702E 02
	-2.0738E 01	-5.0279E 01	4.2507E 01	-4.8589E 01	-8.2920E 02	-7.9635E 01
ROW 12	-5.5523E 00	-1.5271E 00	-7.1712E 00	-8.9605E 00	-8.7615E 00	-1.6115E 01
	-2.7731E 00	5.7185E-01	-1.7230E 01	3.9579E 00	-6.1034E 00	1.4091E 03

```
01          12 X 12                                                MACH 0.9

ROW  1
 1.9481E 00 -4.4879E 00  1.1648E-01  6.7021E 00  7.1834E-01  6.1263E 00
-3.3040E 00 -5.8746E 00  1.0261E 01 -1.4278E 01 -6.4003E-01  1.3524E 02

ROW  2
-9.8980E-01 -9.1740E-01 -1.5322E 00 -2.5339E 00 -4.0815E 00 -1.5200E 00
-7.7526E 00 -7.6146E 00 -1.6832E 01  6.2710E 00 -8.8228E 00  1.5889E 02

ROW  3
 2.1709E 00 -1.7734E-01  5.3933E 00  3.3795E 00  2.6616E 00  3.7096E-01
 6.4606E 00  6.1068E 00  2.2304E 01 -1.1120E 01  2.3044E 01 -1.2104E 02

ROW  4
 1.3481E 00 -4.7379E-01  2.3086E 00  1.7395E 00 -3.9118E-01 -2.4298E 00
 2.8340E 00  3.1502E 00  1.0124E 01 -4.3321E 00  1.2349E 01 -9.1771E 01

ROW  5
 4.0978E 00 -4.2679E 00  1.4985E 01  1.1580E 01  4.4207E 00  4.7157E 00
 7.8641E 00  5.5979E 00  3.6458E 01 -2.2270E 01  1.1087E 01 -1.9830E 02

ROW  6
 9.3984E 00 -7.6212E 00  3.2354E 01  2.4291E 01  1.2086E 01  9.5746E 00
 2.2250E 01  1.7782E 01  8.9803E 01 -5.3904E 01  2.7002E 01 -4.4391E 02

ROW  7
-2.9475E 00  1.7083E 00 -9.0909E 00 -7.2246E 00 -4.6998E 00 -3.2869E 00
-8.2460E 00 -6.8604E 00 -2.8960E 01  1.6813E 01 -1.1028E 01  1.1072E 02

ROW  8
-5.2301E 00  3.3077E 00 -1.6437E 01 -1.2864E 01 -7.6147E 00 -4.9959E 00
-1.4230E 01 -1.1950E 01 -5.1215E 01  2.9602E 01 -1.9108E 01  2.2751E 02

ROW  9
-2.3032E 00  2.8649E 00 -6.8090E 00 -7.6634E 00 -2.0556E 00 -3.6174E 00
-3.0631E 00 -1.4704E 00 -1.4627E 01  9.8283E 00 -9.8874E 00  4.8685E 01

ROW 10
-9.4167E-02 -9.0025E-01 -4.9056E-01 -9.3176E-01 -1.2779E 00  1.6787E-01
-2.5666E 00 -2.6969E 00 -5.6499E 00  1.5035E 00 -2.0622E 00  1.7739E 01

ROW 11
-4.4519E 00  3.1454E 00 -1.1883E 01 -9.7865E 00 -3.4143E 00 -1.5030E 00
-9.2813E 00 -7.9932E 00 -3.5935E 01  2.2123E 01 -1.8260E 01  2.0794E 02

ROW 12
-4.4113E-01  1.1537E 00  1.6566E-01  1.4645E 00  5.5239E 00  1.5298E-01
-3.5411E 00 -7.3023E 00 -2.6696E 00  1.7380E 00 -3.9716E 00  9.0021E 01

'd1'        1 X 12

ROW  1
4.0000E-03  4.0000E-03  4.0000E-03  4.0000E-03  4.0000E-03  4.0000E-03
4.0000E-03  4.0000E-03  4.0000E-03  4.0000E-03  4.0000E-03  4.0000E-03
```

D2 12 X 12 MACH 0.9

ROW 1

1.2121E 01 4.0699E 01 -1.1258E 02 -6.5021E 01 -3.7702E 01 -4.2341E 01
-5.4239E 01 -3.7220E 01 -2.8233E 02 1.9683E 02 -1.3737E 02 3.8572E 02

ROW 2

5.3872E 00 3.2411E 01 -8.7669E 01 -5.2993E 01 -6.2804E 00 -3.1957E 01
1.4340E 01 2.8780E 01 -7.7724E 01 8.2420E 01 -1.2562E 01 -7.7097E 01

ROW 3

-3.9671E 00 -2.3243E 01 4.5079E 01 4.2449E 01 -2.3187E 00 3.6369E 01
-1.8689E 01 -3.1764E 01 1.7372E 01 -3.3853E 01 -1.8733E 02 1.6401E 02

ROW 4

-5.1673E 00 -1.1465E 01 2.8205E 01 2.3925E 01 1.8935E 01 5.1691E 01
6.1403E-01 -1.3123E 01 4.5432E 01 -4.0064E 01 -8.7950E 01 2.7243E 02

ROW 5

3.3958E-01 -9.7622E 00 3.9851E 01 2.7606E 01 2.7686E 01 1.1095E 02
-5.6313E 01 -8.4196E 01 -6.8838E 01 4.6694E 00 -1.1271E 02 1.1968E 03

ROW 6

-4.3462E 00 -4.4656E 01 1.2245E 02 9.4982E 01 2.3114E 01 2.0332E 02
-1.4341E 02 -2.0068E 02 -1.6745E 02 1.8329E 01 -2.5149E 02 1.8221E 03

ROW 7

4.2134E 00 1.7484E 01 -3.9799E 01 -3.0698E 01 1.5396E 01 -2.2666E 01
4.9953E 01 5.3466E 01 7.5634E 01 -1.8127E 01 1.0434E 02 -1.2111E 02

ROW 8

6.4207E 00 3.1493E 01 -7.7318E 01 -5.8900E 01 8.9817E 00 -7.4529E 01
8.3901E 01 1.0733E 02 1.0410E 02 -1.2794E 01 1.7108E 02 -5.1079E 02

ROW 9

7.0984E 00 -4.6743E 00 4.0062E 00 1.3571E 01 4.4531E 00 1.1897E 01
1.5353E 01 1.0633E 01 5.5990E 01 -2.1559E 01 9.0883E 01 -9.2616E 01

ROW 10

-3.7819E 00 1.0074E 01 -2.2528E 01 -2.2474E 01 3.5102E 00 -2.1952E 01
2.0414E 01 2.7361E 01 1.2546E 01 7.4041E 00 2.5811E 01 -2.6911E 01

ROW 11

9.8110E 00 3.2218E 01 -7.5087E 01 -5.8113E 01 -1.4335E 01 -8.8467E 01
5.6445E 01 8.4134E 01 4.6538E 01 -4.8903E 00 1.6673E 02 -2.2154E 02

ROW 12

6.3579E 00 1.7106E 01 -7.5120E 01 -5.2248E 01 -9.7460E 01 -2.5461E 02
3.8717E 01 1.0319E 02 -8.4749E 01 6.3734E 01 7.9194E 01 -8.0030E 02

'd_2' 1 X 12

ROW 1

1.2000E-02 1.2000E-02 1.2000E-02 1.2000E-02 1.2000E-02 1.2000E-02
1.2000E-02 1.2000E-02 1.2000E-02 1.2000E-02 1.2000E-02 1.2000E-02

D3 12 X 12 MACH 0.9

ROW 1

-1.0216E 02 -5.1129E 01 5.9118E 01 2.5751E 00 2.3899E 01 -1.5684E 02
2.1141E 02 2.4591E 02 5.4851E 02 -3.2062E 02 8.1508E 02 -1.2710E 03

ROW 2

-5.6623E 01 -4.4520E 01 1.3105E 02 6.6958E 01 -2.8379E 01 -1.2100E 02
4.5875E 01 6.6421E 01 2.0373E 02 -1.8033E 02 2.2375E 02 -5.1497E 02

ROW 3

2.7407E 01 4.6325E 01 -1.4471E 02 -9.5137E 01 -5.8915E 01 -2.1911E 02
2.9123E 01 8.5764E 01 -1.9369E 02 1.6860E 02 5.1357E 02 -1.1083E 03

ROW 4

3.1047E 01 3.1738E 01 -6.9227E 01 -4.3629E 01 -9.2671E 01 -2.2939E 02
-1.7652E 01 3.7082E 01 -2.3294E 02 1.5377E 02 2.1780E 02 -9.2596E 02

ROW 5

2.1533E 01 4.5474E 01 -1.9009E 02 -1.1036E 02 -1.6672E 02 -4.4086E 02
6.7782E 01 1.7455E 02 -1.8950E 02 1.9856E 02 1.5524E 02 -2.7073E 03

ROW 6

6.1742E 01 1.2197E 02 -4.8603E 02 -3.0404E 02 -1.9577E 02 -7.1092E 02
2.2758E 02 4.1246E 02 -1.9198E 02 3.2251E 02 4.8455E 02 -4.1570E 03

ROW 7

-1.6076E 01 -2.9106E 01 1.3353E 02 9.6838E 01 -5.2257E 01 -6.5930E 00
-8.3611E 01 -9.2772E 01 -1.1247E 02 -2.7650E 00 -2.9816E 02 -3.9294E 01

ROW 8

-3.7661E 01 -6.3193E 01 2.6641E 02 1.7646E 02 7.2139E 00 1.5712E 02
-1.3836E 02 -1.8589E 02 -4.6668E 01 -9.4681E 01 -4.2587E 02 8.0684E 02

ROW 9

-2.7595E 00 1.8604E 01 -5.8224E 01 -2.7295E 01 -1.1303E 02 -2.7511E 02
1.7215E 01 8.2577E 01 -1.4902E 02 7.9757E 01 -2.1550E 02 -1.0277E 03

ROW 10

-1.9967E 00 -2.3800E 01 1.2512E 02 7.5438E 01 7.3554E 01 2.1800E 02
-5.3882E 01 -1.0418E 02 5.9984E 01 -8.1854E 01 -7.9518E 01 5.4738E 02

ROW 11

-5.2431E 01 -7.1465E 01 2.1033E 02 1.4398E 02 3.1740E 01 1.9081E 02
-1.0495E 02 -1.6412E 02 6.5834E 00 -5.9766E 01 -4.1026E 02 1.0615E 01

ROW 12

-1.0757E 02 -1.4251E 02 3.6956E 02 1.9779E 02 4.4145E 02 1.0593E 03
-1.0868E 02 -3.7032E 02 5.1820E 02 -3.6429E 02 -2.4969E 02 1.7352E 03

'd_3' 1 X 12

ROW 1

2.0000E-02 2.0000E-02 2.0000E-02 2.0000E-02 2.0000E-02 2.0000E-02
2.0000E-02 2.0000E-02 2.0000E-02 2.0000E-02 2.0000E-02 2.0000E-02

MACH 0.9

D4 12 X 12

ROW 1
3.5247E 01 -1.7267E 00 1.3946E 02 9.5417E 01 1.1250E 02 4.3850E 02
-2.0754E 02 -3.1227E 02 -2.5158E 02 9.6022E 01 -8.0071E 02 1.3694E 03

ROW 2
4.9752E 01 -4.4731E-01 -2.0502E 01 -9.2241E 00 9.1267E 01 2.9272E 02
-7.4178E 01 -1.4039E 02 -7.0139E 01 6.8052E 01 -2.6473E 02 7.1910E 02

ROW 3
-5.9106E 01 -5.7183E 01 1.6712E 02 -8.1614E 01 1.3766E 02 -3.5062E 02
-1.3411E 01 -9.6288E 01 2.9941E 02 -2.1799E 02 -3.6673E 02 1.1416E 03

ROW 4
-5.2329E-01 -4.7747E 01 6.7656E 01 2.8011E 01 1.2543E 02 2.9985E 02
1.3681E 01 -5.5930E 01 2.7330E 02 -1.5691E 02 -1.4362E 02 8.2974E 02

ROW 5
-5.5437E 01 -6.6126E 01 1.6927E 02 8.4657E 01 1.9286E 02 -4.5487E 02
-2.5925E 01 -1.3394E 02 3.0069E 02 -2.3117E 02 -4.3662E 00 1.7582E 03

ROW 6
-1.2701E 02 -1.3430E 02 4.6730E 02 2.5281E 02 2.7850E 02 -7.4906E 02
-1.2585E 02 -3.1157E 02 4.2430E 02 -4.0831E 02 -2.2802E 02 2.7817E 03

ROW 7
1.8469E 01 1.1413E 01 -1.4385E 02 -9.4641E 01 2.2779E-01 3.8708E-01
5.1008E 01 5.3393E 01 5.1384E 01 2.6541E 01 2.5461E 02 4.7063E 01

ROW 8
5.5627E 01 4.5468E 01 -2.6083E 02 -1.5888E 02 -4.0393E 01 -1.6725E 02
7.5805E 01 1.1975E 02 -6.0335E 01 1.3081E 02 3.1699E 02 -5.0558E 02

ROW 9
-3.8420E 01 -4.8929E 01 9.2838E 01 2.8532E 01 1.6310E 02 3.7280E 02
-2.7040E 01 -1.1409E 02 1.9222E 02 -1.1780E 02 2.2494E 02 9.8425E 02

ROW 10
3.4129E 01 3.7565E 01 -1.5360E 02 -7.9156E 01 -1.3487E 02 -3.0739E 02
3.1814E 01 9.9920E 01 -1.3942E 02 1.1763E 02 1.0456E 01 -5.1575E 02

ROW 11
6.9762E 01 6.0346E 01 -1.9332E 02 -1.1844E 02 -6.6605E 01 -2.1708E 02
7.2644E 01 1.3174E 02 -6.9847E 01 8.7131E 01 2.0448E 02 9.8666E 01

ROW 12
-2.0870E 02 -2.1742E 02 3.7291E 02 1.7313E 02 4.5196E 02 -1.0379E 03
8.4406E 01 3.3368E 02 -5.6072E 02 3.3565E 02 1.7931E 02 -5.3276E 02

'd_4' 1 X 12

ROW 1
2.8000E-02 2.8000E-02 2.8000E-02 2.8000E-02 2.8000E-02 2.8000E-02
2.8000E-02 2.8000E-02 2.8000E-02 2.8000E-02 2.8000E-02 2.8000E-02

'R_0'   12 X 2

ROW 1	
-1.0290E 04	0.0
ROW 2	
-6.5238E 03	0.0
ROW 3	
4.8012E 03	0.0
ROW 4	
1.8760E 03	0.0
ROW 5	
2.8130E 03	0.0
ROW 6	
1.1029E 04	0.0
ROW 7	
-3.9592E 03	0.0
ROW 8	
-7.1730E 03	0.0
ROW 9	
-5.0858E 02	0.0
ROW 10	
-1.0890E 02	0.0
ROW 11	
-7.0987E 03	0.0
ROW 12	
6.0136E 02	0.0

'R_1' 12 X 2

ROW 1	-7.4816E 03	0.0
ROW 2	-3.4121E 03	0.0
ROW 3	-4.1471E 03	0.0
ROW 4	-3.8131E 03	0.0
ROW 5	-2.2781E 03	0.0
ROW 6	-4.1784E 03	0.0
ROW 7	2.1371E 03	0.0
ROW 8	3.1560E 03	0.0
ROW 9	5.3377E 03	0.0
ROW 10	-2.3497E 03	0.0
ROW 11	-1.1750E 03	0.0
ROW 12	1.9011E 03	0.0

'R_2' 12 X 2

ROW 1	8.9379E 04	0.0
ROW 2	5.3039E 04	0.0
ROW 3	1.2470E 04	0.0
ROW 4	2.1058E 04	0.0
ROW 5	-1.9336E 02	0.0
ROW 6	-2.4286E 04	0.0
ROW 7	1.1831E 03	0.0
ROW 8	9.1033E 03	0.0
ROW 9	-4.5191E 04	0.0
ROW 10	2.6873E 04	0.0
ROW 11	4.4949E 04	0.0
ROW 12	-9.0401E 03	0.0

'β_1' 1 X 2

ROW 1	4.0000E-03	4.0000E-03

'β_2' 1 X 2

ROW 1	1.2000E-02	1.2000E-02

'R3'	12 X 2	'R4'	12 X 2
ROW 1		ROW 1	
-1.2204E 05	0.0	4.8552E 04	0.0
ROW 2		ROW 2	
-7.5773E 04	0.0	3.1733E 04	0.0
ROW 3		ROW 3	
-4.8463E 04	0.0	3.7118E 04	0.0
ROW 4		ROW 4	
-5.1044E 04	0.0	3.2936E 04	0.0
ROW 5		ROW 5	
-1.0700E 04	0.0	1.1609E 04	0.0
ROW 6		ROW 6	
4.5710E 03	0.0	1.5646E 04	0.0
ROW 7		ROW 7	
-1.1172E 04	0.0	-1.0923E 04	0.0
ROW 8		ROW 8	
7.9562E 03	0.0	-1.4081E 04	0.0
ROW 9		ROW 9	
-8.7815E 04	0.0	-4.7225E 04	0.0
ROW 10		ROW 10	
-5.2532E 04	0.0	2.7871E 04	0.0
ROW 11		ROW 11	
-5.7408E 04	0.0	1.8708E 04	0.0
ROW 12		ROW 12	
9.3901E 03	0.0	-2.2831E 03	0.0

'β3'	1 X 2	'β4'	1 X 2
ROW 1		ROW 1	
2.0000E-02	2.0000E-02	2.8000E-02	2.8000E-02

'C_1' 12 X 12 MACH 0.6

ROW						
ROW 1	4.7460E 04	2.5078E 04	6.4968E 03	9.1901E 03	-5.3778E 03	-6.8244E 03
	-3.6244E 03	-1.9705E 03	-1.1249E 04	6.3522E 03	3.7518E 03	4.3007E 03
ROW 2	2.5493E 04	2.1347E 04	6.6525E 03	9.3211E 03	-5.8028E 02	-8.6790E 03
	4.3350E 03	7.1167E 03	-1.7981E 03	3.7316E 03	2.5417E 03	3.6573E 03
ROW 3	9.4387E 03	1.4473E 04	2.4392E 04	1.7518E 04	8.9907E 03	1.2865E 04
	4.0663E 02	-2.3460E 03	2.1099E 03	4.7422E 02	-6.0346E 02	-2.9933E 03
ROW 4	8.8273E 03	1.2418E 04	1.8260E 04	1.5588E 04	9.7364E 03	1.0233E 04
	3.4742E 03	1.5967E 03	4.1523E 02	2.5677E 03	-1.9091E 02	-2.5677E 03
ROW 5	7.1756E 03	6.0247E 03	1.8323E 04	1.6224E 04	1.9332E 04	2.7398E 04
	5.0466E 03	-1.3298E 02	6.4256E 03	5.1948E 02	-2.5940E 03	-1.0927E 04
ROW 6	9.4001E 03	4.6343E 03	2.9896E 04	2.0574E 04	2.1586E 04	4.5409E 04
	-2.3325E 03	-1.2375E 04	7.9100E 03	-9.7202E 01	-4.8372E 03	-1.8044E 04
ROW 7	3.0378E 03	4.1363E 03	-9.2136E 02	3.6794E 03	1.0033E 04	4.3186E 03
	1.3788E 04	1.4981E 04	1.0690E 04	2.8356E 03	-6.9369E 02	3.0787E 03
ROW 8	2.3357E 02	3.9117E 03	-7.4493E 03	-3.2618E 02	6.7929E 03	-4.5816E 03
	1.6246E 04	1.9776E 04	1.0584E 04	3.5875E 03	3.3742E 02	8.2182E 03
ROW 9	1.2225E 04	7.8981E 03	2.1737E 03	1.9881E 03	9.8275E 03	1.2333E 04
	9.9762E 03	9.4457E 03	2.5478E 04	-6.8827E 03	-3.0069E 03	-3.9242E 03
ROW 10	-1.0046E 04	-2.8998E 03	1.7804E 02	1.3457E 03	9.7577E 02	-1.2423E 03
	5.4785E 03	6.4613E 02	-2.7010E 03	1.4621E 04	1.0259E 03	1.4864E 04
ROW 11	-1.6170E 02	-2.3746E 02	-3.4011E 03	-1.5186E 03	-6.1672E 02	-5.0258E 03
	1.3344E 03	2.7010E 03	-2.6251E 03	1.1342E 03	8.8329E 03	-4.7933E 02
ROW 12	-2.4267E 04	-1.7066E 04	1.4977E 04	1.1281E 04	4.0160E 03	-1.0777E 04
	6.5704E 03	1.0156E 04	-1.8144E 03	1.4906E 04	-4.3960E 02	1.0673E 05

'C_2'   12 X 12   MACH 0.6

```
ROW  1
 5.1277E 03  2.2057E 03  2.7793E 03  2.0486E 03  3.1136E 03  5.2697E 03
 2.5456E 02 -7.9039E 02  3.6918E 03 -2.7168E 03 -1.9341E 03 -7.4683E 03

ROW  2
 2.6944E 03  1.3164E 03  2.1486E 03  1.5901E 03  1.9876E 03  3.6138E 03
 2.9303E 02 -4.3663E 02  2.5539E 03 -1.1957E 03 -1.2916E 03 -4.7062E 03

ROW  3
-1.7731E 02  6.2025E 02  2.3567E 03  1.6563E 03  1.8361E 03  3.4730E 03
 3.6369E 02 -4.3311E 02  2.4428E 03 -8.0601E 02  9.8260E 01 -5.4166E 03

ROW  4
 6.5030E 02  7.1904E 02  1.6550E 03  1.3599E 03  1.5452E 03  2.6544E 03
 5.1534E 02 -6.6416E 01  2.0145E 03 -5.3189E 02 -9.9699E 00 -4.0147E 03

ROW  5
-9.6674E 01 -2.4462E 02  3.9587E 01  4.0444E 02  1.6170E 03  1.8623E 03
 1.1161E 03  8.1395E 02  2.0727E 03 -4.7380E 02  1.1486E 03 -3.3161E 03

ROW  6
-1.0234E 03 -1.1507E 03  7.5550E 02  4.4742E 02  2.2077E 03  3.2857E 03
 3.6311E 02  1.8488E 02  2.6653E 03 -1.0313E 03  2.0609E 03 -6.3367E 03

ROW  7
 5.5115E 01  3.1250E 02 -3.1515E 02  2.0638E 01  3.0680E 02  1.3308E 01
 8.3065E 02  9.3429E 02  7.9090E 02  5.9839E 02  4.0393E 02  1.5746E 03

ROW  8
 4.0242E 02  6.4790E 02 -4.9104E 02 -9.4461E 01 -6.1539E 01 -6.2102E 02
 7.8539E 02  1.0442E 03  3.7236E 02  8.7647E 02 -2.0887E 01  3.3316E 03

ROW  9
-1.1532E 03 -5.9398E 02 -1.5283E 02 -3.1627E 01  1.1084E 03  1.8264E 03
 6.8937E 02  3.8626E 02  2.3987E 03 -5.0724E C2  1.3057E 03 -2.8917E 03

ROW 10
 4.3366E 02  5.5303E 02  4.6505E 01  1.8974E 02 -7.0895E 02 -1.1345E 03
-4.4127E 01  2.0431E 02 -1.2418E 03  1.5108E 03 -2.8202E 02  6.7008E 03

ROW 11
 1.4438E 03  1.0195E 03 -3.6290E 02 -1.4285E 02 -1.3575E 03 -2.3194E 03
-3.9269E 02  7.3179E 01 -1.6858E 03  7.8464E 02 -1.2631E 03  3.6698E 02

ROW 12
-1.1124E 03 -4.8510E 02 -1.6467E 03 -1.0990E 03 -1.9553E 03 -3.6521E 03
-9.3900E 01  7.4527E 02 -2.6280E 03  2.0326E 03  2.6899E 02  3.2635E 04
```

'C_3'   12 X 12   MACH 0.6

ROW 1
3.3089E 01 -3.3020E 00 3.7339E 01 6.3298E 01 8.0791E 01 -1.6008E 02
4.7277E 00 -3.4043E 01 1.2928E 02 -7.6545E 01 1.0225E 00 -8.9723E 02

ROW 2
2.0197E 01 2.9481E-01 5.3532E 01 3.9683E 01 6.3745E 01 1.2830E 02
2.0611E 00 -2.7523E 01 9.6721E 01 -4.2112E 01 -1.0569E 01 -5.4716E 02

ROW 3
-7.0292E 00 1.2593E 01 -1.2161E 01 -6.1573E 00 8.3163E 00 -3.9562E 00
1.9206E 01 2.1322E 01 3.0137E 01 7.7914E 00 5.6726E 01 -3.3057E 02

ROW 4
3.3238E-01 7.6994E 00 2.1411E 00 5.4126E 00 1.7377E 01 2.6895E 01
1.4138E 01 9.6350E 00 3.8515E 01 -1.7719E 00 3.0117E 01 -2.9320E 02

ROW 5
-4.0040E 00 7.9978E-01 -1.7741E 01 -4.0109E 00 -1.3937E 01 -3.4577E 01
1.3521E 01 2.2413E 01 1.4388E 00 1.9117E 01 5.5526E 01 -1.5432E 02

ROW 6
-2.2263E 01 5.7763E 00 -5.9319E 01 -3.4549E 01 -5.9076E 01 -1.3621E 02
2.7356E 01 6.1506E 01 -3.2695E 01 4.6905E 01 1.3034E 02 -1.9706E 02

ROW 7
9.2675E 00 -3.0712E 00 1.1935E 01 1.2610E 01 1.7575E 01 4.0806E 01
-4.3968E 00 -1.3620E 01 8.3472E 00 5.5942E 00 -1.9963E 01 6.1667E 01

ROW 8
1.6208E 01 -5.1834E 00 2.8724E 01 2.3575E 01 3.4771E 01 7.9629E 01
-1.0482E 01 -2.9288E 01 2.0325E 01 -5.8532E 00 -5.2685E 01 1.1027E 02

ROW 9
-4.1695E 00 -2.3167E 00 -2.9177E 01 -1.6541E 01 -2.2658E 01 -4.1678E 01
-5.6931E 00 5.6582E 00 -5.1212E 01 4.4093E 01 5.2813E 01 -5.7752E 01

ROW 10
4.7579E 00 1.7854E 00 1.9431E 01 1.2356E 01 2.2008E 01 4.5502E 01
3.0520E 00 -6.6492E 00 3.3311E 01 -1.7727E 01 -5.9536E 01 3.2514E 02

ROW 11
2.0194E 01 -5.5345E 00 5.2675E 01 3.1905E 01 4.7211E 01 1.0840E 02
-1.6329E 01 -4.3548E 01 4.6092E 01 -4.8391E 01 -7.2577E 02 -1.0275E 02

ROW 12
-3.3233E 00 -9.0809E-01 -7.9316E 00 4.1457E 00 9.7433E 00 -1.6034E-01
-2.1054E 00 1.7063E 00 -1.5736E 01 6.9273E 00 -7.3191E 00 1.1394E 03

D1 12 X 12 MACH 0.6

```
ROW  1
-9.2663E-01 -9.8346E-02 -7.4020E 00 -3.5901E 00 -7.3656E 00 -1.4969E 01
-4.0506E-01  2.9973E 00 -1.3350E 01  3.7823E 00  5.5193E 00  3.7208E 01

ROW  2
-7.7224E-01  2.9296E-01 -5.4310E 00 -2.8843E 00 -4.4705E 00 -9.3900E 00
-2.6774E-01  1.9603E 00 -9.3011E 00  6.3651E 00  4.7439E 00  2.0538E 01

ROW  3
-3.6918E-01  6.6199E-01 -1.9547E 00 -1.4865E 00 -1.8157E 00 -4.5263E 00
 1.1230E 00  2.2961E 00 -1.1884E-01  6.4079E-01  1.3512E 00 -5.2235E 00

ROW  4
-3.1930E-01  4.9520E-01 -1.6026E 00 -1.1793E 00 -1.4773E 00 -3.6416E 00
 8.3391E-01  1.7701E 00 -3.6363E-01  6.2991E-01  1.4473E 00 -3.2557E 00

ROW  5
 5.5741E-01 -7.6646E-01 -3.0925E 00 -1.8172E 00 -8.8741E-01  2.7871E 00
-5.1386E-01 -1.3433E 00  3.3799E 00 -3.4904E 00 -5.6007E 00  6.9554E 00

ROW  6
 8.5792E-01 -9.0877E-01 -4.6747E 00  2.6937E 00 -1.1036E 00  3.0445E 00
 4.7261E-01 -4.7624E-01  7.8969E 00 -6.3482E 00 -7.4217E 00 -3.2571E 00

ROW  7
 5.4759E-02 -2.6379E-01  2.8955E-01  1.4373E-01  4.1366E-01  1.5857E 00
-1.2052E 00 -1.6037E 00 -2.4045E 00  9.2200E-01 -1.5296E 00  1.2298E 01

ROW  8
-1.1175E-01 -1.6610E-01 -7.0187E-01 -3.9999E-01 -1.2088E-01  9.9312E-01
-1.5544E 00 -1.7816E 00 -4.7188E 00  2.5376E 00 -2.4353E-01  1.6040E 01

ROW  9
 1.6506E-01 -5.4418E-01 -5.7014E-02  1.1890E-01 -1.8482E-01 -1.2829E 00
-2.2490E 00 -2.6506E 00 -4.9044E 00  1.9867E 00 -5.3662E 00  3.0653E 01

ROW 10
-1.1403E-01  4.5093E-01 -2.4348E-01 -2.4512E-02 -8.4256E-01 -4.7709E-01
 1.4300E 00  1.4269E 00  3.6260E 00 -1.4739E 00  4.1491E 00 -2.4122E 01

ROW 11
-5.2130E-01 -7.2559E-01 -2.0970E 00 -1.4072E 00 -2.2976E-01 -1.3563E 00
 4.9533E-01  9.8509E-01 -1.8543E 00  2.1318E 00  3.9271E 00 -2.3157E 00

ROW 12
-2.9598E-01 -3.2374E-02 -2.3827E 00 -1.2342E 00 -2.5216E 00 -5.0135E 00
 1.5035E-01 -9.3930E-01  4.1493E 00 -2.5745E 00 -1.3959E-01 -1.4374E 01
```

'd_1' 1 X 12

```
ROW  1
4.0000E-03  4.0000E-03  4.0000E-03  4.0000E-03  4.0000E-03  4.0000E-03
4.0000E-03  4.0000E-03  4.0000E-03  4.0000E-03  4.0000E-03  4.0000E-03
```

Q2 12 X 12 MACH 0.6

```
ROW  1
-9.0951E 00 -1.5430E 00  3.5405E 01  9.1194E 00  6.6661E 01  1.2365E 02
 7.3248E 00 -1.7599E 01  9.8431E 01 -6.1950E 01 -4.9426E 01 -1.6680E 02

ROW  2
-6.2681E 00 -2.6015E 00  2.7393E 01  8.9449E 00  3.9805E 01  7.1633E 01
 1.1091E 01 -3.7157E 00  8.3446E 01 -5.3713E 01 -4.0952E 01 -9.9422E 01

ROW  3
-5.2141E 00 -1.4450E 01 -3.5952E 01  2.5265E 01  2.1014E 01 -5.6887E 01
-1.1517E 01 -2.7370E 01  2.0960E 01 -1.9037E 01 -1.6837E 01 -3.8130E 01

ROW  4
-3.3964E 00 -9.2316E 00  2.4095E 01  1.6423E 01  1.5614E 01 -4.1584E 01
-8.7295E 00 -2.0002E 01  1.2845E 01 -1.2175E 01 -1.6797E 01 -1.6891E-01

ROW  5
 2.1634E 00 -4.3523E 00 -2.1949E 01 -1.0328E 01 -9.7702E 00 -1.7642E 01
-6.8947E 00 -2.8270E 00 -5.0791E 01  4.1531E 01  5.1001E 01 -7.3520E 01

ROW  6
 6.6285E-01 -4.2475E 00 -8.3291E 00  3.0147E 00 -4.6054E 00  8.4373E 00
-2.5880E 01 -3.0242E 01 -8.4030E 01  5.8331E 01  6.0542E 01 -9.4157E 01

ROW  7
 1.6963E 00  3.5111E 00 -2.1257E 01 -1.4666E 01 -9.9094E 00 -3.3595E 01
 1.5666E 01  2.5270E 01  1.2749E 01 -3.4634E-01  2.1188E 01 -6.0414E 01

ROW  8
 1.7773E 00  1.1288E 01 -2.3508E 01 -1.8394E 01 -9.3967E 00 -3.9160E-01
 2.4016E 01  3.5890E 01  3.3489E 01 -1.3063E 01  1.2251E 01 -5.4246E 01

ROW  9
-1.5391E 00  6.0710E 00 -1.7842E 01 -1.1945E 01 -4.2583E 00 -2.9490E-01
 2.5539E 01  3.4117E 01  3.9864E 01 -1.1569E 01  6.2786E 01 -3.1783E 02

ROW 10
 2.2390E 00 -2.2373E 00  6.7669E 00  5.1959E 00 -4.7160E 00  2.6413E 00
-1.3130E 01 -1.4718E 01 -2.4778E 01  6.5048E 00 -4.6058E 01  2.4707E 02

ROW 11
 1.2755E 00  2.0999E 00 -2.3434E 00 -1.4240E 00 -2.9430E 00 -7.9857E 00
 4.1927E 00  6.6277E 00  1.6752E 01 -1.6869E 01 -3.5012E 01  1.3510E 02

ROW 12
 4.6771E 00  4.3075E 00 -1.6923E 01 -8.0370E 00 -2.2446E 01 -4.3829E 01
-1.6573E 00  3.2799E 00 -3.4475E 01  2.9564E 01 -1.5049E-03  1.2580E 02
```

'd_2' 1 X 12

```
ROW  1
 1.2000E-02  1.2000E-02  1.2000E-02  1.2000E-02  1.2000E-02  1.2000E-02
 1.2000E-02  1.2000E-02  1.2000E-02  1.2000E-02  1.2000E-02  1.2000E-02
```

```
D3          12 X 12                                                    MACH 0.6

ROW  1
 7.6239E 01  6.3821E 01 -1.1738E 02 -4.5361E 01 -2.2576E 02 -4.3477E 02
 1.3519E 00  9.7558E 01 -2.5020E 02  1.6124E 02  1.5743E 02  5.8737E 02

ROW  2
 5.3742E 01  3.7348E 01 -6.3043E 01 -1.7623E 01 -1.3389E 02 -2.2258E 02
-4.6971E 01 -1.5685E 00 -2.7004E 02  1.6988E 02  1.1134E 02  4.7312E 02

ROW  3
 5.2121E 01  4.9483E 01 -1.0291E 02 -6.6450E 01 -4.4047E 01 -1.2997E 02
 1.6116E 01  5.3919E 01 -1.0364E 02  7.4939E 01  4.0100E 01  1.6302E 02

ROW  4
 3.5849E 01  3.5885E 01 -7.7529E 01 -4.9180E 01 -3.8559E 01 -1.0993E 02
 1.7995E 01  4.8987E 01 -6.5383E 01  5.0016E 01  4.8208E 01  5.0366E 01

ROW  5
-2.5040E 01 -1.1828E 01  3.7810E 01  1.0296E 01  4.4151E 01  3.4808E 01
 6.6755E 01  6.4574E 01  2.3569E 02 -1.6395E 02 -1.2760E 02 -1.6852E 01

ROW  6
-1.0357E 01  1.2339E 01 -2.2377E 01 -4.0282E 01  4.9169E 01 -3.1055E 01
 1.3916E 02  1.6130E 02  3.5776E 02 -2.2941E 02 -1.4655E 02 -1.2971E 02

ROW  7
-2.2469E 01 -2.9630E 01  8.5147E 01  5.6390E 01  2.6716E 01  1.0463E 02
-4.8033E 01 -7.9322E 01 -2.3327E 01 -6.9956E 00 -6.9524E 01  2.1621E 02

ROW  8
-2.3879E 01 -3.7104E 01  1.0434E 02  7.5000E 01  1.6271E 01  1.1933E 02
-8.3919E 01 -1.2353E 02 -1.0146E 02  3.9111E 01 -5.0080E 01  2.8472E 02

ROW  9
-9.7666E 00 -2.7922E 01  1.1726E 02  7.5989E 01  3.5679E 01  1.4485E 02
-7.7570E 01 -1.1915E 02 -5.9098E 01 -7.9485E 00 -2.1294E 02  8.6957E 02

ROW 10
-4.2937E 00  5.9873E 00 -5.1968E 01 -3.3962E 01 -3.4841E 00 -3.4973E 01
 2.5632E 01  3.6214E 01  7.9302E 00  2.3232E 01  1.4770E 02 -6.2459E 02

ROW 11
 8.5170E-01 -2.7673E 00 -1.3262E 01  5.6201E-01 -1.5754E 01  2.3710E 00
-3.7339E 01 -4.2816E 01 -1.2004E 02  9.1176E 01  1.0365E 02 -1.6018E 02

ROW 12
-3.6092E 01 -2.7976E 01  3.9460E 01  1.8797E 01  5.7417E 01  1.1638E 02
 2.4104E-01 -2.7527E 01  7.8402E 01 -4.5560E 01  3.3909E 00 -3.6167E 02
```

'd_3'   1 X 12

```
ROW  1
 2.0000E-02  2.0000E-02  2.0000E-02  2.0000E-02  2.0000E-02  2.0000E-02
 2.0000E-02  2.0000E-02  2.0000E-02  2.0000E-02  2.0000E-02  2.0000E-02
```

```
04        12 X 12                                                    MACH 0.6

ROW  1
-1.1484E 02 -1.0014E 02  1.1630E 02  5.5830E 01  1.9850E-02  4.1336E 02
-3.5390E 01 -1.3338E 02  1.4349E 02 -9.5885E 01 -1.4337E 02 -4.1322E 02

ROW  2
-6.9484E 01 -4.9883E 01  2.4280E 01 -1.8297E 00  1.1697E-02  1.8110E 02
 4.4743E 01  9.1600E 00  2.1289E 02 -1.3224E 02 -8.5406E 01 -3.7901E 02

ROW  3
-7.3252E 01 -4.4803E 01  6.4999E 01  3.6769E 01  1.8192E 01  5.7052E 01
 1.2539E 01 -5.2834E 00  1.3108E 02 -8.1411E 01 -1.4828E 01 -2.4334E 02

ROW  4
-5.2256E 01 -3.4974E 01  5.7500E 01  3.3071E 01  2.2664E 01  6.6965E 01
-1.7599E 00 -2.1334E 01  8.1194E 01 -5.3521E 01 -3.2220E 01 -1.0647E 02

ROW  5
 2.4573E 01  3.5272E 00  1.7036E 01  2.4318E 01 -4.7636E 01 -2.0550E 00
-9.3667E 01 -1.0493E 02 -2.4011E 02  1.5533E 02  8.5117E 01  7.6603E 01

ROW  6
-6.2641E 00 -2.1669E 01  9.3237E 01  8.1508E 01 -6.8101E 01  4.2701E 01
-1.5597E 02 -1.8915E 02 -3.2514E 02  2.0359E 02  1.0179E 02  1.0282E 02

ROW  7
 4.0803E 01  3.0976E 01 -3.7957E 01 -5.6152E 01 -1.9063E 01 -8.5593E 01
 3.4046E 01  6.0927E 01 -1.0570E 01  2.0067E 01  5.5853E 01 -1.0670E 02

ROW  8
 4.8429E 01  3.9295E 01 -1.2039E 02 -8.1576E 01 -3.4802E 00 -9.8116E 01
 6.9334E 01  1.0509E 02  5.2025E 01 -1.7039E 01  4.2525E 01 -1.4502E 02

ROW  9
 2.8527E 01  3.0499E 01 -1.3782E 02 -9.6260E 01 -4.7428E 01 -1.5616E 02
 5.5830E 01  9.9485E 01 -1.1344E 01  4.2992E 01  1.8958E 02 -6.3141E 02

ROW 10
 1.0962E 00 -1.2424E 00  5.1944E 01  3.1264E 01  1.7240E 01  4.0509E 01
-2.7311E 00 -1.1920E 01  4.8005E 01 -5.1682E 01 -1.2564E 02  4.5355E 02

ROW 11
 4.2056E 00  7.9316E 00 -7.3191E 00 -1.3600E 01  3.2235E 01  6.3564E 00
 4.9680E 01  5.6726E 01  1.2728E 02 -9.1686E 01 -8.6292E 01  1.3565E 02

ROW 12
 4.9036E 01  3.5255E 01 -2.6293E 01 -1.2648E 01 -3.6061E 01 -8.1371E 01
 5.3943E 00  2.6628E 01 -4.2675E 01  2.2838E 01 -6.2397E 00  2.8712E 02

'd4'         1 X 12

ROW  1
 2.8000E-02  2.8000E-02  2.8000E-02  2.8000E-02  2.8000E-02  2.8000E-02
 2.8000E-02  2.8000E-02  2.8000E-02  2.8000E-02  2.8000E-02  2.8000E-02
```

'R_0' 12 X 2

```
ROW  1
-8.5541E 03   0.0

ROW  2
-5.5602E 03   0.0

ROW  3
4.0936E 03   0.0

ROW  4
1.6256E 03   0.0

ROW  5
2.4432E 03   0.0

ROW  6
9.5018E 03   0.0

ROW  7
-3.5431E 03   0.0

ROW  8
-6.3209E 03   0.0

ROW  9
-8.1299E 02   0.0

ROW 10
1.1637E 02   0.0

ROW 11
-6.0906E 03   0.0

ROW 12
5.9621E 02   0.0
```

'R_1' 12 X 2

ROW 1
-6.6437E 03 0.0

ROW 2
-4.6572E 03 0.0

ROW 3
-1.6045E 03 0.0

ROW 4
-2.0849E 03 0.0

ROW 5
7.0969E 02 0.0

ROW 6
2.0593E 03 0.0

ROW 7
-3.7517E 01 0.0

ROW 8
-8.5915E 02 0.0

ROW 9
4.5557E 03 0.0

ROW 10
-3.2227E 03 0.0

ROW 11
-4.7949E 03 0.0

ROW 12
6.2651E 02 0.0

'R_2' 12 X 2

ROW 1
6.1798E 04 0.0

ROW 2
4.5701E 04 0.0

ROW 3
1.2361E 04 0.0

ROW 4
1.7928E 04 0.0

ROW 5
-8.7957E 03 0.0

ROW 6
-3.5323E 04 0.0

ROW 7
4.9878E 03 0.0

ROW 8
1.4974E 04 0.0

ROW 9
-3.6692E 04 0.0

ROW 10
2.8147E 04 0.0

ROW 11
4.6012E 04 0.0

ROW 12
-4.3853E 03 0.0

'β_1' 1 X 2

ROW 1
4.0000E-03 4.0000E-03

'β_2' 1 X 2

ROW 1
1.2000E-02 1.2000E-02

'R_3' 12 X 2

ROW		
1	-6.4245E 04	0.0
2	-5.5803E 04	0.0
3	-5.5791E 04	0.0
4	-4.9346E 04	0.0
5	-1.0546E 03	0.0
6	7.4443E 03	0.0
7	9.0187E 03	0.0
8	6.7696E 03	0.0
9	7.0649E 04	0.0
10	-5.2665E 04	0.0
11	-4.7831E 04	0.0
12	5.0120E 03	0.0

'R_4' 12 X 2

ROW		
1	1.4556E 04	0.0
2	1.8304E 04	0.0
3	4.3192E 04	0.0
4	3.3070E 04	0.0
5	8.1462E 03	0.0
6	1.9012E 04	0.0
7	-1.0913E 04	0.0
8	-1.5933E 04	0.0
9	-3.5804E 04	0.0
10	2.7079E 04	0.0
11	9.3986E 03	0.0
12	-1.0364E 03	0.0

'β_3' 1 X 2

ROW		
1	2.0000E-02	2.0000E-02

'β_4' 1 X 2

ROW		
1	2.8000E-02	2.8000E-02

```
PHI1        6 X 12

ROW  1
 4.8690E-01   2.9351E-01  -1.8744E-01  -9.7880E-02  -4.0404E-01  -7.1440E-01
-1.3657E-01   1.3880E-02  -4.4214E-01   1.4984E-01   0.0          0.0

ROW  2
 6.0038E-01   2.9211E-01   1.6570E-01   9.6900E-02  -8.0510E-02   3.0320E-02
-3.2230E-01  -3.7513E-01  -1.4114E-01  -4.7882E-01   0.0          0.0

ROW  3
 5.8104E-01   3.9365E-01  -4.9700E-02  -4.4300E-03  -3.5541E-01  -7.0587E-01
-1.3751E-01  -6.4000E-04  -5.7452E-01   8.2220E-02   0.0          0.0

ROW  4
 6.9682E-01   4.3555E-01   3.2310E-01   2.6220E-01   6.1270E-02   1.5134E-01
-2.1133E-01  -2.8303E-01  -8.7530E-02  -4.6163E-01   0.0          0.0

ROW  5
 7.0458E-01   5.5337E-01  -1.8754E-01   2.1641E-01  -1.5723E-01  -5.0210E-01
-2.9420E-02   7.5310E-02  -5.4619E-01   7.5360E-02   0.0          0.0

ROW  6
 8.0811E-01   6.1226E-01   5.3957E-01   4.3564E-01   3.0990E-01   3.9941E-01
 1.7360E-02  -3.7270E-02   1.0786E-01  -3.3316E-01   0.0          0.0
```

3.0 B-52 AIRPLANE AND AEROELASTIC MODEL RIDE CONTROL SYSTEM

Synthesis of forward fuselage vertical ride control (RC) systems for a 375,000 pound gross weight B-52E airplane and the NASA one-thirtieth scale B-52E aeroelastic model are described in this section. Identical RC systems were designed to obtain at least 30 percent reductions in airplane and model root mean square (RMS) vertical accelerations at the pilot stations due to random atmospheric turbulence.

The airplane RC system will be flight tested on NB-52E, AF56-632 CCF flight test airplane and the model RC system will be tested in the Langley Transonic Dynamic Wind Tunnel. Test data will be evaluated and correlation between the airplane and model RC system performances will be shown.

3.1 Background and Introduction

A synthesis study was conducted under Contract NAS1-10885 in 1971 and 1972 to design a full fuselage vertical RC system for the NASA one-thirtieth scale B-52E aeroelastic model. Scaled airplane equations of motion without model cable mount effects were used for the study. The elevator/aileron, elevator/horizontal canards and elevator/horizontal canards/flaperon were the primary control surface combinations investigated for this system. Results of this study are contained in Reference 1.

The forward fuselage RC syntheses presented in Section 3.3 were conducted on the model using 25 degree-of-freedom equations of motion generated using mass, stiffness and damping estimated from ground vibration test (GVT) data. Cable mount effects were also included in the equations.

The airplane and model RC systems were synthesized at the equivalent test conditions shown in Table 3-I. Identical sensor/surface locations and types were used for the two systems. Feedback gains were identical for the systems, but signal shaping filter time constants were appropriately scaled for the model RC system. Also, to account for differences in the airplane and model actuator dynamic characteristics, a high frequency compensating filter was added to the model system.

Figures 3.1 and 3.2 show the airplane and model RC system performance, respectively. The airplane RMS vertical acceleration at the pilot station is reduced by 30.2 percent and model acceleration by 48.3 percent.

The airplane and model RC system compatibility is shown in Section 3.4, and the model canard mechanization is described in Section 3.5.

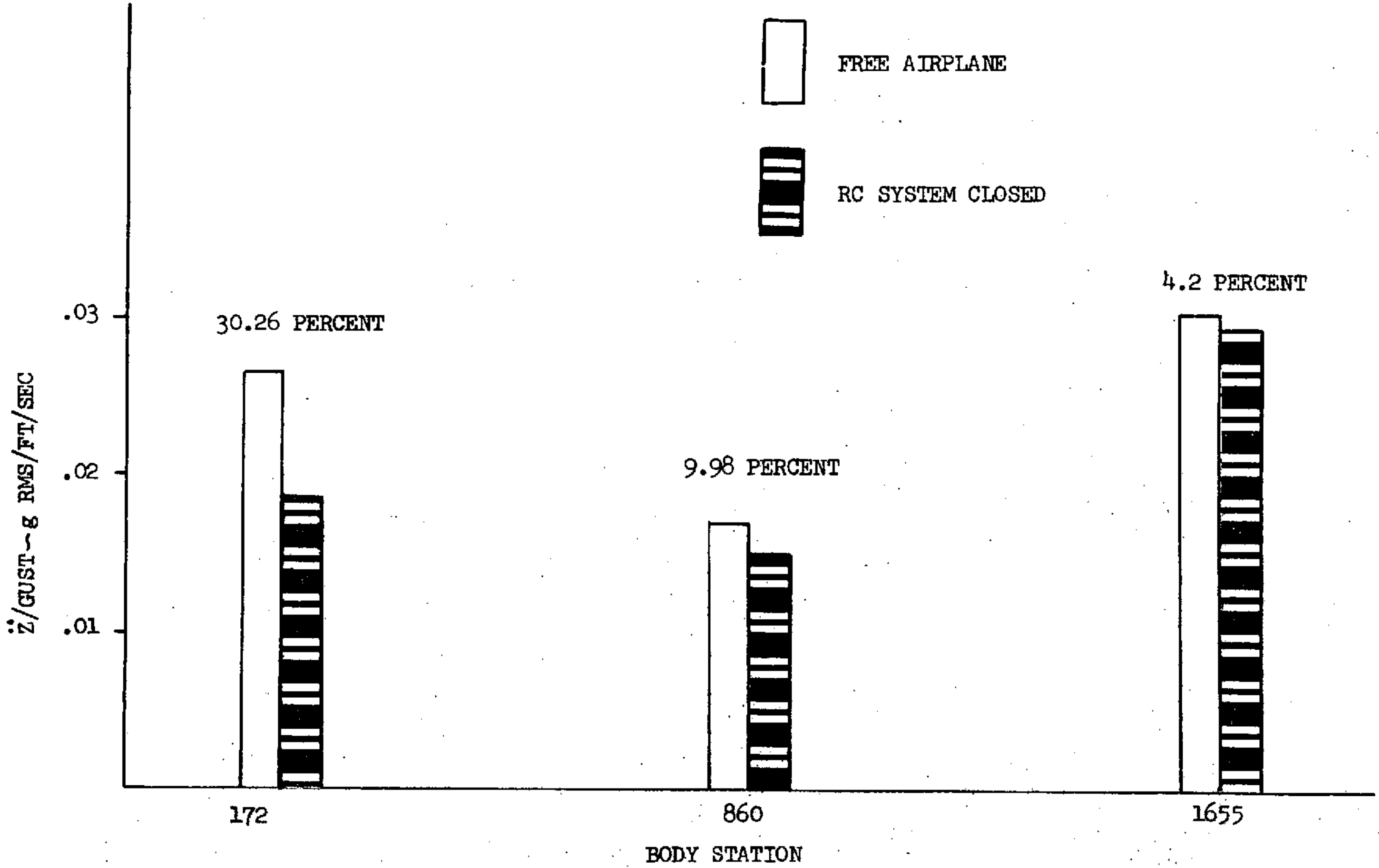

FIGURE 3.1: AIRPLANE RC SYSTEM PERFORMANCE

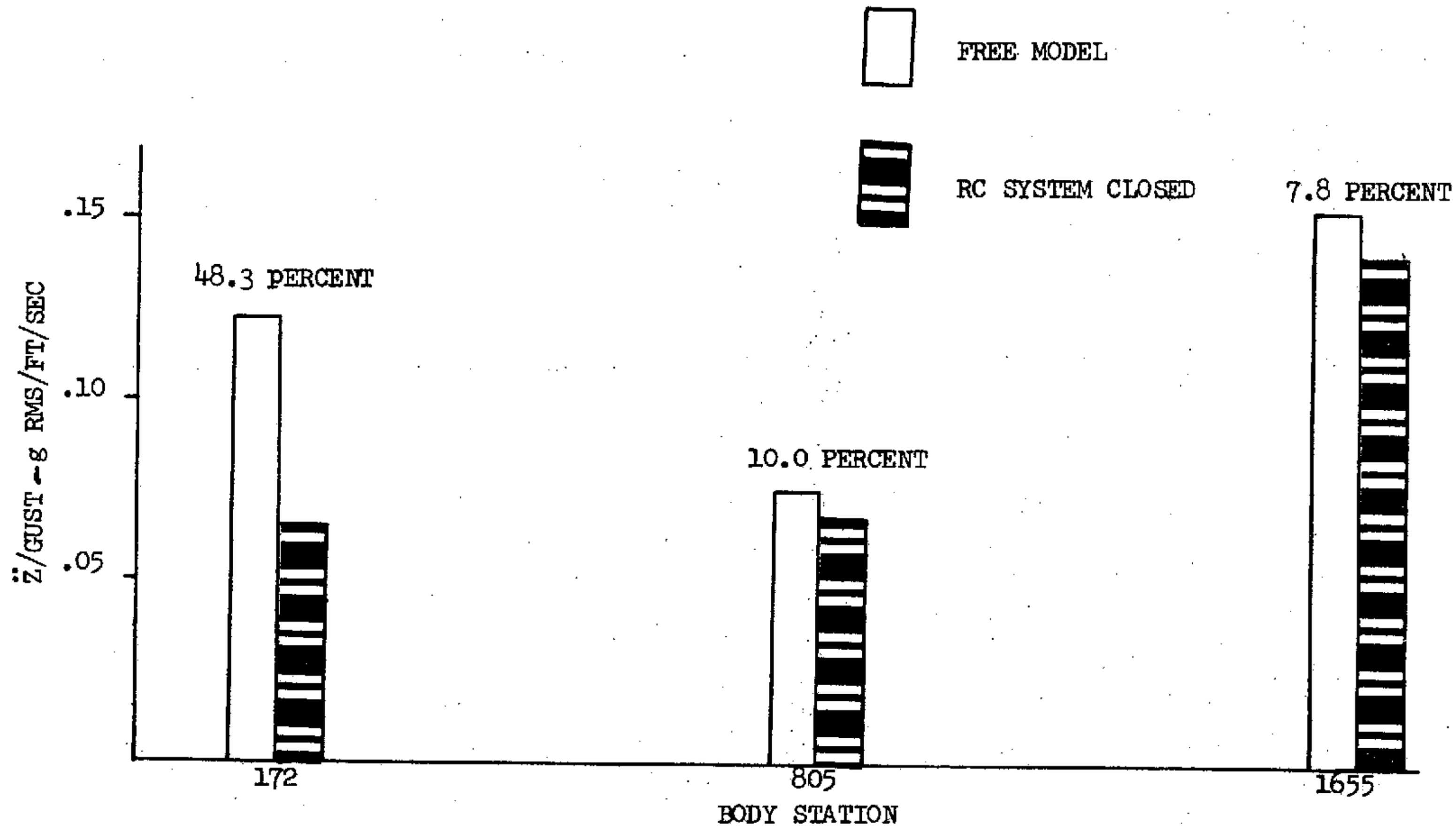

FIGURE 3.2: MODEL RC SYSTEM PERFORMANCE

TABLE 3-I: AIRPLANE AND MODEL RC TEST CONDITIONS

	Unit	Airplane	Model
Gross Weight	Pounds	375,000	56.7
Altitude	Feet	5,400	-
Density	Slugs/Ft^3	0.00202	0.008 (95% Freon)
Calibrated Airspeed	Knots	330	-
True Airspeed	Knots	356	65
Mach	--	0.548	0.218
Dynamic Pressure	Lbs/Ft^2	365.4	48.15

3.2 Airplane Ride Control Analysis

A ride control system was designed for a 267,000 pound gross weight B-52E airplane under the Control Configured Vehicles (CCV) program. The same system was analytically evaluated on a 375,000 pound gross weight, 5,400 feet altitude and 330 KCAS condition. The RC system signal shaping filter was modified to obtain the design goal of 30 percent reduction in vertical acceleration at the pilot station.

3.2.1 Mathematical Model

A 30 degree-of-freedom symmetric axis math model was developed for the 375,000 pound gross weight B-52E airplane with Mach 0.6 aerodynamic parameters. Unsteady aerodynamic effects were included in the math model and the final equations of motion were written in the form shown in Section 2.2.

The symmetric distribution of vertical gust predicted by the von Karman atmospheric turbulence model with characteristic gust length of 2,500 feet was used in the analysis.

The horizontal canard actuator dynamics were represented by the following transfer function:

$$\frac{\delta_{SURFACE}}{V_{COMMAND}} = \frac{(1.2)\ (45.6)(134000)}{(S + 45.6)(S^2 + 310\ S + 134000)} \quad \frac{\text{Deg}}{\text{Volt}}$$

3.2.2 Ride Control Analysis

Figure 3.3 shows open loop power spectral density and cumulative root mean square (PSD-RMS) plots of vertical acceleration at the pilot station (BS 172)

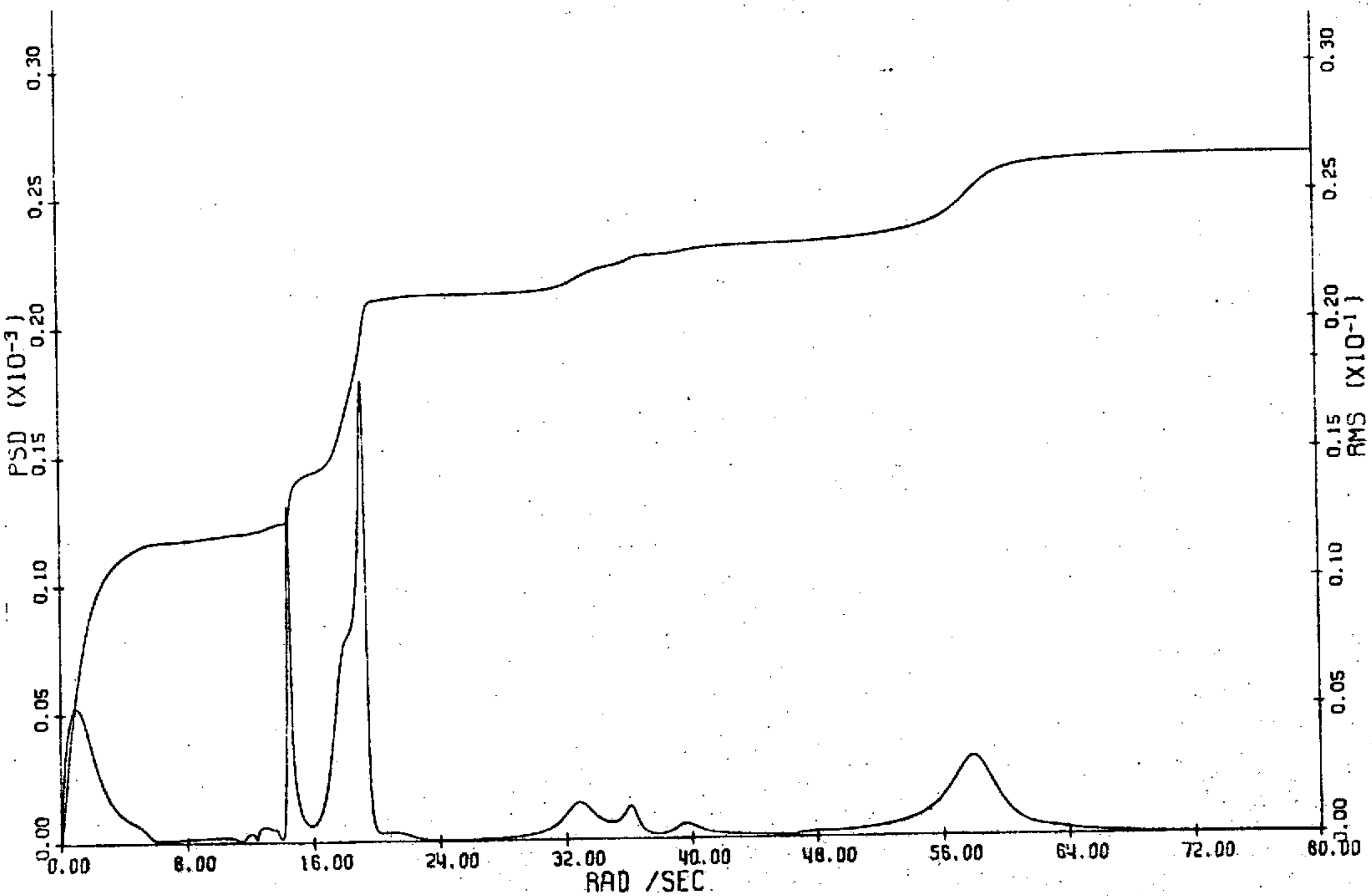

FIGURE 3.3: OPEN LOOP AIRPLANE $\ddot{Z}$(BS 172)/GUST PSD-RMS

due to random vertical gust. All airplane PSD-RMS analyses were conducted for a frequency range of 0 to 80 radians per second. The units of the PSD and RMS axes on the plots are $(g's/ft/sec)^2$ /radian/sec and g's/ft/sec respectively. Table 3-II lists the airplane rigid body and elastic modes significant to the vertical accelerations at the pilot station.

TABLE 3-II: MODES CONTRIBUTING TO $\ddot{Z}$(BS172)

MODE	Frequency Rad/Sec
Short Period	1.18
Elastic Mode 6	14.5
Elastic Mode 8	19.4
Elastic Mode 10	33.0
Elastic Mode 11	36.0
Elastic Mode 16	58.2

Figures 3.4 and 3.5 are the PSD-RMS plots of the free airplane vertical acceleration at the center of gravity (BS 860) and at the aft fuselage (BS 1655).

The ride control system shown in Figure 3.6 was designed to improve ride quality at the pilot station by obtaining at least a 30 percent reduction in RMS vertical acceleration due to atmospheric gust. The system uses pilot station vertical acceleration feedback to the horizontal canards through the signal shaping filter to provide desired loop gain and phase characteristics. A root locus analysis was conducted to design the feedback filter. Figures 3.7(a) thru 3.7(d) show the effects of feedback gain and phase variations on the closed loop characteristic roots. The root loci also show that the system is stable for at least ± 6 dB gain and ± 60 degrees phase variations.

Vertical acceleration at the pilot station of 0.0184 g RMS/foot per second RMS gust was obtained with the RC system on, compared to 0.265 g RMS/fps RMS gust with the system off. This represents a 30.2 reduction in RMS acceleration due to atmospheric turbulence and, therefore, the system performance meets the design goal. PSD-RMS plots of closed loop accelerations due to gust at Body Stations 172, 860 and 1655 are shown in Figures 3.8 to 3.10. RMS accelerations at BS 860 and 1655 are reduced by 10.0 and 4.2 percent, respectively.

PSD-RMS plots of canard displacement and rate are shown in figures 3.11 and 3.12. Horizontal canard displacement of 0.724 degree RMS and canard rate of 7.5 degrees/second RMS are required per foot per second RMS gust.

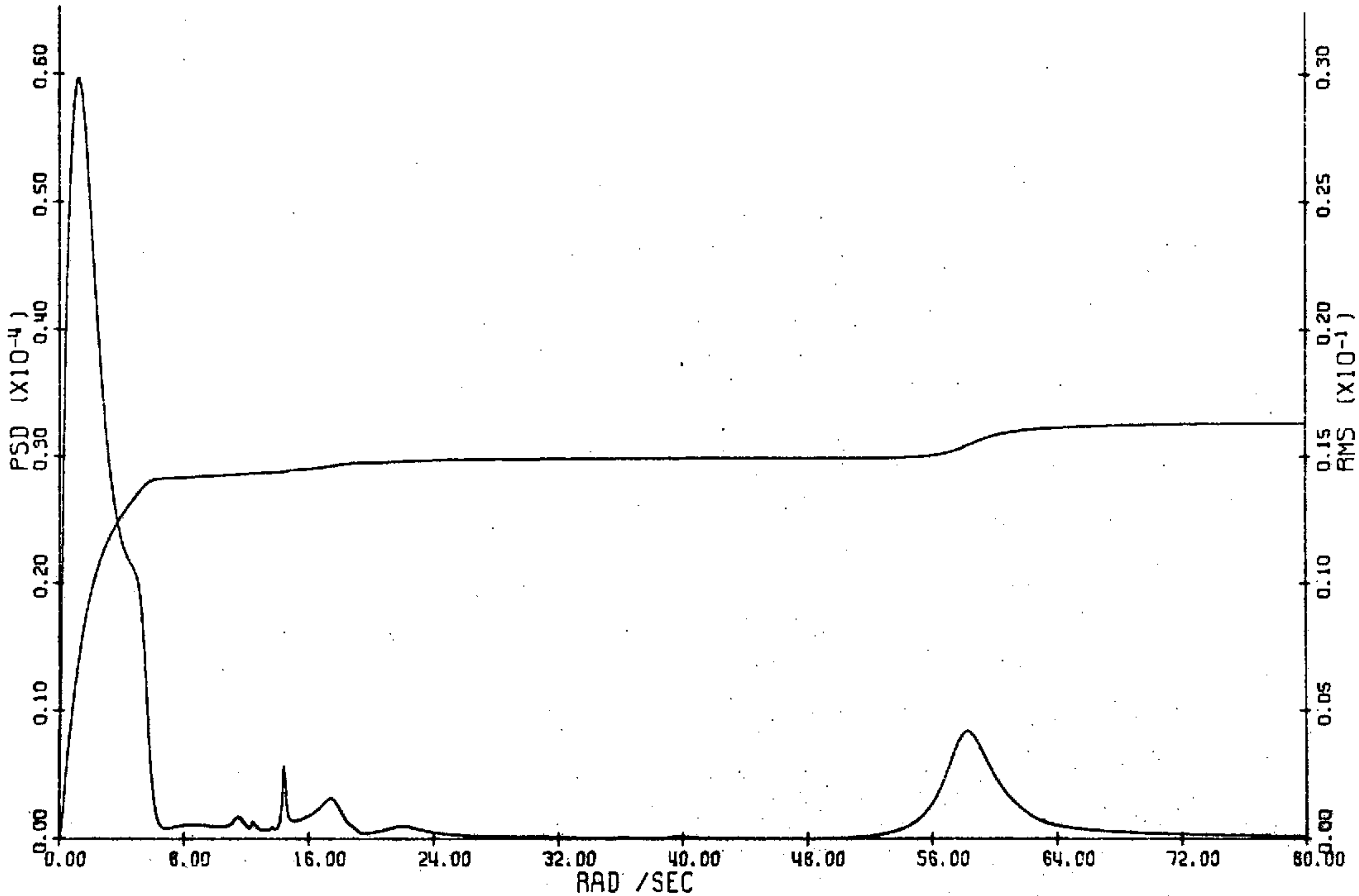

FIGURE 3.4: OPEN LOOP AIRPLANE $\ddot{Z}$(BS 860)/GUST PSD-RMS

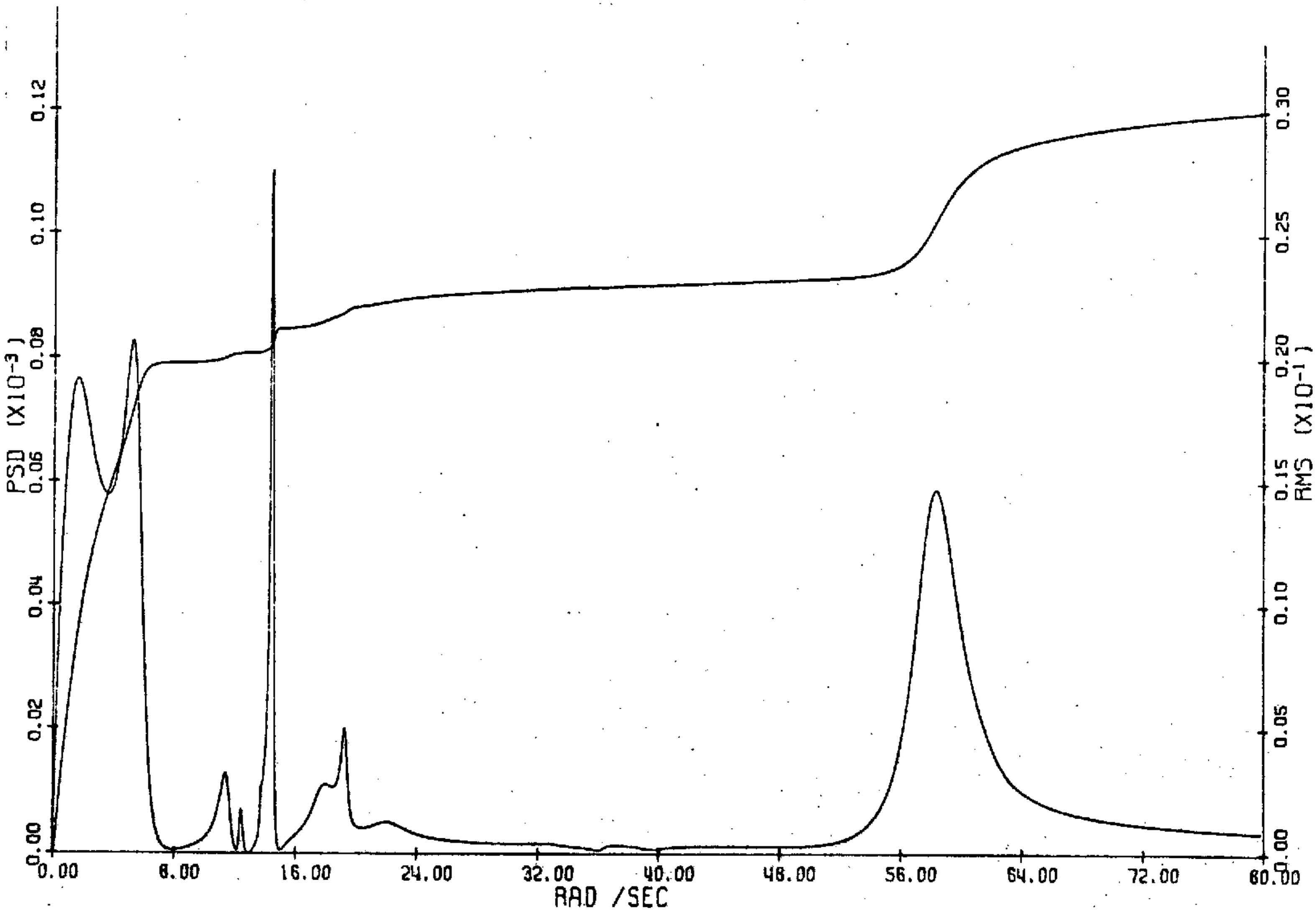

FIGURE 3.5: OPEN LOOP AIRPLANE $\ddot{Z}$(BS 1655)/GUST PSD-RMS

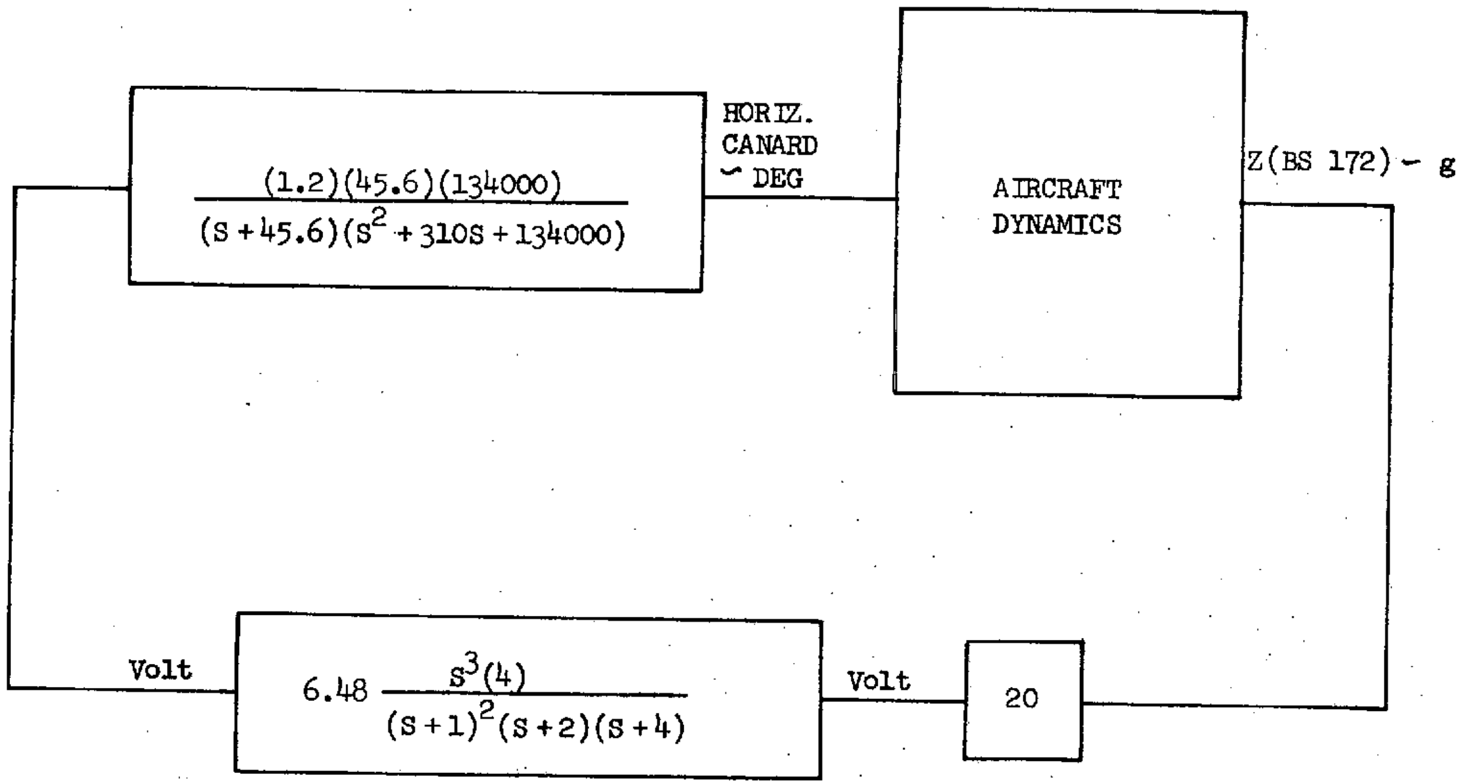

FIGURE 3.6: AIRPLANE RC SYSTEM BLOCK DIAGRAM

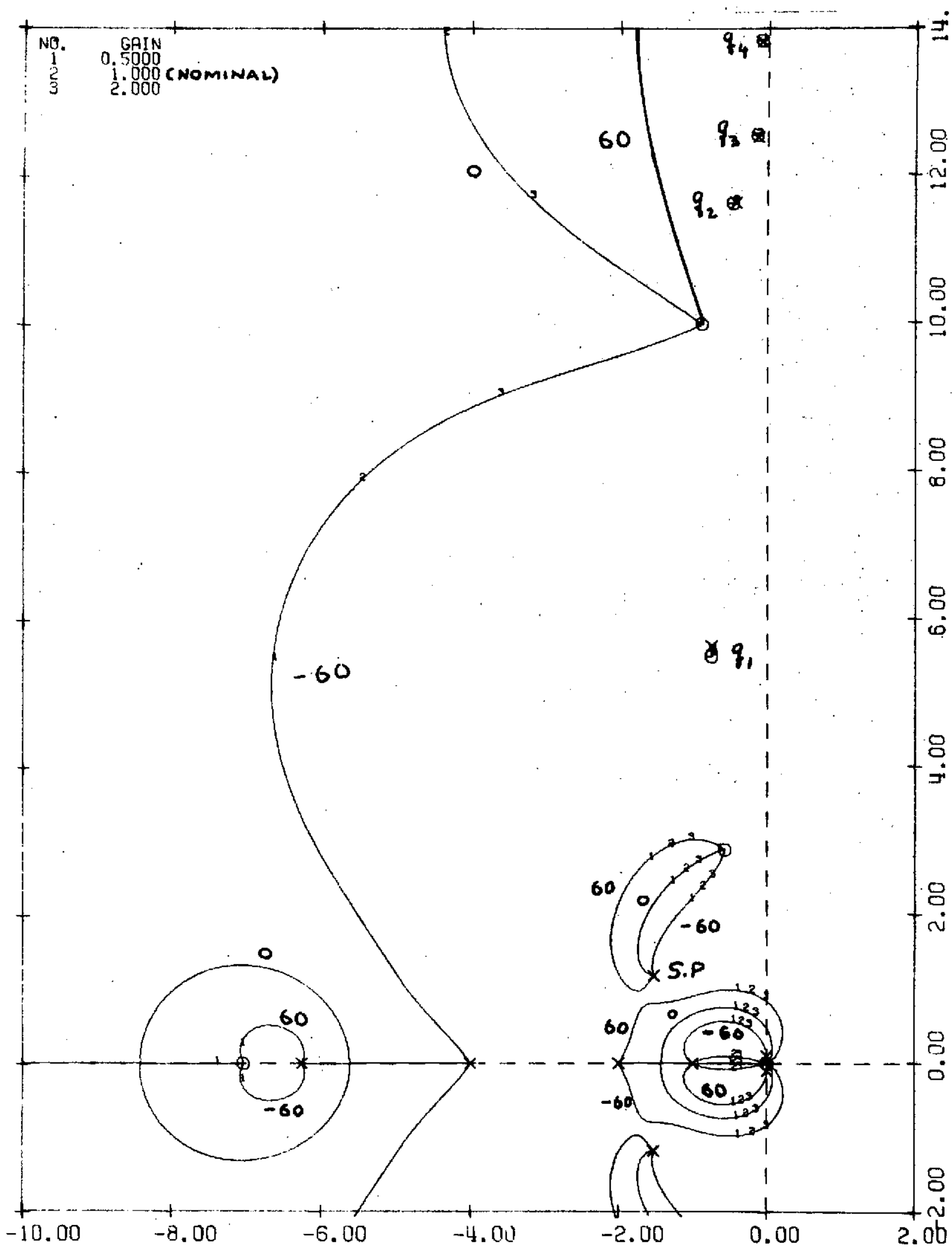

FIGURE 3.7(a): AIRPLANE RC SYSTEM GAIN/PHASE ROOT LOCUS

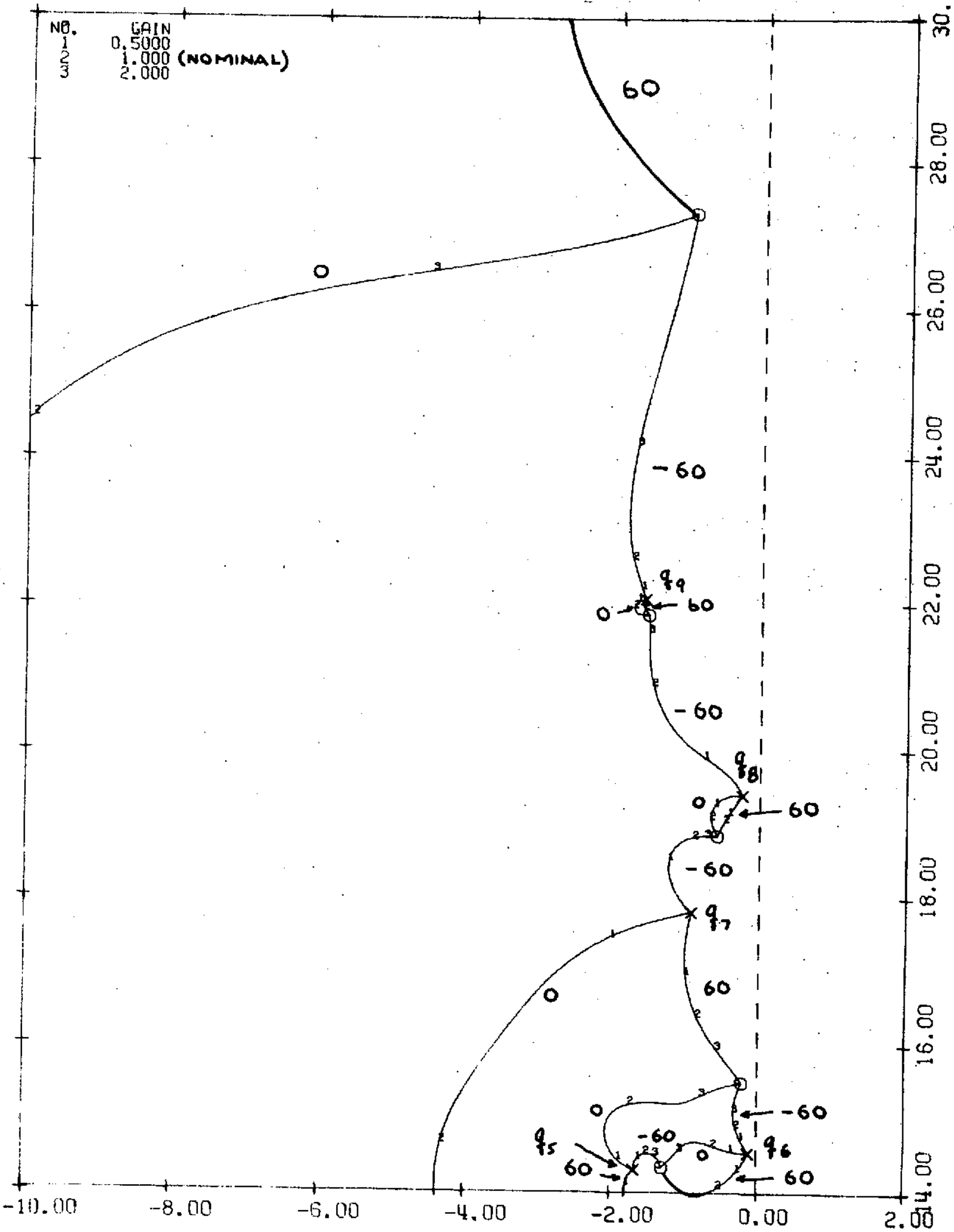

FIGURE 3.7(b): AIRPLANE RC SYSTEM GAIN/PHASE ROOT LOCUS

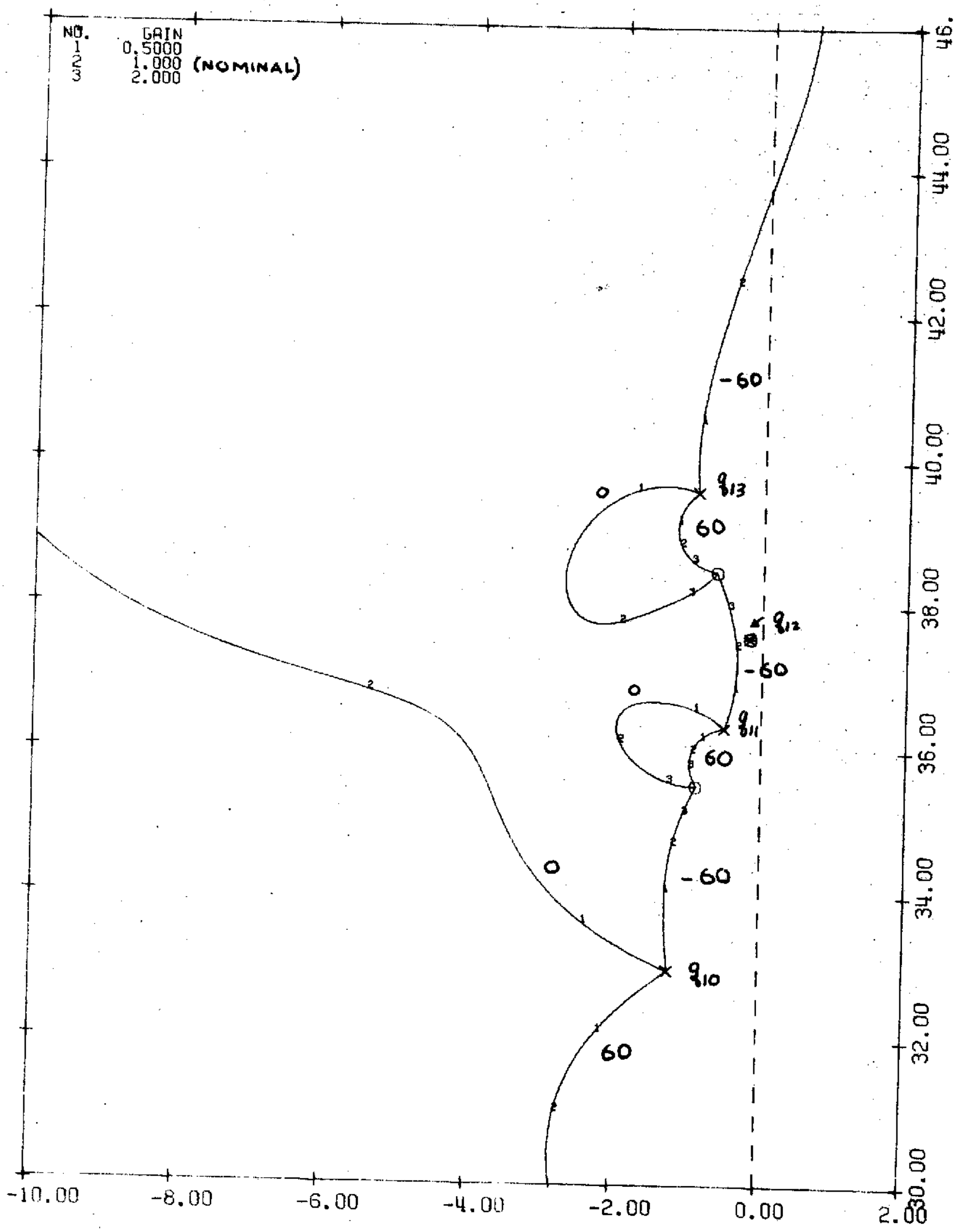

FIGURE 3.7(c): AIRPLANE RC SYSTEM GAIN/PHASE ROOT LOCUS

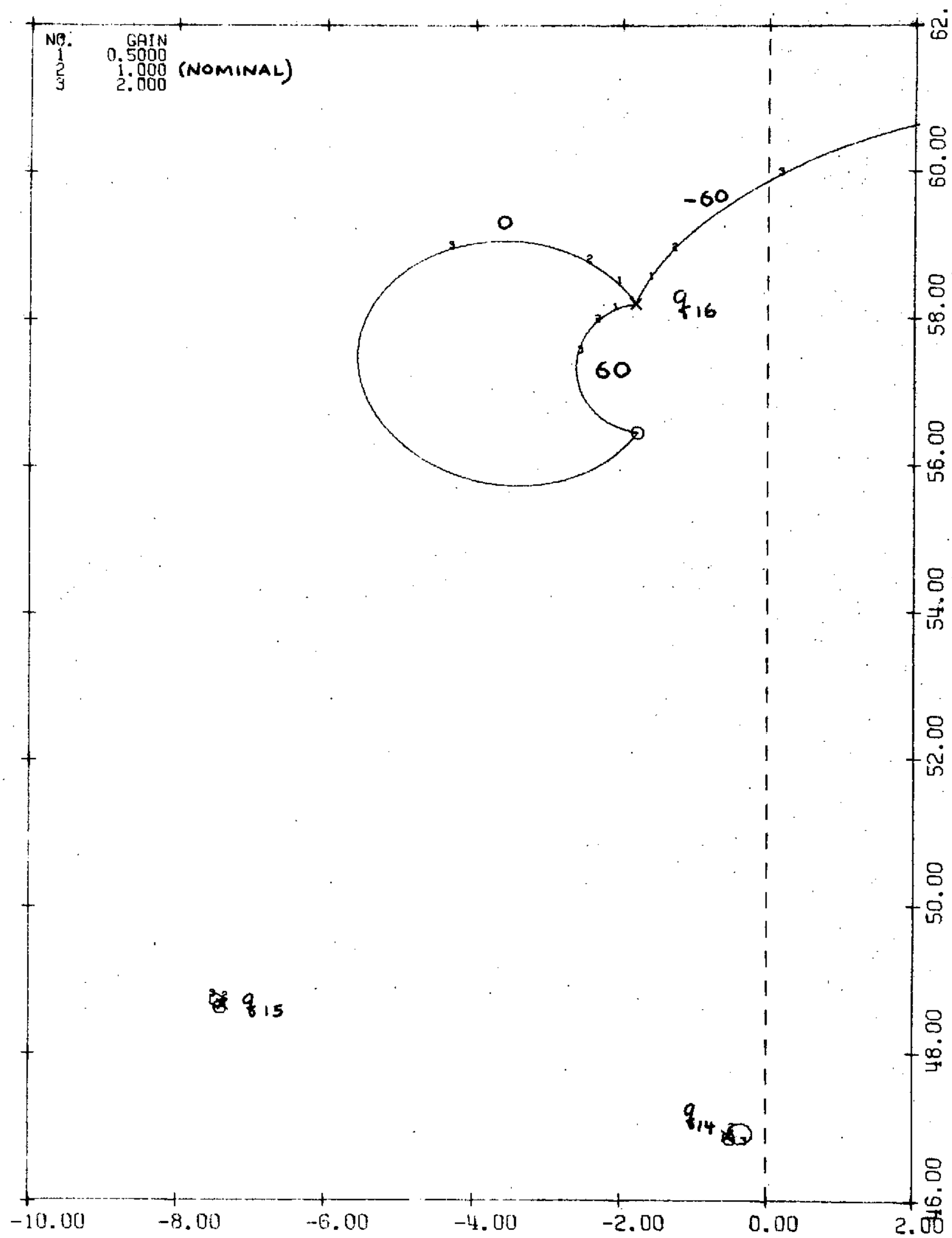

FIGURE 3.7(d): AIRPLANE RC SYSTEM GAIN/PHASE ROOT LOCUS

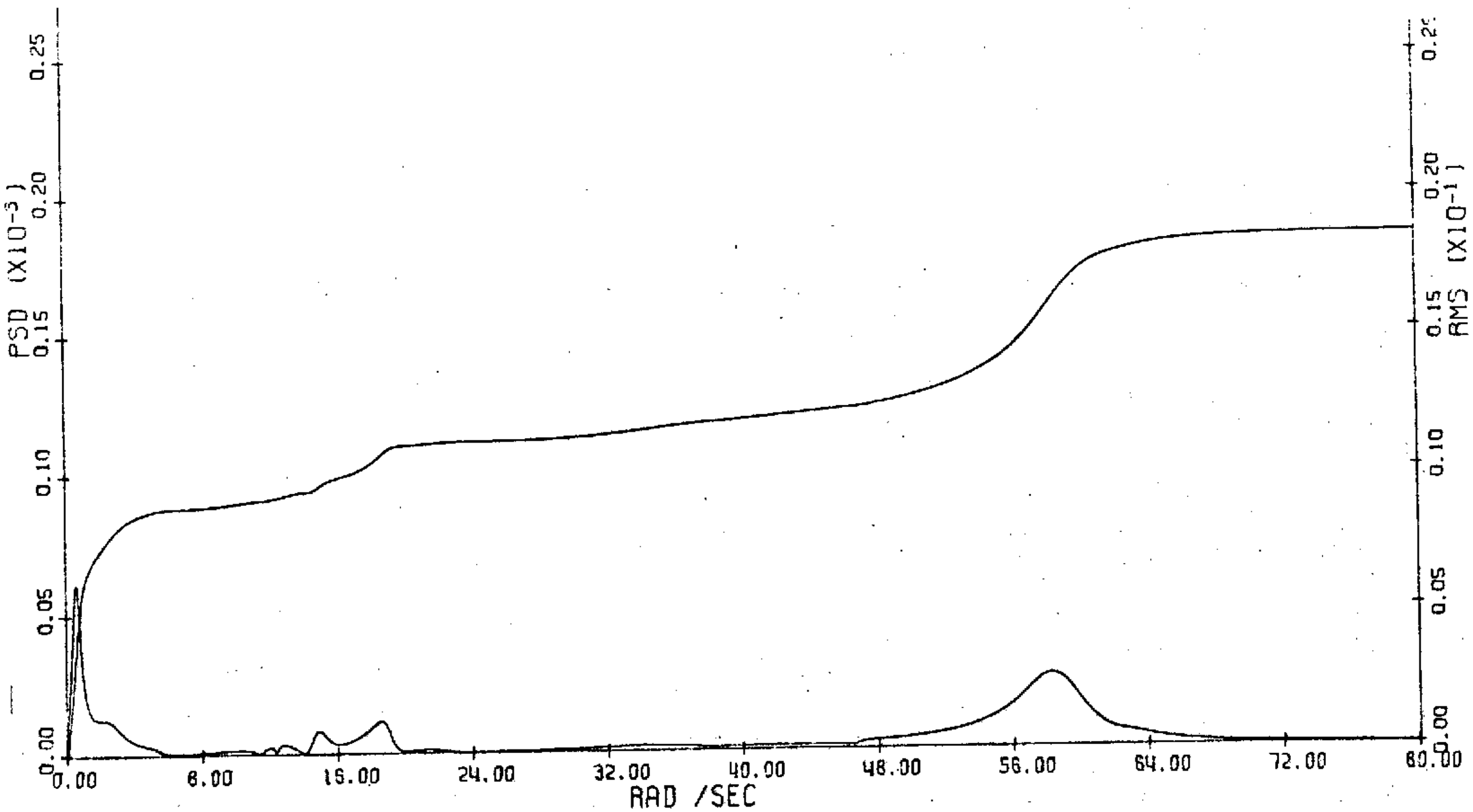

FIGURE 3.8: CLOSED LOOP AIRPLANE $\ddot{Z}$(BS 172)/GUST PSD-RMS

REV LTR:

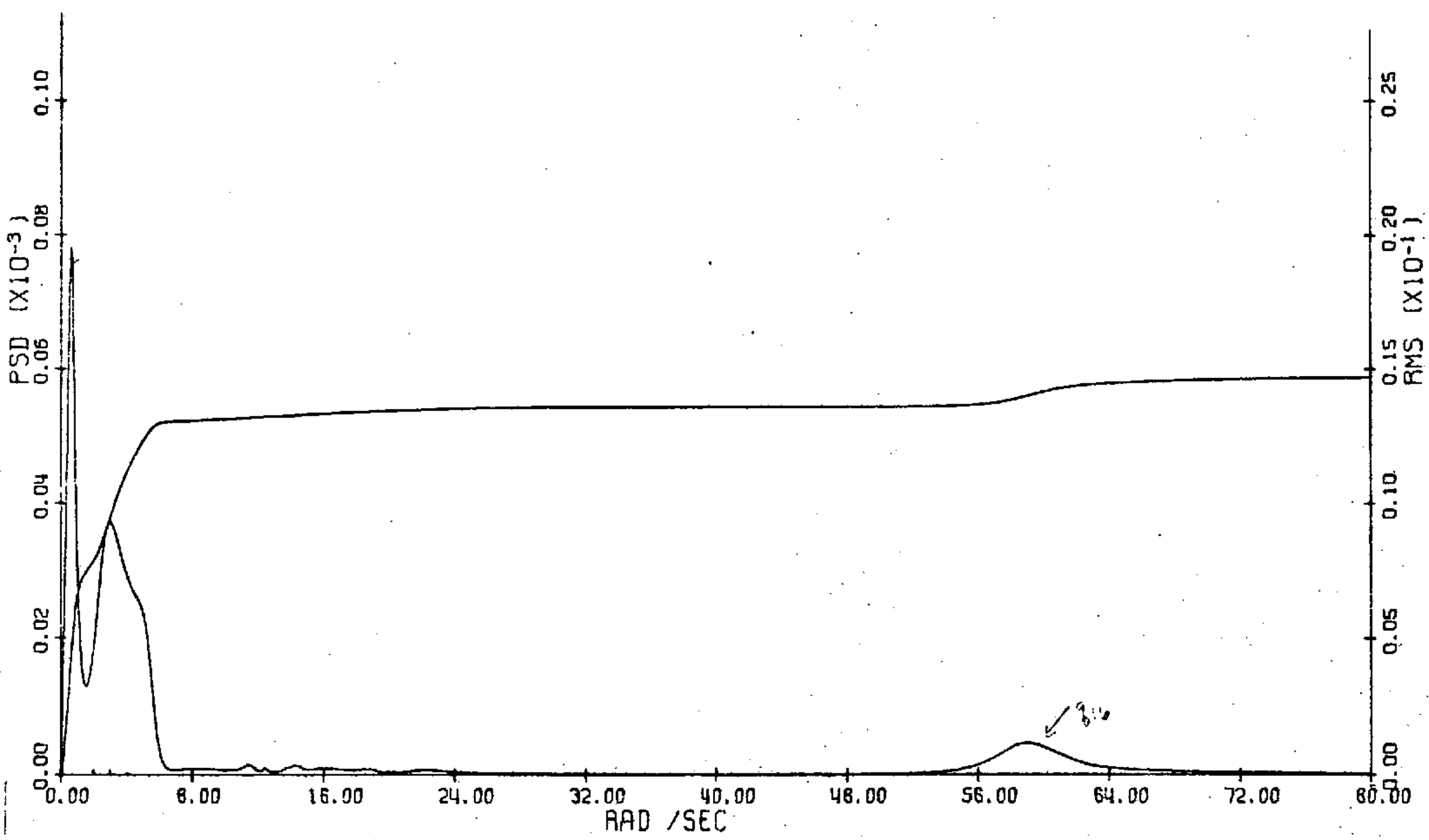

FIGURE 3.9: CLOSED LOOP AIRPLANE $\ddot{Z}$(BS 860)/GUST PSD-RMS

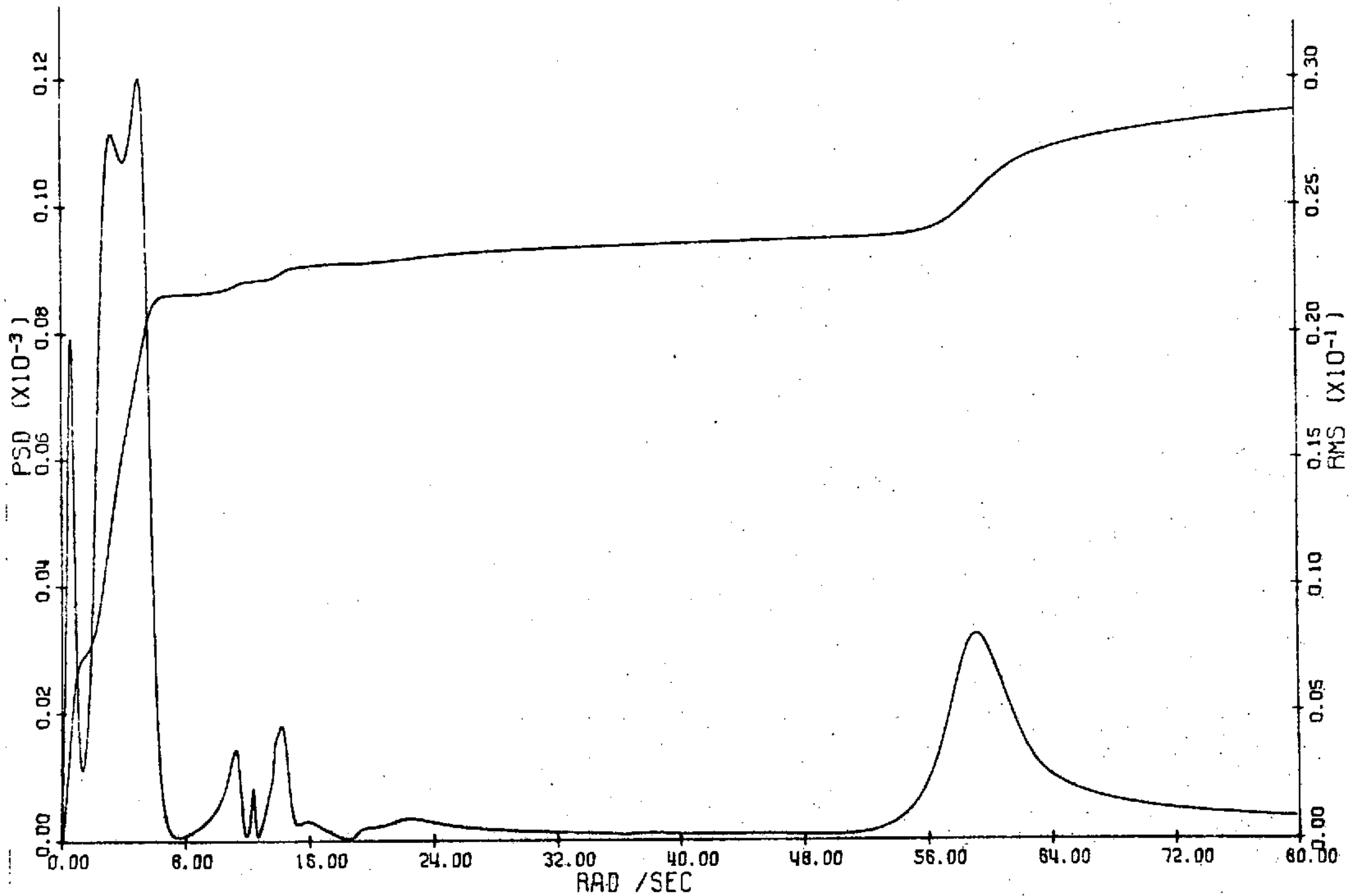

FIGURE 3.10: CLOSED LOOP AIRPLANE $\ddot{Z}$(BS 1655)/GUST PSD-RMS

REV LTR:

E-3033 R1

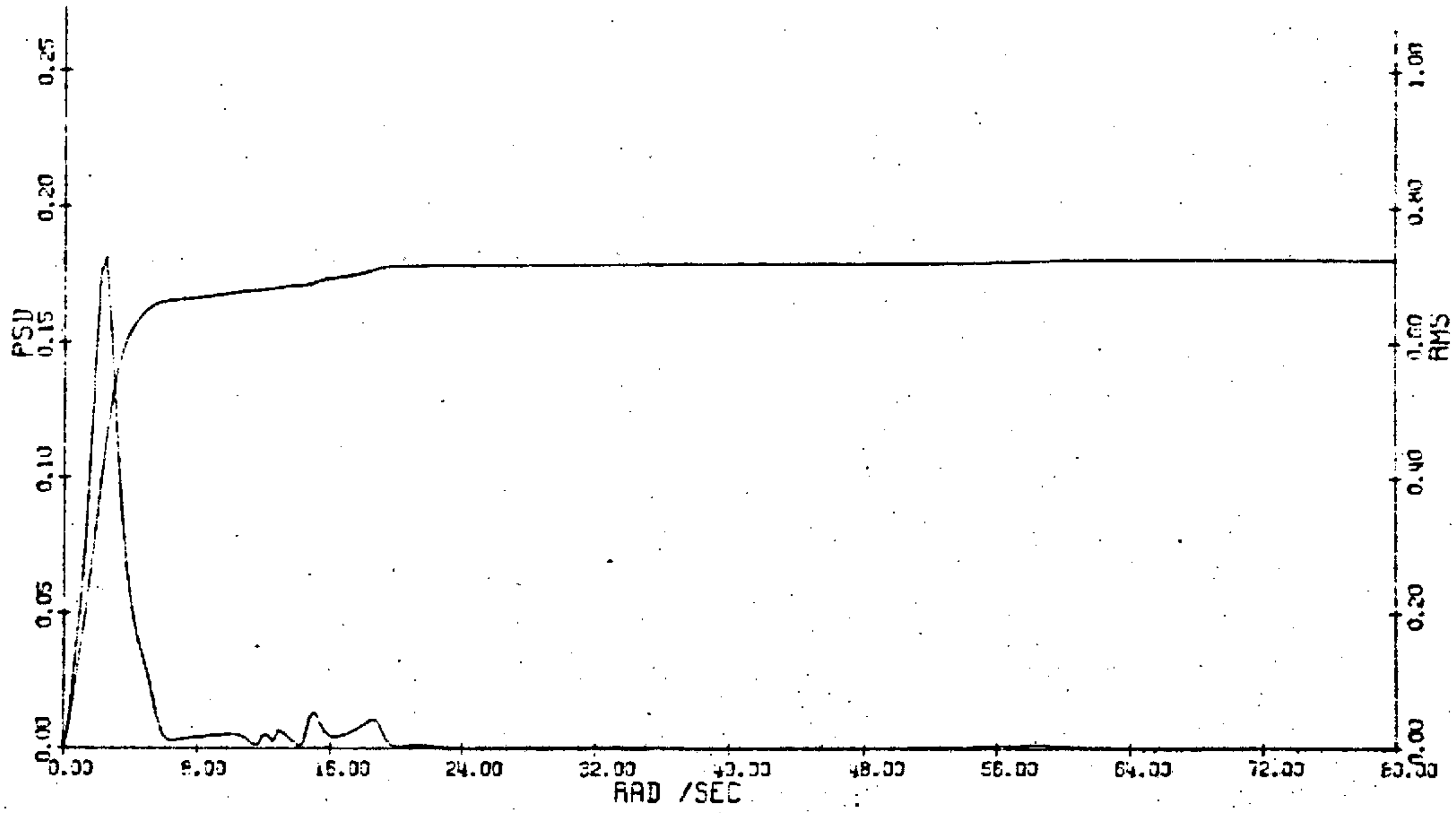

FIGURE 3.11: AIRPLANE RC SYSTEM CANARD DISPLACEMENT PSD-RMS

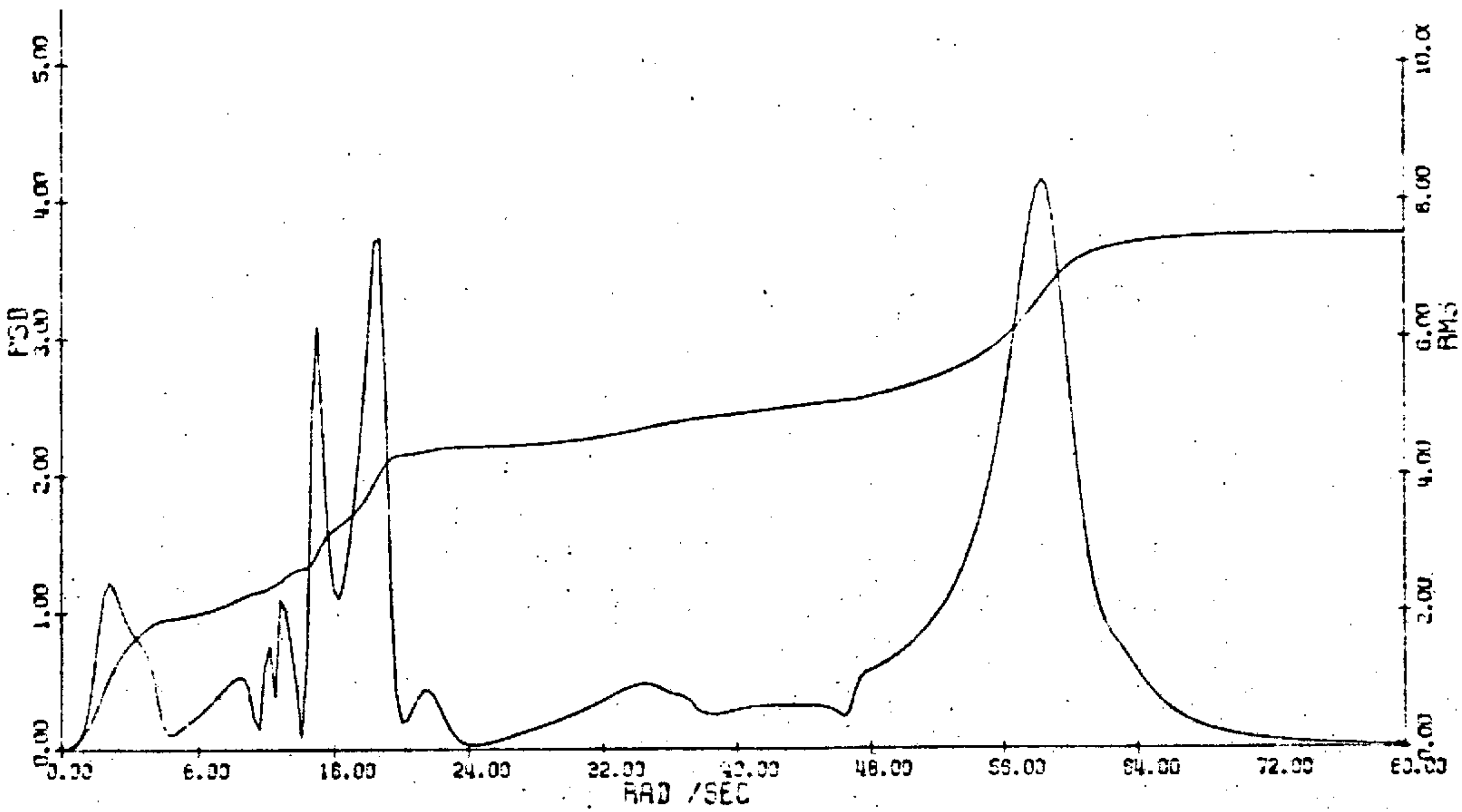

FIGURE 3.12: AIRPLANE RC SYSTEM CANARD RATE PSD-RMS

3.3 Aeroelastic Model Ride Control System

The objectives of this analysis were to evaluate the appropriately scaled airplane ride control system described in Section 3.2 on the B-52E aeroelastic model equations of motion and, if necessary, modify the system to obtain a minimum of 30 percent reduction in RMS acceleration at the equivalent pilot station.

3.3.1 Mathematical Model

Structural mass, frequency and damping data measured during the GVT of the modified model were received from NASA. Model modifications included revised nacelle struts and wing tip tanks, and installation of control surfaces and actuation systems. The outboard nacelles were revised to match the model and airplane flutter characteristics.

The measured mass, frequency and damping data were used to generate a 25 degree-of-freedom symmetric axis mathematical model. Cable mount effects were included in the vertical translation and pitch degrees-of-freedom. The equations of motion were generated with Mach 0.24 aerodynamic loading and the effects of unsteady aerodynamics were included. The final equations of motion were written in terms of Laplace operator "S" as shown below:

$$\left([M+\rho C_1]s^2 + [D+\rho V C_2]s + [K+\rho V^2 C_3] + \rho V^2 \sum_{K=1}^{4} [D_K] \frac{s}{s+V d_K} \right) q + \rho V \left([R_0] + \sum_{K=1}^{4} [R_K] \frac{s}{s+V\beta_K} \left[e^{-\frac{x_i}{V} s} \right] \right) W_{g_i} = 0$$

where:

$\underline{q}$	=	Cable mount, model elastic and control surface degrees of freedom
W_{g_i}	=	Spanwise distribution of vertical gust at reference station X = 0
X_i	=	Gust penetration distances from reference station X = 0
V	=	Velocity of fluid relative to the model
ρ	=	Wind tunnel fluid density
S	=	Laplace operator
M, D, K	=	Structural mass, density and stiffness
C_1, C_2, C_3	=	Aerodynamic parameters
d_k, β_k	=	Lift growth parameters
D_K, R_K	=	Aerodynamic parameters for unsteady lift
R_0	=	Turbulence forcing function coefficients

Model fuselage and wing station designations used in this analysis are in airplane scale, but all data is in model scale.

The von Karman gust spectrum representing vertical atmospheric turbulence was used for the model excitation, but the characteristic gust length of the spectrum was scaled down by a factor of 30 to make the gust spectrum compatible with model frequencies. The characteristic gust length of 2,500 feet was therefore scaled to 83.33 feet for the model analysis.

The canard actuation system was represented by the second order transfer function shown below. This transfer function was obtained from the measured frequency response of the system.

$$\frac{\delta_{Horiz.Canard}}{\delta_{Command}} = \frac{(250)^2}{S^2 + 2(0.3)(250)\,S + (250)^2} \quad \frac{deg}{deg}.$$

3.3.2 Model Ride Control System Design

Figures 3.13 to 3.15 show PSD-RMS plots of the open loop vertical accelerations at the pilot station (BS 172), mid body (BS 805), and aft body (BS 1655) in atmospheric turbulence environment. All PSD-RMS analyses were conducted for 0 to 350 radians per second frequency range. Two cable constraint modes and the first sixteen elastic modes were included in the analysis. Modes listed in Table 3-III are significant to the ride quality at the pilot station.

TABLE 3-III

MODES SIGNIFICANT TO RIDE AT BS 172

Mode	Frequency Rad/Sec
Second Cable Constraint	11.0
Elastic Mode 6	80.0
" " 8	105.5
" " 10	180.0
" " 11	205.0
" " 15	285.0

The analysis began with an evaluation of the scaled airplane ride control (RC) feedback shaping filter with model actuator dynamics. The airplane and model RC filters are given below:

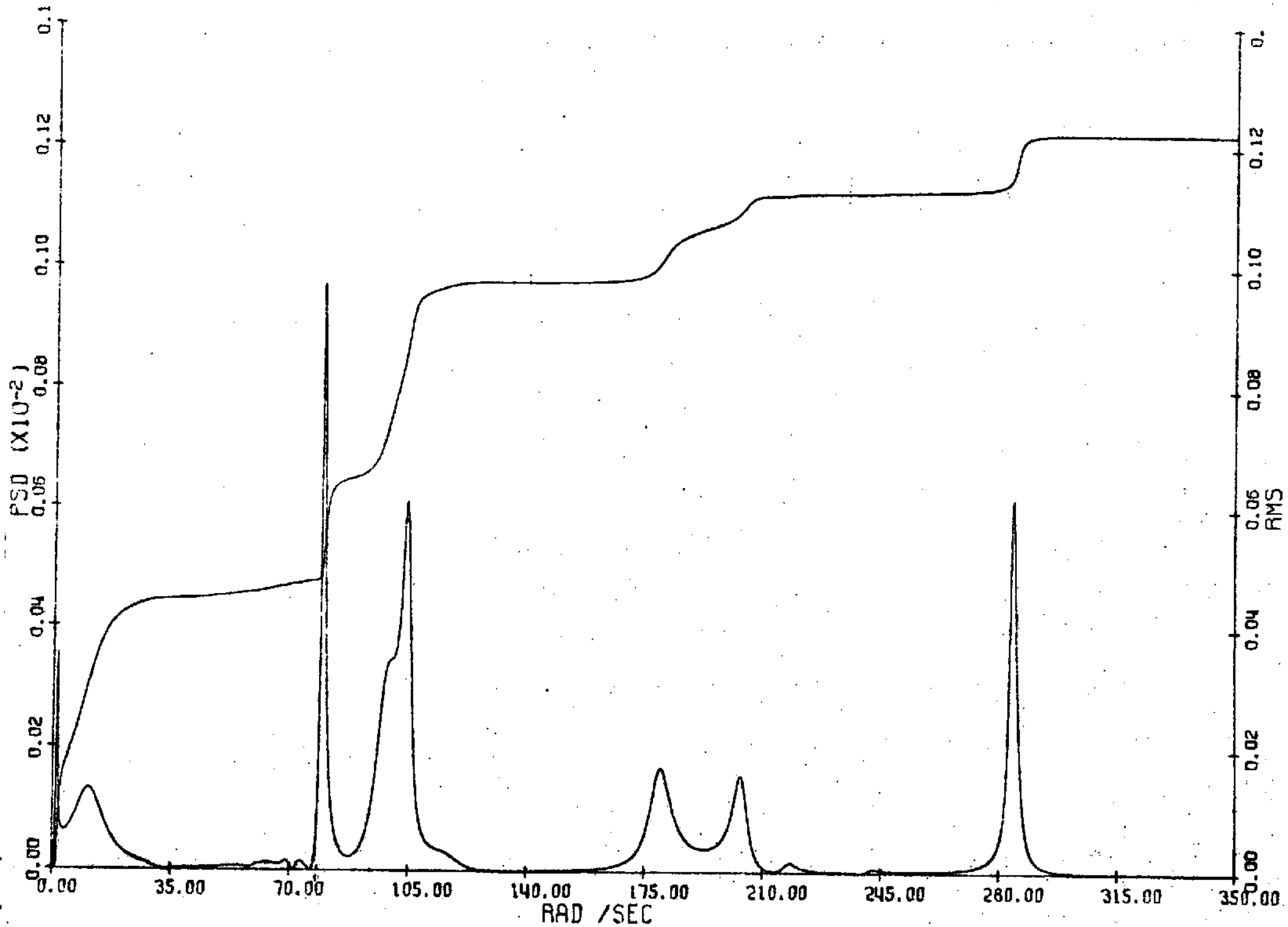

FIGURE 3.13: OPEN LOOP MODEL $\ddot{Z}$(BS 172)/GUST PSD-RMS

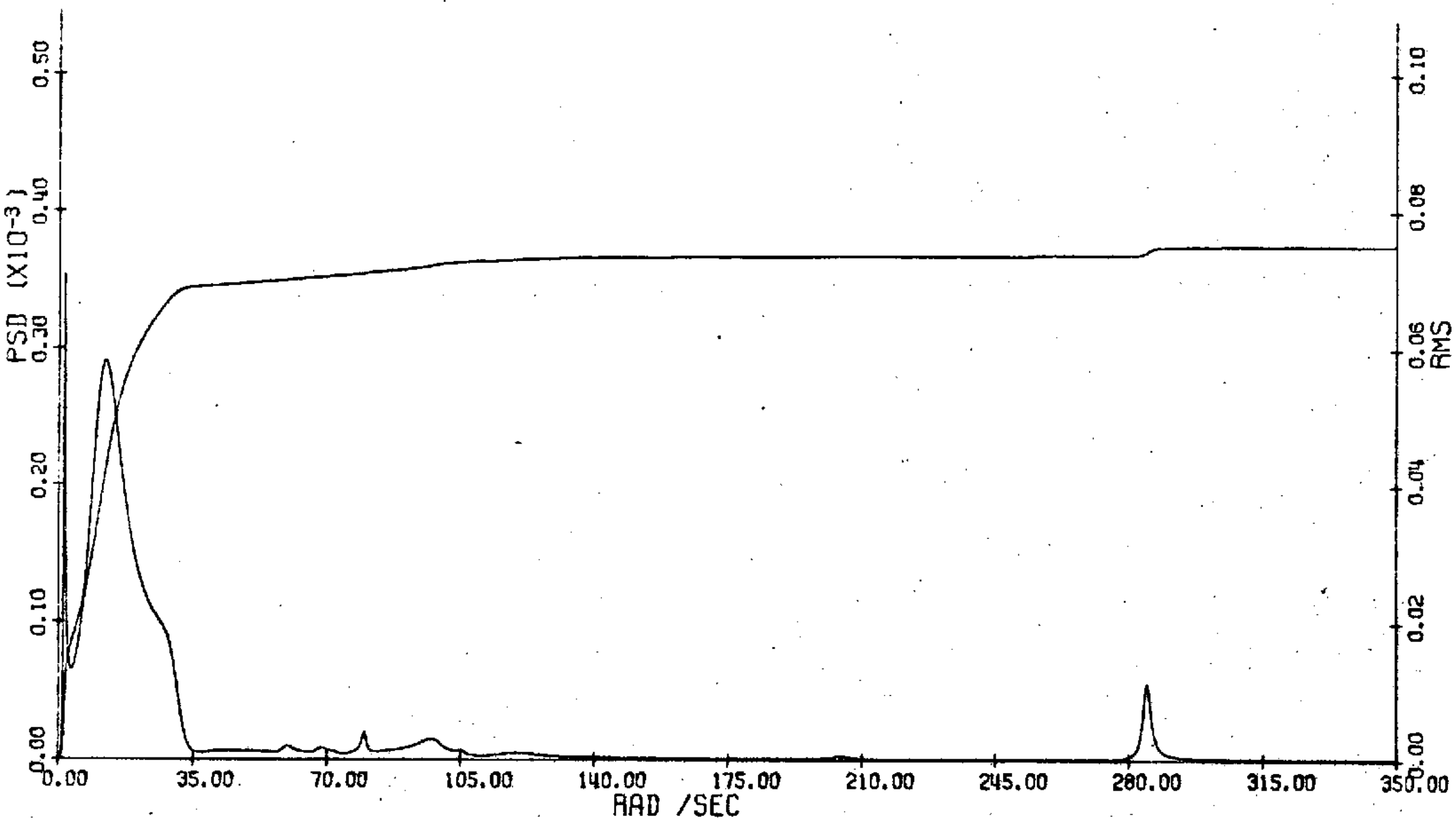

FIGURE 3.14: OPEN LOOP MODEL $\ddot{Z}$(BS 805)/GUST PSD-RMS

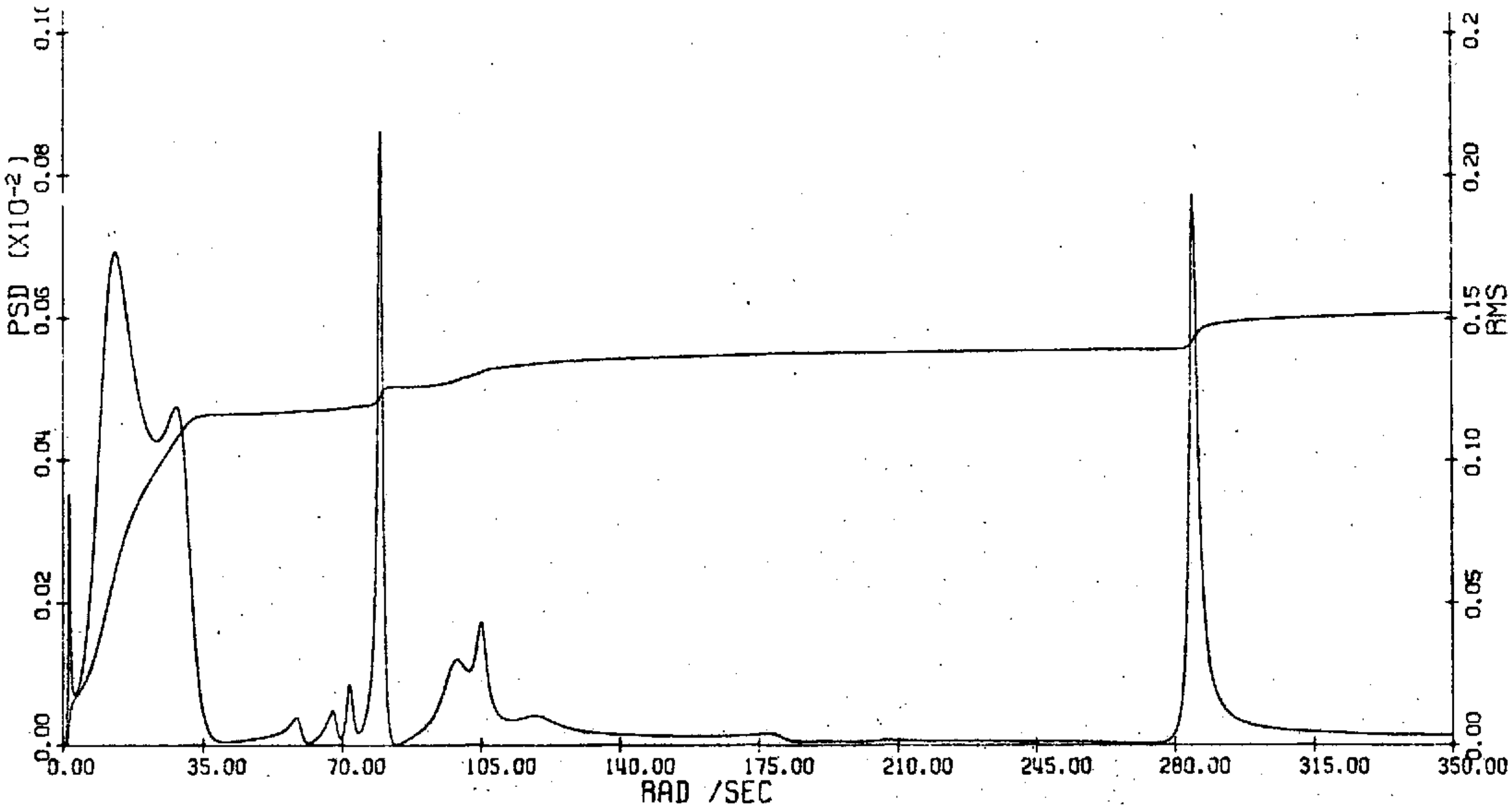

FIGURE 3.15: OPEN LOOP MODEL $\ddot{Z}$(BS 1655)/GUST PSD-RMS

Airplane Filter

$$\frac{6.48\ S^3(4)}{(S+1)^2(S+2)(S+4)}$$

Model Filter

$$\frac{6.48\ S^3\ (21.92)}{(S+5.48)^2(S+10.96)(S+21.92)}$$

Gain root loci in Figures 3.16(a) to 3.16(c) indicate that the scaled airplane filter worked satisfactorily on the lower frequency modes but, as shown in Figure 3.16(d), system coupling with the higher frequency modes caused the thirteenth and fifteenth elastic modes to be unstable at nominal system gains.

The adverse coupling with the elastic modes in the 240 to 300 rad/sec frequency range was caused by increased feedback gain and phase introduced by the lightly damped ($\zeta = 0.3$) second order canard actuator dynamics. The system performance can be improved to obtain a stable closed loop model by increasing the actuator frequency to 300 rad/sec and the damping ratio to 0.4. However, increased actuator frequency and damping ratio did not provide adequate gain and phase margins as indicated by the root locus in Figure 3.17.

A high frequency compensation filter was added to the basic airplane scaled filter to obtain pseudo airplane actuator dynamics of a first order lag at 250 rad/sec. A block diagram of the modified RC control system is given in Figure 3.18. Gain and phase root locus of the modified RC system in Figures 3.19(a) to 3.19(e) indicate that the system provides ±6 dB gain margin and +60 and -50 degrees phase margin.

Pilot station vertical acceleration of 0.1223 g RMS/ft/sec RMS gust was obtained with the RC system off, but with the system on the acceleration was reduced to 0.0632 g RMS/ft/sec RMS gust. Therefore, a reduction of 48.3 percent in acceleration at BS 172 was attained. Accelerations at BS 805 and BS 1655 were also reduced by 10 and 7.8 percent respectively. PSD-RMS plots of the closed loop accelerations at BS 172, 805 and 1655 are given in Figures 3.20 to 3.22.

Canard surface displacement of 2.66 degrees RMS and canard rate of 143.6 deg/sec RMS g per ft/sec gust were required to operate the RC system. Figures 3.23 and 3.24 show PSD-RMS plots of model canard displacement and rate.

Figure 3.25 shows effects of feedback gain variation on system performance and on the required surface activity.

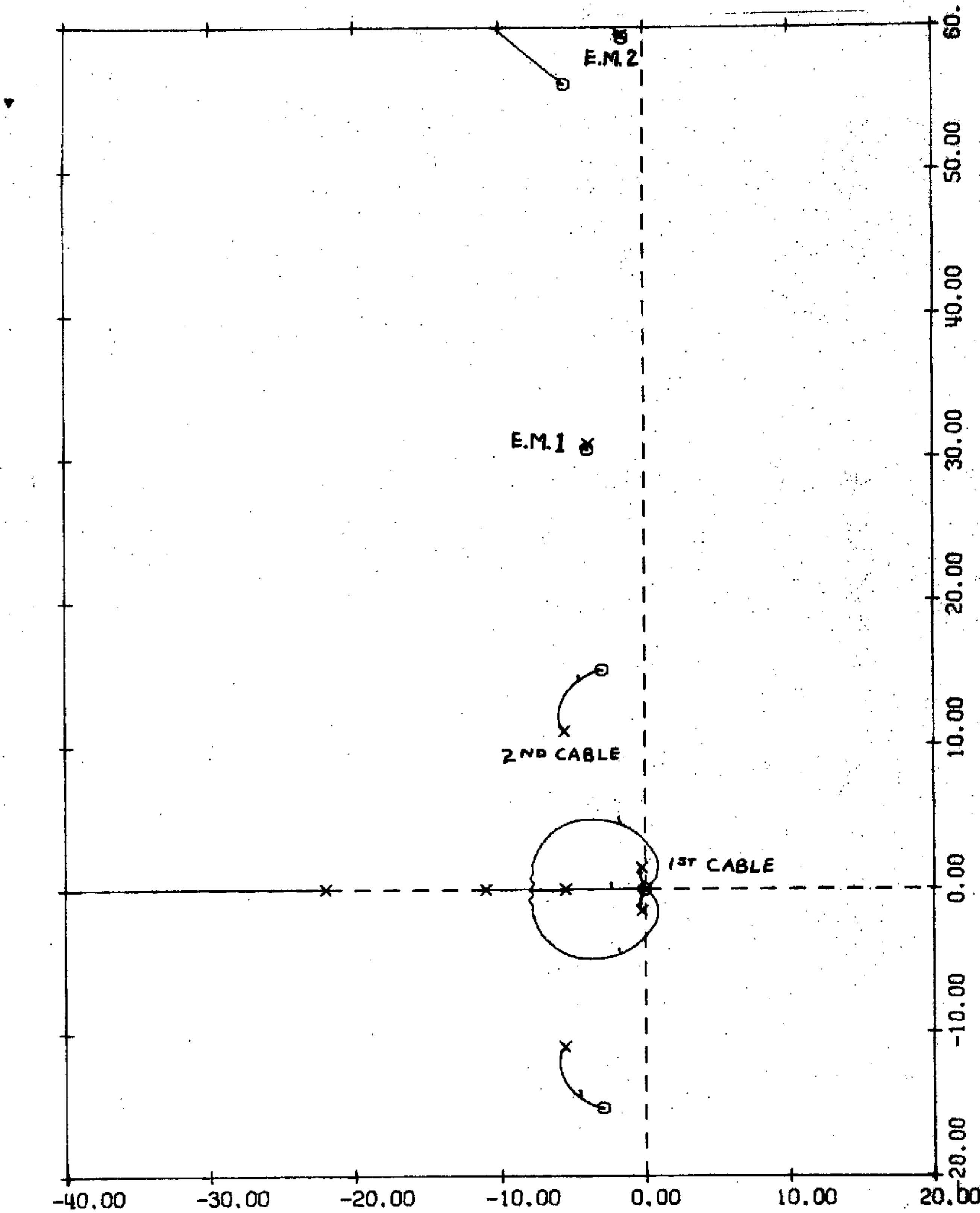

FIGURE 3.16(a): MODEL RC SYSTEM GAIN ROOT LOCUS
NOMINAL MODEL ACTUATOR DYNAMICS (ω_n = 250 rps, ζ = .3)

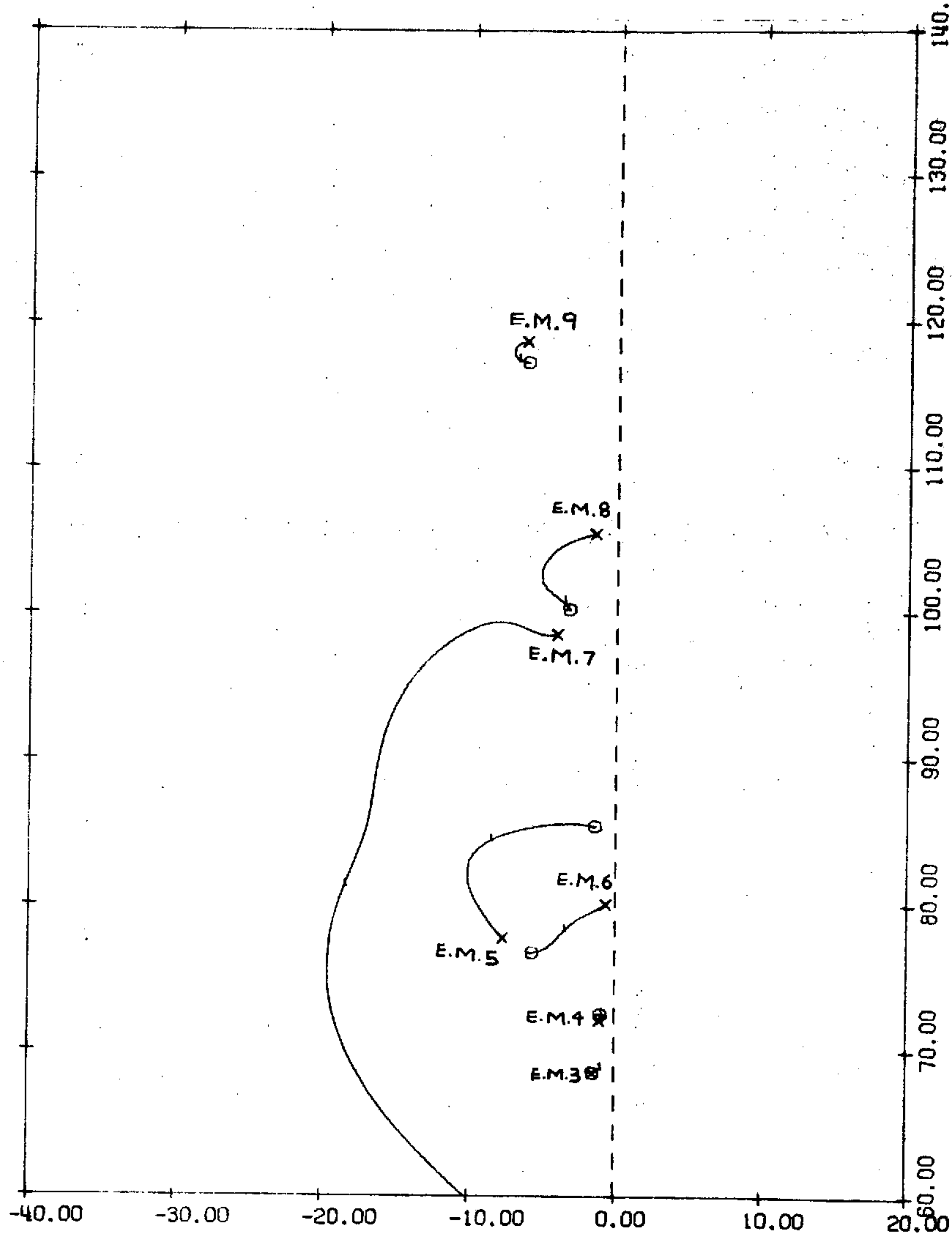

FIGURE 3.16(b): MODEL RC SYSTEM GAIN ROOT LOCUS
NOMINAL MODEL ACTUATOR DYNAMICS (ω_n = 250 rps, ζ = .3)

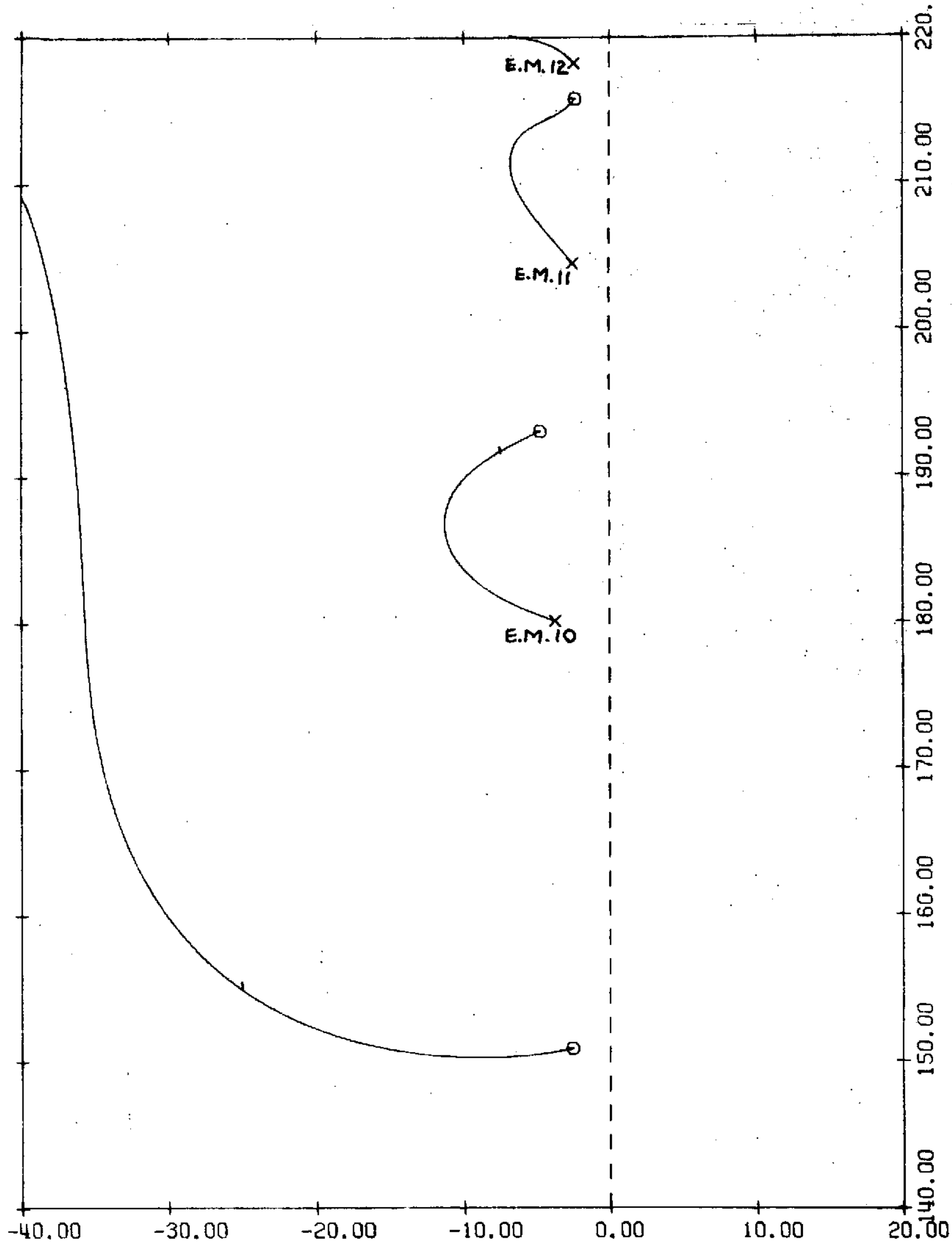

FIGURE 3.16(c): MODEL RC SYSTEM GAIN ROOT LOCUS
NOMINAL MODEL ACTUATOR DYNAMICS (ω_n = 250 rps, ζ = .3)

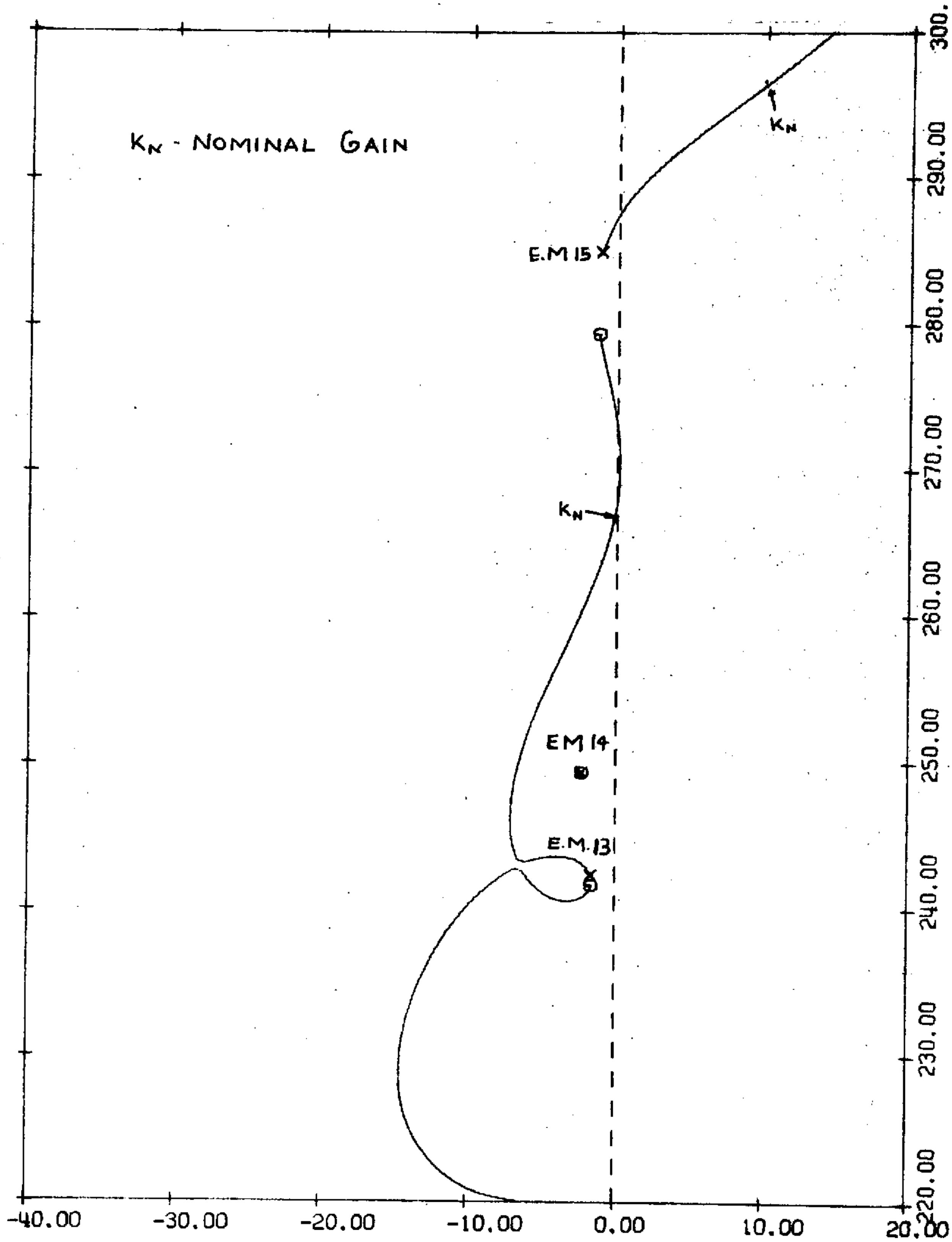

FIGURE 3.16(d): MODEL RC SYSTEM GAIN ROOT LOCUS
NOMINAL MODEL ACTUATOR DYNAMICS (ω_n = 250 rps, ζ = .3)

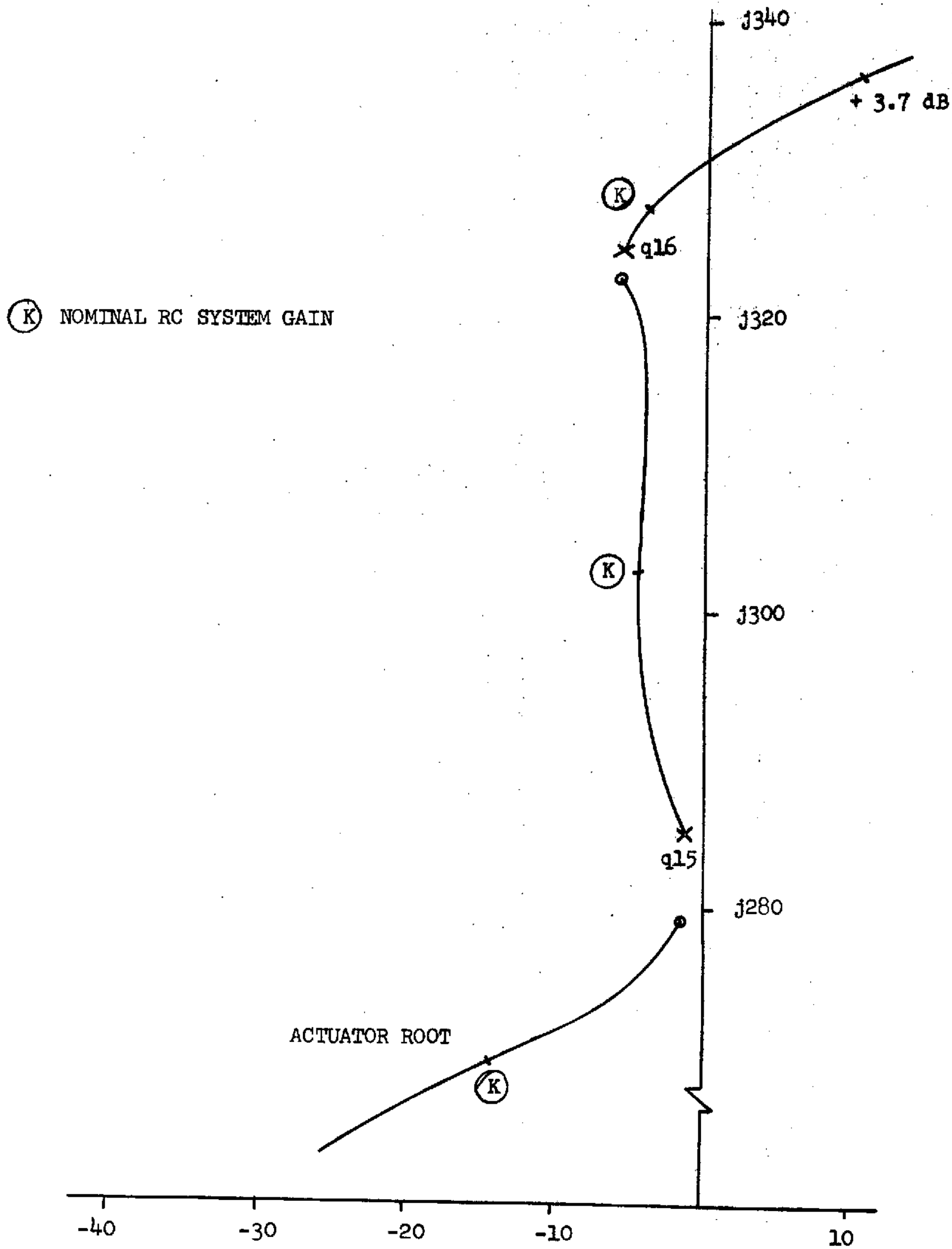

FIGURE 3.17: MODEL RC SYSTEM ROOT LOCUS
REVISED MODEL ACTUATOR
(ω_n = 300 rps, ζ = 0.4)

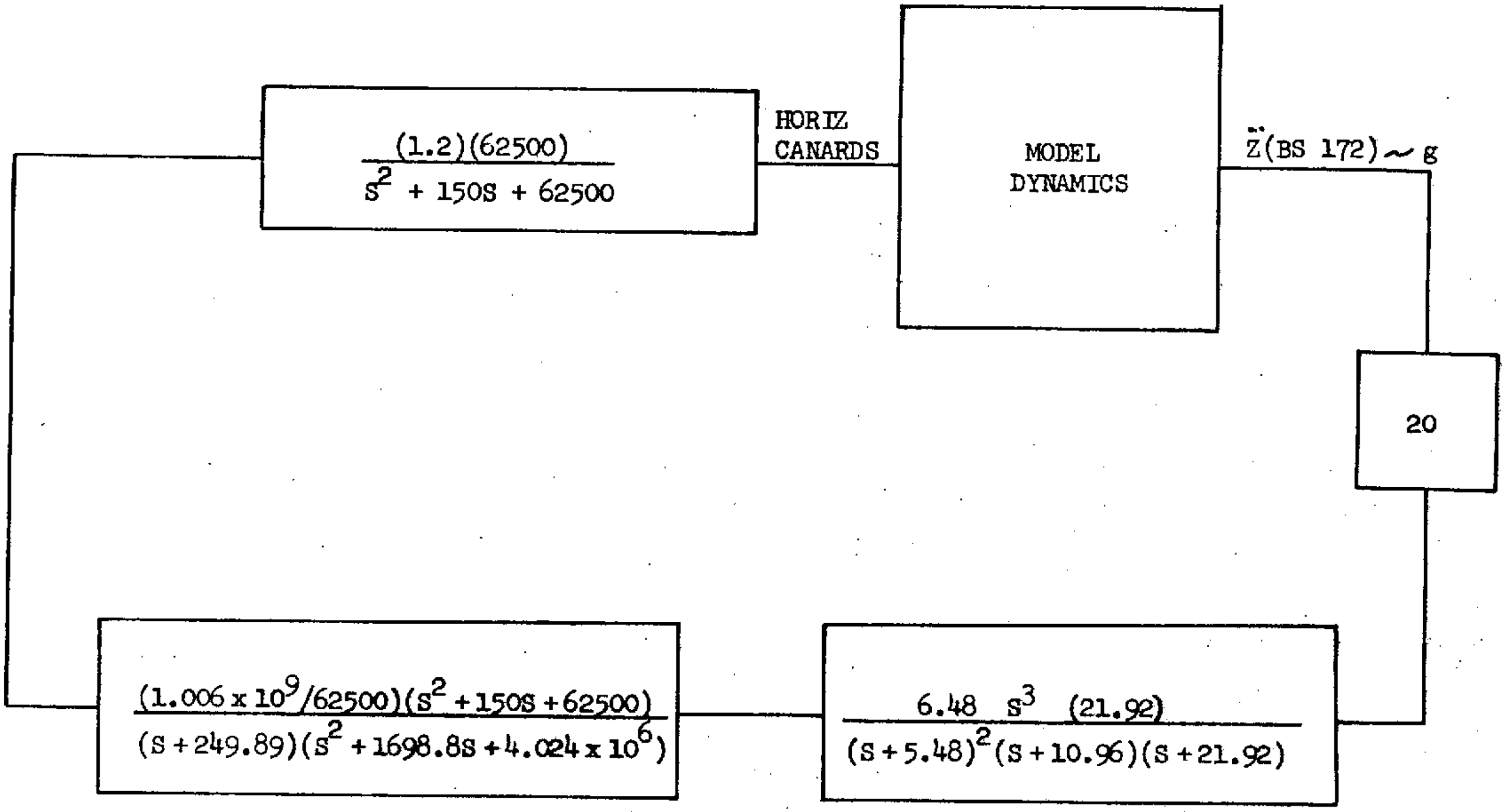

FIGURE 3.18: MODEL RC SYSTEM BLOCK DIAGRAM

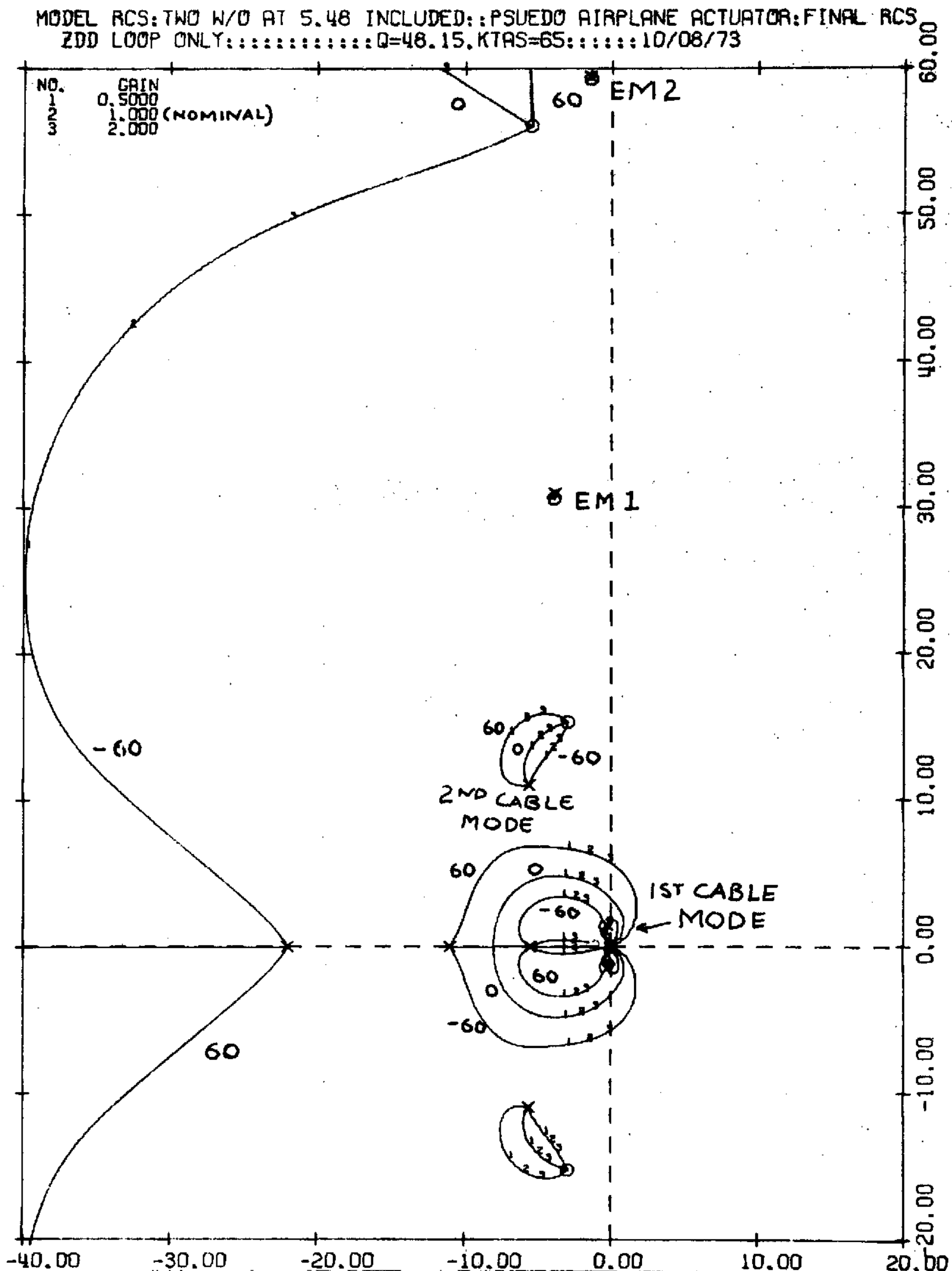

FIGURE 3.19(a): MODEL RC SYSTEM GAIN/PHASE ROOT LOCUS
PSEUDO AIRPLANE ACTUATOR DYNAMICS

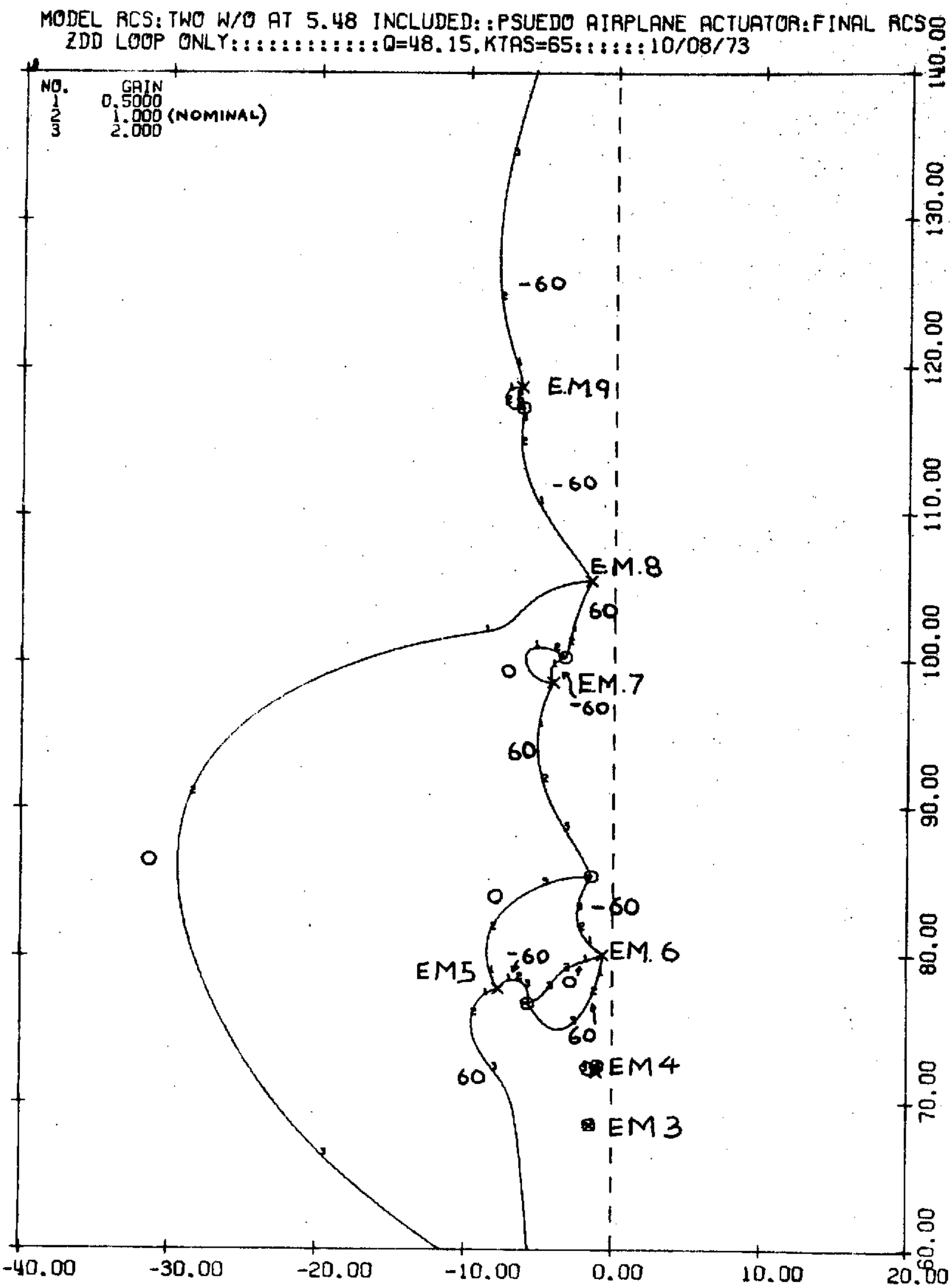

FIGURE 3.19(b): MODEL RC SYSTEM GAIN/PHASE ROOT LOCUS
PSEUDO AIRPLANE ACTUATOR DYNAMICS

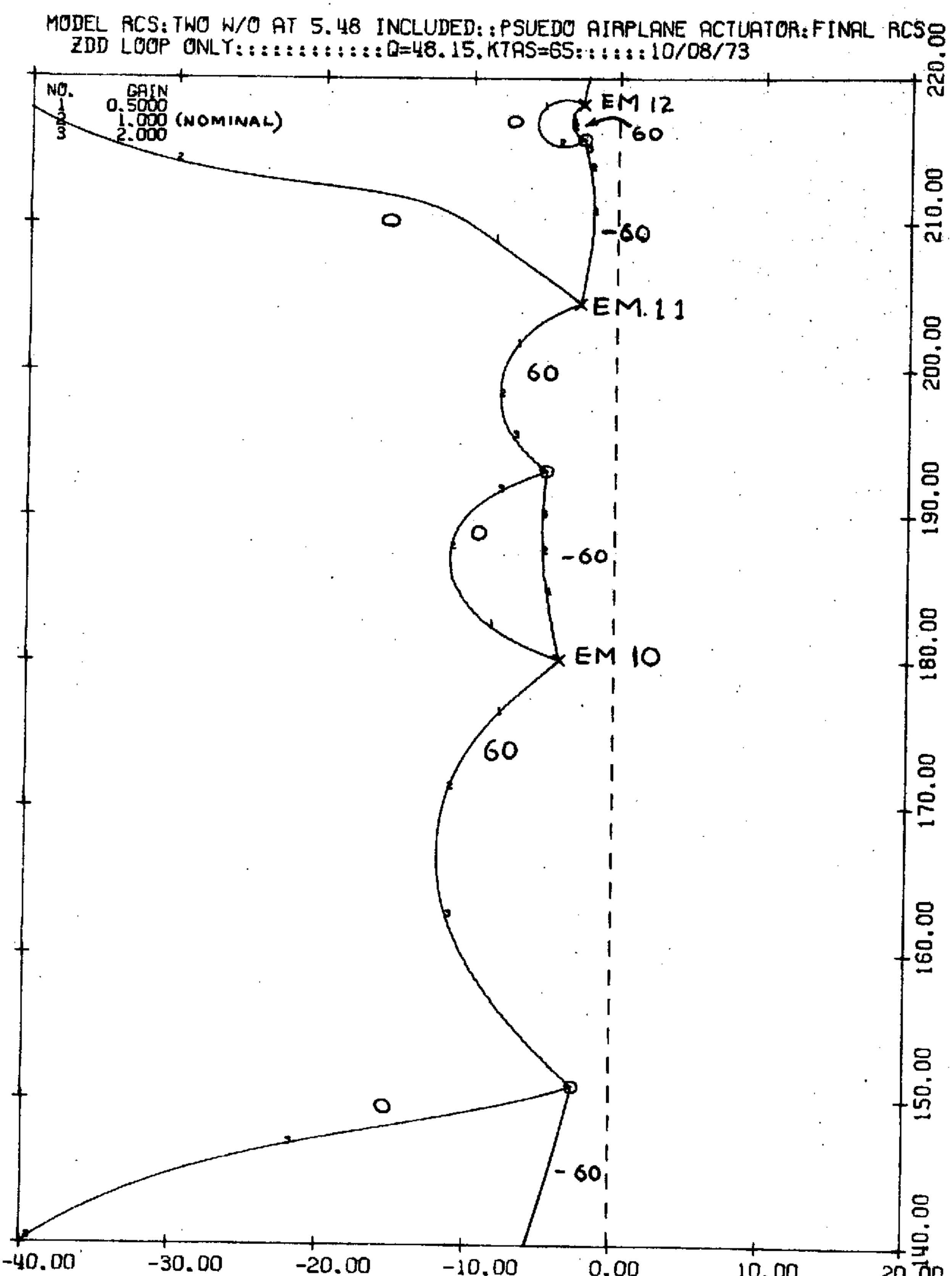

FIGURE 3.19(c): MODEL RC SYSTEM GAIN/PHASE ROOT LOCUS
PSEUDO AIRPLANE ACTUATOR DYNAMICS

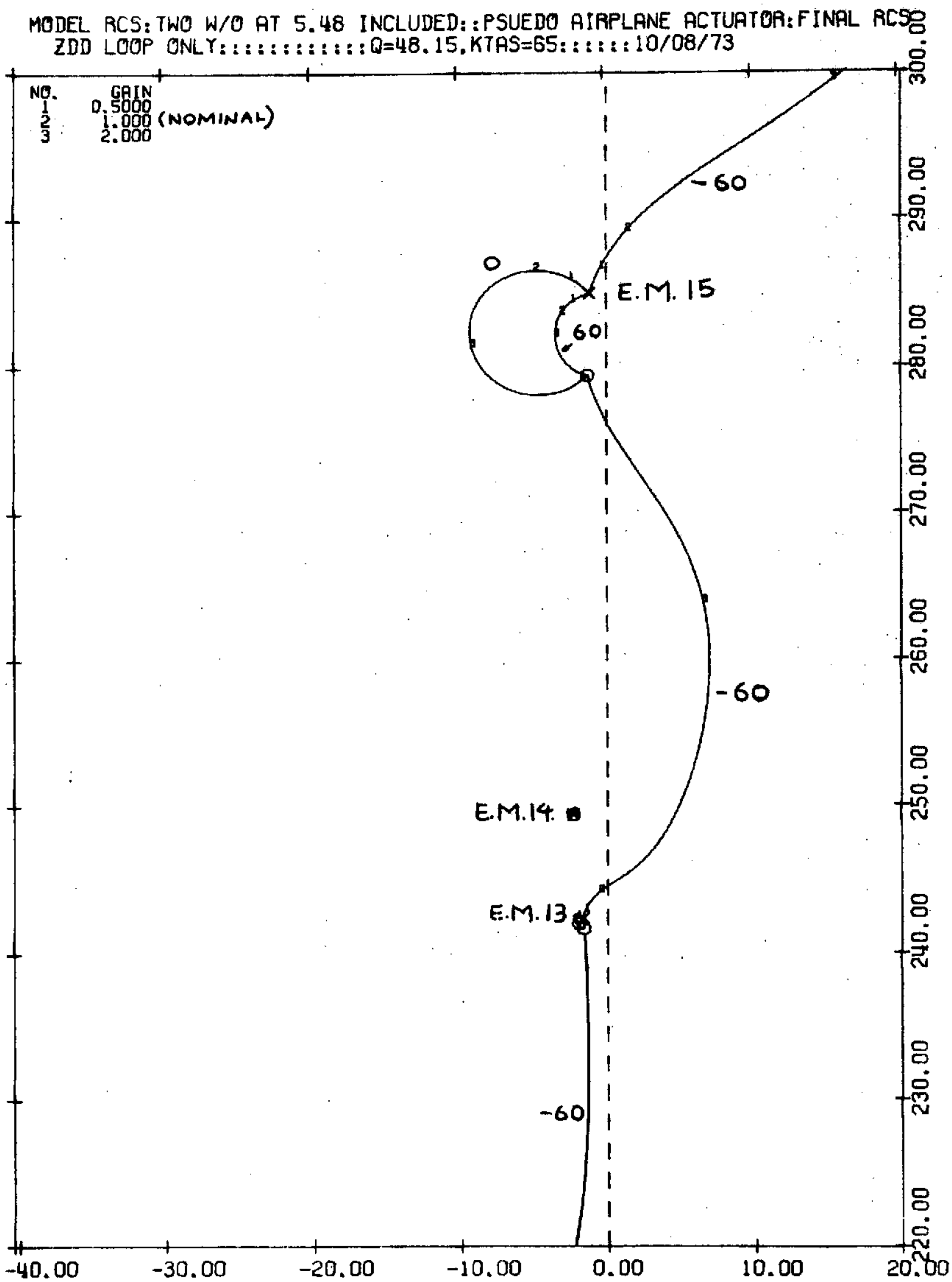

FIGURE 3.19(d): MODEL RC SYSTEM GAIN/PHASE ROOT LOCUS
PSEUDO AIRPLANE ACTUATOR DYNAMICS

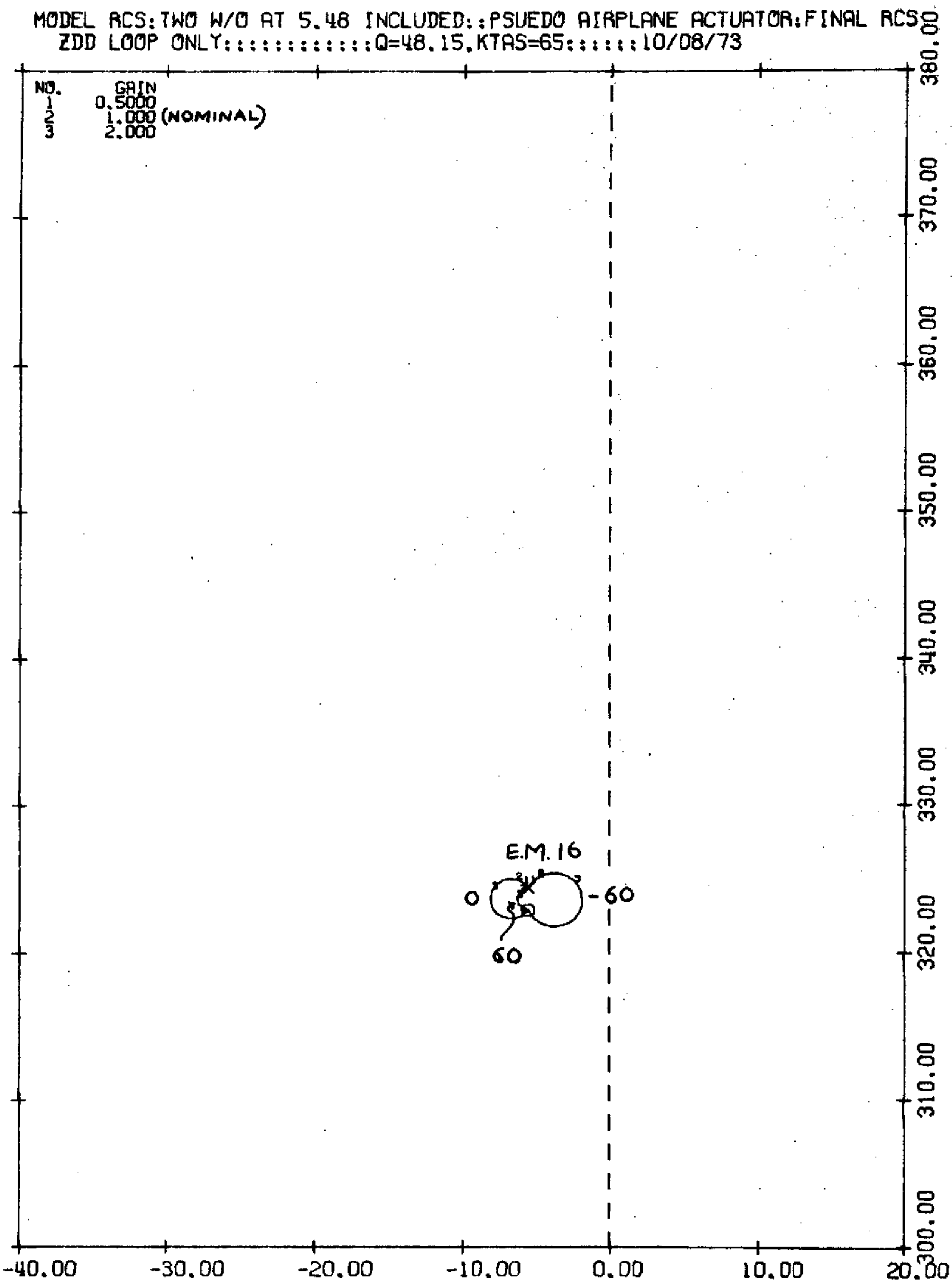

FIGURE 3.19(e): MODEL RC SYSTEM GAIN/PHASE ROOT LOCUS
PSEUDO AIRPLANE ACTUATOR DYNAMICS

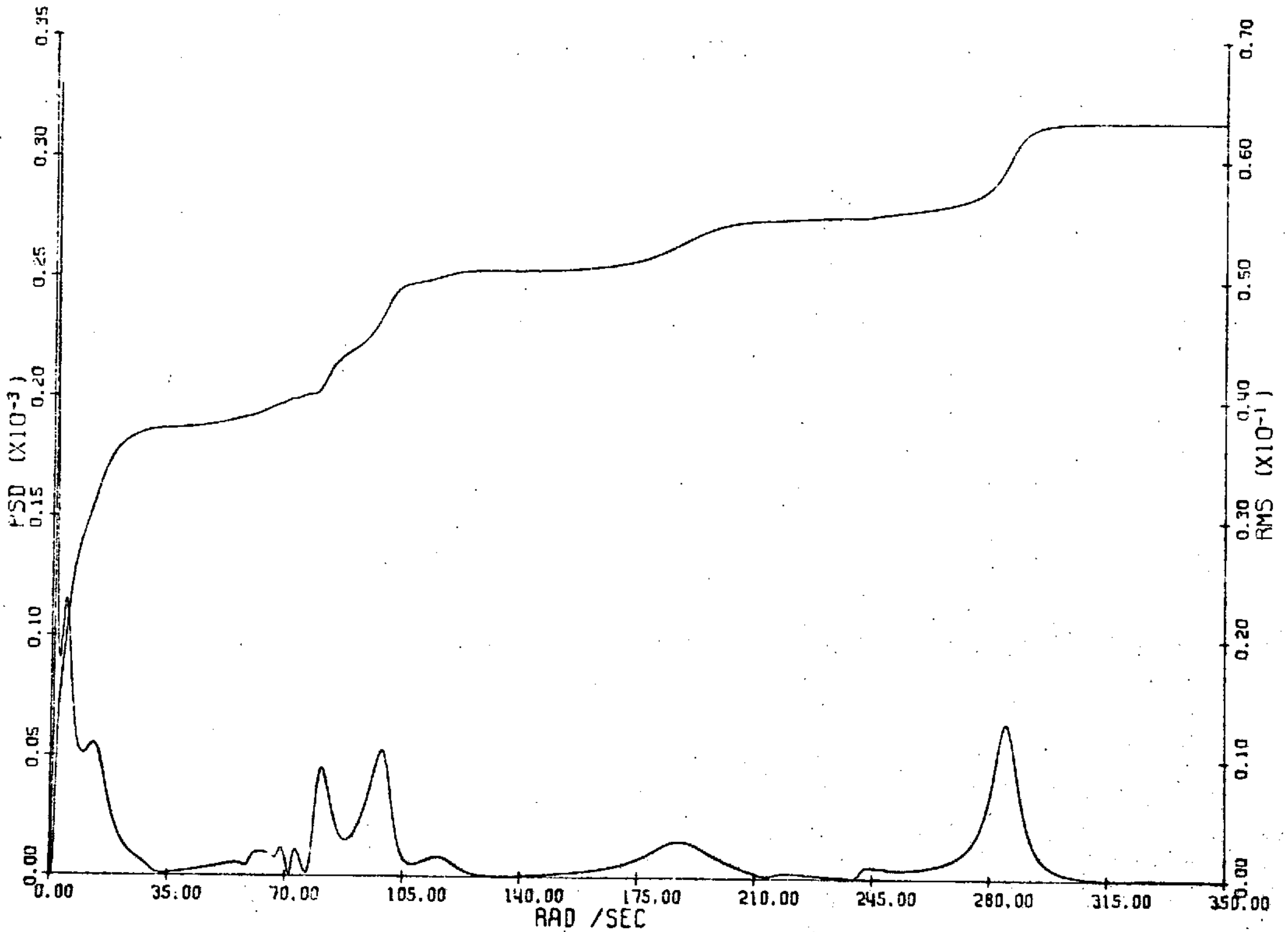

FIGURE 3.20: CLOSED LOOP MODEL $\ddot{Z}$(BS 172)/GUST PSD-RMS

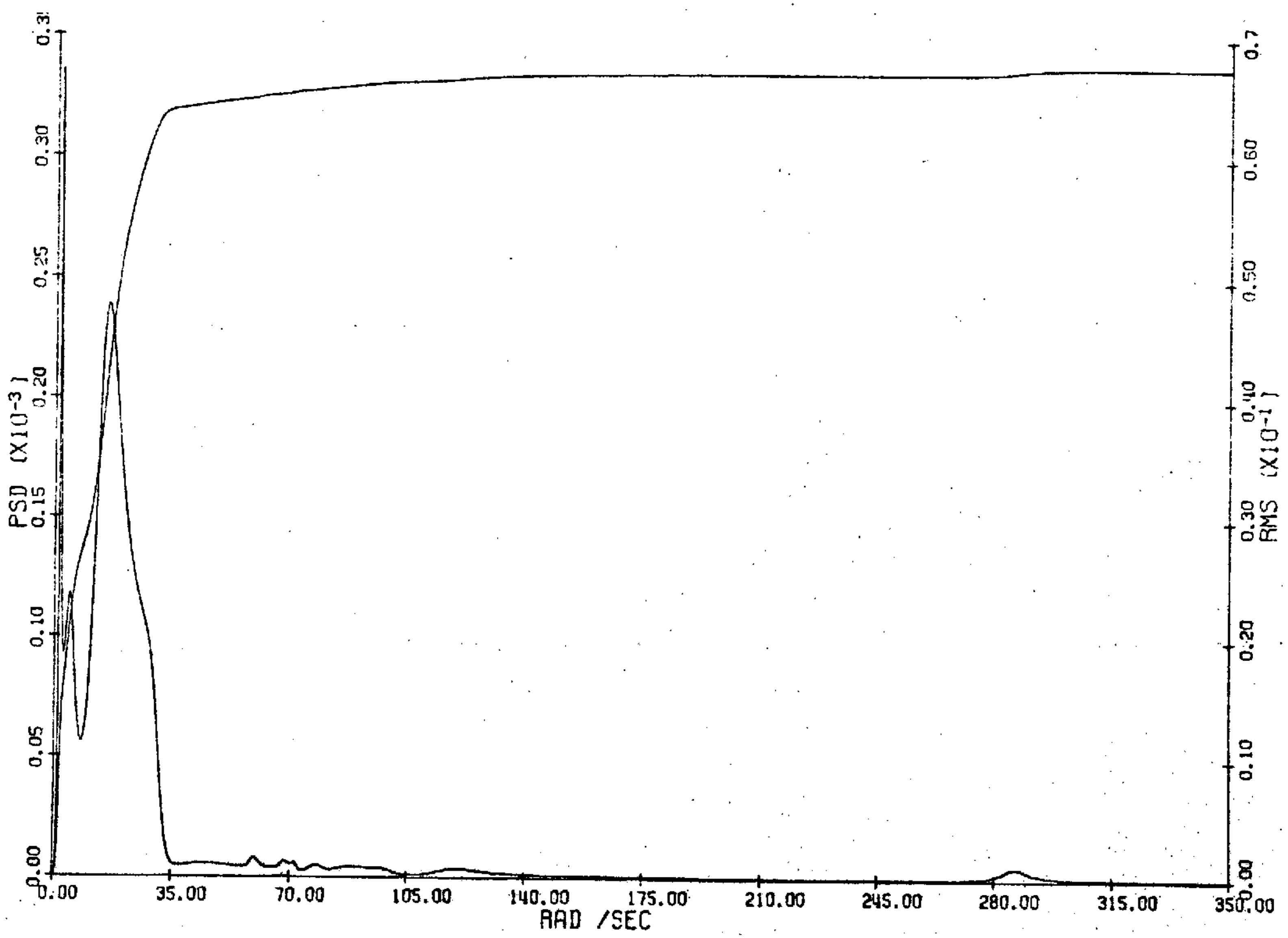

FIGURE 3.21: CLOSED LOOP MODEL $\ddot{Z}$(BS 805)/GUST PSD-RMS

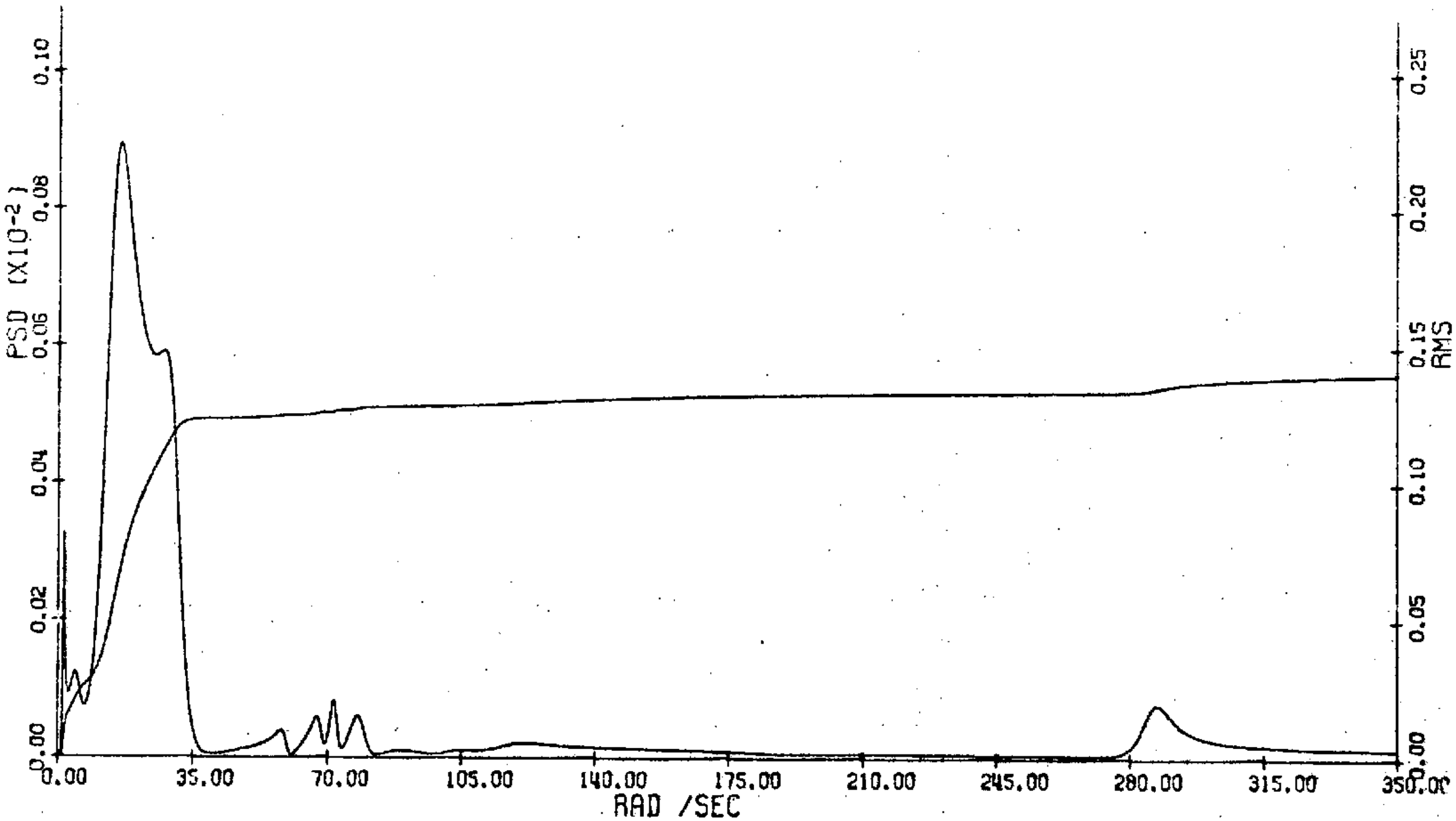

FIGURE 3.22: CLOSED LOOP MODEL $\ddot{Z}$(BS 1655)/GUST PSD-RMS

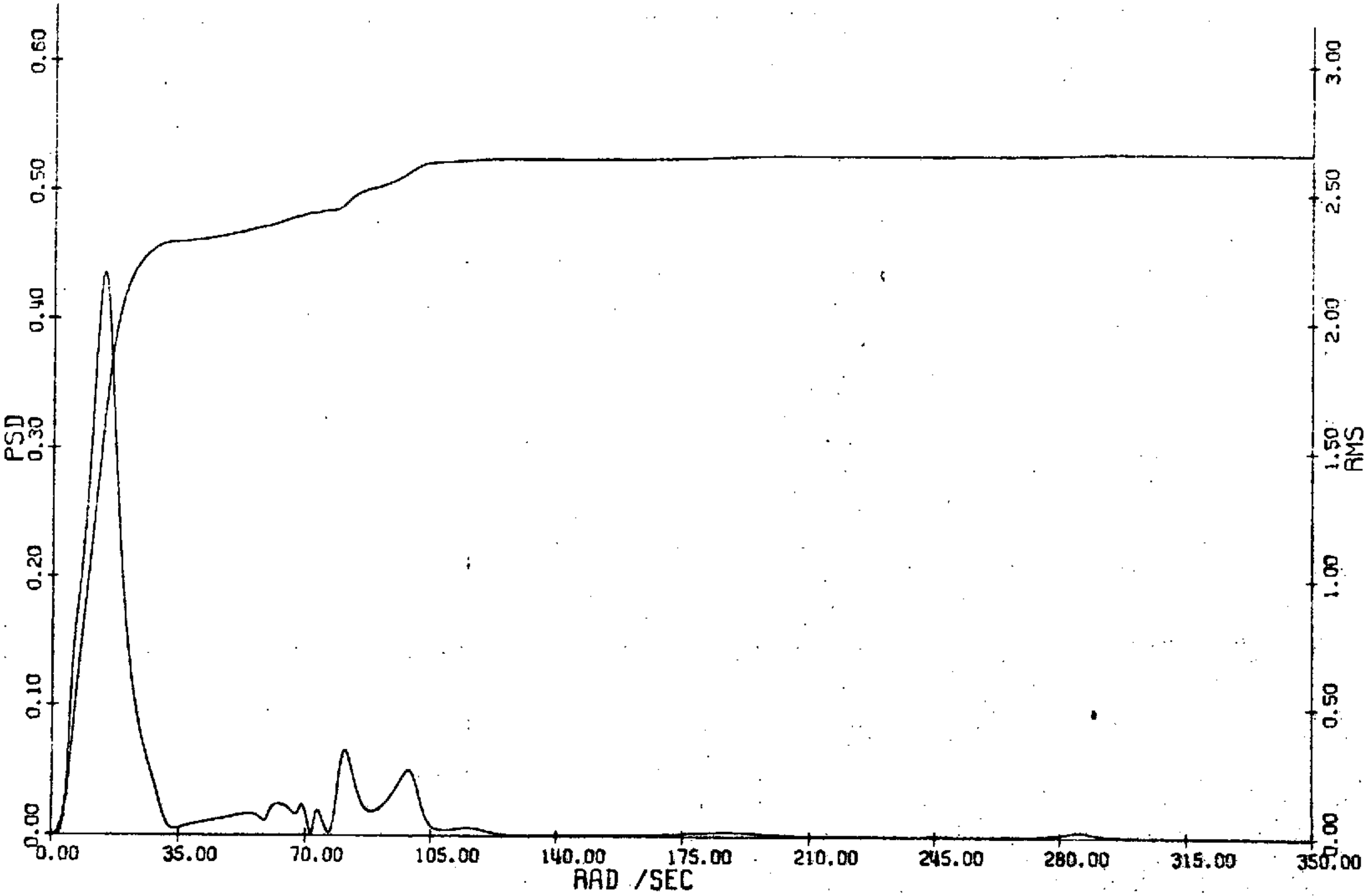

FIGURE 3.23: MODEL RC SYSTEM CANARD DISPLACEMENT PSD-RMS

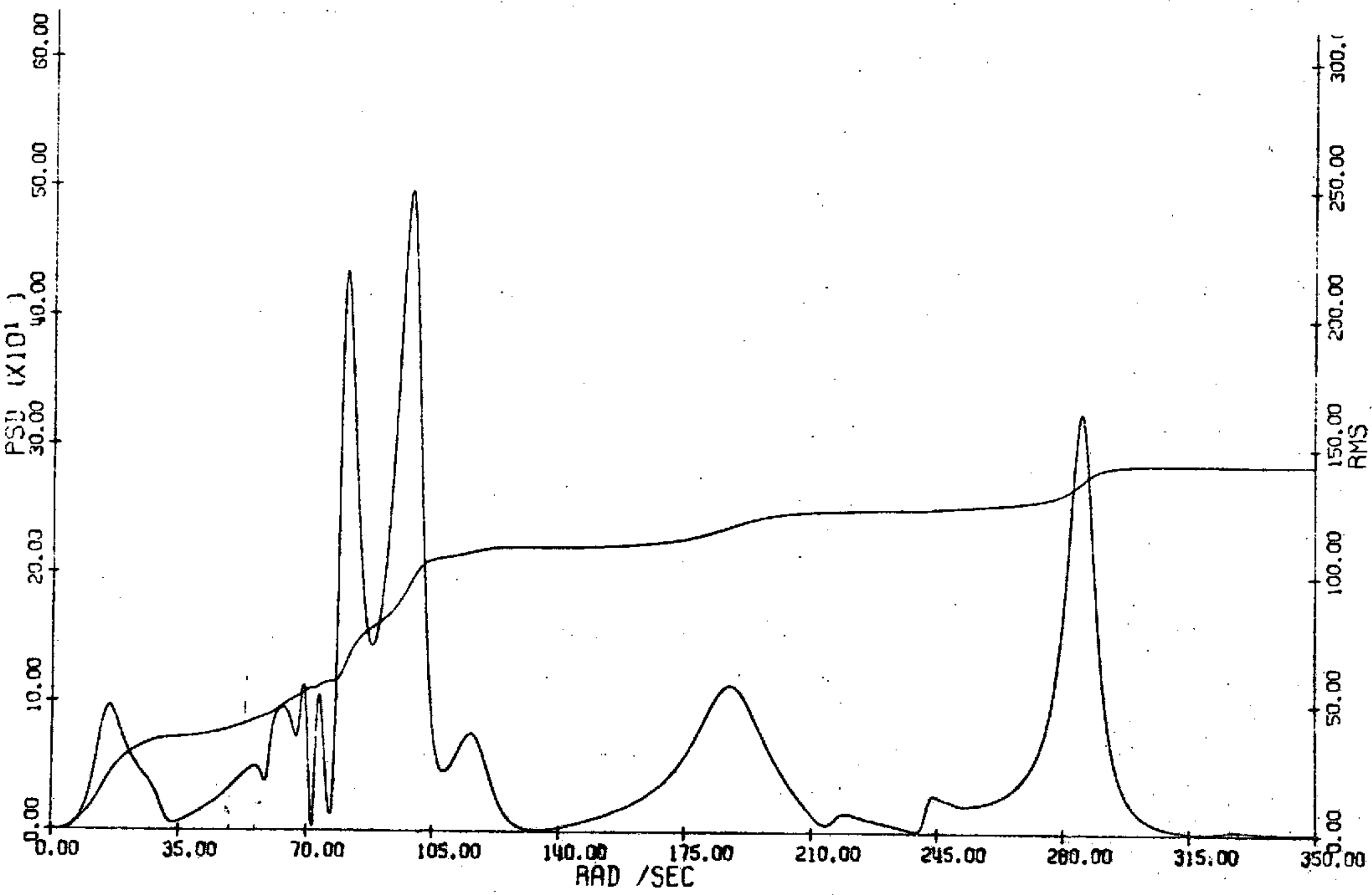

FIGURE 3.24: MODEL RC SYSTEM CANARD RATE PSD-RMS

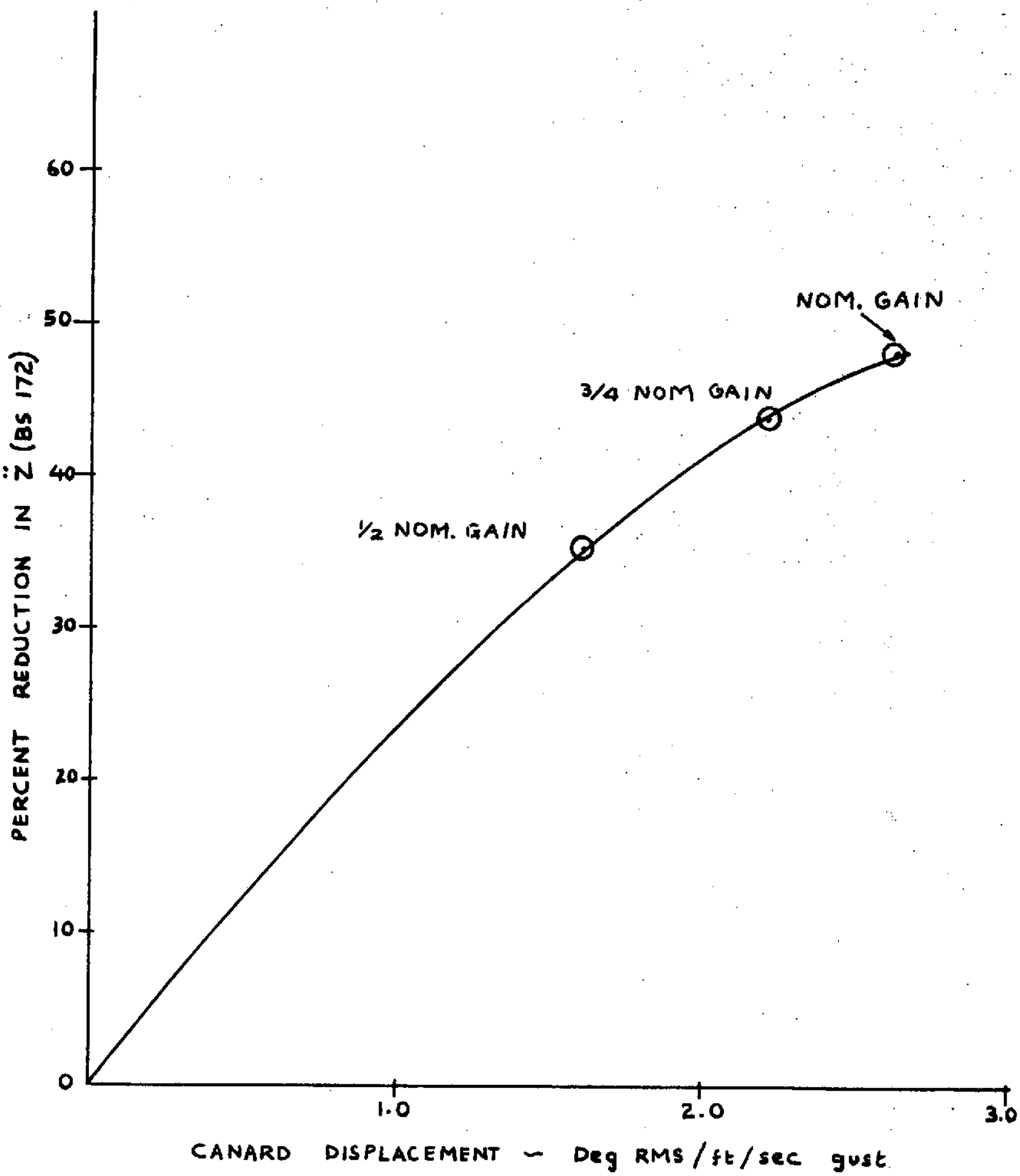

FIGURE 3.25: EFFECTS OF MODEL RC SYSTEM GAIN VARIATION

3.4 Airplane and Model RC Compatibility

This section presents a comparison between the open and closed loop model and airplane characteristics. The basic airplane and model compatibility is shown by comparing the open loop characteristic roots and the PSD-RMS plots of vertical accelerations at the pilot station. The model and airplane RC system compatibility is also established by comparing system performance and the gain/phase root loci.

3.4.1 Free Airplane and Model Comparison

The airplane and model characteristic roots significant to ride quality at the pilot station are listed in Table 3-IV. The model rigid body dynamics include effects of cable mass, tension and aerodynamic drag. The cable attach point effects on the model pitch degree-of-freedom are also included. As shown by the characteristic roots, some differences occur in the rigid body dynamics of the "free-flying" airplane and the model suspended from cables in the wind tunnel. Frequencies of the airplane and model elastic modes are almost identical, but damping ratios of the model roots are somewhat lower than the airplane.

TABLE 3-IV

COMPARISON OF BASIC AIRPLANE AND MODEL CHARACTERISTIC ROOTS

Mode	Airplane	Model	
		Model Scale	Airplane Scale
RB	-0.00187 ± j 0.0992	-0.2 ± j 1.51	-0.0365 ± j 0.2755
RB	-1.526 ± j 1.182	-5.55 ± j 11.0	-1.013 ± j 2.0
EM6	-0.1127 ± j 14.54	-0.672 ± j 80.0	-0.1226 ± j 14.61
EM8	-0.238 ± j 19.4	-1.547 ± j 105.5	-0.282 ± j 19.25
EM10	-1.239 ± j 32.96	-0.376 ± j 180.12	-0.686 ± j 32.87
EM11	-0.9138 ± j 39.58	-2.54 ± j 204.6	-0.462 ± j 37.33
EM16	-1.8 ± j 58.22	-1.19 ± j 285.0	-0.217 ± j 52.0

The PSD-RMS plots of the airplane and model accelerations given in Figures 3.3 and 3.13 indicate similar airplane/model dynamic responses to the atmospheric turbulence. Figure 3.26 compares open loop airplane and model accelerations contributed by the elastic modes in 6.4 - 25, 25 - 43, and 43 - 80 rad/sec frequency ranges. Total acceleration at the pilot station is 0.0265 g RMS/ft/sec gust for the airplane as compared to 0.0222 g RMS/ft/sec gust for the model (airplane scale).

Comparing the characteristic roots and the PSD-RMS plots show that the basic airplane and model are compatible.

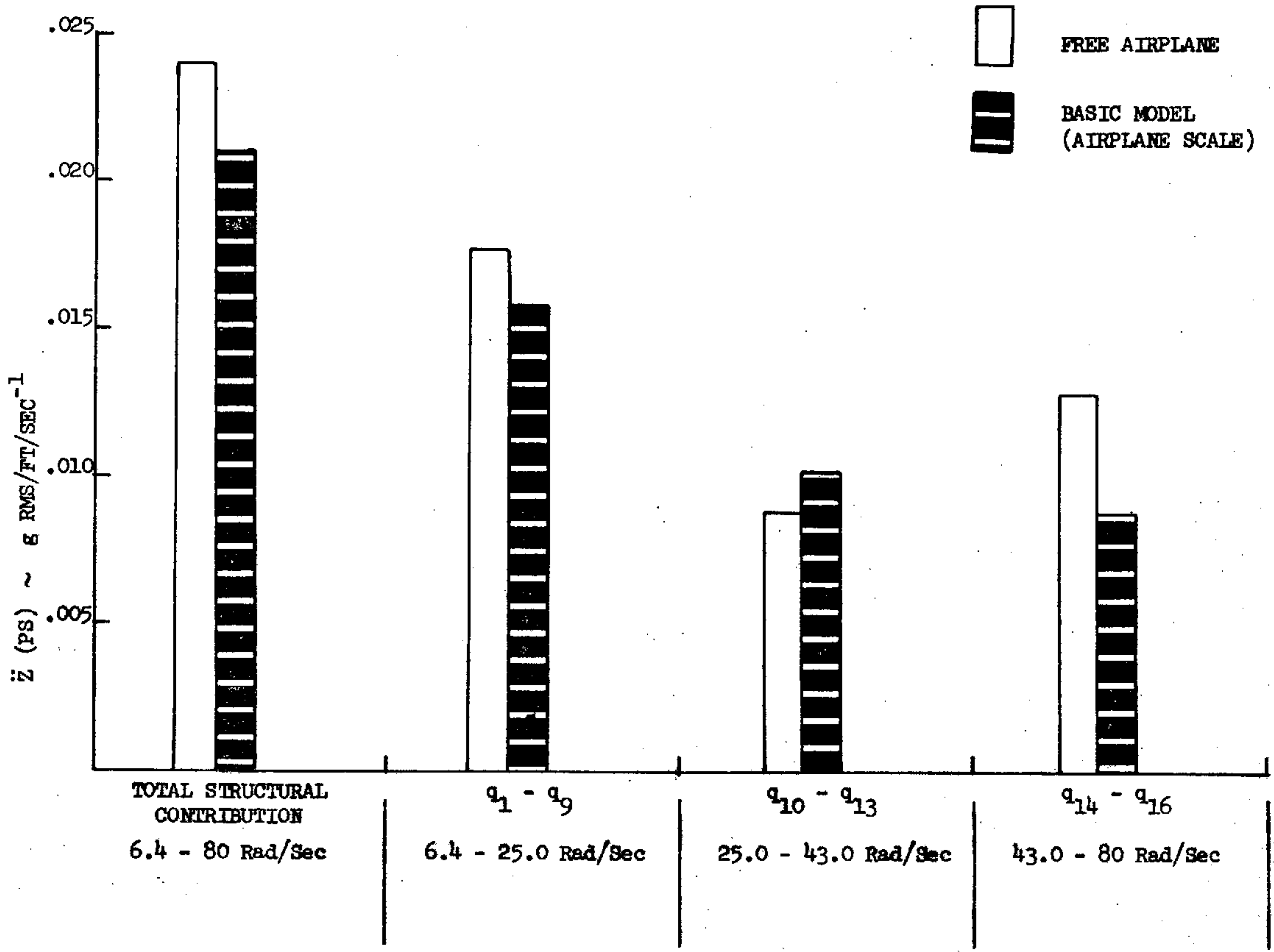

FIGURE 3.26: COMPARISON OF OPEN LOOP AIRPLANE AND MODEL PILOT STATION ACCELERATION

3.4.2 Comparison of Airplane and Model RC Systems

The model RC system uses pseudo airplane actuator dynamics and, therefore, the system provides feedback compensation similar to the airplane system. As shown by the gain/phase root loci in Figures 3.7(a) - 3.7(d) and 3.19(a) - 3.19(e), the feedback gain and phase have the same effects on the airplane and model characteristic roots.

Figure 3.27 shows a comparison of the augmented airplane and model accelerations contributed by the elastic modes in 6.4 - 25, 25 - 43, and 43 - 80 rad/sec frequency ranges. Also, the horizontal canard displacements required for satisfactory operation of the airplane and model RC systems are shown in Figure 3.28. The model data in Figures 3.27 and 3.28 are given in airplane scale. Table 3-V contains a comparison summary of the airplane and model accelerations with RCS off and on, and horizontal canard requirements for the two RC system operations.

TABLE 3-V

AIRPLANE/MODEL RCS SUMMARY

	Acceleration at BS172 g RMS/FT/SEC^{-1}		Canard Displancement	Canard Rate Deg/Sec
	Open Loop	Closed Loop	DEG RMS/FT/SEC^{-1}	RMS/FT/SEC^{-1}
Airplane	0.0265	0.0183	0.724	7.51
Model	0.1223	0.0632	2.66	143.6
Ratio Model/Airplane	4.62	3.45	3.67	19.12
Scale Factors Model/Airplane	5.48	5.48	5.48	30.00

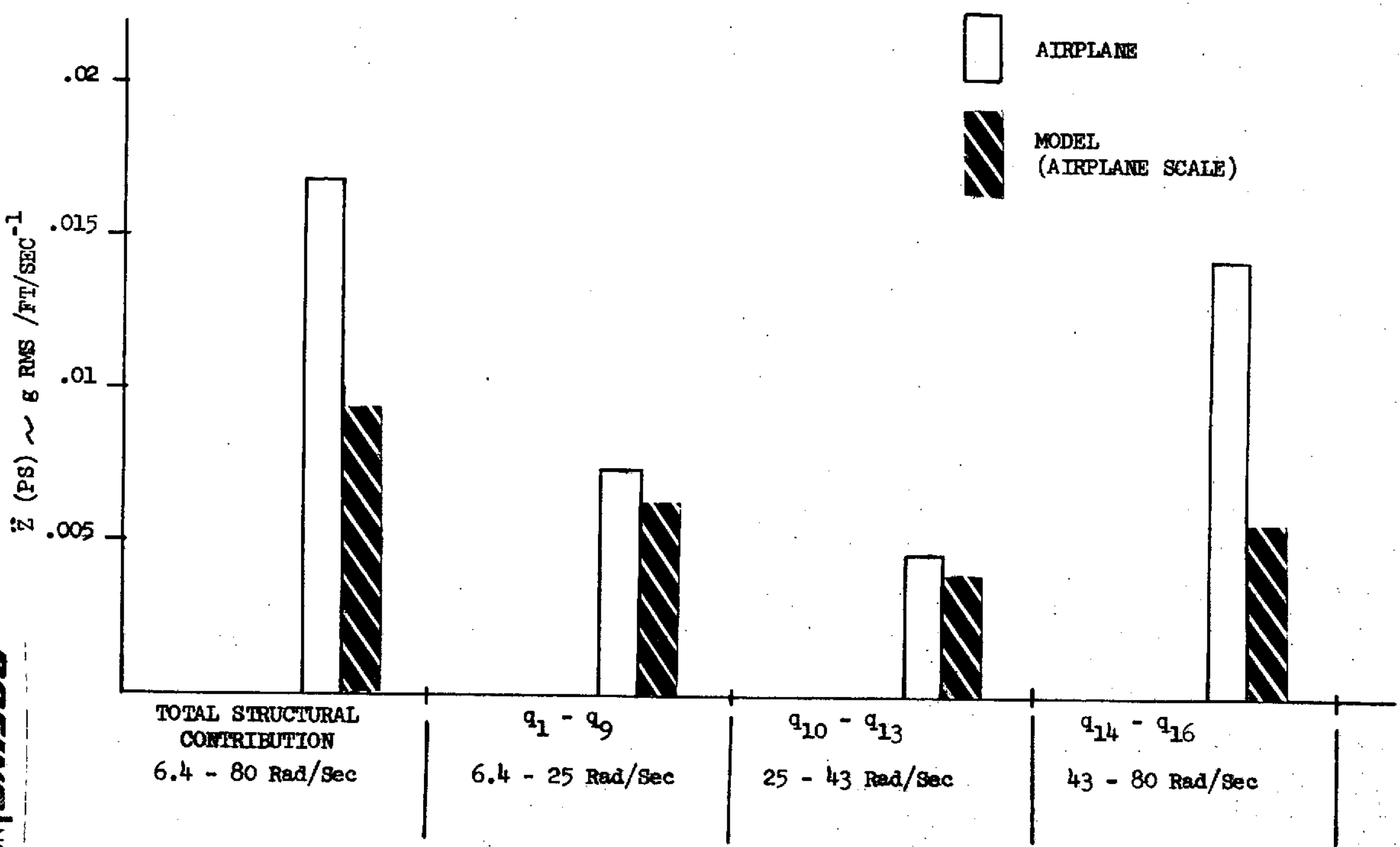

FIGURE 3.27: COMPARISON OF CLOSED LOOP AIRPLANE AND MODEL PILOT STATION ACCELERATION

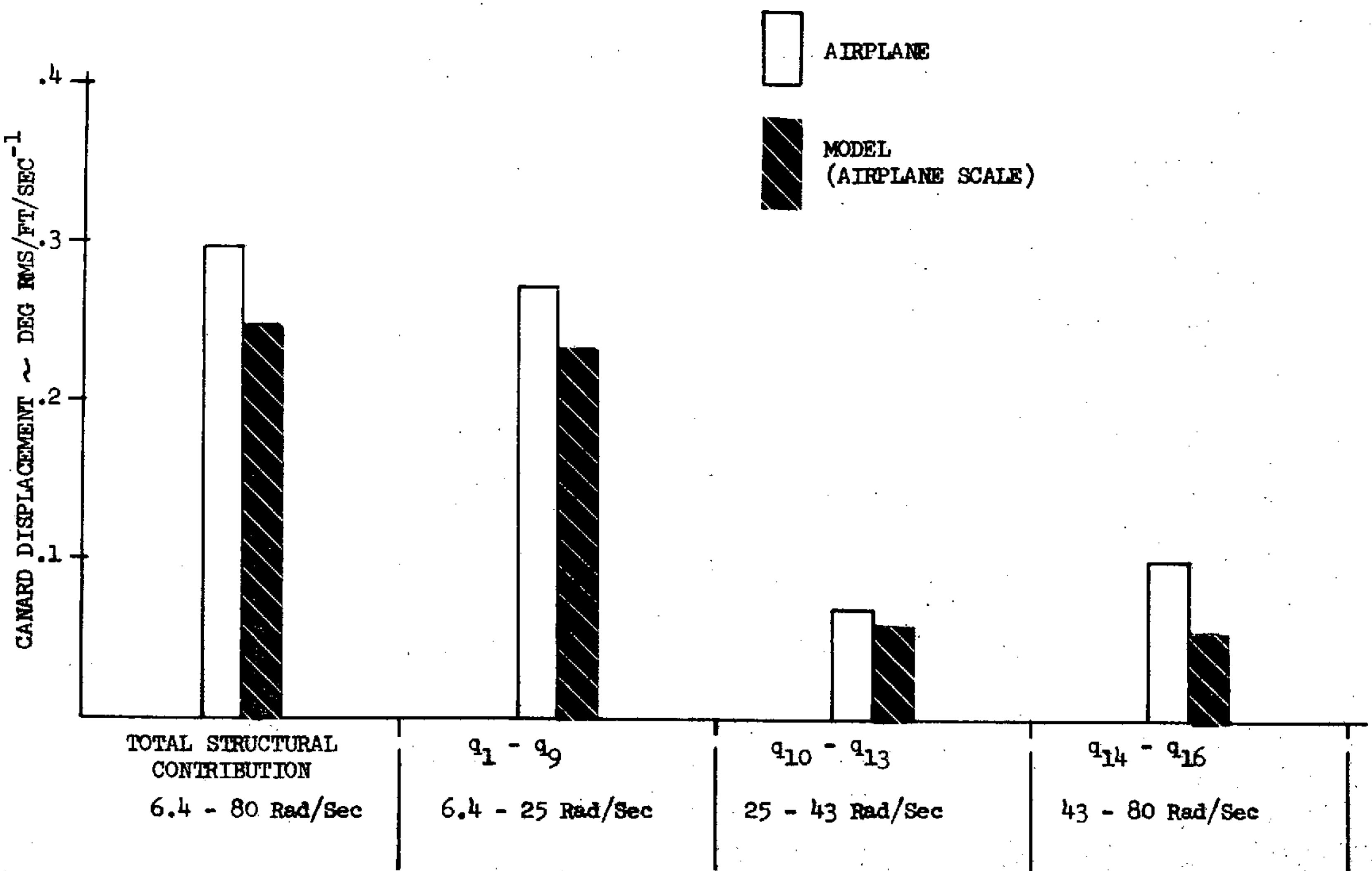

FIGURE 3.28: COMPARISON OF AIRPLANE AND MODEL CANARD DISPLACEMENT REQUIREMENTS

3.5 Model Horizontal Canard Mechanization

The B-52 aeroelastic model was modified to add an electromechanical actuation system for horizontal canards. Components for the system were selected to meet performance criteria dictated by the two ride control systems to be tested. The torque motor, potentiometer and tachometer were integrated into a compact package to mount in the model fuselage near the canard surfaces at the model equivalent pilot station. Actuation system performance was verified through dynamic testing with the system installed in the model.

3.5.1 Performance and Stability Requirements

Actuation system requirements were established to insure dynamic performance to control model elastic modes up to 25 Hz. The desired performance and stability are summarized below:

- System frequency response shall not exceed three dB attenuation and 45 degrees phase lag at 25 Hz for three degree amplitude sinusoidal command.
- The motor-load resonance (dominant second order) shall have a nominal damping ratio of 0.3.
- System shall be capable of producing at least 6 degrees amplitude up to 20 Hz without power amplifier saturation.
- Canard surface deflection capability must be at least ±25 degrees.
- Peak torque at ±19 degrees deflection shall be at least 5 oz-in.
- Control surface hysteresis shall not exceed ±0.20 degrees.

The first two requirements translate into a motor-load resonance at about 250 rad/sec with 0.3 damping ratio.

3.5.2 Actuation System Design

Electromechanical components were selected to satisfy the performance and stability requirements. A linear analysis was then conducted to evaluate performance of the components selected using estimated surface inertia and hinge moment loads. Parts were designed and fabricated to install the actuation system in an area made available by removing the model data system components in the forward fuselage.

3.5.2.1 Component Selection

Characteristics of the components selected for the actuation system are presented in Table 3-VI, as summarized from manufacturers' specifications. An Aeroflex Laboratories, Inc., TQ18-7H torque motor driven by a TA-42DC power amplifier was selected as the torque source. A New England Instruments 78ESB102 poten-

TABLE 3-VI

CANARD ACTUATION SYSTEM DESIGN VALUES

DESCRIPTION	SYMBOL	VALUES	UNITS
1. Torque Motor, TQ18-7H			
Armature Resistance	R_a	48.0	ohms
Torque Sensitivity	K_i	15.0	in-oz/amp
Motor Inertia	J_M	6.7×10^{-4}	in-oz-sec^2
Viscous Damping	D	.0331	$\frac{\text{in-oz}}{\text{rad/sec}}$
Electrical Time Constant	τ_a	2×10^{-4}	sec
Torque Output, Continuous	T	8.0	in-oz
2. Power Amplifier, TA-42DC			
Output (Maximum)	V_a(max)	22	VDC
Voltage Gain	K_a	10.0	volt/volt
Rated Load	--	12.0	ohms
3. Tachometer, TG10Y-5H			
Output Sensitivity	--	.18	$\frac{\text{Volt}}{\text{rad/sec}}$
Rotor Inertia	J_T	4×10^{-5}	in-oz-sec^2
4. Potentiometer, 78ESB102			
Resistance	--	1000	ohms
Electrical Angle		340	deg
5. Canard Surfaces			
Estimated Inertia (Including Linkage)	J_L	4×10^{-4}	in-oz-sec^2
Estimated Hinge Moment	K_L	0.15	in-oz/deg

tiometer was chosen to provide torque motor shaft angular position feedback signal with an Aeroflex TG10Y-5H tachometer providing rate feedback required for stability.

The linearized electromechanical equations of motion for a d.c. torque motor driving an inertia load have been derived previously (see Reference 2). The transfer function of motor shaft angular deflection due to amplifier voltage is:

$$\frac{\theta_M}{V_A}(s) = \frac{57.3\, K_T / \tau_a (J_M + J_L) \quad \text{DEG/VOLT}}{s^3 + \frac{1}{\tau_a} s^2 + \frac{\tau_a K_L + D}{\tau_a (J_M + J_L)} s + \frac{K_L}{\tau_a (J_M + J_L)}}$$

where $K_T = \frac{K_i}{RA} = 0.3125$ in-oz/volt, and the other symbols are explained in Table 3-VI. This transfer function is formed assuming rigid linkage between the shaft and the surfaces and negligible friction. With component values from Table 3-VI, this transfer function becomes:

$$\frac{\theta_M}{V_A}(s) = \frac{7.006 \times 10^7 \quad \text{DEG/VOLT}}{s^3 + 5000\, s^2 + 1.295 \times 10^5\, s + 1.024 \times 10^4}$$

The system block diagram is shown in Figure 3.29.

The closed loop transfer function $\frac{\theta_M}{V_c}$ can be easily formed using block diagram algebra.

$$\frac{\theta_M}{V_c}(s) = \frac{7.006 \times 10^8 \quad \text{DEG/VOLT}}{s^3 + 5000\, s^2 + (1.295 \times 10^5 + 7.006 \times 10^8 K_R)\, s + (1.024 \times 10^4 + 7.006 \times 10^8 K_P)}$$

The requirements specify a dominant second order response with undamped natural frequency of 250 radians/second with 0.3 damping ratio. The gains required to produce this response can be determined by equating the closed loop characteristic polynomial in terms of open loop parameters to the polynomial in terms of desired response

$$s^3 + 5000\, s^2 + (1.295 \times 10^5 + 7.006 \times 10^8 K_R)\, s + (1.024 \times 10^4 + 7.006 \times 10^8 K_P)$$
$$= (s + a)(s^2 + 2\zeta\omega_n s + \omega_n^2) = (s + a)(s^2 + 150\, s + 6.25 \times 10^4)$$

Solving the three simultaneous equations formed by equating coefficients of like powers of S produces the three unknowns:

$K_R = 9.428 \times 10^{-4}$ volt/deg/sec, $\quad K_P = 0.433$ volt/deg,

$a = 4850$ rad/sec.

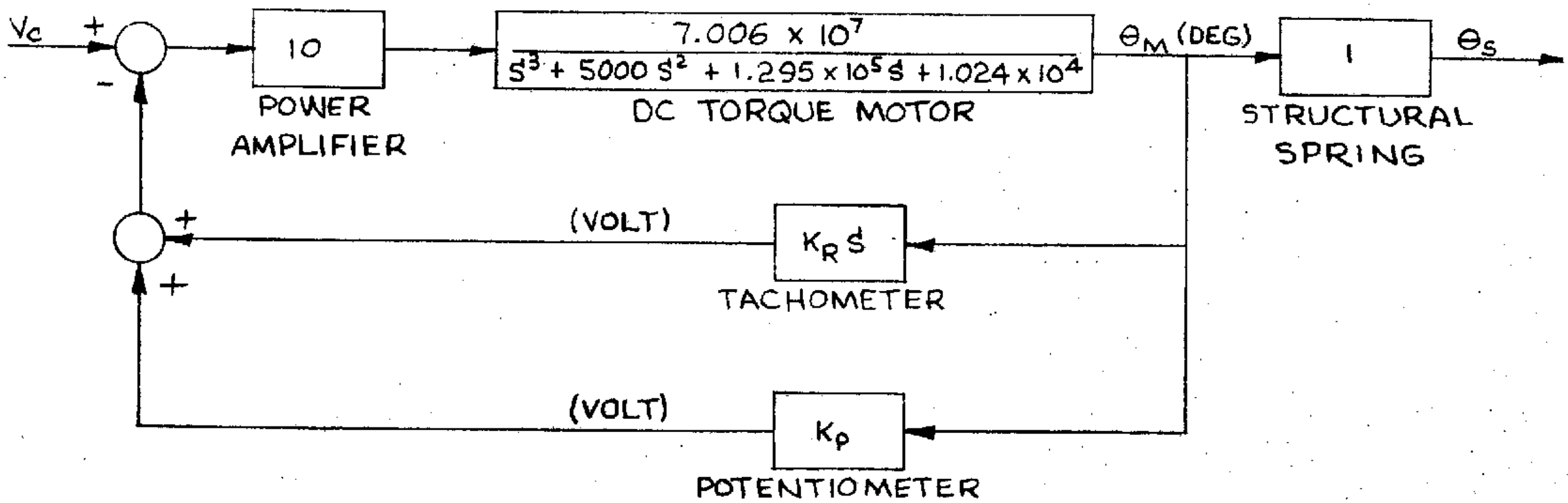

FIGURE 3.29

CANARD ACTUATION SYSTEM BLOCK DIAGRAM

The feedback gains are reasonable and can be easily attained by scaling the potentiometer and tachometer outputs on an analog computer. Using the torque motor transfer function, $\frac{\theta_M}{V_a}(S)$, the maximum amplitude attainable at 20 Hz can be estimated. Assuming pure sinusoidal motion, the transfer function can be written as

$$\frac{\theta_M}{V_a}(\omega) = \frac{7.006 \times 10^7 \text{ VOLT/DEG}}{(j\omega)^3 + 5000(j\omega)^2 + 1.295 \times 10^5 (j\omega) + 1.024 \times 10^4}$$

and taking the amplitude only

$$\left|\frac{\theta_M}{V_a}(\omega)\right| = \frac{7.006 \times 10^7 \text{ VOLT/DEG}}{[(1.024 \times 10^4 - 5000\omega^2)^2 + (1.295 \times 10^5 \omega - \omega^3)^2]^{\frac{1}{2}}}$$

At 20 Hz this ratio is

$$\left|\frac{\theta_M}{V_a}(2\pi \times 20)\right| = .874 \text{ DEG/VOLT}$$

The power amplifier saturates at 22 volts, so the maximum amplitude attainable at 20 Hz is

$$\theta_{M_{M(x)}}(20 \text{ Hz}) = (.874)(22) \text{ DEG} = 19.23 \text{ DEG}$$

Thus, the amplitude capability is more than required.

The analytical evaluation of the components selected indicates that the desired performance can be attained. Actual feedback gains required and actuation system performance were established through dynamic testing of the system installed in the model.

3.5.2.2 System Installation

A photograph of the canard actuation system installed in the model is shown in Figure 3.30. The model fuselage shell is removed in this photograph. The canard surface shafts are located at Body Station 5.73 and Water Line 5.43, equivalent to the canard location on the CCV airplane. Canard surfaces of 8.4 and 10.0 ft^2/side airplane scale were fabricated to be interchangeable. The smaller surfaces are required for the model full fuselage ride control system and the other set is used for the CCV forward body ride control system.

The surfaces, potentiometer and tachometer are driven through crank-pushrod linkages by the d.c. torque motor. The linkages were assembled with minimum friction and no perceptible mismatch between the rod ends and clevises. The

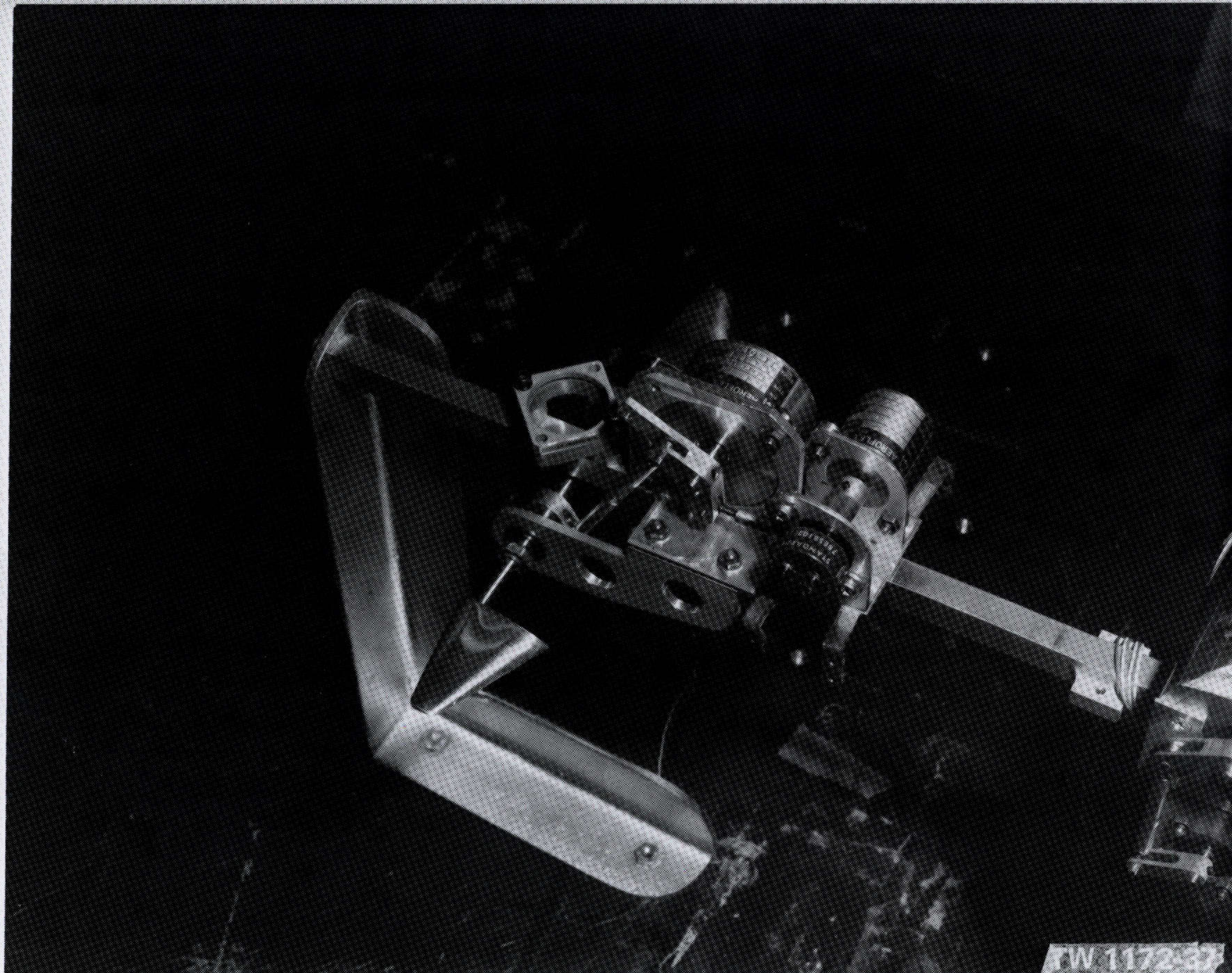

FIGURE 3.30: INSTALLED CANARD ACTUATION SYSTEM

surfaces are installed with the forward fuselage shell in place. The $\frac{1}{4}$-inch precision shaft is bored on each end to accept the surface shafts. The ends of this shaft are slotted and threaded so that as the locknuts are tightened the surface shafts are clamped inside the $\frac{1}{4}$-inch shaft.

During laboratory and wind tunnel testing, feedback loops were mechanized on an EAI TR-48 analog computer. Prior to wind tunnel entry a wiring harness was installed in the model and umbilicals fabricated to connect the model hardware with the analog computer and power amplifiers located in the tunnel control room.

3.5.3 Actuation System Performance

Performance of the actuation system was determined just after installation in the model at Boeing and again with the model fully assembled immediately before the wind tunnel entry at NASA. Testing was conducted to determine system transient and frequency responses and hysteresis.

Position and rate feedback gains were set through examination of step responses. With the rate gain set to give damping below 0.05, the position gain was adjusted to give the 250 rad/sec undamped natural frequency. Then, rate gain was increased to give the 0.30 damping ratio as determined by the percent overshoot for a step command (assuming pure second order response). The final step responses are shown in Figure 3.31 for a three degree command. The external command is:

$$V_c = K_p \ \theta_c = (0.53 \ \frac{\text{Volt}}{\text{Deg}})(3 \text{ deg}) = 1.59 \text{ volts.}$$

The frequency response shown in Figure 3.32 was obtained with these feedback gains. The response indicates an undamped natural frequency of about 262 rad/sec (41.7 Hz) with 0.29 damping ratio. No attempt was made to adjust the gains to give more nearly the desired response.

Figure 3.33 shows a plot of motor angular displacement as a function of commanded displacement. This plot indicates about ±0.21 degrees hysteresis. The hysteresis was caused primarily by residual magnetism of the TQ18-7H torque motor, with friction in the rod ends, potentiometer and bearings causing the remainder. There was no perceptible backlash in the linkage so hysteresis at the surface should be the same as at the motor shaft.

NOTES: POSITION FEEDBACK GAIN 0.53 VOLT/DEG; RATE FEEDBACK GAIN 0.00128 VOLT/DEG/SEC

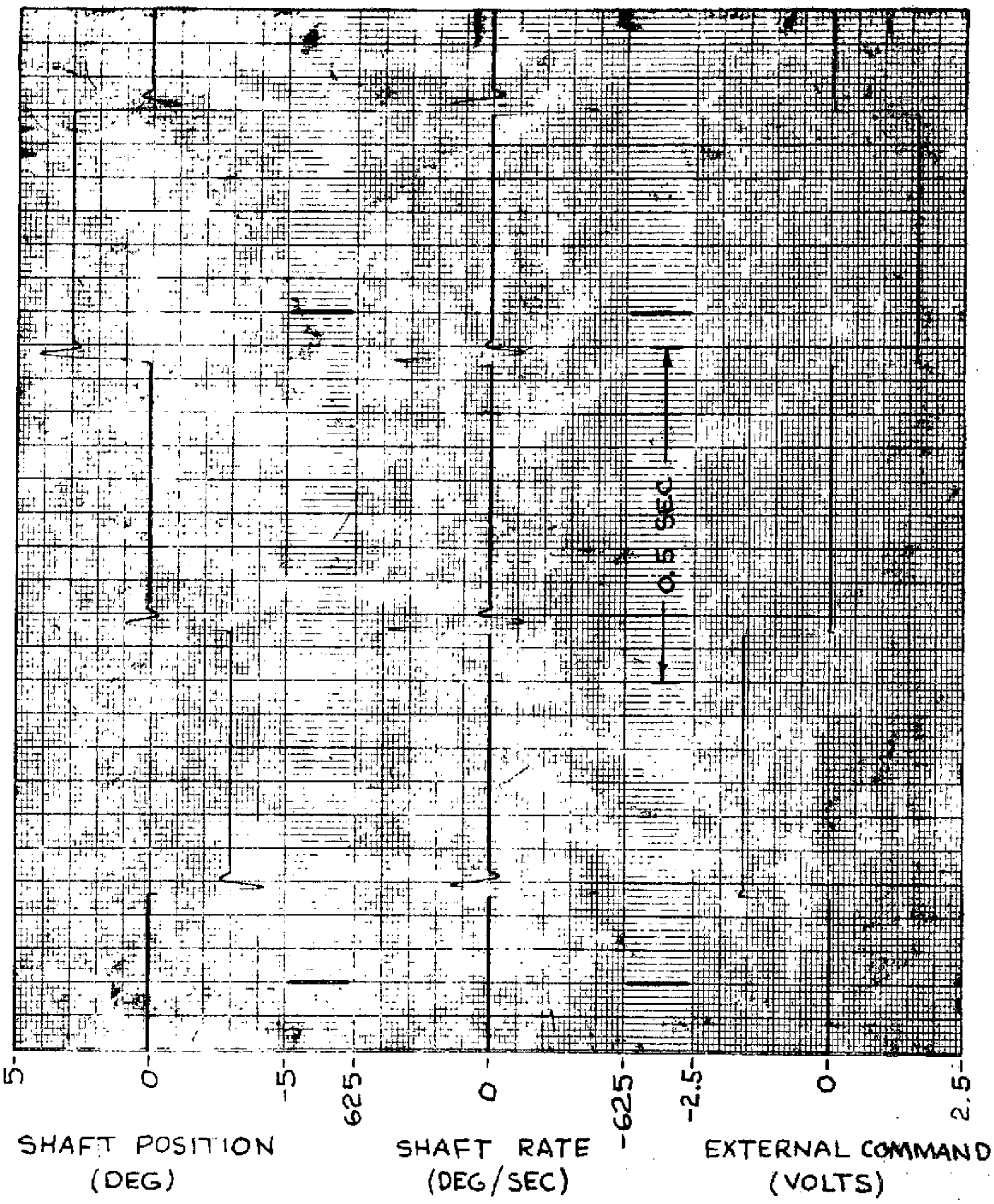

FIGURE 3.31: MODEL CANARD ACTUATION SYSTEM TRANSIENT RESPONSES

5-29-73

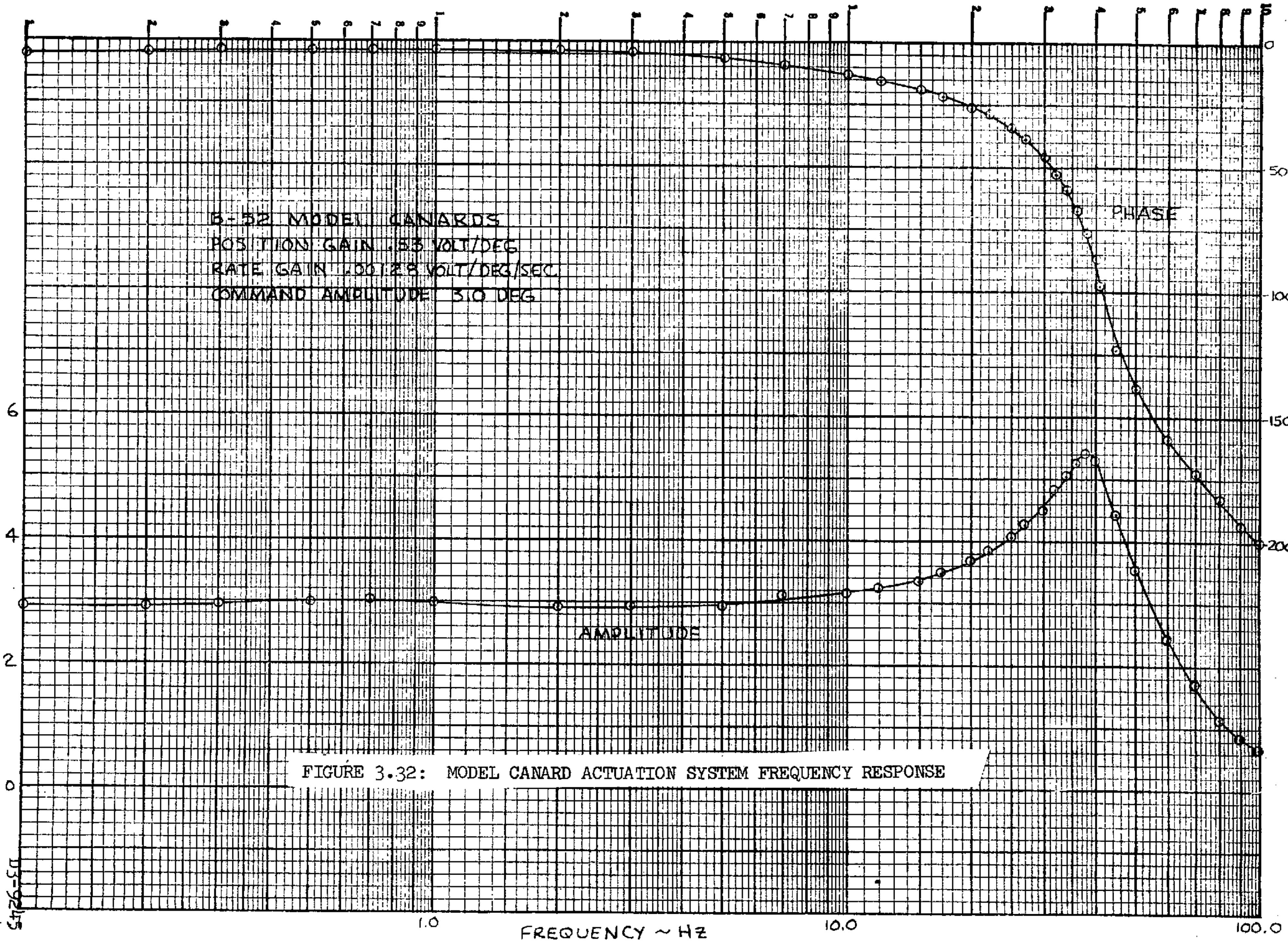

FIGURE 3.32: MODEL CANARD ACTUATION SYSTEM FREQUENCY RESPONSE

HEWLETT-PACKARD 9270 1006

5-29-73

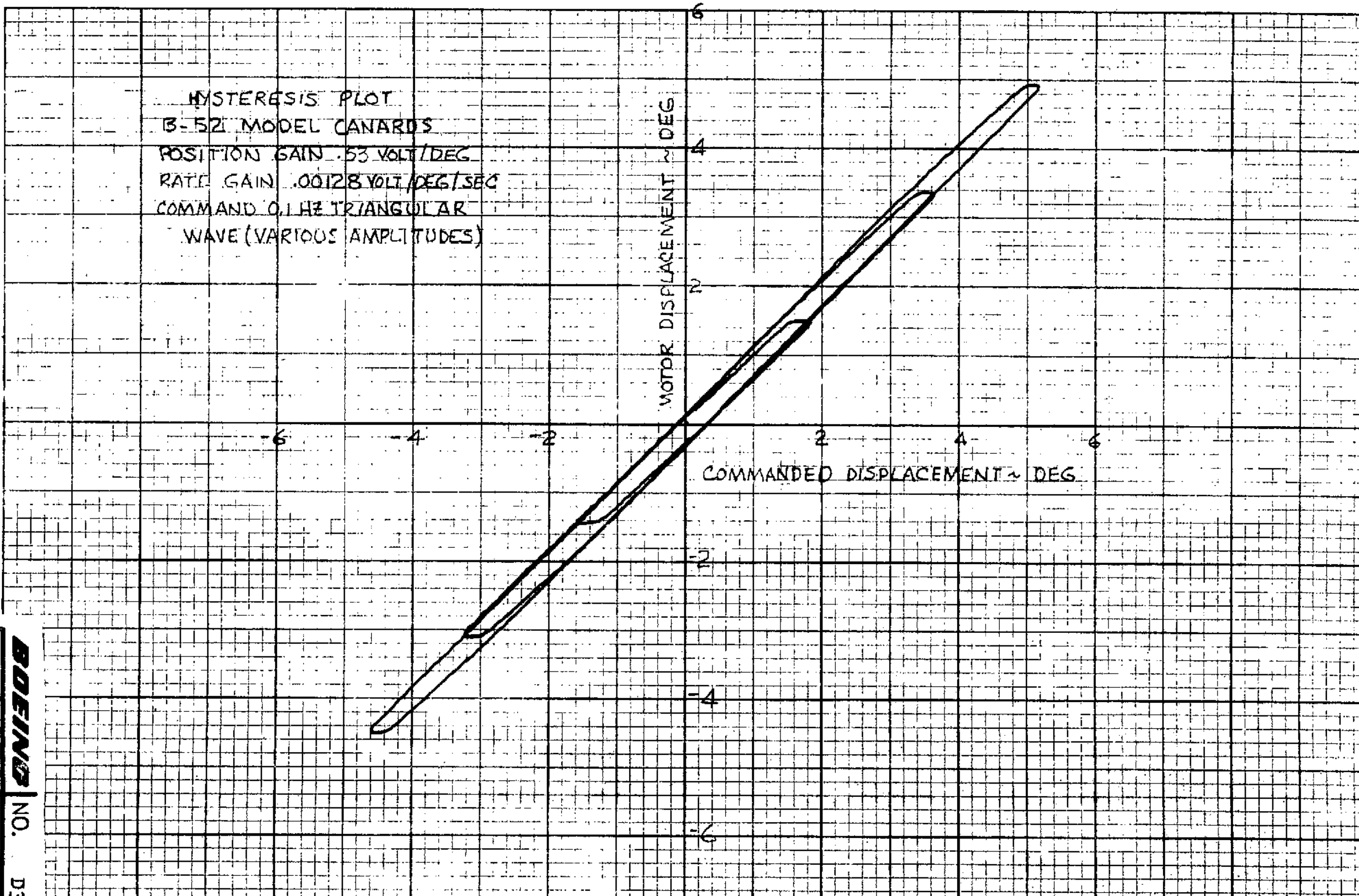

FIGURE 3.33: MODEL CANARD ACTUATION HYSTERESIS

4.0 B-52 AIRPLANE MANEUVER LOAD CONTROL SYSTEM

This section describes the 375,000 pounds gross weight B-52E airplane maneuver load control (MLC) system which will be flight tested under the CCV program. Presently, the NASA one-thirtieth scale B-52E model MLC analysis is being conducted and the final model MLC system will be mechanized and wind tunnel tested at the Langley Research Center to permit correlation of model and airplane test results.

4.1 Introduction

The objective of this study was to design a maneuver load control system to reduce wing root vertical bending moments per 1.0 g incremental maneuver by at least 10 percent of the airplane structural design limit. Airplane and model test conditions are given in Table 4-I. The airplane maneuvers will be truncated to ±0.5 g and ±0.25 g at flight conditions 1 and 2 respectively. Ramp and hold and triangular column inputs shown in Figure 4.1 were used for typical airplane maneuvers in the analyses.

TABLE 4-I

AIRPLANE AND MODEL MLC SYSTEM TEST CONDITIONS

		Flight Condition 1		Flight Condition 2	
	Units	Airplane	Model	Airplane	Model
Gross Weight	Pounds	375000	56.7	375000	56.7
Altitude	Feet	21000	-	21000	-
Calibrated Airspeed	KCAS	280	-	225	-
True Airspeed	Ft/Sec	642	117.5	522	95.6
Mach	-	.622	0.247	.505	0.200
Dynamic Pressure	Pounds/Ft^2	253	34.4	164.5	22.4
Density	Slugs/Ft^3	0.00122	0.00498	0.00122	0.00498

The MLC system designed for the CCV program has been modified to provide the desired bending moment reduction for the two airplane conditions. The system utilizes the elevator, flaperon and outboard aileron control surfaces with vertical acceleration at Body Station 860 and pitch rate at Body Station 810 feedback through appropriate signal shaping filters.

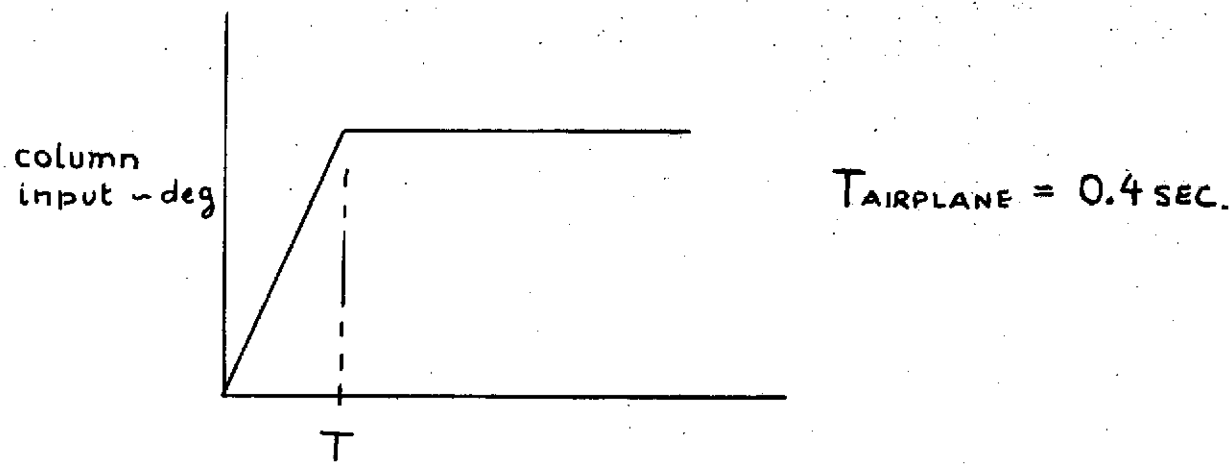

(a) RAMP AND HOLD

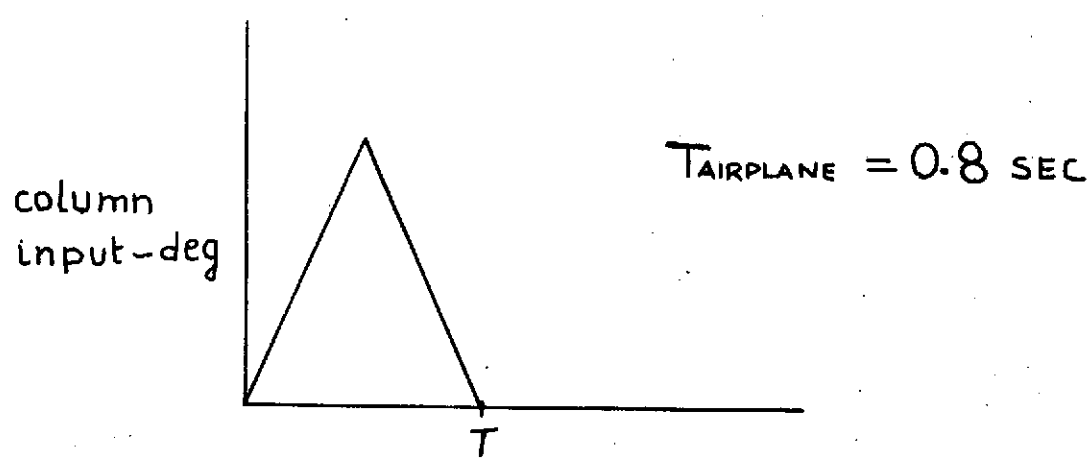

(b) TRIANGULAR

FIGURE 4.1 TYPICAL COLUMN INPUTS

Open and closed loop airplane wing root bending moments for 1.0 g maneuvers with ramp and hold and triangular inputs are given in Table 4-II.

TABLE 4-II

AIRPLANE WING ROOT BENDING MOMENTS

Inch Pound/g

Type of Column Input	OPEN LOOP		CLOSED LOOP	
	Flight Cond. 1 280 KCAS	Flight Cond. 2 225 KCAS	Flight Cond. 1 280 KCAS	Flight Cond. 2 225 KCAS
Ramp and Hold (Steady State Loads)	-38.23×10^6	-41.26×10^6	-24.14×10^6	-30.40×10^6
Triangular (Peak Loads)	-34.41×10^6	-34.41×10^6	-31.24×10^6	-32.42×10^6

Since airplane structural design limit is 80×10^6 inch pounds, the airplane MLC system was required to reduce the maximum wing root bending moments by at least 8×10^6 inch pounds. From plots of open and closed loop wing root bending moments versus calibrated airspeed in Figure 4.2, it is seen that the airplane MLC system performance meets the design requirements at both test conditions.

4.2 Airplane MLC Analysis

A maneuver load control system for 267,000 pounds gross weight airplane was designed under the Control Configured Vehicles (CCV) program. This MLC system was initially evaluated on the heavy gross weight (375,000 pounds) airplane at test conditions given in Table 4-I. The system was then modified to obtain the required wing root bending moment reduction of 10 percent of the structural design limit.

4.2.1 Mathematical Model

A 30 degree-of-freedom symmetric axis math model was developed for the 375,000 pounds B-52E airplane with Mach 0.6 aerodynamic parameters. Unsteady aerodynamic effects were included and the final equations of motion were written in the form shown in Section 2.2. The elevator, flaperon and outboard aileron actuation system dynamics given below were used in the analysis.

Elevator

$$\frac{\delta_{Surface}}{V_{Command}} = \frac{1.88}{\left(\frac{S}{46} + 1\right)\left(\frac{S^2}{95^2} + \frac{.35S}{95} + 1\right)} \quad \frac{\text{deg}}{\text{volt}}$$

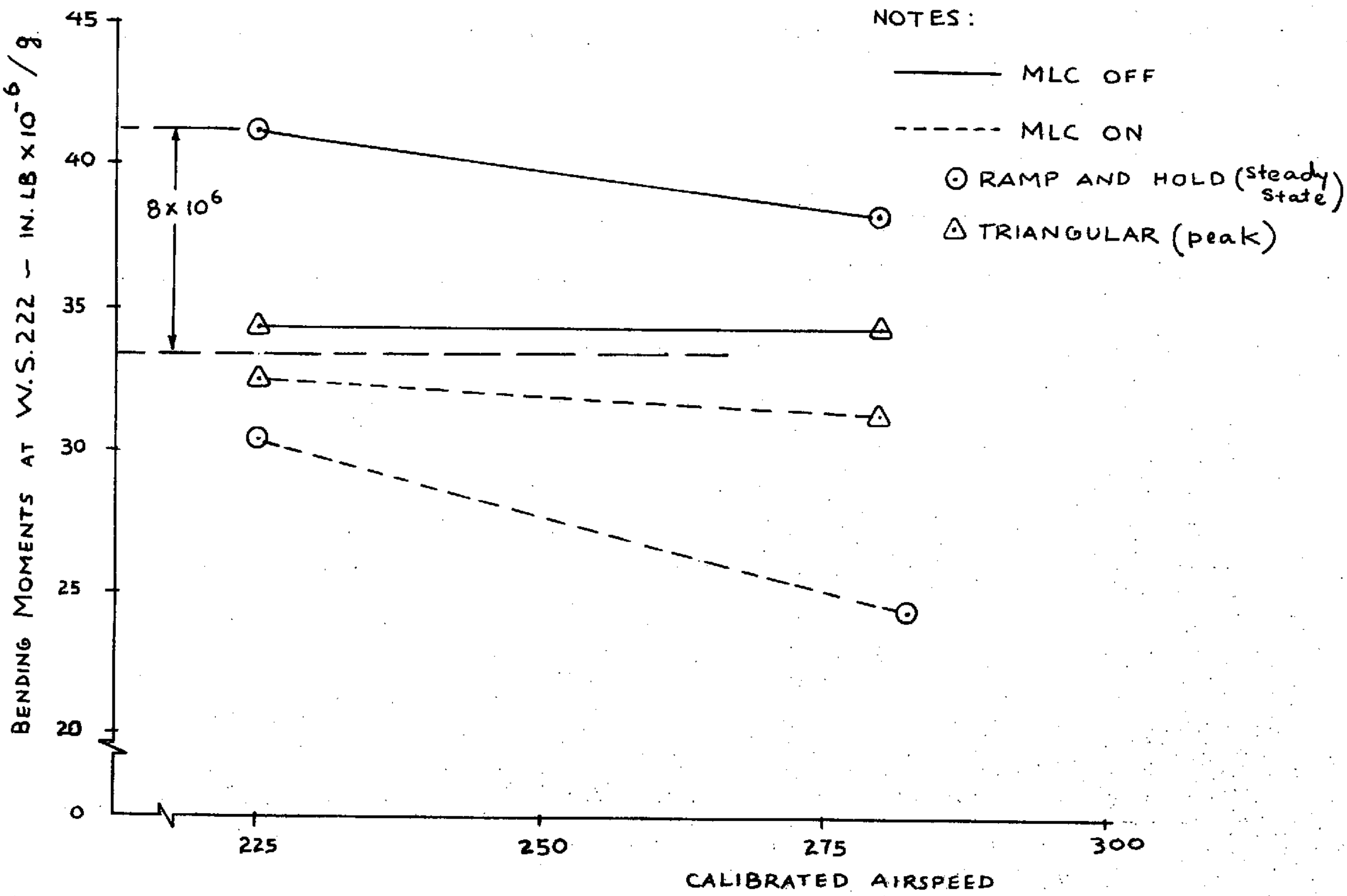

FIGURE 4.2 AIRPLANE MLC SYSTEM PERFORMANCE

Flaperon

$$\frac{\delta_{Surface}}{V_{Command}} = \frac{2.0}{\left(\frac{S}{51} + 1\right)\left(\frac{S^2}{181^2} + \frac{.76S}{181} + 1\right)} \quad \frac{deg}{volt}$$

Outboard Aileron

$$\frac{\delta_{Surface}}{V_{Command}} = \frac{2.0}{\left(\frac{S}{51} + 1\right)\left(\frac{S^2}{200} + \frac{.76S}{200} + 1\right)} \quad \frac{deg}{volt}$$

In addition, the open loop column input to the elevator actuator was applied through an electromechanical servo given by the following transfer function:

$$\frac{19/17}{\left(\frac{S^2}{8.15^2} + \frac{S}{8.15} + 1\right)} \quad \frac{deg}{volt}$$

4.2.2. MLC Analysis

The MLC analysis was conducted with the short period rigid body mode and the first eleven elastic modes. Open loop time histories of vertical acceleration at the center of gravity and wing root (Wing Station 222) bending moments due to ramp and hold and triangular inputs were obtained. Figures 4.3 to 4.6 show the open loop responses for the 225 KCAS and 280 KCAS test conditions. Steady state and peak wing root bending moments for a 1.0 g incremental acceleration were calculated for ramp and hold and triangular inputs respectively. The open loop loads are tabulated in Table 4-II.

The MLC system in Figure 4.7 was evaluated on the heavy gross weight airplane with system gains selected for the 267,000 pounds gross weight airplane but the nominal system did not provide satisfactory wing root bending moment reduction. Therefore, a prefilter crossfeed gain (K_{C_F}) and washout time constant (τ) variation study was conducted. Figures 4.8 and 4.9 show effects of crossfeed gain and washout time constant on system performance. The column gain (K_C) was computed to obtain steady state 1.0 g acceleration for a 6 degree column input with MLC off and the elevator gain (K_E) was calculated to obtain similar 1.0 g steady state closed loop airplane response with the flaperon and outboard aileron gains (K_F and K_A) at 10 degrees/g. Final system gains for both test conditions are given in Table 4-III.

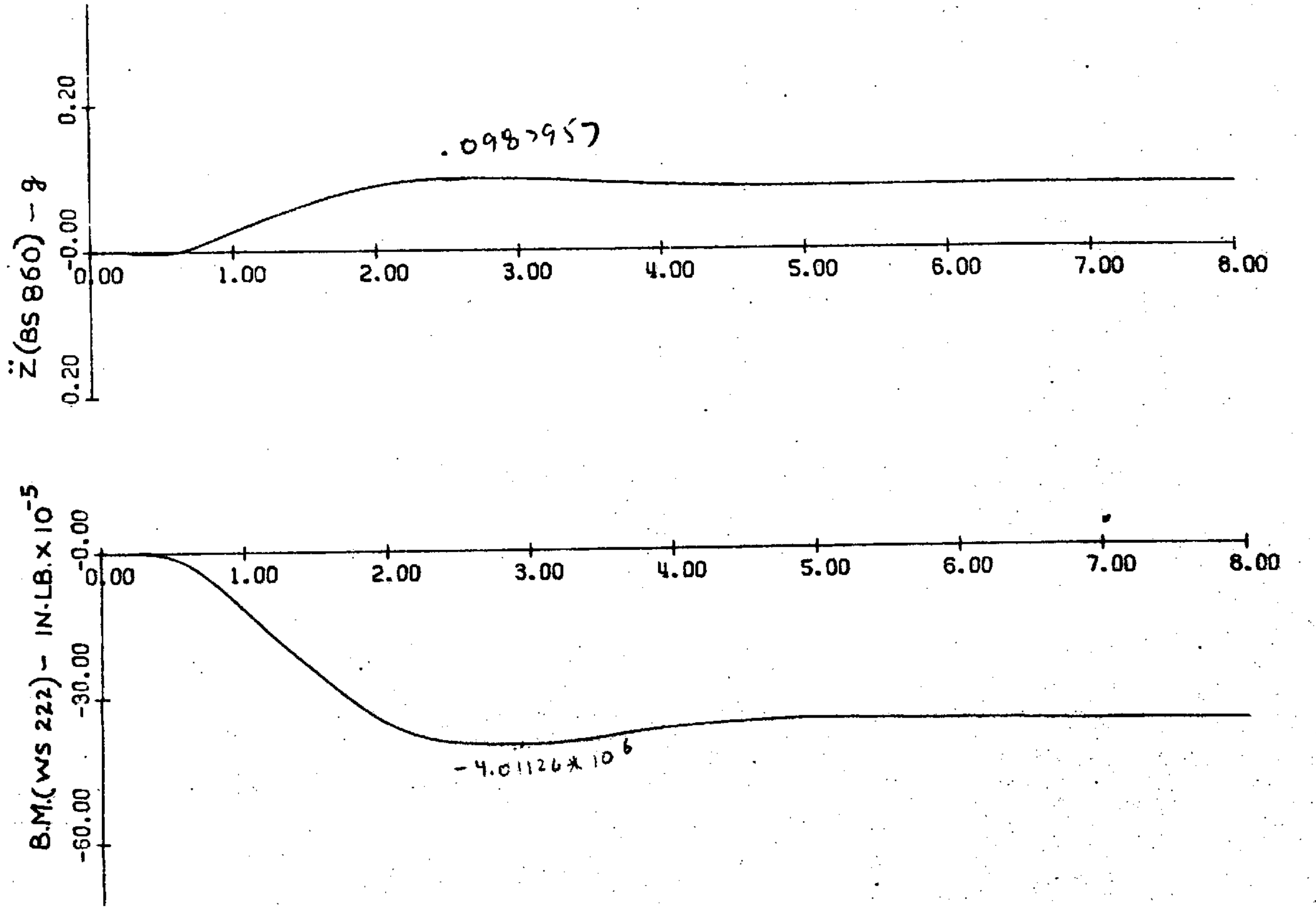

FIGURE 4.3 225 KCAS, OPEN LOOP RAMP AND HOLD RESPONSES

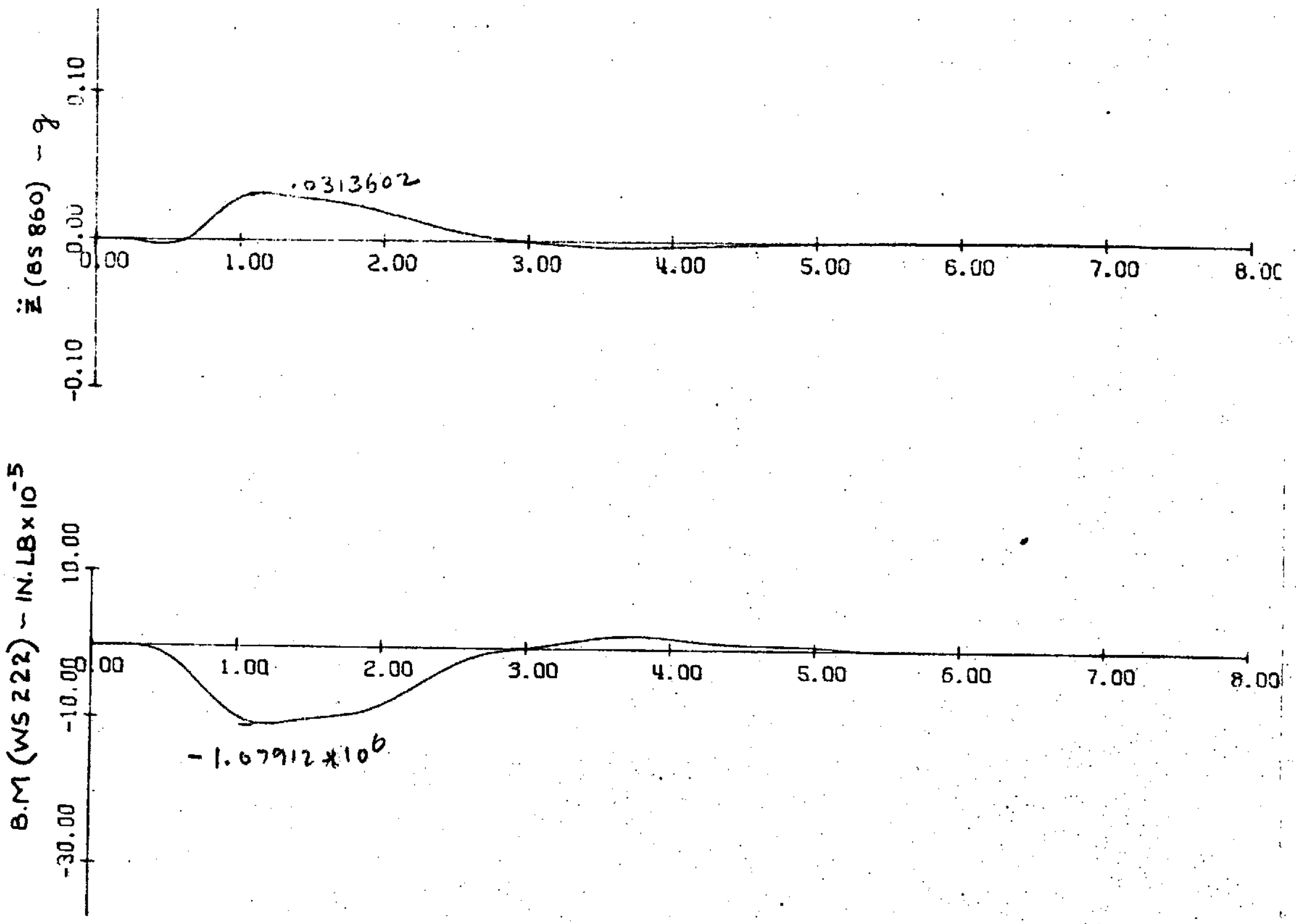

FIGURE 4.4 225 KCAS, OPEN LOOP TRIANGULAR RESPONSES

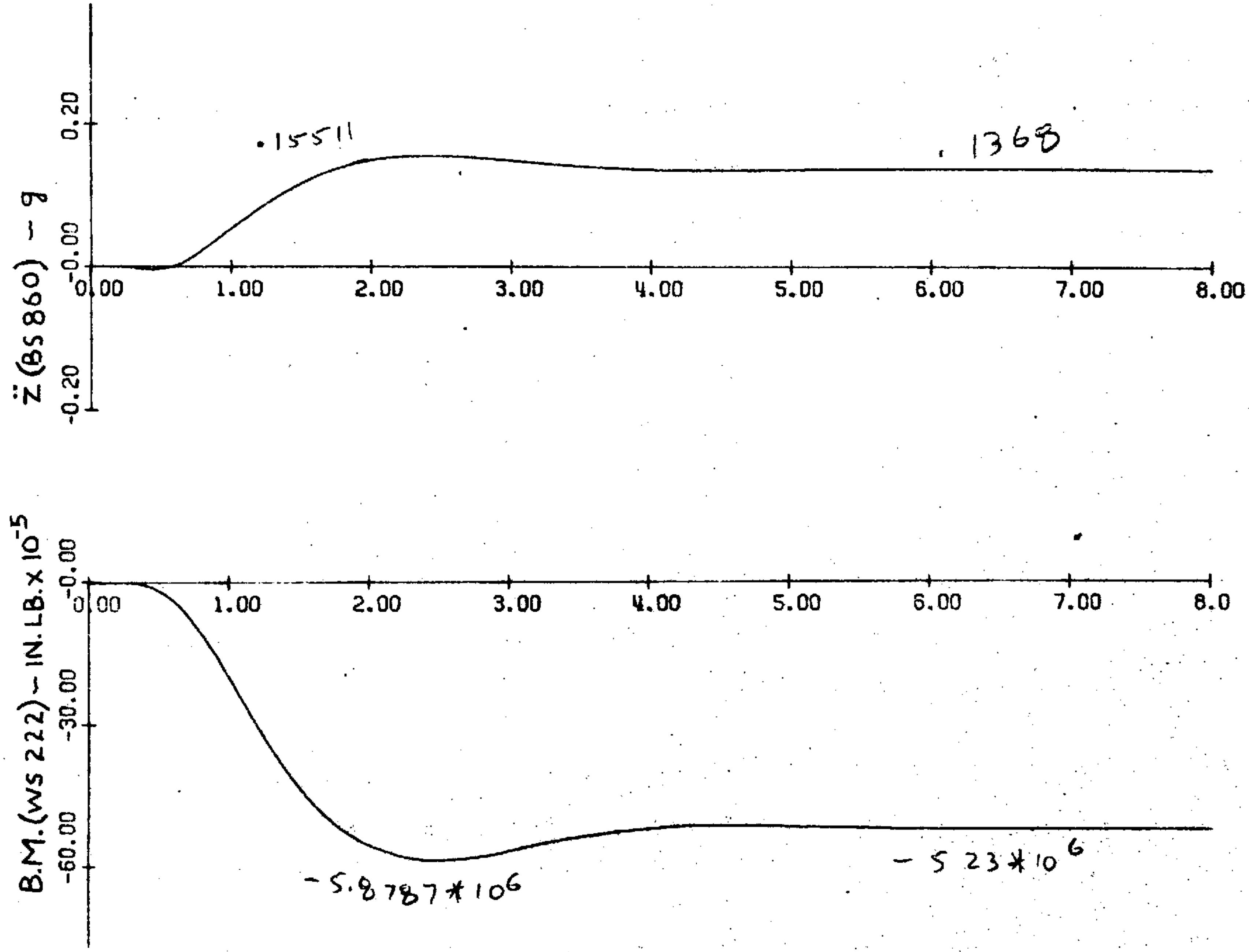

FIGURE 4.5 280 KCAS, OPEN LOOP RAMP AND HOLD RESPONSES

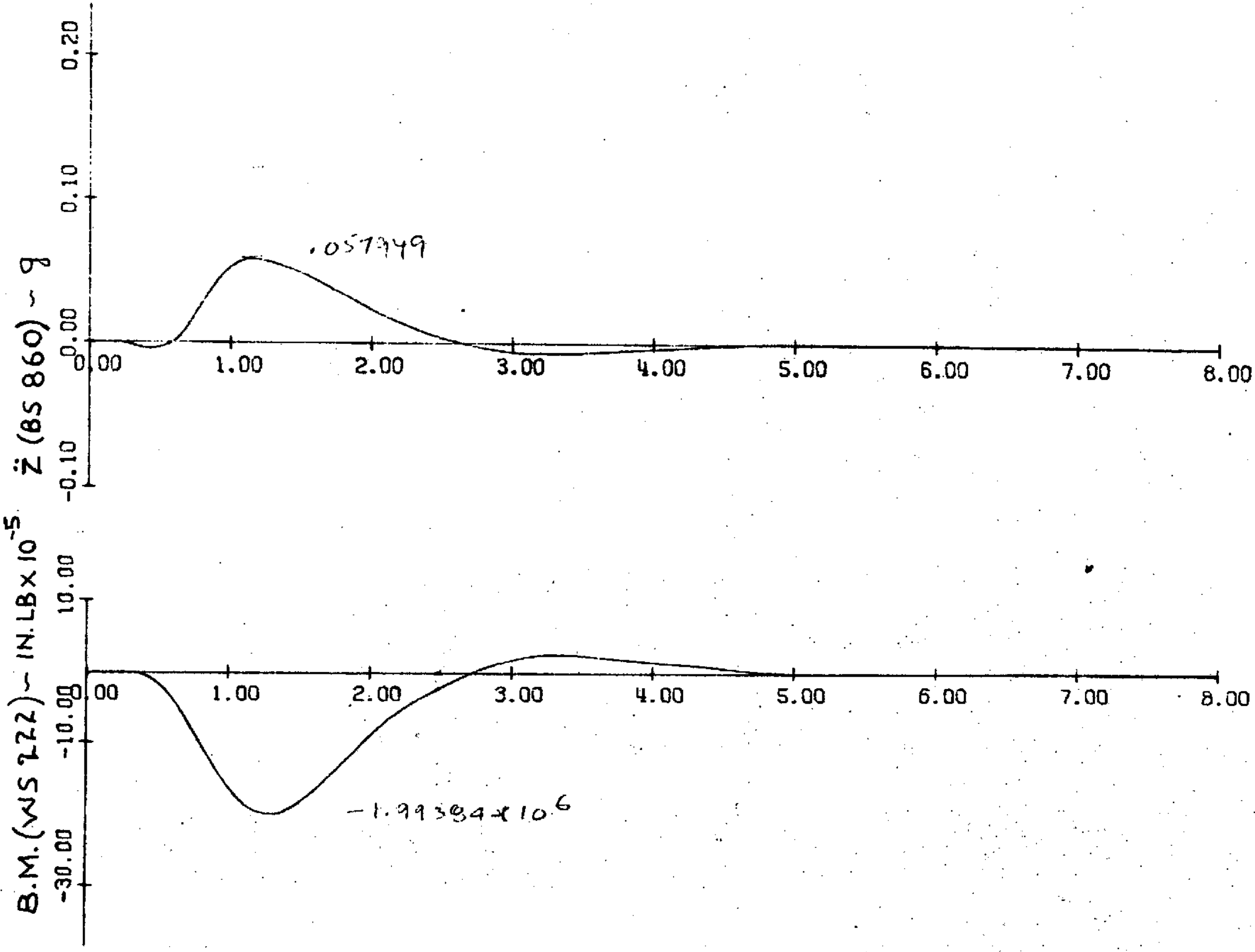

FIGURE 4.6 280 KCAS, OPEN LOOP TRIANGULAR RESPONSES

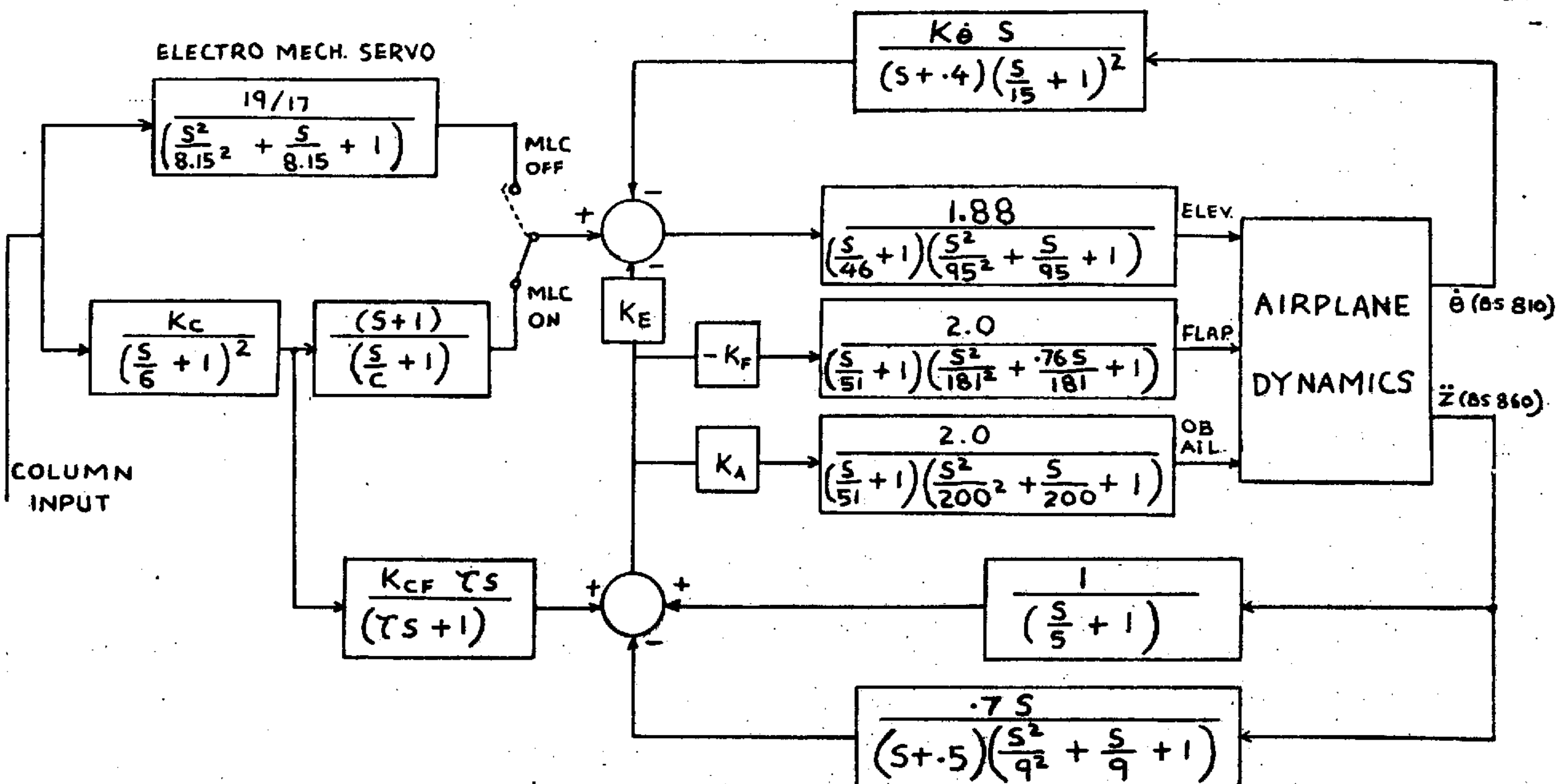

FIGURE 4.7 AIRPLANE MLC BLOCK DIAGRAM

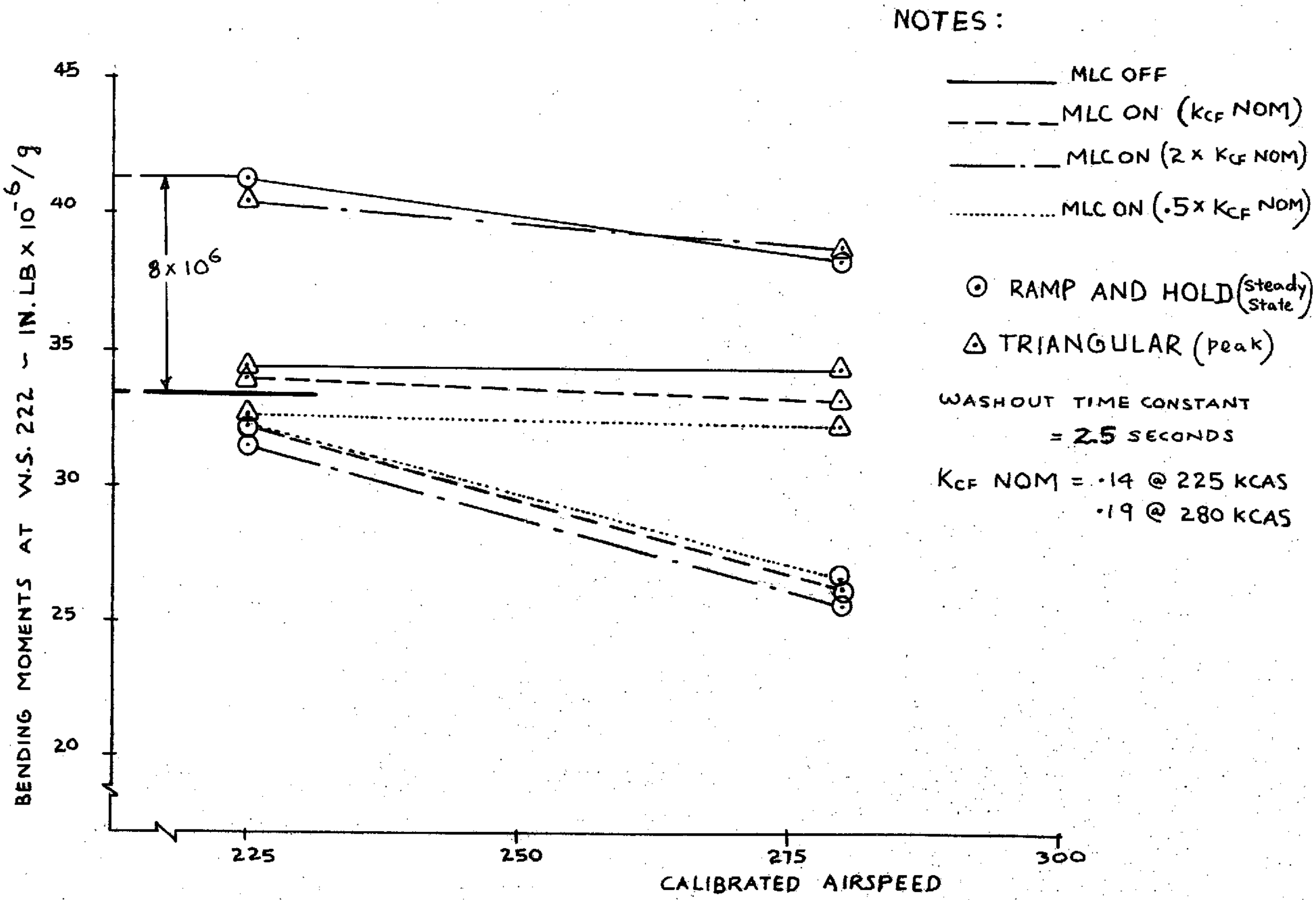

FIGURE 4.8 CROSS FEED GAIN (K_{CF}) VARIATION

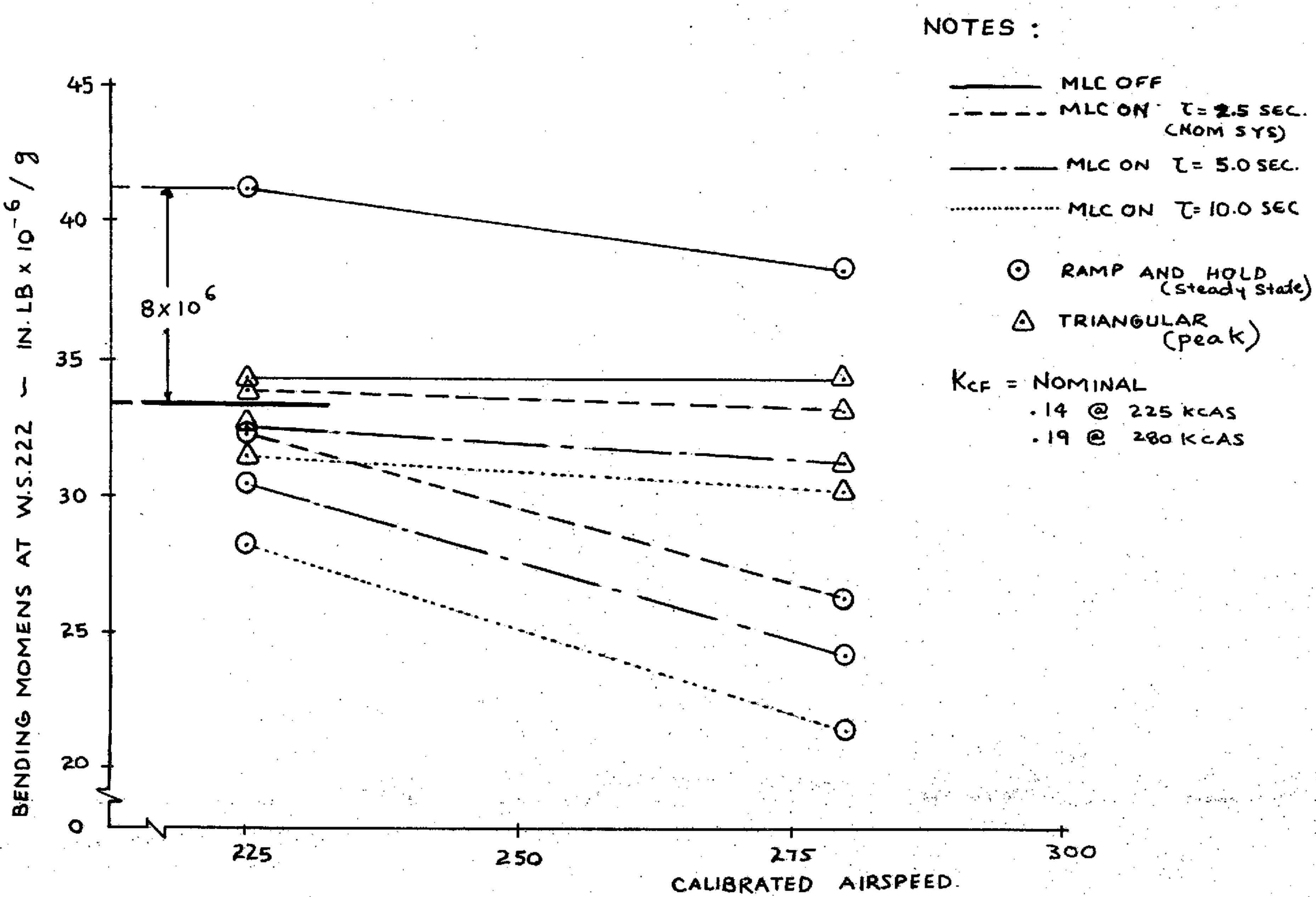

FIGURE 4.9 WASHOUT TIME CONSTANT (τ) VARIATION

TABLE 4-III

MLC SYSTEM PARAMETERS

Test Condition	K_E	K_F	K_A	K_θ	K_C	C	K_{C_F}	τ
1 (280 KCAS)	4-24	10	10	0.29	0.72	2	0.19	5
2 (225 KCAS)	4-38	10	10	0.36	1.13	2	0.14	5

Figures 4.10 to 4.17 show closed loop airplane responses for ramp and hold and triangular inputs at both test conditions. Bending moments at Wing Station 222 for a 1.0 g incremental acceleration were calculated. Table 4-II lists these closed loop loads at the wing root.

Maximum open loop wing root bending moments of 41.26×10^6 inch pounds steady state per g are obtained with the ramp and hold column input. The MLC system is required to reduce maximum loads by 8×10^6 inch pounds per g. Therefore, the closed loop bending moment must not exceed 33.26 inch pounds per g. Figure 4.2 indicates that the airplane MLC system reduces the closed loop loads below the required limit at both test conditions.

4.3 Remaining Work

Initial model analysis was conducted with the airplane MLC filter time constants appropriately scaled and the column and elevator (K_C and K_E) gains computed to obtain a 1.0 g steady state maneuver for 6 degree column inputs with MLC off and on. The results indicate that due to the differences in the rigid body dynamics of the "free-flying" airplane and the cable constrained model, the airplane and model responses to the ramp and hold and triangular column inputs are considerably different. The model steady state and peak loads per 1.0 g maneuver could not be calculated from the model responses.

Further analysis should therefore be conducted to define column inputs which would generate acceptable model and airplane responses. Also, if necessary, the scaled airplane MLC system should be modified to obtain the required MLC performance.

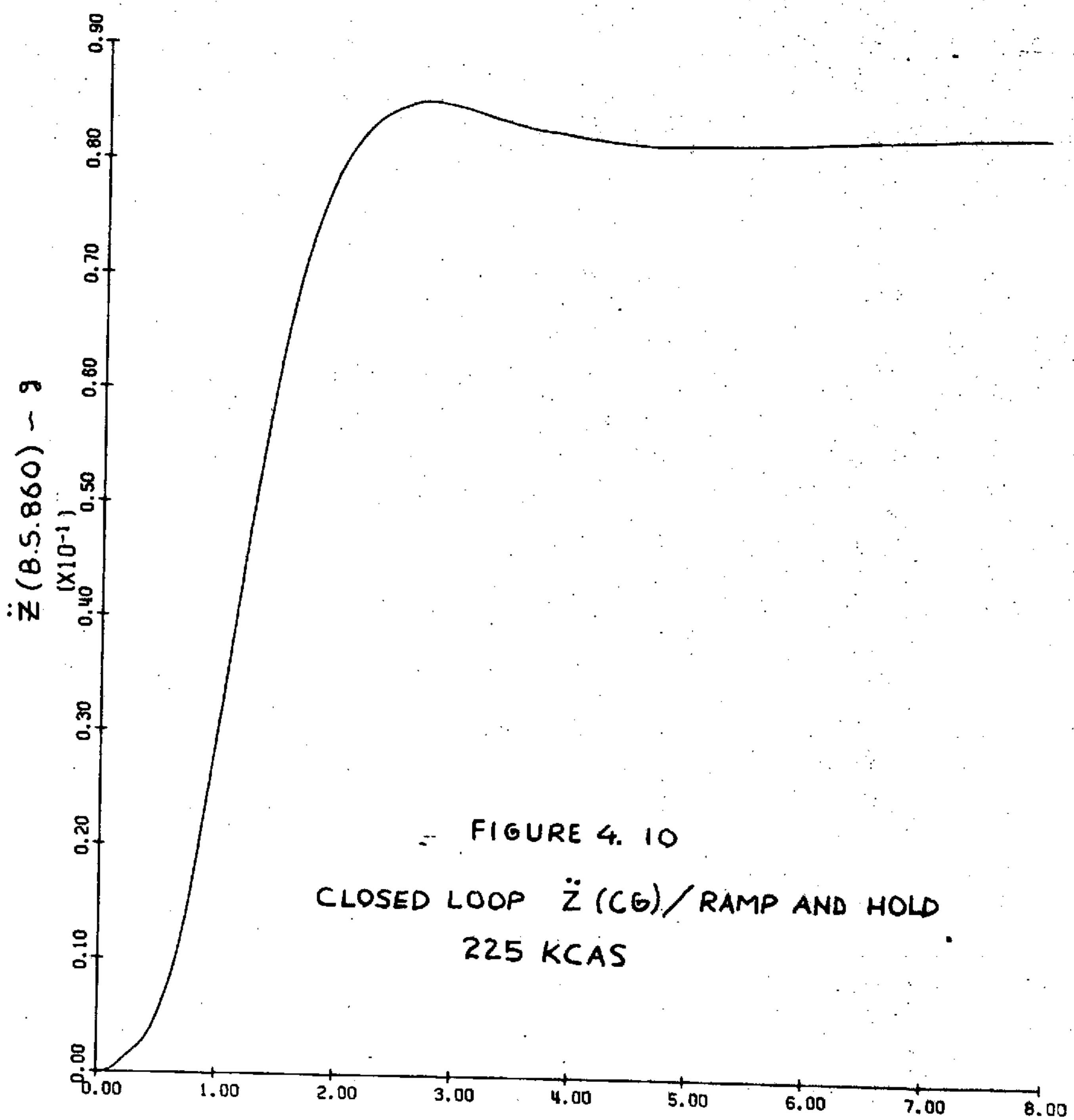

FIGURE 4.10

CLOSED LOOP $\ddot{Z}$ (CG)/RAMP AND HOLD
225 KCAS

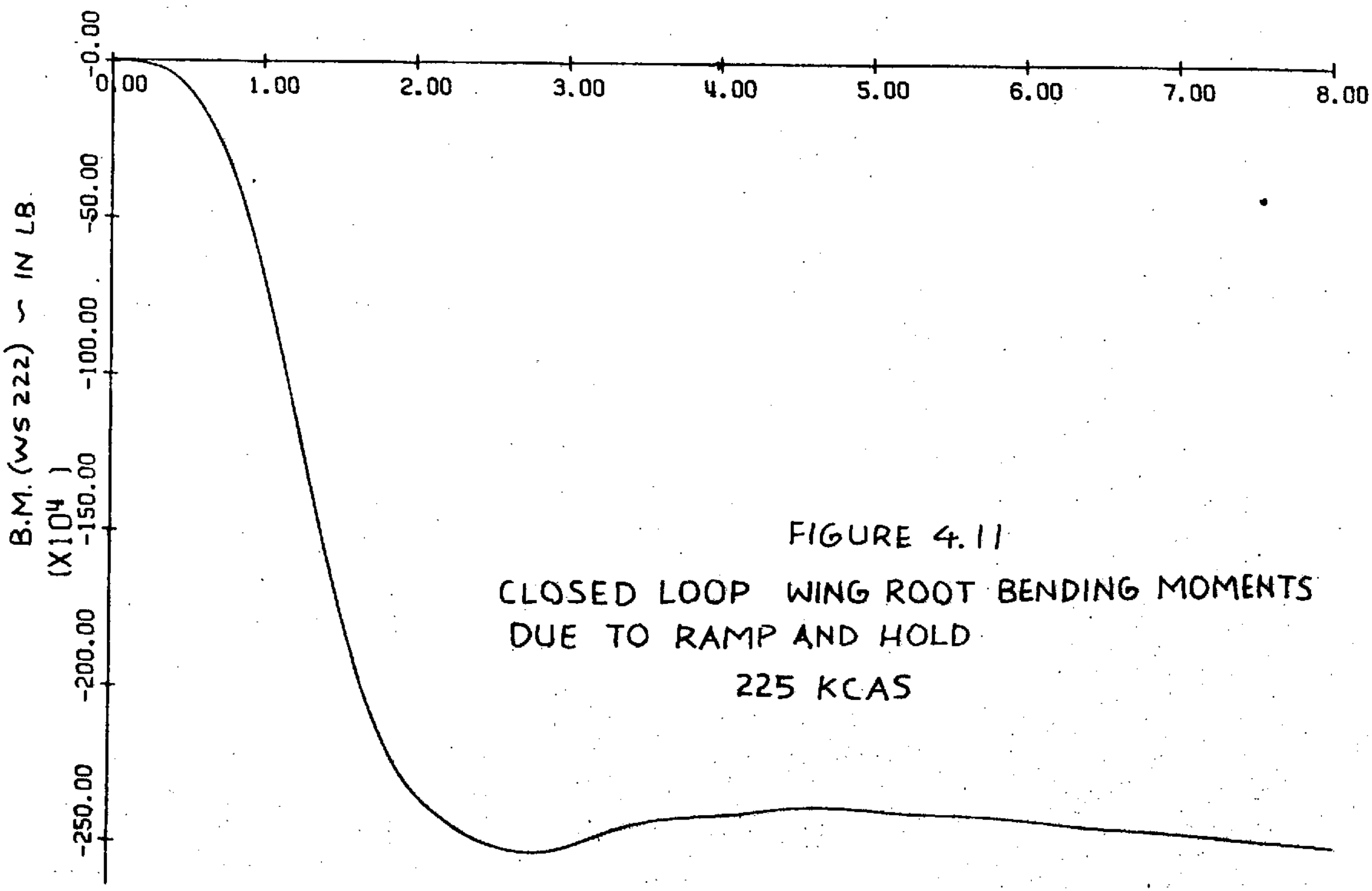

FIGURE 4.11

CLOSED LOOP WING ROOT BENDING MOMENTS
DUE TO RAMP AND HOLD
225 KCAS

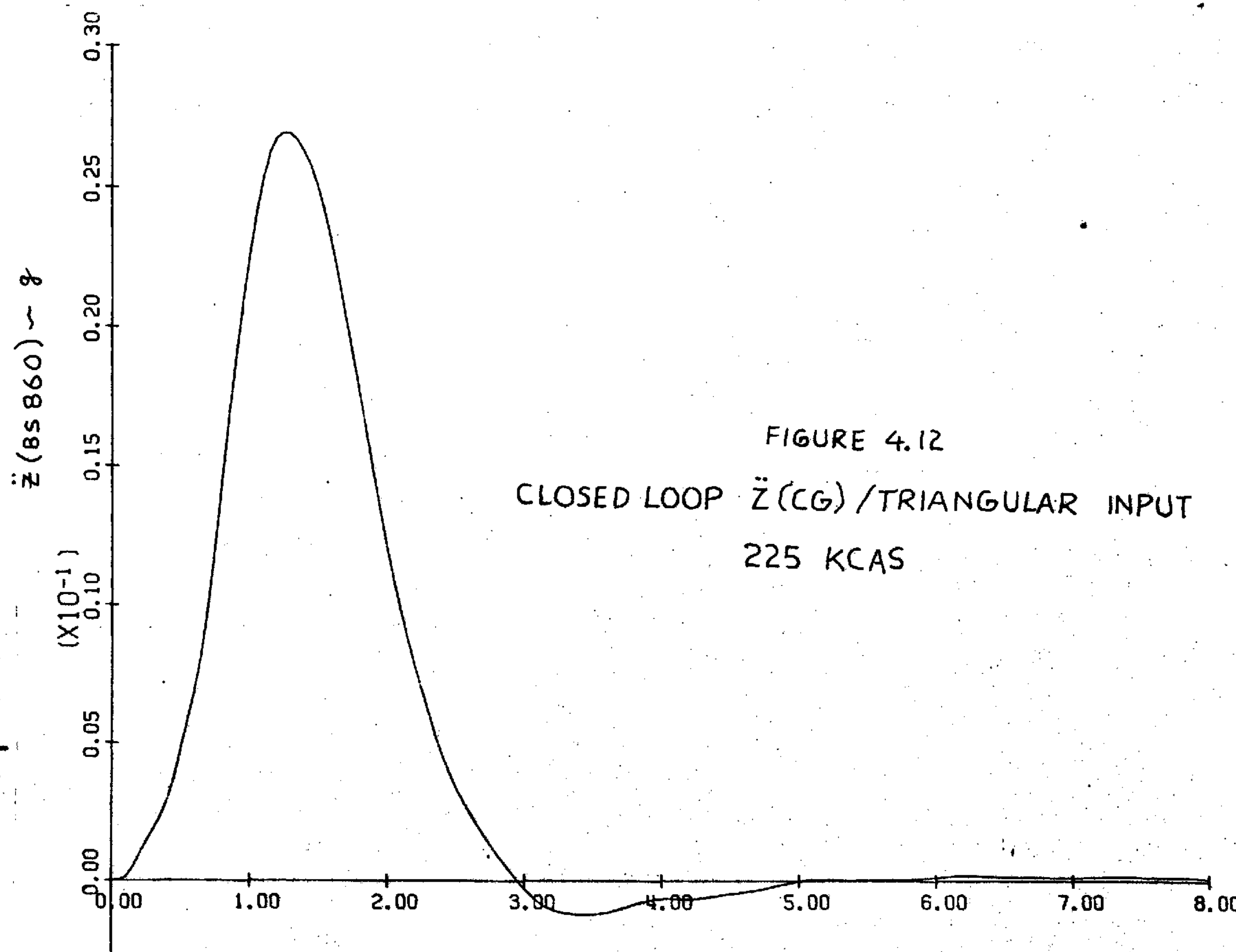

FIGURE 4.12

CLOSED LOOP $\ddot{Z}$ (CG) / TRIANGULAR INPUT

225 KCAS

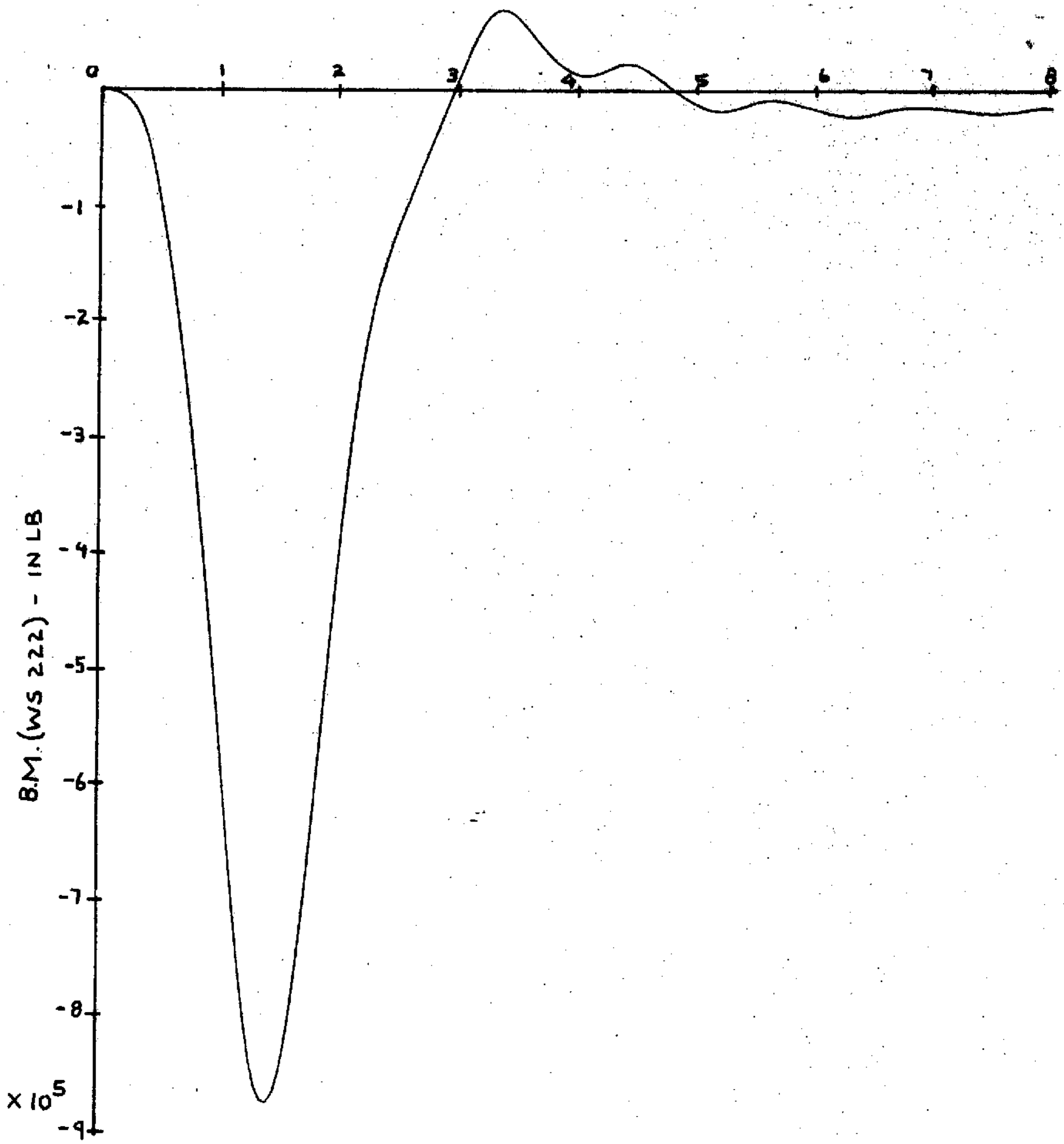

FIGURE 4.13

CLOSED LOOP WING ROOT BENDING MOMENTS / TRIANGULAR INPUT 225 KCAS

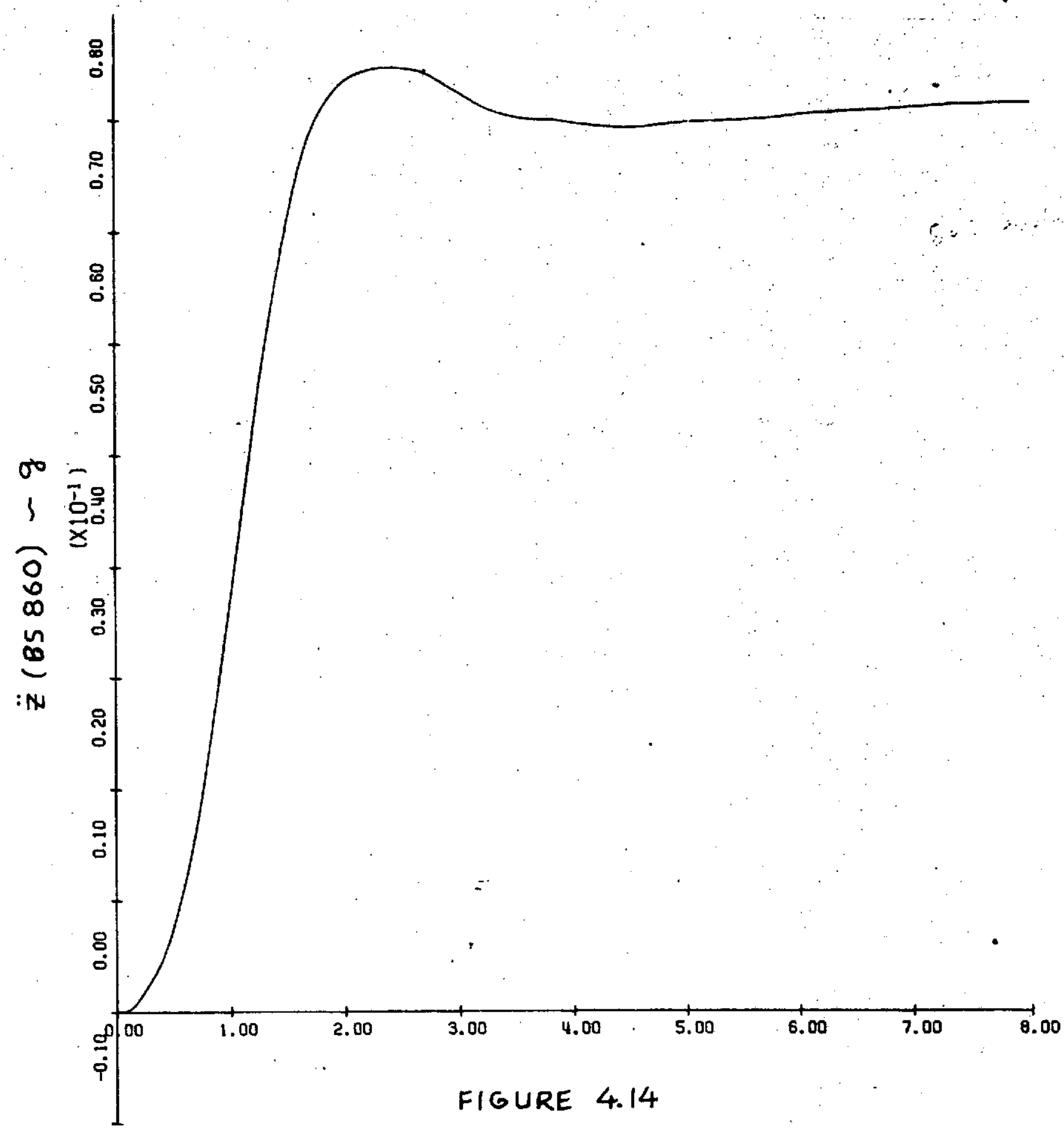

FIGURE 4.14

CLOSED LOOP $\ddot{Z}$ (CG)/RAMP AND HOLD
280 KCAS

REV LTR:

E-3033 R1

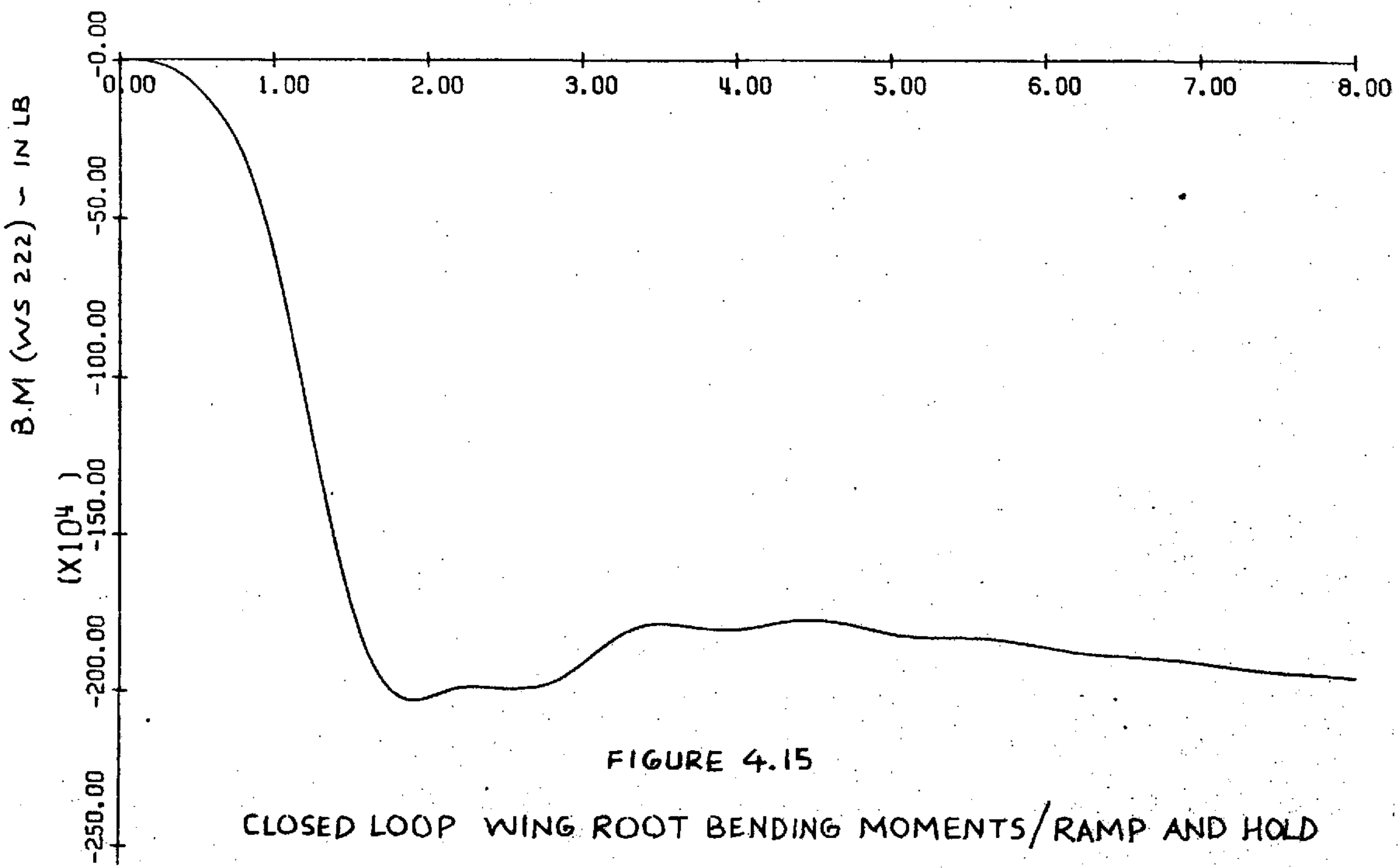

FIGURE 4.15

CLOSED LOOP WING ROOT BENDING MOMENTS/RAMP AND HOLD

280 KCAS

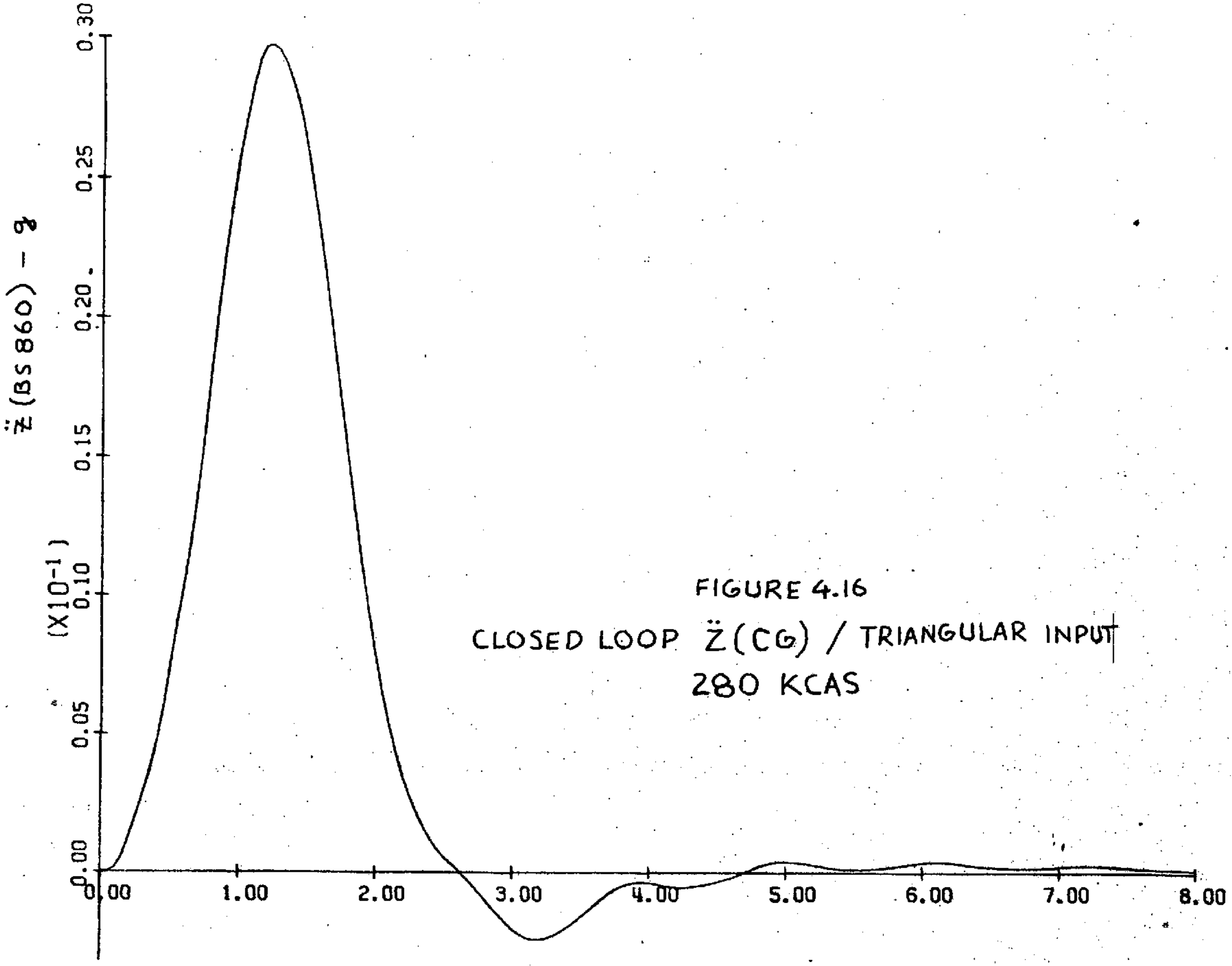

FIGURE 4.16
CLOSED LOOP $\ddot{Z}$(CG) / TRIANGULAR INPUT
280 KCAS

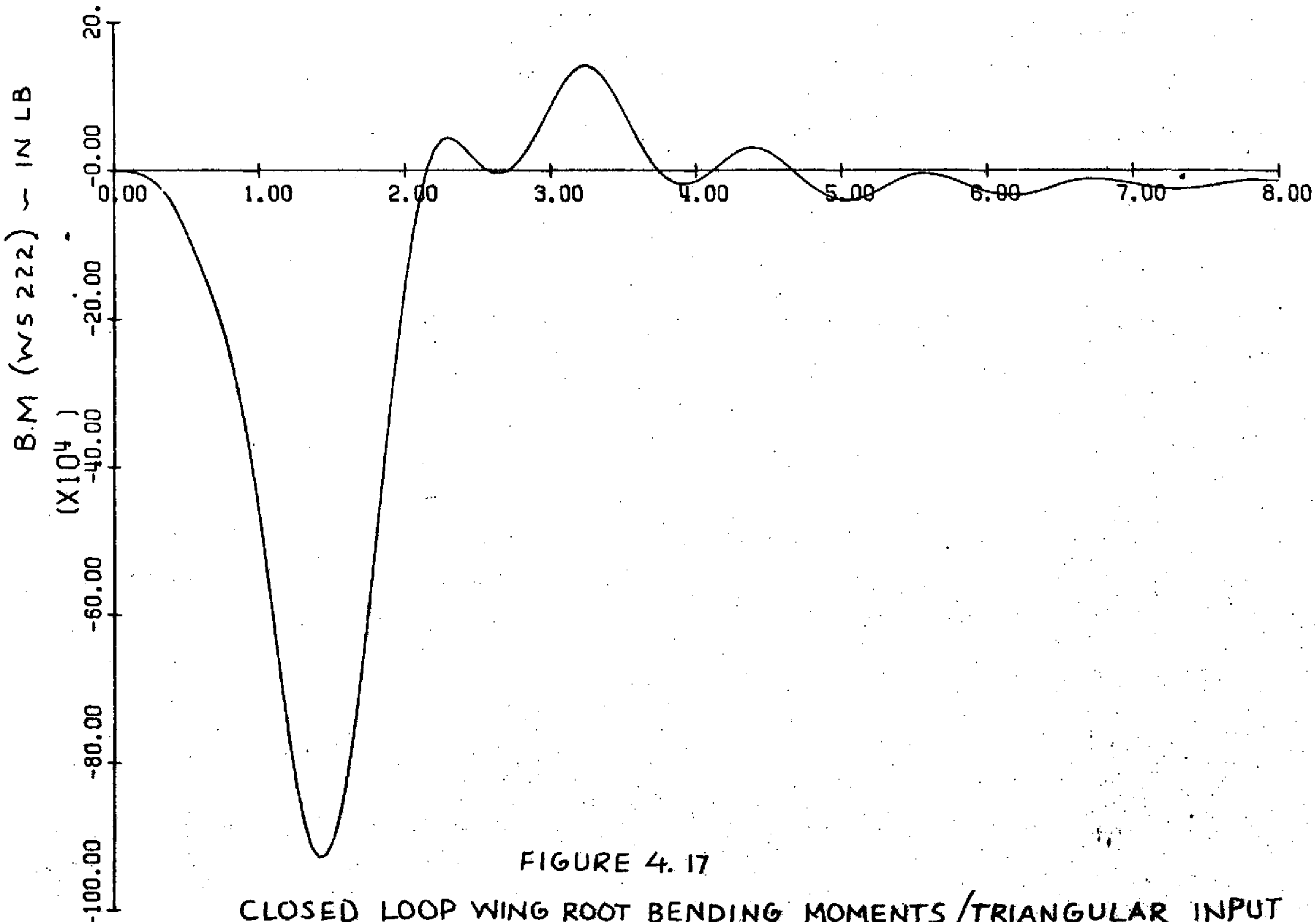

FIGURE 4.17

CLOSED LOOP WING ROOT BENDING MOMENTS/TRIANGULAR INPUT

280 KCAS

5.0 REFERENCES

1. Boeing Document D3-8884, "Analysis and Testing of Stability Augmentation Systems - Final Report," 13 June 1972.

2. Boeing Document D3-8390-3, "Evaluation of B-52 Aeroelastic Model Control Surface Actuation Systems," 4 March 1971.